materials innovation institute

ISBN: 978-90-365-4666-9
DOI: 10.3990/1.9789036546669

Towards a Fundamental Understanding of the Tribological Behaviour of Cam-Roller Follower Contacts Shivam Alakhramsing

Towards a Fundamental Understanding of the Tribological Behaviour of Cam-Roller Follower Contacts

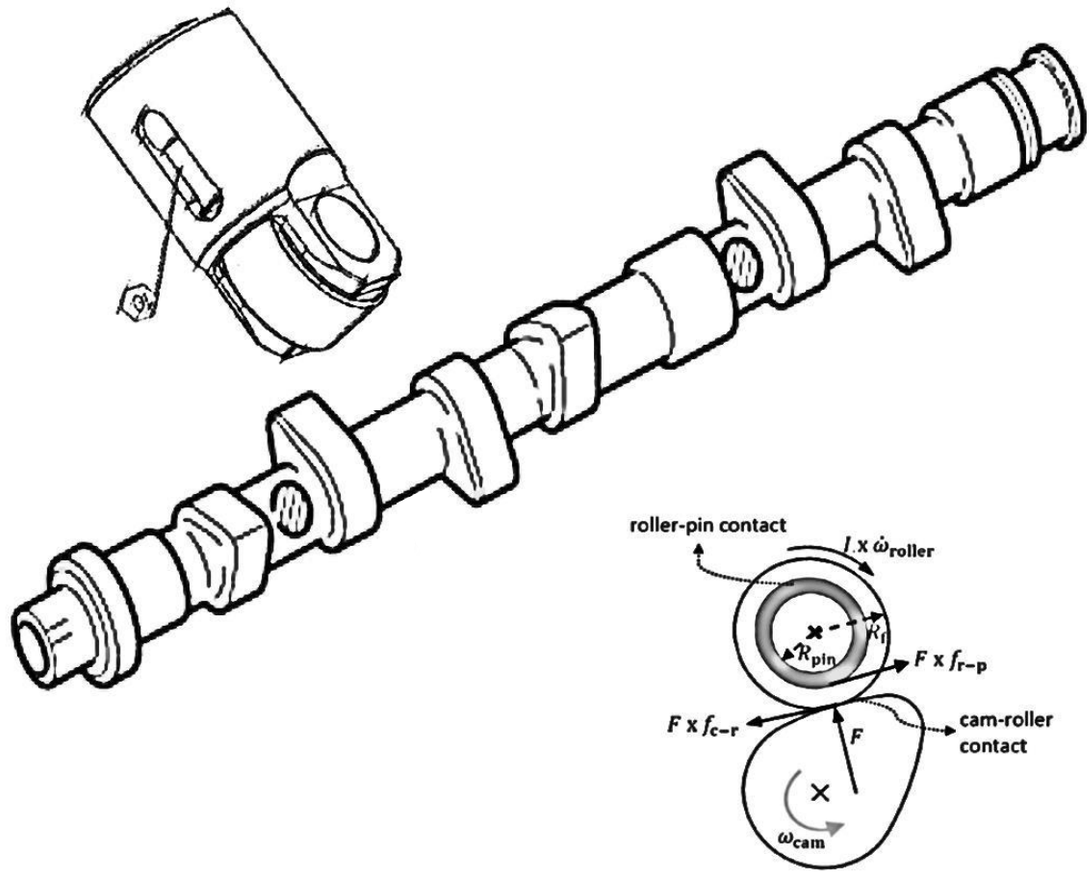

Shivam Alakhramsing

Towards a Fundamental Understanding of the Tribological Behaviour of Cam-Roller Follower Contacts

Shivam Sharwien Alakhramsing

Faculty of Engineering Technology,
Department of Surface Technology and Tribology,
University of Twente

This research was carried out under project number F21.1.13502 in the framework of the Partnership Program of the Materials innovation institute M2i (www.m2i.nl) and the Netherlands Organization for Scientific Research (www.nwo.nl).

Graduation committee:
Prof. dr. G.P.M.R. Dewulf, University of Twente, Chairman/secretary
Dr.ir. M.B. de Rooij, University of Twente, Supervisor
Prof. dr.ir. D.J. Schipper, University of Twente, Co-supervisor
Prof. dr. ir. A. de Boer, University of Twente
Prof.dr.ir. A.H. van den Boogaard, University of Twente
Dr.ir. R.A.J. van Ostayen, Delft University of Technology
Prof. dr. A. Almqvist, Luleå University of Technology

Shivam Alakhramsing
Towards a fundamental understanding of the tribological behaviour of cam-roller follower contacts,
PhD Thesis, University of Twente, Enschede, the Netherlands, January 2019

ISBN: 978-90-365-4666-9
DOI :10.3990/1.9789036546669

TOWARDS A FUNDAMENTAL UNDERSTANDING OF THE TRIBOLOGICAL BEHAVIOUR OF CAM-ROLLER FOLLOWER CONTACTS

DISSERTATION

to obtain
the degree of doctor at the University of Twente,
on the authority of the rector magnificus,
prof.dr. T.T.M. Palstra,
on account of the decision of the graduation committee,
to be publicly defended
on Wednesday the 23rd of January 2019 at 14:45 hours

by

Shivam Sharwien Alakhramsing
born on the 24th November 1991
in Paramaribo, Suriname

This dissertation has been approved by
Supervisor: Dr.ir. M.B. de Rooij
Co-supervisor: Prof. dr.ir. D.J. Schipper

to Reshmi and Sid
to my mother, Sila
in memory of my father, Jai

Summary

Cam-roller followers are part of the valve train mechanisms found in internal combustion engines. Valve train friction losses may contribute up to 10% of the total engine friction losses. The lubricated cam-roller follower unit consists of two lubricated contacts, namely the cam-roller contact and roller-pin contact. While the former is a non-conformal contact, the latter is a conformal contact. The traction induced by the cam-roller contact drives the roller. It is important to study friction between the cam and roller as it influences the engine efficiency and the onset of wear – and thus ultimately lifetime – of components. Understanding lubrication conditions in the cam-roller contact is complicated due to transient variations of the geometry, force and friction in the roller-pin contact. A very important variable, affecting the cam-roller lubrication performance, is the frictional force (which resists the motion of the roller) at the roller-pin contact. The lubricated cam-roller contact studied in this thesis is highly loaded with contact forces up to 16 kN. Important lubrication performance indicators of the cam-roller contact are the pressure, film thickness and frictional force.
This thesis focuses on the factors influencing the aforementioned lubrication performance indicators. Relying on the aforementioned, the factors studied in this work are:

- *The influence of axial shape of the roller:*
  The axial shape of the roller and its influence on the generated film thickness, pressure and friction in the cam-roller contact. This was done by means of a smooth surface finite element method (FEM)-based finite line contact elastohydrodynamic lubrication (EHL) model. The model shows the effects of parameters describing the axial shape of the roller, velocity, load and material properties on the lubrication performance indicators.

- *The influence of elastic deformation in the roller-pin contact:*
  In order to better quantify the friction, film thickness and pressure in the roller-pin contact a similar smooth surface FEM-based EHL model was developed for the roller-pin contact. The model demonstrates the importance of allowing for elastic deformation of the conformal roller-pin contact and its effect on film thickness, pressure and friction coefficient.

- *The influence of roller-pin contact friction in the **high** slide-to-roll ratio (SRR) domain of the cam-roller contact:*
  At increasing levels of friction in the roller-pin contact the amount of sliding at the cam-roller contact increases, in turn affecting the film thickness, pressure and cam-roller contact friction coefficient. In order to analyse the effects of higher values of roller-pin friction coefficient on the cam-roller lubrication performance, an infinite

line contact mixed-thermo-elastohydrodynamic (TEHL) model was developed for the cam-roller contact. The mixed-lubrication model is based on the load-sharing concept and uses real surface roughness measurement data as input. The complete model is based on a smooth surface FEM-based EHL line contact model and a boundary element method (BEM)-based dry rough normal contact solver. The model exposes the influence of roller-pin friction coefficient on non-Newtonian, thermal and surface roughness effects in the cam-roller contact.

- *The influence of roller-pin contact friction in the **low** SRR domain of the cam-roller contact:*
  In order to improve mixed friction predictions under low sliding velocities, the dependence of boundary layer friction on sliding velocity was incorporated into the previously developed infinite line contact mixed lubrication model. This was done by means of a BEM-based dry rough tangential contact solver which was added to the previously developed model. The model shows how the shear stress-slip relationship influences the macroscopic frictional force in the cam-roller contact, under low sliding velocity operating conditions.

This thesis consists of two parts. The first part, which is Part A, comprises a summary of the work done. The second part, which is Part B, consists of the journal articles in which the details are described.

Samenvatting

Nok-rol volgers, zoals die genoemd worden, maken deel uit van de kleppentreinmechanismen in verbrandingsmotoren. Wrijvingverliezen behorende bij de kleppentreinen kunnen bijdragen tot wel 10% van de totale wrijvingsverliezen in de motor. Het gesmeerd nok-rol volger component bestaat uit twee gesmeerde contacten, namelijk het nok-rolcontact en het rol-pencontact. Terwijl de eerste een non-conform contact is, is de laatste een conform contact. De tractie geïnduceerd door het nok-rolcontact drijft de rol aan. Het is belangrijk om de wrijving tussen de nok en de rol te bestuderen, omdat dit de efficiency van de motor en de initiatie van slijtage - en dus de uiteindelijke levensduur - van de componenten beïnvloedt. Het begrijpen van smeringscondities in het nok-rolcontact is gecompliceerd vanwege tijdsafhankelijke variaties van de geometrie, kracht en wrijving in het contact. Een zeer belangrijke variabele, die de nok-rolsmering beïnvloedt, is de wrijvingskracht (die weerstand biedt aan de beweging van de rol) in het rol-pencontact. Het gesmeerd nok-rolcontact, bestudeerd in dit proefschrift, is een zwaar belast contact met contactkrachten tot wel 16 kN. Belangrijke smeringsprestatie-indicatoren van het nok-rolcontact zijn de druk, de smeeroliefilmdikte en de wrijvingskracht.
Dit proefschrift richt zich op de factoren die van invloed zijn op de smering van het hierboven beschreven contact. In dit proefschrit worden de volgende effecten bestudeerd:

- *De invloed van de axiale vorm van de rol:*
  De axiale vorm van de rol en zijn invloed op de gegenereerde filmdikte, druk en wrijving in het nok-rolcontact. Dit werd geanalyseerd middels een op de eindige-elementenmethode (FEM) gebaseerd elastohydrodynamisch smeerfilm (EHL) model. Dit model is geformuleerd op basis van een glad oppervlakkig eindig-lijncontact. Het model toont de effecten van parameters die de axiale vorm van de rol, snelheid, belasting en materiaaleigenschappen beschrijven, op de smeeringsprestatie-indicatoren.

- *De invloed van elastische vervorming in het rol-pencontact:*
  Om de wrijving, filmdikte en druk in het contact tussen rol en pen beter te kwantificeren, werd een FEM gebaseerd EHL-model ontwikkeld voor het rol-pencontact. Het model demonstreert het belang van het toestaan van elastische vervorming in het conforme rol-pencontact en het effect daarvan op de filmdikte, druk en wrijvingscoëfficiënt.

- *De invloed van rol-pencontactwrijving voor* ***hoge*** *slip percentages in het nok-rolcontact:*
  Bij toenemende wrijvingsniveaus in het rol-pencontact neemt de mate van glijden

bij het nok-rolcontact toe, hetgeen invloed heeft op de filmdikte, druk en nok-rolcontactwrijvingscoëfficiënt. Om de effecten van hogere waarden van de wrijvingscoëfficiënt van het rol-pencontact op de smering van de nokkenrollen te analyseren, werd een oneindig lijncontact gemengd gesmeerd thermo-elastohydrodynamisch (TEHL) model ontwikkeld voor het nok-rolcontact. Het gemengd smeringsmodel is gebaseerd op de zogenaamde "load-sharing concept" en maakt gebruik van werkelijke oppervlakteruwheidsmeetgegevens als invoer. Het complete model is gebaseerd op een EHL-model (op basis van de FEM) en een op een randelementenmethode (BEM) gebaseerd, droog, ruw, normaal contactmodel. Het model legt de invloed van de wrijvingscoëfficiënt in het rol-pencontact op niet-Newtoniaanse, thermische en oppervlakteruwheidseffecten in het nok-rolcontact bloot.

- *De invloed van rol-pencontactwrijving voor **lage** slip percentages in het nok-rolcontact:* Om de voorspelling van gemengde wrijving onder lage glijsnelheden te verbeteren, werd de afhankelijkheid van grenslaagwrijving op de glijsnelheid opgenomen in het eerder ontwikkelde gemengde smeringsmodel voor eindige lijncontacten. Dit werd gedaan door middel van een op het BEM-gebaseerd, droog, ruw, contact-model. Dit model neemt de tangentiele kracht mee, en is in staat om partiele slip te modelleren. Het model laat zien hoe de schuifspanning-sliprelatie de macroscopische wrijvingskracht in het nok-rolcontact beïnvloedt, bij lage glijsnelheid-werkomstandigheden.

Dit proefschrift bestaat uit twee delen. Het eerste deel, dat deel A is, bevat een samenvatting van het uitgevoerde werk. Het tweede deel, dat deel B is, bestaat uit de tijdschriftartikelen waarin de details worden beschreven.

Acknowledgements

Writing the acknowledgements marks the end of an extensive and fruitful period of research. The work herein is highly attributable to a number of people. I eagerly would like to take this opportunity to thank these people.

First of all I would like to thank my daily supervisor Matthijn de Rooij for his valuable input and motivation during this project and giving me the freedom and chance to do the present research independently. I always got more energy to tackle the problems after our regular discussions, which helped a lot!

Secondly, I would like to thank my co-supervisor Dik Schipper for his valuable inputs and comments from time to time. Our constructive discussions, which could sometimes easily take hours, always broadened my way of thinking.

I am also thankful to my colleagues at DAF Trucks N.V. for their critical point of view on the project. A special thanks to Mark van Drogen, for his valuable support and suggestions. His input always reminded me of the context in which the present work was placed, and hence closely kept me to the scope of the project. Mark, likewise all other research studies there are more questions after the research than before the research. Nevertheless, we have a much better understanding now of how the cam-roller follower unit works.

A big thanks to all my colleagues at the Surface Technology and Tribology department of the University of Twente for the nice working atmosphere, and also from whom I learned a lot: Melkamu, Tanmaya, Michel, Matthijs, Aydar, Mohammad Bazrafshan, Muhammad Khafidh, Yibo, Yuxin, Can, Ida, Hilwa, Nadia, Dmitry, Xavier, Febin and Dariush. I also am very thankful to Debbie and Belinda for their kind help. I also extend my appreciation to Piet, Rob, Erik and Walter for their support from time to time.

I would also like to extend my appreciation to the committee members for their time and effort. Thank you Ton van den Boogaard, André de Boer, Andreas Almqvist and Ron van Ostayen.

All my friends and family in the Netherlands, and in particular Enschede, many thanks to all of you!

Without the support of my parents, brother, sister, parents-in-law and brother-in-law I would not have been able to come this far. Their constant support, love and motivation can simply not be described in words. Thank you for being such an amazing family!

The emotional support, motivation and constant love of my dearest Reshmi, made everything seem less hard than it was. Her input in my PhD journey can simply not be described in words. Also, our little son Sid, thank you for making our lives enjoyable every second! More particularly, thank you for making Enschede unforgettable for us!

Shivam Alakhramsing, 2019, Enschede, The Netherlands

Contents

Part B

Paper A. *Elastohydrodynamic lubrication of coated finite line contacts*, Shivam S. Alakhramsing, Matthijn B. de Rooij, Dirk J. Schipper, and Mark van Drogen, Proceedings of the Institution of Mechanical Engineers, Part J: Journal of Engineering Tribology, 232 (9), 1077-1092, 2018. DOI:10.1177/1350650117705037

Paper B. *Lubrication and frictional analysis of cam-roller follower mechanisms*, Shivam S. Alakhramsing, Matthijn B. de Rooij, Dirk J. Schipper, and Mark van Drogen, Proceedings of the Institution of Mechanical Engineers, Part J: Journal of Engineering Tribology, 232 (3), 347-363, 2018. DOI:10.1177/1350650117718083

Paper C. *A full numerical solution to the coupled cam–roller and roller–pin contact in heavily loaded cam–roller follower mechanisms*, Shivam S. Alakhramsing, Matthijn B. de Rooij, Dirk J. Schipper, and Mark van Drogen, Proceedings of the Institution of Mechanical Engineers, Part J: Journal of Engineering Tribology, 232 (10), 1273-1284, 2018. DOI:10.1177/1350650117746899

Paper D. *A mixed-TEHL analysis of cam-roller contacts considering roller slip: on the influence of roller-pin contact friction*, Shivam S. Alakhramsing, Matthijn B. de Rooij, Aydar Akchurin, Dirk J. Schipper, and Mark van Drogen, ASME Journal of Tribology, 141 (1), 011503-011503-15, 2019. DOI:10.1115/1.4040979

Paper E. *The influence of stick–slip transitions in mixed-friction predictions of heavily loaded cam–roller contacts*, Shivam S. Alakhramsing, Matthijn B. de Rooij, Mark van Drogen, and Dirk J. Schipper, Proceedings of the Institution of Mechanical Engineers, Part J: Journal of Engineering Tribology, Epub ahead of print 26 July 2018. DOI:10.1177/1350650118789515

PART A

Nomenclature

a Hertzian contact half-width, $a = \sqrt{\frac{8FR_x}{\pi LE'}}$ (m)

A roller crowning curvature (m)

C radial clearance (m)

c lubricant heat capacity (J/kg·K)

c_c cam material heat capacity (J/kg·K)

c_r roller material heat capacity (J/kg·K)

e roller eccentricity (m)

E Young's elasticity modulus (Pa)

E' reduced elasticity modulus, $E' = \frac{2}{\frac{1-\nu_\mathrm{c}^2}{E_\mathrm{c}} + \frac{1-\nu_\mathrm{r}^2}{E_\mathrm{r}}}$ (Pa)

g axial surface profile function (m)

G dimensionless material property parameter, $G = \alpha E'$ (-)

h film thickness (m)

H dimensionless film thickness, $H = \frac{hR_x}{a^2}$

h_0 rigid body displacement (m)

I roller inertia (kg.m^2)

k lubricant thermal conductivity (W/m·K)

k_c cam material heat capacity (W/m·K)

k_r roller material heat capacity (W/m·K)

l vertical displacement of follower / lift (m)

L roller axial length (m)

L_s roller straight length (m)

L_x, L_y calculation domain lengths for dry rough contact solver (m)

m_r roller mass (kg)

p pressure (Pa)

P dimensionless pressure, $P = \frac{p}{p_\mathrm{Hertz}}$ (-)

p_av average Hertzian pressure, $p_\mathrm{av} = \frac{F}{2aL}$ (Pa)

p_Hertz maximum Hertzian pressure, $p_\mathrm{Hertz} = \frac{2F}{\pi La}$ (Pa)

$\bar{p}_\mathrm{a}$ auxiliary pressure (Pa)

q asperity shear stress (Pa)

R_x reduced radius of curvature in rolling direction (m)

R_y reduced radius of curvature in axial direction (m)

R_q RMS surface roughness (m)

R_pin pin radius (m)

R_f outer radius roller (m)

R_b base circle radius (m)

S Sommerfeld number (-)

SRR slide-to-roll ratio (-)

T temperature (K)

T_0 ambient temperature (K)

U dimensionless speed parameter, $U = \frac{2\eta_0 U_\mathrm{m}}{E' R_x}$ (-)

U_c cam surface velocity at point of contact (m/s)

U_r roller surface velocity at point of contact (m/s)

U_m lubricant mean entrainment velocity (m/s)

U_m lubricant sum velocity (m/s)

W dimensionless load parameter, $W = \frac{F/L}{E' R_x}$ (-)

x, y, z spatial coordinates (m)

X, Y, Z dimensionless spatial coordinates, $X = \frac{x}{a}$, $Y = \frac{y}{2L}$, $Z = \frac{z}{h}$ (-)

z_{m} roller crown drop (m)

α Roelands pressure-viscosity coefficient (Pa^{-1})

β Roelands temperature-viscosity coefficient (K^{-1})

β_T Dowson-Higginson temperature-density coefficient (K^{-1})

η lubricant viscosity (Pa·s)

η_0 lubricant viscosity at ambient conditions(Pa·s)

δ elastic displacement (m)

δ_{r} combined radial elastic displacement roller-pin contact (m)

θ cam angle (rad)

Θ circumferential coordinate (rad)

ϕ circumferential coordinate defined as starting from the minimum film thickness (rad)

τ shear stress (Pa)

τ_0 characteristic Eyring shear stress (Pa)

ρ lubricant density ($\mathrm{kg/m}^3$)

ρ_0 lubricant density at ambient conditions ($\mathrm{kg/m}^3$)

ν Poisson's ratio (-)

μ coefficient of friction (-)

μ_{a} friction coefficient in boundary lubrication(-)

ω_{c} cam rotational velocity (rad/s)

ω_{r} roller rotational velocity (rad/s)

Λ film parameter (-)

Subscripts Abbreviations

a asperity

BEM boundary element method

c cam

c-r cam-roller

EHL elastohydrodynamic lubrication

f follower

fc follower centre

FEM finite element method

lim limiting

min minimum

max maximum

r roller

r-p roller-pin

TEHL thermo-elastohydrodynamic lubrication

Chapter 1

Introduction

1.1 Problem definition

Consumer demand, environmental protection and government mandate are all factors which are accelerating the development of more fuel-efficient vehicles. Heavy-duty vehicles such as trucks, buses and coaches produce around 25% of CO_2 emissions from road transport in the EU and around 6% of the EU's total CO_2 emissions [22]. In order to contribute to the achievement of the EU's commitments under the Paris Agreement [21] the EU has set out mandatory targets, one of which is that the average CO_2 emissions of new heavy duty vehicles will have to be 15% lower in 2025 than in 2019 [22].

FIGURE 1.1: Example of a truck used for road transport. Adopted from reference [15].

In order to achieve these stringent fuel efficiency requirements without degradation of vehicle performance, vehicle manufacturers have been making significant hardware modifications such as better vehicle aerodynamics, engine downsizing, usage of lightweight materials and low rolling resistance tires. Another way of improving the fuel economy is by reducing the internal friction losses of the engine. Thus, lubricant manufacturers have

also developed highly advanced lubricants to reduce engine friction losses. Lubricants that are fuel-efficient are often formulated by the use of high-quality low-viscosity base oils with advanced additive technologies. Downsizing engines means increasing the power density, due to their smaller size and higher output, and thus increasing loads on mechanical components. This, together with the use of even lower viscosity oils, causes main engine components to operate under harsh conditions, which may eventually lead to accelerated surface wear and thus ultimately to a shortened engine life.
Cam-roller followers as part of valve-train mechanisms in internal combustion engines are of crucial importance. Figure 1.2 shows an example of a camshaft and a roller follower unit.

(a)

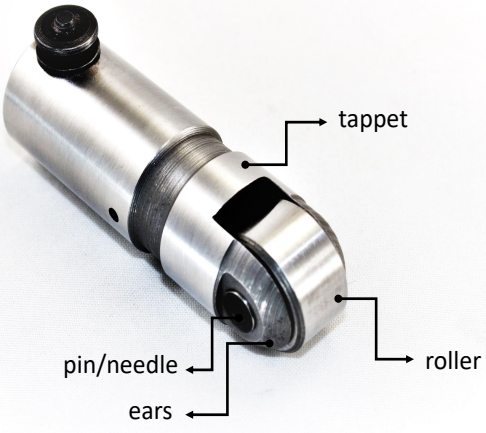

(b)

FIGURE 1.2: Example of a) camshaft and b) roller follower assembly.

Anderson [3] reported that the valve train mechanism accounts for 6-10% of the internal engine friction losses. The cam-roller contact is a lubricated contact, experiencing highly dynamic and/or abruptly varying operational conditions in terms of load and velocity,

coming from the camshaft that drives it. To elaborate somewhat, this contact is subjected to very high pressures coming from the fuel injector. Peak pressure values of 2 GPa are not uncommon. Related to this, the degree of separation between surfaces, defined as specific film thickness, has a very strong influence on the type and amount of wear.

(a) (b)

FIGURE 1.3: Example of a cam experiencing adhesive wear at a) initial stage and b) a more progressed stadium.

As an example, engine manufacturers often utilize accelerated testing in the development stage to guarantee lifetime of components. Accelerated testing of mechanical systems implies complex scaling of the different physical phenomena involved, such as heat generation, hydrodynamic pressure generation in the lubricant and contact mechanics. Consequently, strong non-linear effects can occur in the contact, such as a transition to a different wear mode [10] or a transition from mild to severe/adhesive wear. Figure 1.3 shows an example of a cam which has experienced adhesive wear.

Fundamental understanding of the cam-follower contact is thus critically important to ensuring engine durability in the pursuit of high fuel efficiency. In the aforementioned example a fundamental understanding of the tribological behaviour of the cam-roller contact would, as a first step, be essential in developing and interpreting accelerated testing strategies to ultimately ensure high reliability and durability of the cam-roller follower contact.

In this thesis, the tribological interaction between a cam and roller follower, as part of the fuel injection equipment in a heavy duty diesel engine, is studied. The outcome of the study should yield more fundamental knowledge of and insight into highly dynamic lubricated contacts as well as a thorough understanding of the tribological behaviour of these contacts. This knowledge should serve as a basis for further optimization of the cam-follower unit in terms of durability and fuel efficiency.

1.2 Lubricated contacts

For mechanical components of an internal combustion engine it is important to study friction as this mainly influences the engine efficiency and the onset of wear – and ultimately lifetime – of components. An effective way to reduce friction and hence wear of interacting components is lubrication. Introducing a lubricant between two interacting surfaces prevents direct solid-solid contact and thus reduces friction and its consequences [76]. Lubrication between the two surfaces remains intact due to squeeze and wedge effect. The latter mechanisms cause generation of a hydrodynamic pressure distribution that carries the applied load, also referred to as hydrodynamic lubrication (HL).
Next, the different types of contacts will be explained. These can be divided into two categories: conformal and non-conformal contacts. In case of conformal contacts, the contacting surfaces closely fit onto each other (for example journal bearings), indicating a large contact area. In the case of non-conformal contacts, the contacting elements meet along a line (for example a cam-follower) or a point (for example ball bearings) in an unloaded and dry contact situation. The non-conformal cam-roller follower contact considered in this thesis can be categorized as a line contact. This means that prior to any deformation the contacting elements would meet along a straight line. In the Hertzian contact theory [78] it is common to translate all type of line contacts to a simple contact of a cylinder, with an equivalent reduced radius of curvature R_x, on a plane as follows:

$$\frac{1}{R_{1,x}} + \frac{1}{R_{2,x}} = \frac{1}{R_x} \tag{1.1}$$

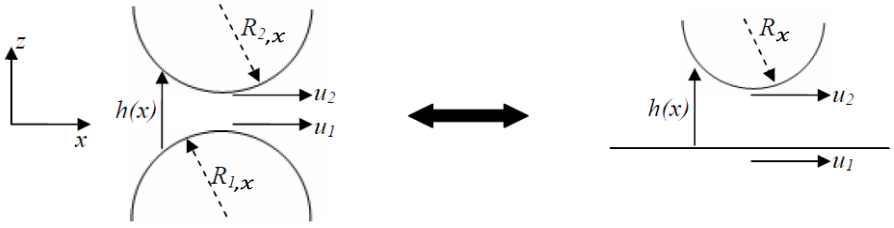

FIGURE 1.4: Schematic translation of two cylinders (with radius $R_{1,x}$ and $R_{2,x}$), meeting along a line, to an equivalent cylinder (with radius R_x) on a plane. Adopted from reference [33].

Interacting components are usually profiled in axial direction to reduce edge loading [49]. For the sake of clarity, the axial direction is the direction perpendicular to the rolling direction. "Line contacts" will be redefined accordingly later on in this thesis.

A characteristic of non-conformal contacts is that the contact area is small and thus high stress levels are associated with this type of contacts. Commonly, for lubricated non-conformal contacts the hydrodynamically generated pressure within the lubricant film reaches really high values (in the order of GPa's) which indicates a certain degree of (elastic) deformation of the opposing objects. In this case the shape of the film thickness is determined not only by the geometry but also largely by the elastic deformation of the respective components. This type of lubrication in which two elastic objects are moving relative to each other is also referred as ElastoHydrodynamic Lubrication (EHL). As mentioned earlier, high pressures are involved in EHL, pointing towards significant variations in lubricant properties such as density and viscosity within the contact. The latter aspects may significantly affect the film thickness and frictional force, which are crucial performance indicators as they have a very strong influence on the type and amount of wear.

Roughness levels of mechanical components are often defined during production or after running-in. The surface roughness level has an influence on the transition between the friction situation when the opposing surfaces have a high degree of direct contact (also referred as Boundary Lubrication (BL)) and the situation when the surfaces are fully separated by a lubricant film (EHL). The transition between the EHL and the BL regime is often referred to as the Mixed Lubrication (ML) regime. In the ML regime part of the load is carried by the hydrodynamic pressure in the lubricant film and the other part is carried by interacting asperities. The latter aspect is much more significant for the BL regime. In fact, when the load is carried by the asperities, the frictional force is controlled by shearing of boundary layers that are present on the solid bodies. In the BL regime the coefficient of friction is almost independent of the load and velocity [30] and thus constant. However, if the boundary layers cannot be formed on the opposing solids, the friction coefficient approximates the "dry" value (e.g. 0.4-1). This may occur, for instance, when the locally as critical temperature has been exceeded [10]. For contacts in the BL regime the coefficient of friction typically ranges between 0.1 and 0.15.

The EHL, ML and BL regimes can be represented using the Stribeck curve (see Figure 1.5). This graph is named after Richard Stribeck [72, 71], who published a few papers concerning journal and rolling element bearings in which he systematically graphed the influence of surface roughness, velocity and load on the coefficient of friction.

From the Stribeck curve, it can be seen that with increasing velocity or decreasing nominal contact pressure, a contact changes from being in contact (BL) to being fully separated by a thin (in the order of μm thick) fluid film due to hydrodynamic pressure generation in the lubricant layer (EHL regime). As stated earlier, (between these regimes) in the ML regime, the load is carried partly by the (rough) contacting surfaces and partly by the lubricant pressure developed in the contact. Roughly speaking, if less than 2%

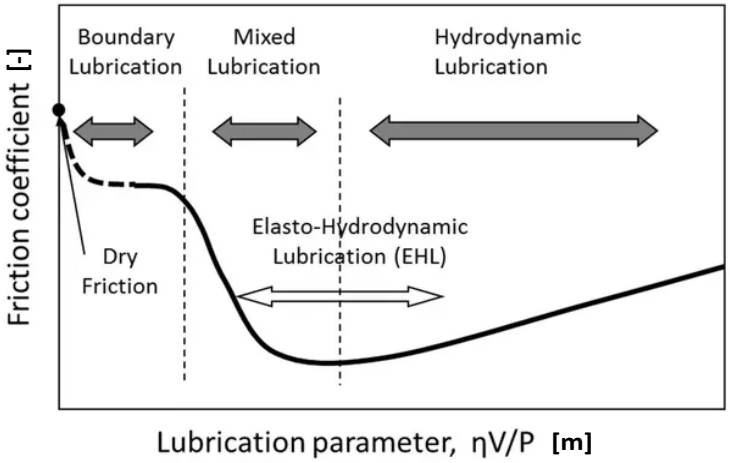

FIGURE 1.5: The Stribeck curve, clearly representing the different lubrication regimes. Reproduced from [46].

load is carried by the film, the contact is operating in the BL regime, while if less than 2% is carried by the asperities it can be considered to be in the EHL regime [52]. The ML regime accounts for the remaining 96% of the load-partitioning range.
As the aforementioned criterion is rather implicit, it is more convenient to distinguish the lubrication regimes using a film parameter $\Lambda = \frac{h}{\sqrt{R_{q,1}^2+R_{q,2}^2}}$, where h is the hydrodynamic film thickness and $R_{q1,2}$ the RMS surface roughness of respectively surface 1 and surface 2. Based on Λ, as a rule of thumb, the lubrication regimes are as follows:

- EHL : $\Lambda \geqslant 3$
- ML : $1 < \Lambda < 3$
- BL : $\Lambda \leqslant 1$

It is worth mentioning that there is no strict criterion for differentiation between the three lubrication regimes. The transition from one to another regime is not associated with a single value and in reality is a smooth process.
The Stribeck curve can be predicted for steady state conditions, using multi-scale models which describe contact at asperity level and shear of boundary layers adsorbed on steel surfaces in BL, as well as hydrodynamic pressure generation in the thin fluid film confined between the surfaces (see for instance [31, 28, 43]). In fact, lubrication conditions in terms of film thickness and friction coefficient can be obtained once the following are known: i) the lubricant rheological properties, ii) applied load, iii) geometrical parameters of the interacting solids, iv) mechanical properties of the solids, v) lubricant entrainment velocity and vi) surface topography.
However, designing a tribological application is not a straightforward task as this requires

fundamental knowledge about the operational lubrication regime and the parameters (contact pressures, roughness levels, lubricant properties etc.) influencing it.

1.3 Cam-roller follower tribology

Cam and follower mechanisms are used to convert a rotational motion into a translational motion. Typically, the function of a camshaft in an engine is to open and close the valves. Various types of cam follower configurations exist, such as a cam and flat faced follower, a cam and spherical faced follower and a cam and roller follower. In this thesis the cam and roller follower configuration (see Figure 1.6(a)) is considered.
The displacement of the valve is controlled by the shape of the cam, so in the design process of the lateral profile of a cam it is important to minimize dynamic effects by careful consideration of the *lift* it provides to the valve. In fact, great care should be taken that the valve lift profile and its first, second and third derivatives with respect to cam angle (velocity, acceleration and jerk respectively) are smooth (see Figure 1.6(b)). The latter ensures that dynamic effects on the valve motion are minimal.
Satisfactory lubrication of the cam-roller contact in internal combustion engines is a difficult tribological design challenge due to its complex nature. This type of contact is one which constantly moves in space and its operating conditions are instantaneous and capricious. Lubrication is of crucial importance: it separates the interacting surfaces, thus preventing metal to metal contact and premature cam failure. Related to this, the degree of separation between surfaces, in its turn related to the film thickness, has a very strong influence on the type and amount of wear. The film thickness, which strongly governs the frictional force and occurrence of metal to metal contact, is highly affected by the operating conditions, such as the normal contact load, material properties, lubricant properties and the lubricant entrainment velocity. The lubricant entrainment velocity is the sum of the surface velocities of the cam and roller at the point of contact. It is very likely that the lubricant entrainment velocity will be influenced by the shape of the cam. The normal force at the point of contact is also related to the springs attached to the follower unit and hence to the tappet lift profile, i.e. the shape of the cam.

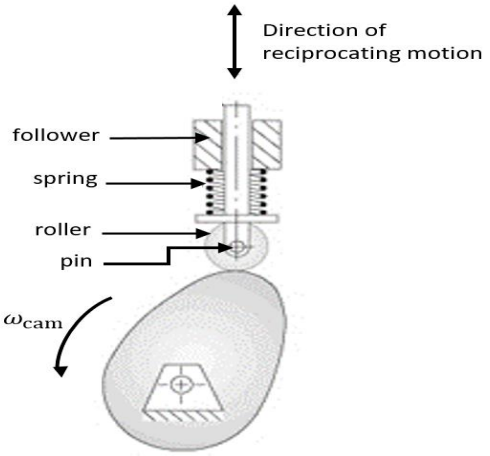

(a)

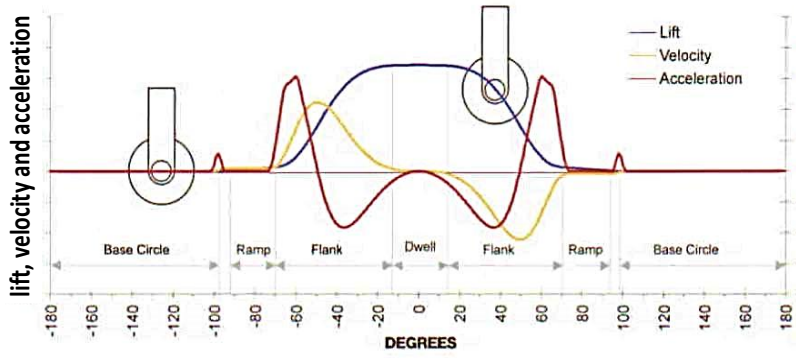

(b)

FIGURE 1.6: Schematic of a) cam-roller follower unit and b) tappet lift, velocity and acceleration as a function of the cam angle (adopted from reference [42]). Note that the magnitudes of the lift, velocity and acceleration are not of the same order in practice. This Figure only depicts the trends.

Nevertheless, it is clear that while some parameters of the model can be assumed to be constant during one revolution of the camshaft, many parameters are variable and must be calculated as a function of the cam angle:

- The cam radius of curvature in the rolling direction is a function of the cam's lateral shape, i.e. the lift profile.
- The entrainment velocity U depends both on cam and roller peripheral velocities.
- The normal load at the contact F is directly linked to the lift profile.
- The surface roughness levels along the whole cam's lateral surface are not the same.

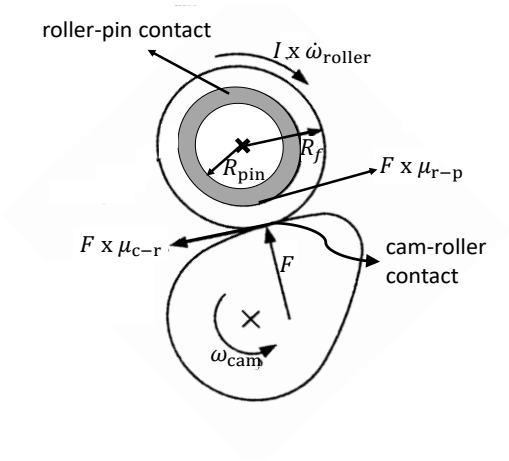

FIGURE 1.7: Cam-roller follower configuration showing the frictional forces acting at the cam-roller and roller-pin contact.

In short, the contact experiences highly dynamic conditions due to variations in kinematics and contact geometry, as well as loading. As a result the tribological behaviour of the lubricant through the contact, in terms of friction, pressure and film thickness, may be instantaneous and capricious.

To add more complexity to the problem, there are two potential lubricated contacts within the cam-roller follower unit (see Figure 1.7). The first one is the cam-roller contact, which is a non-conformal contact. The second contact is the roll-pin contact, which is a conformal contact. The roller is allowed to rotate freely along its axis. The roller angular speed is a function of the acting frictional forces at the cam-roller and roller-pin contact and inertia torque caused by angular acceleration of the roller itself (see Figure 1.7).

The roller-pin contact ideally functions as a "low-friction" hydrodynamic journal bearing. The term "low-friction" is used here deliberately as the intention is to keep the friction levels in the roller-pin contact as low as possible to allow a low resisting torque and hence less sliding at the cam-roller contact. The latter is often referred to in the literature as roller slip. Roller slippage also strongly governs the frictional force at the cam-roller contact. From the latter it directly follows that the lubrication performance at the cam-roller contact is strongly dependent on the lubrication performance at the roller-pin contact. It is therefore equally important to consider the lubrication conditions at the roller-pin contact when modelling the cam-roller contact as a tribo-system, i.e. the complete system should be seen as two coupled lubricated contacts.

In this work, the primary focus is on gaining a thorough understanding of the lubrication performance in cam-roller contacts. The cam-roller contact needs to be optimized with respect to friction as well as wear. The resulting frictional characteristics are affected by the shear of the lubricant film and the interaction of rough surfaces themselves. Related

to this, the film thickness within the contact is a crucial performance indicator as it provides information regarding potential asperity contact and thus wear. In fact, it is important to know in which lubrication regime the cam-roller contact operates. However, it becomes very complex and almost impossible to correlate the lubrication conditions of the cam-roller contact, under all possible operating conditions, to a single frictional map or curve such as the Stribeck curve. This is due to the fact that i) transient effects may be significant, ii) the nominal contact pressure, lubricant entrainment velocity and surface roughness vary as a function of cam angle and iii) the camshaft rotational velocity may also vary. Moreover, roller slippage will also vary as a function of cam angle and therefore also the lubricant entrainment velocity.
Once a better understanding regarding the frictional behaviour of the cam-roller contact is gained, potential wear zones could more easily be identified. For instance, the transition from mild to severe/adhesive wear (scuffing) is typically assumed to be thermally driven [10]. In fact the boundary layers on the surface, governing the friction, break down once a critical temperature is exceeded. This means that some heat generation (on asperity level) is a prerequisite for failure. The combination of significant roller slippage, high associated pressure and operating in the mixed lubrication regime could therefore be indicators of potential scuffing.

1.4 Research scope

As described earlier, the tribological behaviour of the cam-roller contact is highly dependent on the operating conditions. As such, numerical modelling becomes inevitable in predicting performance indicators such as pressure, film thickness and coefficient of friction over the full range of operating conditions of such a cam-roller contact.
Therefore, this thesis comprises a step by step construction of a model for cam-roller follower contacts, taking into account all the aforementioned variables. As such, the model should be able to cope with the highly dynamic conditions and also be able to identify potential wear zones.
The ultimate goals in this research are threefold, namely:

- The development of a state-of-art lubrication model of the coupled cam-roller and roller-pin contact system which is able to accurately predict crucial lubrication performance indicators.
- Interpretation of the results obtained from the model should be such that a more fundamental understanding of the cam-roller contact, and the underlying physics affecting its tribological behaviour, is obtained.

- The knowledge obtained from the model could be used to understand the initiation of related wear processes - and in line with this - identification of potential wear zones. Also, the knowledge should form a basis for future research from the perspective of interpreting accelerated testing strategies, and robust design optimization of cam-roller follower units.

The most important assumptions made in this research with regard to model development are:

- Macroscopic wear is not considered, i.e. surface topographical changes due to wear (running-in wear).
- Detailed investigation into boundary layer friction mechanisms (such as tribo-chemistry and surface reactivity) are not considered. Instead, the boundary layer is assumed to remain intact under all circumstances.

Chapter 2

Theoretical background

2.1 Elastohydrodynamic lubrication

Ideally, the film thickness in the lubricated contact should be high enough to fully separate the surfaces and thus preventing metal to metal contact. In this case all the load is counterbalanced by the hydrodynamic pressure build-up. The hydrodynamic pressure, especially in non-conformal contacts, can reach really high values, such that elastic deformation of solids cannot be neglected anymore. The aforementioned mechanism is referred to as elastohydrodynamic lubrication (EHL). The solution of an EHL problem consists of the pressure distribution within the lubricated contact and the shape of the film thickness. The pressure distribution within the contact is governed by the "Reynolds equation" for thin films. The aforementioned equation is a realistic simplification of the well-known Navier-Stokes equation (see reference [37] for a full derivation). The commonly used Reynolds equation can be written in the following form:

$$\underbrace{\frac{\partial}{\partial x}\left(h\rho U_{\mathrm{m}}\right)}_{\text{Couette flow}} + \underbrace{\frac{\partial h\rho}{\partial t}}_{\text{Squeeze motion}} = \underbrace{\frac{\partial}{\partial x}\left(\frac{h^3\rho}{12\eta}\frac{\partial p}{\partial x}\right) + \frac{\partial}{\partial y}\left(\frac{h^3\rho}{12\eta}\frac{\partial p}{\partial y}\right)}_{\text{Pouseuille flow}} \tag{2.1}$$

where the first term on the LHS represents the flow induced by the surface entrainment of the lubricant and the second term on the LHS accounts for squeeze motion of the bounding surfaces. The RHS represents the flow that is driven due to the pressure gradients. As can be observed already, the Reynolds equation is basically a superposition of the well-known Couette and Pouseuille flow [47]. If U_1 and U_2 are the velocities of opposing surfaces at the point of contact, the lubricant mean entrainment velocity can be obtained as follows:

$$U_{\mathrm{m}} = \frac{U_1 + U_2}{2} \tag{2.2}$$

where the entrainment velocity U_{m} represents the motion that basically drags lubricant into the contact and thus creating a surface driven flow. It is thus one of the most important parameters influencing the film thickness in the contact.
The film thickness for a line contact can be written as follows:

$$h\left(x\right) = h_0 + \frac{x^2}{2R_x} - \delta\left(x\right) \tag{2.3}$$

As can be seen from eq. 2.3 the film thickness distribution is determined by a vertical penetration h_0 (a constant) of the undeformed geometry $\frac{x^2}{2R_x}$ and the elastic deformation δ. R_x is the reduced radius of curvature as defined by eq. 1.1. The vertical displacement constant h_0 is obtained by globally balancing the applied load with the hydrodynamically generated force, whereas the elastic deformation of solids is calculated from the hydrodynamic pressure.
Figure 2.1 provides an example of a (piezo-viscous elastic) EHL solution for a highly loaded line contact. It is clear from Figure 2.1 that for highly loaded contacts the hydrodynamic pressure distribution approximates the dry Hertzian pressure distribution. Along with this, the film thickness distribution within the contact is almost uniform and equal to the central film thickness h_{cent}. From the latter it can be concluded that for highly loaded lubricated line contacts the central film thickness is a better variable than the minimum film thickness for specifying the separation between the surfaces. Another feature of Figure 2.1, and a typical characteristic of the EHL pressure distribution, is the pressure spike near the outlet of the contact. The local pressure spike can be explained using continuity of flow, which dictates that the large pressure gradient must be coupled with a local restriction of the film thickness (the minimum film thickness h_{min}).
In short, the governing EHL equations are the Reynolds equation (to solve the pressure), the elasticity equations (to solve the elastic deformation δ) and the load balance equation (to solve the vertical displacement constant h_0). The film thickness equation links the Reynolds equation to the elasticity equations. The viscosity η and density ρ of the lubricant also vary significantly with pressure. Therefore constitutive equations accounting for these variations also need to be included in the EHL problem formulation.
The first full isothermal numerical solution of the EHL problem was published in 1951 by Petrusevich [64], who also was able to predict the pressure spike near the exit of the lubricated contact (see Figure 2.1).

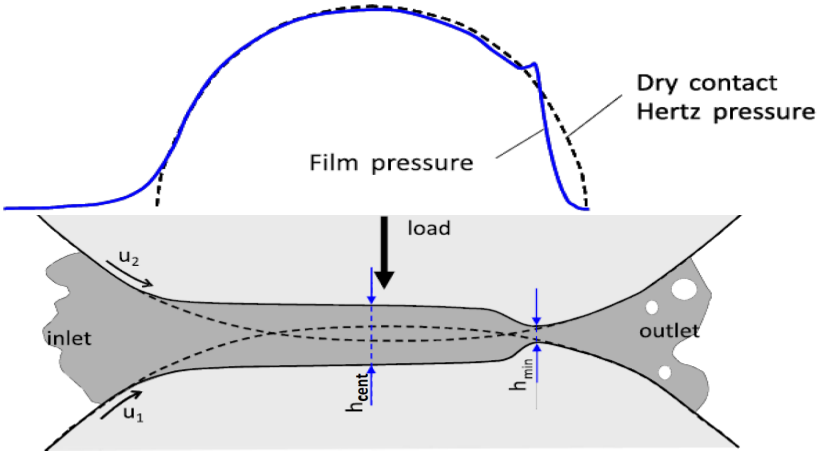

FIGURE 2.1: Pressure and film thickness shape schematically for a typical EHL contact. Reproduced from reference [8].

This pioneering work of Petrusevich was an incentive for many other important contributions. Many of these studies were devoted to linking the central and minimum film thickness with dimensionless parameters indicating operating conditions. Examples include pioneering works of Dowson and Higginson [17, 19], Hamrock and Dowson [35, 36], Nijenbanning et al. [60] and Evans and Snidle [23]. Several numerical techniques have been proposed in past literature, due to complexity of the full EHL problem. A brief review of existing numerical methods to solve the EHL may be found in the work of Lugt and Morales-Espejel [53].

2.2 Friction in rolling-sliding contacts

2.2.1 Smooth surfaces

When the surface velocities U_1 and U_2 at the point of contact are equal the system is said to be in the state of pure rolling. In this case it will only be the Poiseuille flow which will cause shear force due to the developed pressure gradients. Usually the frictional forces under pure rolling conditions in the case of pure EHL (no roughness effects) are very small. As soon as there is a velocity difference between the surfaces, i.e. $U_1 \neq U_2$, additional shear forces arise, which may increase the friction level substantially. The case when $U_1 \neq U_2$ is commonly referred as rolling-sliding contact. The amount of rolling to sliding in an EHL contact is defined as the slide-to-roll ratio (SRR), which is calculated as follows:

$$\mathrm{SRR} = \frac{|U_1 - U_2|}{U_\mathrm{m}} \tag{2.4}$$

where U_m is the lubricant mean entrainment velocity and defined in eq. 2.2. The SRR has a range between 0 and 2. When one surface is stationary and the other moving, i.e. SRR = 2, the system is said to be in a state of simple sliding.
The effective viscosity within the EHL contact governs the viscous friction. The viscosity varies with pressure, temperature and shear rate in a rather complex manner. The rheology of the lubricant is very important in order to accurately predict EHL friction. In fact, the viscosity rises approximately exponentially with pressure, while it decreases approximately exponentially with temperature. As can be imagined, at high SRRs (and thus high shear rates) a lot of heat is generated due to viscous shearing of the lubricant, leading to an increase in temperature. This would directly cause a drop in viscosity and thus friction. Whenever the relationship between lubricant shear stress and shear rate is linear, the lubricant is said to behave like a Newtonian fluid. From Figure 2.2, which provides a generalized example of SRR versus friction response, it is clear that the lubricant shear stress is related to the SRR, but not always follows a linear relationship. Figure 2.2 is commonly known as a traction curve or μ-slip curve.

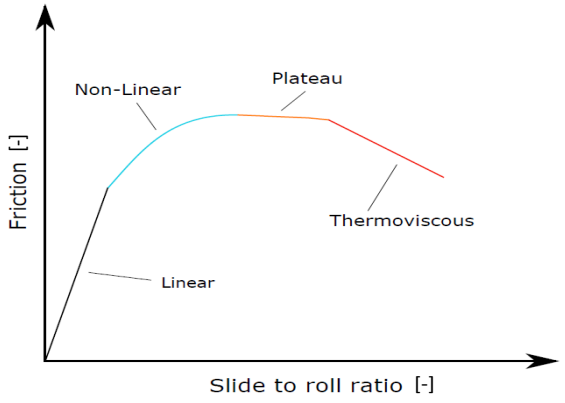

FIGURE 2.2: Example of a generalized traction curve showing different regimes. Reproduced from reference [8].

From Figure 2.2 it can be deduced that for low SRRs (or shear stress), the relationship between SRR and shear stress is linear (black coloured part), indicating Newtonian behaviour of the friction response. From some point in the SRR domain and onwards, the friction increases in a non-linear fashion (blue coloured part) until is saturates at a certain limiting value (or stress). Related to this value, friction asymptotically reaches a "plateau" showing only little variation with shear rate (orange coloured part), before it starts to decrease again with increasing shear rates (red coloured part).
The non-linear decrease of effective viscosity with shear rate is commonly known as the shear thinning effect. The latter is one of the main reasons for the behaviour in the non-linear regime. An abundance of models can be found in literature describing this

non-Newtonian behaviour (see for instance [11, 25, 4]). It is commonly assumed that the occurrence of the "plateau" is due to a limiting shear stress. The latter is a concept originated from the work of Smith [69]. As discussed in the work of Björling [8] there has been a lot of discussion about the reasoning behind the occurrence of the "plateau" and it is still not completely understood.
At even higher shear rates (in the thermoviscous regime), thermal effects start to dominate as heat generation within the contact increases significantly. The temperature increases and the viscosity decreases (also known as thermal softening), leading to a decrease in frictional response.
Nevertheless, it should be stated that even though each regime in the traction curve is dominated by either Newtonian, shear thinning, limiting shear stress or thermal effects, many of these effects could be simultaneous.

2.2.2 Mixed lubrication

In mixed lubrication the load is carried partly by interacting asperities and partly by the lubrication. In equation form this yields:

$$F = F_{\mathrm{a}} + F_{\mathrm{h}} \tag{2.5}$$

where F, F_{a} and F_{h} are the total load, load carried by asperities and load carried by the lubricant respectively. The coefficient of friction μ in ML arises due to shearing of asperities and lubricant. In general one may write:

$$\mu = \frac{\int_{\Omega_{\mathrm{a}}} q \; d\Omega + \int_{\Omega_{\mathrm{h}}} \tau \; d\Omega}{F} \tag{2.6}$$

where q and τ denote the asperity shear stress and hydrodynamic shear stress respectively. Ω_{a} and Ω_{h} denote the asperity and hydrodynamic film contact area respectively. The boundary layer friction coefficient μ_{a} should be determined experimentally at very low speeds where the film thickness is smaller than the composite roughness of the surfaces, i.e. under conditions where the friction due to viscous shear is negligible. μ_{a} is the friction coefficient between the rough surfaces in the presence of boundary layers and should not be confused with the dry friction coefficient between the surfaces. At high pressures (mean contact pressure $p_{\mathrm{av}} > 200$ MPa) it is generally found to be true for most boundary layers that the boundary layer shear stress increases linearly with pressure [30], i.e. a Coulomb-type friction law:

$$\mu_{\mathrm{a,i}} = \frac{q_i}{p_{\mathrm{a,i}}} \tag{2.7}$$

with $p_{\mathrm{a,i}}$ being the pressure acting on the current asperity. If one assumes $\mu_{\mathrm{a,i}}$ to be constant for all asperities, i.e. $\mu_{\mathrm{a,i}} = \mu_{\mathrm{a}}$, the first term of eq. 2.6 may also be written as:

$$\int_{\Omega_{\mathrm{a}}} q \; d\Omega = \mu_{\mathrm{a}} \int_{\Omega_{\mathrm{a}}} p_{\mathrm{a}} \; d\Omega = \mu_{\mathrm{a}} F_{\mathrm{a}} \tag{2.8}$$

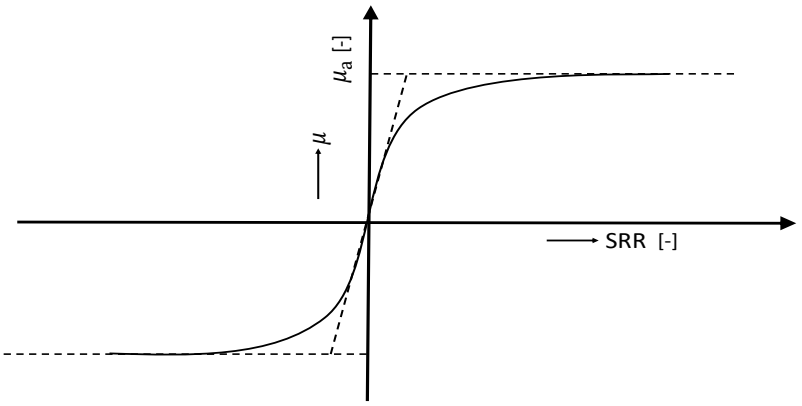

FIGURE 2.3: A schematic traction curve in boundary lubrication, i.e. the EHL friction component is negligible.

It has to be noted that eq. 2.7 generally holds for the situation of simple sliding. For a rolling-sliding contact, an asperity shear stress formulation according to the Coulomb law does not account for the sliding/slippage. This is evident from Figure 2.3, which shows that in the very low SRR domain (typically for SRR < 0.05) the boundary layer friction coefficient increases with increasing SRR until it merges with an asymptotic value. It is this asymptotic value that is defined as the boundary layer friction coefficient μ_{a}. In his work, Gelinck [30] reasoned that the boundary layers present in the micro-contact behave in an elastic-plastic way, i.e. with increasing shear rates the shear stress reaches its plastic limit as in case of a solidified lubricant. According to Gelinck "μ_{a} *is the coefficient of friction in the BL-regime caused by plastically shearing boundary layers*".

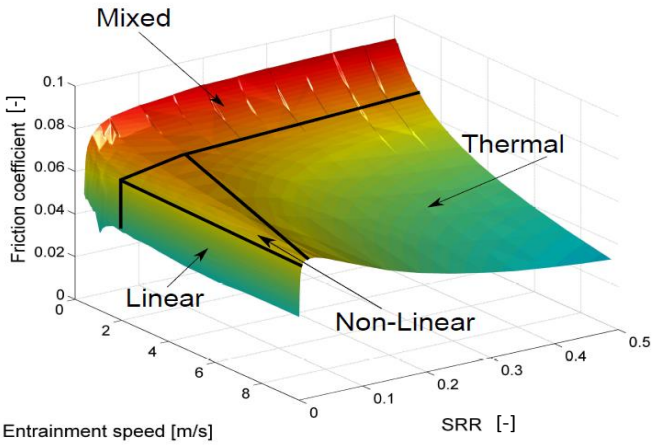

FIGURE 2.4: A 3D friction map showing different regimes. Reproduced from reference [8].

As a complement to the Stribeck curve and traction curve Björling [8] came up with the concept of 3D frictional mapping (see Figure 2.4), allowing a better overview of the friction characteristics. This map is composed of several traction and Stribeck curves and contains the lubricant entrainment velocity, SRR and coefficient of friction. Note that the boundaries, distinguishing the different regimes are not exact and are used for illustration. Figure 2.4 shows that the frictional response for a rolling-sliding contact is extremely complex as there are a lot of parameters affecting it.

2.3 Literature review: Cam-roller follower lubrication analysis

The cam-roller follower unit as a tribo-system is inherently a coupling between two lubricated contacts, namely the cam-roller contact and the roller-pin contact. From past literature (see for instance [85, 16, 55, 48, 77]) one may observe that significant theoretical and experimental work, in terms of lubrication behaviour, has been carried out for cam-flat faced follower configurations (which are simple sliding contacts). This in contrast to the cam-roller follower unit which has gained less attention. Nevertheless, from the early 90s onwards some progress has been made, of which the most relevant studies are mentioned below.

Roller slippage, which strongly governs the frictional force/traction at the cam-roller contact, has been proven experimentally by Duffy [20] and more recently by Khurram et al. [44]. Lee and Patterson [50] reported that the problem of wear still exists if slip occurs. The roller rotational velocity is a function of the torques acting on the roller itself (see Figure 1.7). However, most previous studies (see for instance [29, 54, 14]) assumed

pure rolling conditions at the cam-roller contact, i.e. $U_c = U_r$. Where U_c and U_r are the cam and roller surface velocities at the point of contact.

Chiu [13] and later Ji and Taylor [39] were among the first to develop theoretical lubrication models that take into account variable roller rotational velocity at the cam-roller contact. A fixed coefficient of friction was assumed for the roller-pin contact. Both the aforementioned studies ascertained roller slip at high cam rotational velocities due to simultaneous increase in roller angular momentum. Bair [5] demonstrated in his experiments that roller slippage is strongly governed by the acting contact force, i.e. a higher contact force decreases possible roller slippage due to enhanced traction at the cam-roller contact.

Mixed lubrication conditions were considered by Turturro et al. [74], who presented a steady-state model for a non-Newtonian lubricant to study the effect of viscosity on the friction at cam-roller contact. Khurram et al. [45] studied experimentally the effect of lubricant rheology on roller slip. In that study they highlighted the effect of viscosity improvers on roller slip. Torabi et al. [73] presented a mixed thermo-elastohydrodynamic lubrication (TEHL) model and compared the lubrication behaviour between a flat-faced and roller follower under similar operating conditions. Their conclusion was that the influence of thermal and roughness effects on the film thickness may be significant. Umar et al. [75] developed a mixed lubrication model in which they analysed the effect of flash temperature on cam-follower friction. They compared the sliding and roller follower type configurations and concluded that in both configurations surface roughness plays an important role. Also, the resultant contact temperature was much higher in the case of sliding followers due to higher sliding velocity and friction. In line with this, Abdullah et al. [1] recently investigated the effects of specialized surface treatments on roller slippage. They observed considerable reduction in roller slippage. It is worth mentioning that most of the previously mentioned studies only considered lightly to moderately loaded cam-roller follower contacts, i.e. pressures up to 0.7 GPa approximately. Injection camshafts, which experience much higher pressures (up to 2 GPa), have been studied by Lindholm et al. [51]

Another interesting feature of the cam-roller contact is axial profiling of the cam or roller. Usually it is the roller which is profiled in axial direction as the cam has a larger width. This is done in order to reduce stress concentrations which would have been generated naturally (due to the high geometric discontinuity) at the extremities of the contact. Different types of axial profiling, such as rounded edges, chamfered edges, logarithmic and crowning, can be utilized. In fact, due to axial profiling the effective contact length in axial direction reduces. Both theoretical and experimental studies have shown that the maximum pressure and minimum film thickness are located near the regions where axial profiling starts [80, 59, 49].

At this point it is worthwhile making a distinction between two type of line contacts

according to their modelling approach. The first is the traditional infinite line contact in which the axial pressure distribution is assumed to be uniform and the film thickness is assumed to be located in the central region near the outlet. Note that the term "infinite" stems from the fact that for a line contact the radius of curvature (of approximating paraboloids of the contacting bodies) in one of the principle directions is infinitely large (very broad ellipse). The second type of line contact is the finite line contact which accounts for non-uniform axial pressure distribution and consequently the correct prediction of magnitude and location of minimum film thickness. As pointed out in the aforementioned studies, the minimum film thickness predicted in the central region may be significantly higher than the minimum film thickness near the side constrictions, thus ignoring useful information such as extra deformation near the edges, localized stress concentrations, possible asperity interaction (and thus wear) and fatigue.
EHL behaviour in cam-roller contacts would therefore be more appropriately described by finite line contact models. The cam-roller finite line contact has been studied by Shirzadegan et al. [67]. The aforementioned authors highlighted the use of different type of profiles such as logarithmic and crowning and their influence of film thickness and pressure. However, they did not account for roller slippage at the cam-roller contact.

2.4 Identified research gaps

From the literature review briefly described in the previous section one may conclude that significant effort has been made in order to understand the tribological behaviour of cam-roller units better. However, there are still certain topics which are – despite their high relevance – not fully covered yet in the literature. These topics include:

- The coupled tribological behaviour of the cam-roller and roller-pin contact: the coupling between cam-roller contact and roller-pin contact has never been investigated systematically despite its high interdependency. It is interesting to note that all studies in past literature assumed that the roller-pin contact operates under ideal conditions (low friction coefficient), i.e. the cam-roller contact has gained much more attention than the roller-pin contact. This is of course an incentive to systematically study the cam-roller lubrication performance as a function of roller-pin contact friction level. This exercise should provide useful insight into the coupled tribological behaviour of the two contacts.

- Accurate description of the friction at cam-roller contact and roller-pin contact: from past literature one may observe that mixed-lubrication models for cam-roller contacts either rely on i) semi-analytical formulations for asperity contact

component and Reynolds equation, ii) assumption of pure rolling conditions, iii) assumption of a constant coefficient of friction for the roller-pin contact or iv) assumption of isothermal conditions and Newtonian lubricant behaviour. As such, no full numerical solution accounting for all the aforementioned features has been presented.

- A more fundamental understanding into the tribological behaviour of finite line contacts in the context of cam-roller follower applications: existing studies regarding lubricated finite line contacts provide sufficient knowledge to perform more in-depth investigations in order to gain a more fundamental understanding into the tribological characteristics of these types of contacts. The cam-roller contact is inherent to varying operating conditions such as entrainment velocity, radii of curvature and load. It is very important that the axial surface profile shape is designed optimally from a tribological perspective, considering the full range of operating conditions.

The next chapter comprises the presentation of a series of models (ultimately leading to a mixed lubrication model) along with their corresponding results, which systematically cover the topics mentioned above.
First a smooth finite line contact EHL model was developed and simulations were carried out in order to gain a more fundamental understanding concerning finite line contact EHL behaviour in terms of film thickness and pressure distribution. Based on this understanding the model was adapted to the case of a cam-roller contact problem in which the frictional losses, film thickness and pressures were related to the axial shape of the rollers. The roller-pin contact model, which is inherently 3D due to its construction, was then modelled to accurately predict the frictional force, film thickness and pressure. The model was further expanded to include roughness (based on real measured surface topography), thermal and non-Newtonian effects, i.e. a mixed-TEHL model. This was done in order to gain more insight into the influence of rheology as well as surface roughness on frictional response at cam-roller contact. Based on the knowledge obtained from the mixed-TEHL simulations interesting regions/spots, in terms of lubrication behaviour, on the cam's lateral surface were identified. The "sensitivity" in lubrication performance, on these identified regions, as a function of roller-pin contact friction level was then assessed. Based on the results obtained from the mixed-TEHL model the friction description on asperity level had to be described in greater detail. To be more specific, the asperity shear stress formulation was then adjusted to that of a rough rolling-sliding contact in the low SRR domain (see Figure 2.3).

Chapter 3

Coupled cam-roller, roller-pin contact modelling

3.1 Torque balance

In section 1.3 it was explained that the cam-roller and roller-pin contact should be seen as a coupled tribological system, as the rotational speed of the roller depends on the lubrication conditions in both contacts. The rotational speed of the roller follower is governed by traction at the cam-roller contact. Friction acting on the inner wall of the roller resists or tries to slow down the motion of the roller. The roller on itself rotates about its own axis and thus has an angular acceleration. This consequently induces an angular moment of the roller, which is defined as the product of the angular acceleration and mass moment of inertia of the roller.
The roller rotational speed is obtained by balancing the tractive torque with the combined torques due to roller-pin friction and roller inertia force. In equation form this yields:

$$\underbrace{\mu_{\mathrm{c-r}} R_{\mathrm{f}} F}_{\text{tractive torque}} = \underbrace{\mu_{\mathrm{r-p}} R_{\mathrm{pin}} F}_{\text{resisting torque}} + \underbrace{I\,\dot{\omega}_{\mathrm{roller}}}_{\text{inertia torque}} \tag{3.1}$$

where friction coefficients $\mu_{\mathrm{c-r}}$ and $\mu_{\mathrm{r-p}}$ denote the cam-roller and roller-pin contact friction coefficient, respectively. $I = 0.5 m_{\mathrm{r}} \left(R_{\mathrm{pin}}^2 + R_{\mathrm{f}}^2 \right)$, denotes the mass moment of inertia of the roller. ω_{r} is adjusted by means of an iterative procedure to satisfy eq. 3.1. From eq. 3.1 it can readily be deduced that if the RHS of the equation is larger than the LHS, the rolling requirement cannot be satisfied and consequently slip will occur. This may be the situation, for example, at high cam rotational velocities. Higher cam rotational velocities will induce higher roller angular accelerations and consequently

higher inertia torques.

3.2 Kinematics

The heavily loaded cam-roller follower unit analysed in this study is part of a fuel injection pump unit of a heavy duty diesel engine of a truck. The type of configuration considered in here is that of a cam and reciprocating roller follower (see Figure 1.7).
As mentioned earlier in section 1.2 the friction coefficient of a lubricated contact depends on many factors, including i) the applied load, ii) the reduced radius of curvature and iii) the lubricant entrainment velocity, at the point of contact. All three of the aforementioned parameters vary throughout the cam's lateral surface. The lubricant mean entrainment velocity of the cam-roller contact is defined as follows:

$$U_{\mathrm{m}} = \frac{U_{\mathrm{c}} + U_{\mathrm{r}}}{2} \tag{3.2}$$

U_{r}, which follows from ω_{r}, is governed by the torque balance eq. 3.1 and thus is an unknown. Hence, from the configuration and geometrical parameters of the cam-roller follower it is possible to deduce only the cam radius of curvature $R_x(\theta)$, the cam surface velocity $U_{\mathrm{c}}(\theta)$ and the contact force $F(\theta)$. The variations of these three aforementioned variables as a function of the cam angle θ are obtained from a kinematic model.

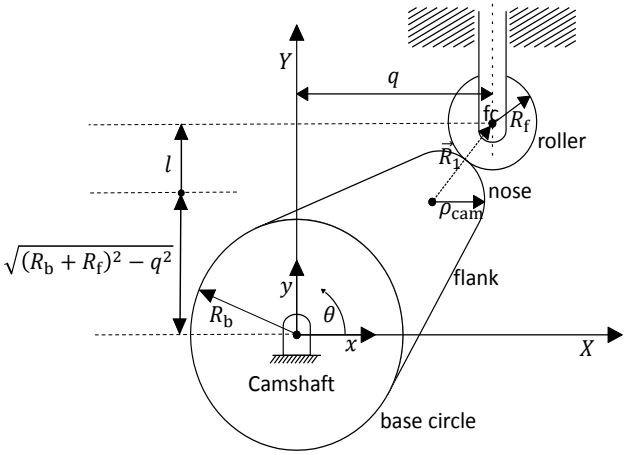

FIGURE 3.1: Cam and roller follower configuration schematically with specifications of coordinate system and nomenclature.

The kinematic model adopted in this work stems from Matthews et al. [54], who developed a general procedure to derive the variations in reduced radius of curvature and entrainment velocity for several types of cam-follower configurations. The details are

described in Paper B. Figure 3.1 shows the cam and reciprocating follower configuration along with nomenclature, coordinate system and angles.

The kinematic analysis of the cam and reciprocating roller follower mechanism requires the lift curve $l(\theta)$[1], outer radius of roller R_{f} and global position of cam and follower as input. Note that subscripts "f " and "fc" denote follower and follower centre respectively.

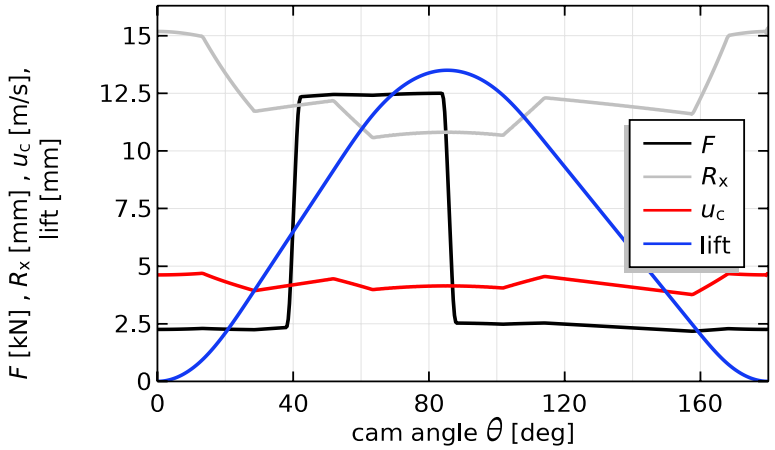

FIGURE 3.2: Variation of the lift, reduced radius of curvature R_x, cam surface speed U_c and contact force F as a function of cam angle θ. The profile for U_{c} corresponds to an ω_{c} of 950 RPM.

The variations of the lift, reduced radius of curvature R_x, cam surface velocity U_{c} and contact force F, as a function of the cam angle θ are depicted in Figure 3.2. The curves for $U_{\mathrm{c}}(\theta)$, $R_x(\theta)$ and $F(\theta)$ have been derived for the given lift curve. The kinematic variations depicted in Figure 3.2 correspond to a cam rotational speed ω_{c} of 950 RPM. From the lift profile one may, for instance, deduce the region (e.g. range of cam angle) in which the nose of the cam is in contact with the roller. From Figure 3.2 it is clear that the centre of the nose region is defined at a cam angle of 90°, i.e. the highest vertical displacement. Regions corresponding to low values in lift or no lift at all are commonly called the flank/base circle regions. The cam shape is repeated after 180° cam angle, i.e the kinematic variations occurring in interval $0° - 180°$ cam angle are identical to those between 180° and 360° cam angle. Hence, Figure 3.2 only depicts the variations occurring between 0° and 180° cam angle. Note that the aforementioned applies only to the specific cam studied in this thesis and does not apply "universally". As can be observed from Figure 3.2, the reduced radius of curvature and cam surface velocity are fairly constant

[1]The lift curve $l(\theta)$ illustrates the vertical displacement of the roller follower centre as depicted in Figure 3.1. The lift curve $l(\theta)$ is specified in n data points. These data points are measured values with increments of a specified angle (usually less than one degree cam angle). The smaller this increment the higher the resolution of the profile and hence accuracy of the solution. The n data points are spline-interpolated with respect to cam angle, i.e. the discrete displacement profile is interpolated to obtain a third-order piecewise continuous polynomial fit for displacement versus cam angle. The derivatives of this polynomial fit will give the velocity and acceleration profiles. A similar procedure was applied to deduce the contact force profile.

(with minor variations) throughout the cam's lateral surface, whereas steep variations occur in the contact force profile. The latter is due to the sudden pumping action of the injection unit, which results to high pressures coming from the fuel injector. More details on this can be found in Paper B.
For the cam-roller follower lubrication analysis described in this thesis the kinematic input conditions are deduced from Figure 3.2.

3.3 Smooth EHL solutions

As mentioned earlier in section 1.2, the friction coefficient of a lubricated contact depends on many factors such as i) the lubricant rheological properties, ii) applied load, iii) geometrical parameters of interacting solids, iv) mechanical properties of the solids, v) lubricant entrainment velocity and vi) surface topography.
Focusing on the cam-roller contact (as this is a non-conformal contact), and as a first step, it is interesting to see whether or not surface roughness effects are significant. This assessment can be done simply by employing a smooth surface-based EHL analysis on this contact. The output should yield the pressure and film thickness distribution within the contact. From the film thickness distribution, information can be acquired regarding the significance of potential asperity contact.
As pointed out earlier in section 2.3, a line contact can be divided into two categories according to their modelling approach. The first is the traditional "infinite" line contact in which the axial pressure distribution is assumed to be uniform and the film thickness to be located in the central region near the outlet. For highly loaded infinite line contacts, a reasonable estimate of the film thickness and pressure distribution can be made using classical film thickness formulas [17, 56] and dry Hertzian contact theory respectively.
The second type of line contact is the finite line contact (due to axial surface profiling) which accounts for non-uniform axial pressure distribution and consequently the correct prediction of magnitude and location of minimum film thickness. For the cam-roller pair considered in this study the roller is profiled in axial direction. Hence, traditional (analytical) solutions are less accurate and a numerical model needs to be developed.
The models developed in this section (and its sub-sections) all assume isothermal conditions and Newtonian behaviour of the lubricant. Compressibility and piezoviscous behaviour of the lubricant are modelled using the Dowson-Higginson [18] and Roelands [65] relations respectively.
Section 3.3.1 elaborates on the basics of lubricated finite line contact characteristics by means of the developed model. Section 3.3.2 adopts and expands the finite line contact model of section 3.3.1 to analyse the cam-roller lubrication performance and the influence

of roller axial profiling. Section 3.3.3 elaborates on the influence of including roller-pin contact elastic deformation on the film thickness, pressures and friction coefficient.

3.3.1 Basics of lubricated finite line contacts

Axial profiling of rollers is utilized to reduce edge loading, i.e. to reduce the magnitude of sharp pressure peaks at the extremities, which would have arisen naturally due to the high geometric discontinuity there in the case of a perfectly straight roller.
Depending on the type of surface profiling, the pressure and film thickness distribution may deviate significantly from that predicted using the infinitely long line contact assumption, i.e. the film shapes near the extremities are very different from those at the central plane. In fact, the absolute minimum film thickness and maximum pressure, which are crucial design parameters, always occur near the position where axial surface profiling starts. This has also been proven both experimentally and theoretically by a number of researchers [80, 32, 59].
For finite line contact analysis the film thickness eq. 2.3 is modified in order to include the axial shape of the roller in the model as follows:

$$h\left(x,y\right) = h_0 + \frac{x^2}{2R_x} + g\left(y\right) - \delta\left(x,y\right) \tag{3.3}$$

where $g\left(y\right)$ can be any function to approximate the geometrical variation of the axial surface profile.
One type of finite line contact EHL results concerning a roller with a fraction of straight length in axial direction and rounded corners at the extremities (see Figure 3.3), on a plate, are presented in Figure 3.4. The results, which are adopted from the pioneering work of Park and Kim [63], correspond to a lowly loaded contact ($p_{\mathrm{h}} = 0.304$ GPa). For lowly loaded contacts the importance of considering axial surface profiling of the roller is better visualized. A more detailed explanation pertaining to the latter will follow later in this section.

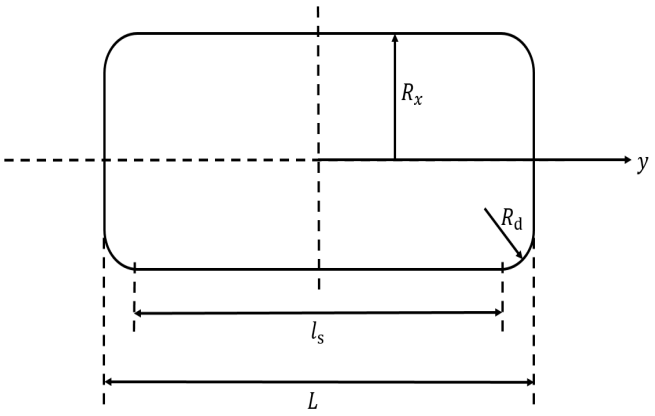

FIGURE 3.3: Considered roller geometry.

Figure 3.4(b) depicts the calculated pressure distribution for the lowly loaded contact, as described in the work of Park and Kim [63]. Flow continuity demands that the pressure gradients should be coupled with local restrictions of minimum film thickness. Hence, the secondary pressure peaks near the side constriction also inhibit lubricant flow in their vicinity. Consequently, small islands (iso-film thickness contours) are formed at the rear of the contact (see Figure 3.4(a)). These are commonly referred to as end closure films in the literature. Section 1-1 is the central line in streamline direction (plotted against $y = 0$) where the minimum film thickness $h_{\text{min,central}}$ occurs. Sections 2-2 and 3-3 correspond to contour sections where respectively the absolute maximum pressure p_{max} and the absolute minimum film thickness h_{min} occur. Section 4-4 and 5-5 are contour sections in transverse direction where respectively the absolute maximum pressure and absolute minimum film thickness occur.

Note that the solution corresponding to section 1-1, i.e. the $y = 0$ plane, would correspond to traditional solutions emerging from infinite line contact analysis. From Figures 3.4(b) and 3.4(c) it is clear that the maximum pressure occurs near the side constriction and rear exit of the lubricated contact area, i.e. where profiling starts. To be more specific, infinite line contact analysis would predict that the (dimensionless) maximum pressure would be around 1.5, while the actual maximum pressure is 3.4. Similarly for the minimum film thickness (see Figure 3.4(d)), as the infinite line contact analysis would predict a (dimensionless) minimum film thickness of around 2 while the actual minimum film thickness is 1.2. The infinite analysis clearly yields a wrong indication of what the contact actually experiences. Finally, Figure 3.4(d) shows that the minimum film thickness also occurs near the position where axial profiling starts.

These findings clearly reveal the importance of including axial surface profiling in the EHL model.

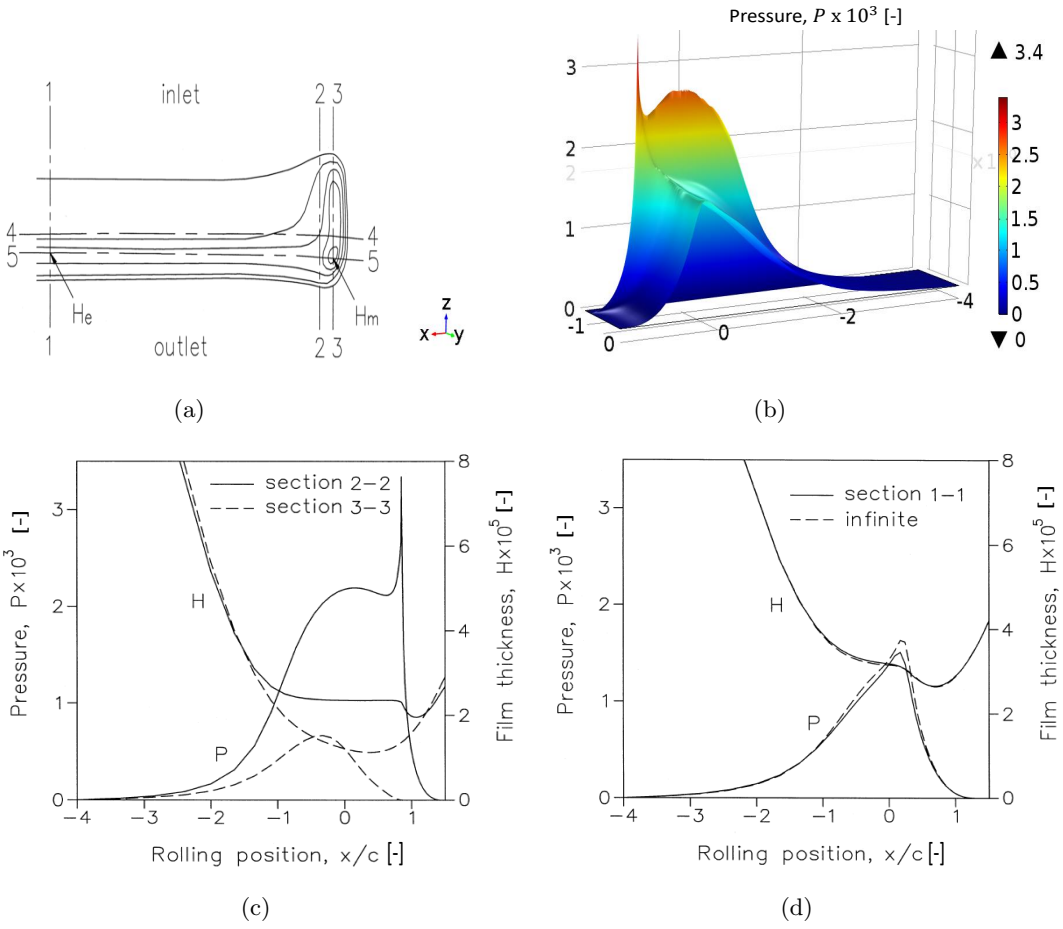

FIGURE 3.4: a) Definition of sections through the lubricated contact, b) height expression of the pressure distribution ($y = 0$ is the symmetry plane) and c-d) cross-sectional view of the pressure and film thickness distributions. Note that here $H = \frac{h}{R_x}$, $P = \frac{p}{E'}$ and c is the dry Hertzian contact half-width. Figures a, c and d are reproduced from reference [63].

A steady state finite line contact EHL model, of which the details are described in Paper A, was developed in order to gain a thorough understanding of the tribological behaviour of this type of contacts. In these calculations isothermal conditions are assumed and non-Newtonian effects are ignored for the sake of simplicity. The model relies on a full system finite element discretization of the EHL governing equations, linear elasticity and the load balance equations. In the current approach the elastic deformation is not calculated using the traditional half-space approximation. Instead, the 3D linear elasticity equations with appropriate boundary conditions are employed on a finite computational domain to solve the displacement field (see Paper A). All governing EHL equations are solved in a fully coupled framework with the assistance of a Newton-Raphson iteration scheme.

The results of the developed model were compared with those obtained by Park and Kim [63]. Good agreement was obtained with their model. Furthermore, the influence of

the operational parameters such as lubricant entrainment velocity, elastic modulus and contact force were studied. The results are shown in Figure 3.5

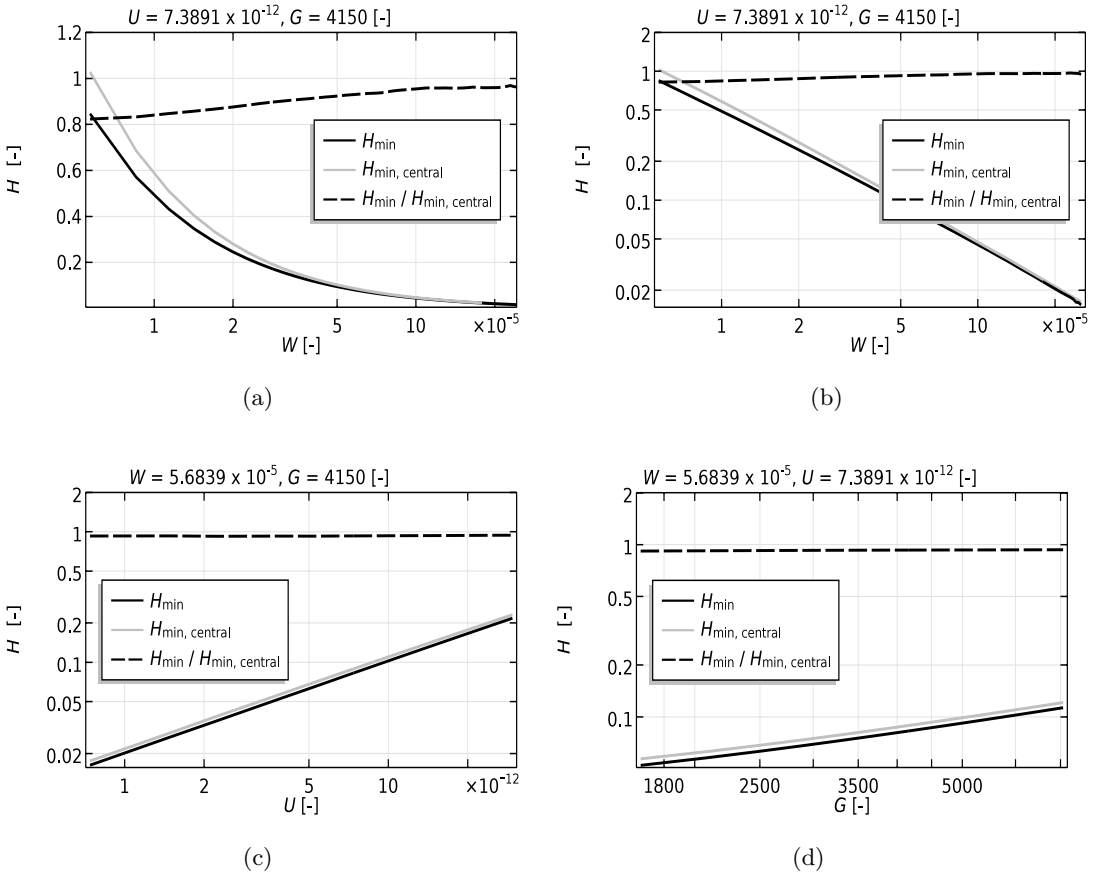

FIGURE 3.5: Variation of $H_{\min}$, $H_{\min,\text{central}}$ and ratio $H_{\min}/H_{\min,\text{central}}$ with dimensionless speed U, material G and load W parameters while keeping two fixed at a time. The minimum film thickness $H_{\min}$ seems to behave differently with increasing load.

Figure 3.5 plots the variation of $H_{\min}/H_{\min,\text{central}}$ as a function of dimensionless speed U, material G and load W parameters. From the results it is clear that the absolute minimum film thickness is highly affected by variations in load. This is in line with previous theoretical [63] and experimental findings [79]. Especially at low to moderate loads this phenomenon is much more visible. For variations in U and G the ratio $H_{\min}/H_{\min,\text{central}}$ seems to remain constant. Note that the behaviour of $H_{\min,\text{central}}$ is much more explainable using traditional EHL solutions for infinite line contacts [63]. It is therefore much more interesting to analyse the behaviour of ratio $H_{\min}/H_{\min,\text{central}}$. The behaviour of $H_{\min}/H_{\min,\text{central}}$ with increasing load can be explained in a similar manner as for elliptical contacts. At increasing loads the effective lubricated area increases, indicating that the contact centre flattens more and the end closure films (small islands of minimum film thickness as shown in Figure 3.4(a)) become smaller. As a result the ratio $H_{\min}/H_{\min,\text{central}}$ increases. A more detailed explanation of this is given in Paper

A. In fact, with increasing loads the effective (lubricated) contact area increases and hence the secondary peak (occurring at the rear of the contact) "smears out". As a consequence the local pressure gradients, near the region where axial profiling starts, will decrease and thus will the ratio $H_{\min}/H_{\min,\text{central}}$ increase.

3.3.2 Influence of roller axial surface profiling

As a basic understanding concerning the characteristics of finite line contacts had now been obtained, the model described in Paper A was expanded to allow for transient conditions to analyse lubrication conditions at the cam-roller contact. Expansion to cam-roller follower analysis included a few additional sub-steps:

- The kinematic variations, i.e. the reduced radius of curvature $R_x(\theta)$, cam surface speed $U_c(\theta)$ and contact force $F(\theta)$, were included in the model. Also, the model was expanded to account for squeeze film motion effects.

- The transient finite line contact EHL model was expanded by allowing for variable rotational velocity of the roller. This was attained by implementing the torque balance eq. 3.1 as an additional global equation, associated with unknown ω_{r}, to the governing system of EHL equations. Hence, possible slippage within the cam-roller contact could be determined.

- Furthermore a quasi-static isoviscous semi-analytical model for film thickness and friction calculation at the roller-pin contact was incorporated in order to improve accuracy for slip and friction loss determination. This is contrary to previous studies which assumed a constant friction coefficient (usually in the order of 0.001-0.005) for the roller-pin contact. The semi-analytical model adopted is based on a "rigid" surface assumption for hydrodynamic journal bearings and stems from the work of San Andres [66]. The aforementioned author derived an approximate analytical solution that gives good results for finite length bearings. In this semi-analytical model the friction coefficient $\mu_{\text{r-p}}$ can be calculated once the eccentricity ratio $n = \frac{e}{C}$ and roller angular velocity ω_{r} are known. e is the offset of the roller from its centre position, which is defined at the centre of the pin. Note that n ranges between zero and one. The film thickness in the roller-pin contact is $h_{\text{roller-pin}} = C(1 - n\cos\phi)$. C is the radial clearance, and the angle ϕ is the circumferential coordinate defined as starting from the minimum film thickness $h_{\text{min,roller-pin}}$.
  The eccentricity ratio n is calculated using an additional equation, which balances

the Sommerfeld number $S = \frac{F}{\eta_0 \omega_r L R_{pin}} \left(\frac{C}{R_{pin}} \right)^2$ with the resultant hydrodynamic forces. This is implemented in the model as an additional global equation, associated with unknown n, to the governing system of EHL equations.

The aforementioned points summarize the cam-roller follower lubrication model. Paper B describes the cam-roller follower lubrication model in full detail.
For the cam-roller analysis, the axial shape of the roller corresponds to a logarithmic function which may be written as follows:

$$g(y) = -A \ln \left\{ 1 - \left[1 - \exp\left(\frac{-z_m}{A} \right) \right] \left(\frac{2y - L_s}{L - L_s} \right)^2 \right\} \tag{3.4}$$

where A represents the degree of crowning curvature, z_m is the crown drop at the extremities and L_s is the straight roller length. The crown drop, which is a more commonly used term in literature, is nothing other than the radius reduction towards the roller ends. Note also that $g(y)$ is valid only for $\frac{L_s}{2} \leq y \leq \frac{L}{2}$, otherwise zero. The degree of geometric discontinuity which is defined according to the axial profile shape will, of course, have an effect on the secondary pressure peak and thus on the absolute minimum film thickness h_{min}. Figure 3.6 depicts the roller axial shape with its defined design parameters L_s, z_m and A.

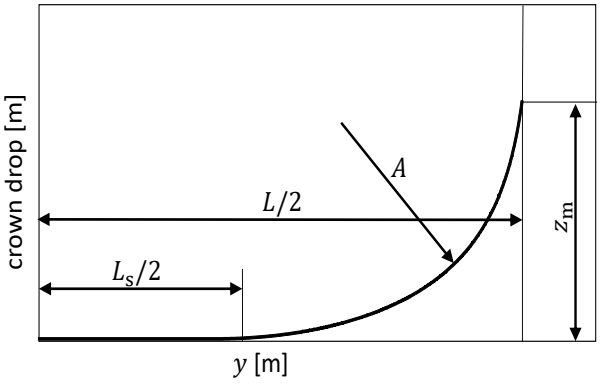

FIGURE 3.6: Roller axial profiling utilizing a logarithmic shape with defined design parameters straight length L_s, crown drop z_m and crowning curvature A.

A comprehensive lubrication analysis of a cam and roller follower pair, as part of a fuel injection pump, was performed. The input parameters are given in Table 3.1. Furthermore, the kinematic variations, such as $R_x(\theta)$, $U_c(\theta)$ and $F(\theta)$ are required as an input for the EHL calculations. These are given in Figure 3.2.

TABLE 3.1: Reference operating conditions and geometrical parameters for cam roller follower analysis. Note that cam and roller share the same mechanical properties.

Parameter	**Value**	**Unit**
E	200	GPa
ν	0.3	-
α	1.78E-8	Pa^{-1}
η_0	0.01	Pa·s
ρ_0	870	$\mathrm{kg/m}^3$
m_r	0.11	kg
R_f	0.018	m
R_pin	0.0095	m
C	74	μm
L	0.021	m
A	17	μm
L_s	0.007	m
z_m	50	μm

The results presented here corresponds to a cam rotational speed of 950 RPM. Figure 3.7(a) provides the variation of the minimum film thickness over the cam's lateral surface. The "dip" in the film thickness profile (between 40°-90°) is due to a rapid increase of contact force (1 kN to 12 kN). It is worth mentioning that for the configuration studied, the entrainment velocity remains approximately constant over the cam periphery (see profile for U_c in Figure 3.2). Furthermore it can be noticed that the infinite line contact analysis results (from which the minimum film thickness can also be calculated analytically using a film thickness formula) overestimate the minimum film thickness as side leakage is ignored in this approach, i.e. infinite line contact models ignore the axial pressure gradient driven flow (second term RHS of eq. 2.1) which accounts for side leakage. Assuming a composite surface roughness of R_q =0.2 μm of the opposing surfaces, it can be concluded that the cam-roller contact operates in the mixed lubrication regime as $\frac{h}{R_q} < 3$. Extension to a mixed lubrication model will be done later on in this thesis.

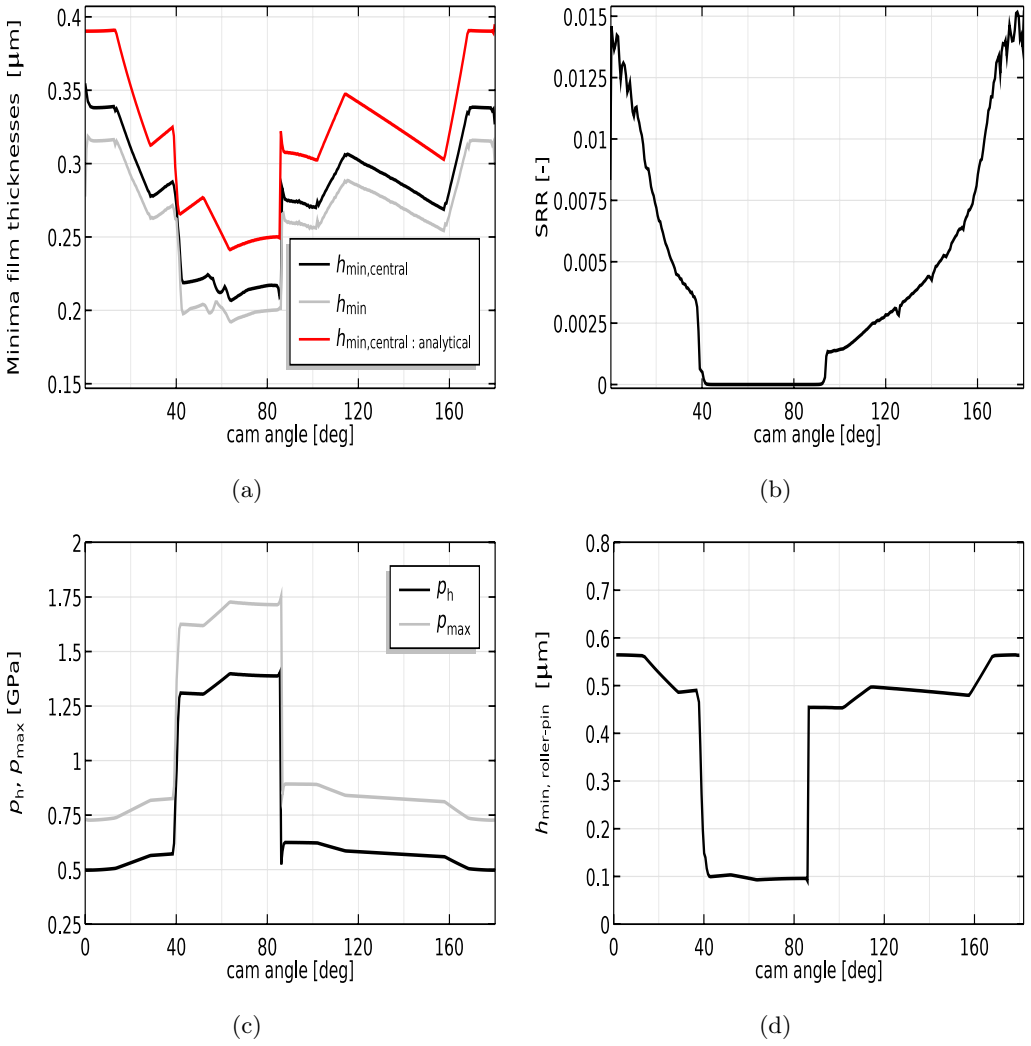

FIGURE 3.7: Evolution of a) minima film thicknesses, b) slide-to-roll ratio SRR as function of cam angle and c) maxima pressures. Note the abrupt variations in the overall solution at a cam angle of between 40°-90°, due to sudden activation of pumping action.

Furthermore, due to the large contact forces involved, negligible slippage occurs. It is evident from Figure 3.7(b) that the slide-to-roll ratio remains less than 2% over the full cycle. Again, the "dips" are due to rapid increase in contact force. The evolution of maximum pressure variation is presented in Figure 3.7(c). It can be seen that the maximum pressure cycles between 0.5 GPa and 1.8 GPa. It can readily be deduced from the aforementioned Figure that infinite line contact analysis significantly underestimates the actual maximum pressure.

Finally, the variation of minimum film thickness at the roller-pin contact is presented in Figure 3.7(d). A low film thickness of approximately 0.1μm is predicted around the nose region, suggesting mixed or even boundary lubrication regime (based on a composite roughness of 0.2μm). The prediction of such a low film thickness may be attributed to the fact that the semi-analytical lubrication model for the roller-pin contact does not

include deformation of solids which might enhance film thickness distribution. Instead, the minimum film thickness is directly linked with the contact force. For instance, in EHL the film thickness varies much less with load than with sum velocity. Accurate calculation of the film thickness distribution in the roller-pin contact is thus very important and should be investigated in more detail.
This will be done in section 3.3.3 of this thesis. Also, the results up till now certainly emphasize the importance of accurate friction calculation in the roller-pin contact as this contact is as important as the cam-roller contact, but often weakly included in previous roller friction models [13, 39]

From the results obtained from the transient analysis it can be deduced that for the considered cam-roller configuration, any position on the nose between the fixed margin of $40°-90°$ cam angle can be chosen to examine the variation of lubrication performance indicators (as both the maximum pressure and the minimum film thickness occur in this region). It would be interesting to study the effect of different axial profile designs on crucial cam-roller contact performance indicators, such as minimum film thickness, maximum pressure and rolling power loss. Note that due to negligible sliding, rolling friction is dominant. Rolling friction is generated due to the pressure driven flow, i.e. due to pressure gradients. More details on this can be found in Paper B.

The axial profile can be optimized for a certain operating point, to obtain a more uniform axial pressure distribution. For the present study three different roller axial surface logarithmic profiles are considered. Table 3.2 presents the design parameters corresponding to the three different logarithmic profiles (see Figure 3.8(a)). Note that design 1 is similar to that given in Table 3.1, which is used for the cam-roller analysis. For the present study the cam angle was fixed at 68°.

	L_s (mm)	A (μm)	z_m (μm)
design 1	7	17	50
design 2	4	100	100
design 3	11	10	10

TABLE 3.2: Considered logarithmic axial surface profiles.

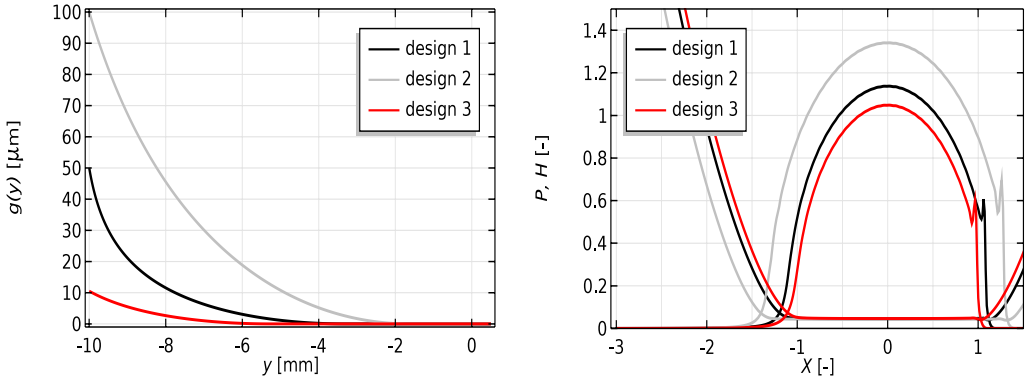

(a) Different considered designs for logarithmic axial surface profiling.

(b) Influence of different logarithmic axial surface profiles on pressure and film thickness distributions, plotted along line $Y = 0$.

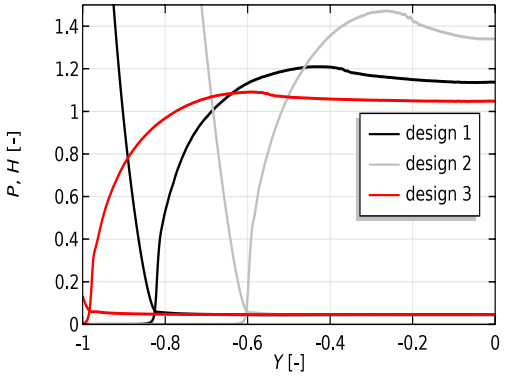

(c) Influence of different logarithmic axial surface profiles on pressure and film thickness distributions, plotted along line $X = 0$.

FIGURE 3.8: Influence of a) considered roller axial surface profiles on b) streamline and c) axial pressure and film thickness distributions.

Figures 3.8(b) and 3.8(c) present the dimensionless pressure and film thickness distributions along the lines $Y = 0$ and $X = 0$ respectively. The most uniform pressure distribution is obtained for design 3. In fact, for design 3 the transverse lubricant flow experiences significantly less geometric discontinuity near the region where axial profiles starts. As a result, the pressure profile inhibits less steep gradients at the rear of the contact and also covers more area to carry the applied load. For this reason the minimum film thickness increases and maximum pressure decreases in comparison with reference design 1 (see Table 3.3). However, due to the fact that the covered contact area increases, the power losses also increase for design 3.

Exactly the opposite is observed for design 2, i.e. due to larger geometric discontinuities the maximum pressure increases and the minimum film thickness decreases. However, due to a decrease in effective lubricated contact area, the power loss decreases. It is clear

from the case studies that maximum pressure and minimum film thickness values are improved, at the expense of higher power losses.

	$h_{\min}$ (μm)	$p_{\max}$ (GPa)	power loss (W)
design 1	0.202	1.68	5.75
design 2	0.175	2.01	4.37
design 3	0.211	1.51	7.10

TABLE 3.3: Influence of considered axial surface profile design on crucial performance indicators around nose region.

3.3.3 Influence of elastic deformation at roller-pin contact

The general framework of the smooth-based cam-roller follower lubrication model (explained in section 3.3.2) relies on a transient finite length line contact EHL model for the cam-roller contact and quasi-static semi-analytical lubrication model for the roller-pin contact. The roller-pin contact was modelled as a full film journal bearing. The basis of the semi-analytical model used for the roller-pin contact relies on the assumption that the interacting surfaces are rigid and that the lubricant exhibits isoviscous behaviour. It is expected that under the extremely high contact forces coming from the fuel injector (ranging from 2kN to 15 kN), which are also directly transmitted to the roller-pin contact, the "rigid surfaces" assumption might not be accurate. It is therefore important to include the elastic deformation of the roller and pin into the analysis.

Past studies [61, 26] have shown that the rigid hydrodynamic solution for journal bearings might significantly overestimate the maximum pressure and underestimate the minimum film thickness. The roller-pin contact model, which is inherently 3D due to its construction (see Figure 1.2(b)), was thus modelled to accurately predict the frictional force, film thickness and pressure. As such, a 3D FEM-based transient EHL model was developed for the roller-pin contact. The roller-pin contact EHL model allows for elastic deformation of roller and pin, and also accounts for the piezoviscous and compressible behaviour of the lubricant. This model was then added to the previously developed EHL model for the cam-roller contact in a fully coupled framework. The two EHL models for cam-roller and roller-pin contact are interlinked via a global torque balance eq. 3.1 applied to the roller, which calculates the roller angular velocity.

The details of interlinked FEM-based EHL models for cam-roller and roller-pin contact are detailed in Paper C.

Due to shrink fitting of the pin in the tappet, the pin has a convex type of shape in between the ears (see Figure 1.2(b)). This is modelled as a type of axial crowning of the

pin. The resulting film thickness equation for the roller-pin takes the following form:

$$h\left(\Theta, y\right) = C - e_{\bar{x}} \cos\Theta - e_{\bar{y}} \sin\Theta + \frac{y^2}{2R_y} + \partial_{\mathrm{r}}\left(\Theta, y\right) \tag{3.5}$$

where R_y is the axial crowning curvature of the pin, Θ is the circumferential coordinate and ∂_{r} is the combined radial elastic deformation of the roller and pin. $e_{\bar{x}}$ and $e_{\bar{y}}$, which are the $\bar{x}$ and $\bar{y}$ components of the eccentricity e, are obtained by globally balancing the hydrodynamically generated force with the applied load. For more details see Paper C. In this study it is assumed that cam-roller contact force F is directly transmitted to the roller-pin contact.

Using the input parameters as given by Table 3.1, the kinematic variations in Figure 3.2, and additionally $R_y = 4.5$m, a transient analysis was performed. The evolution of the friction coefficients, minimum film thickness and pressure distribution were analysed.

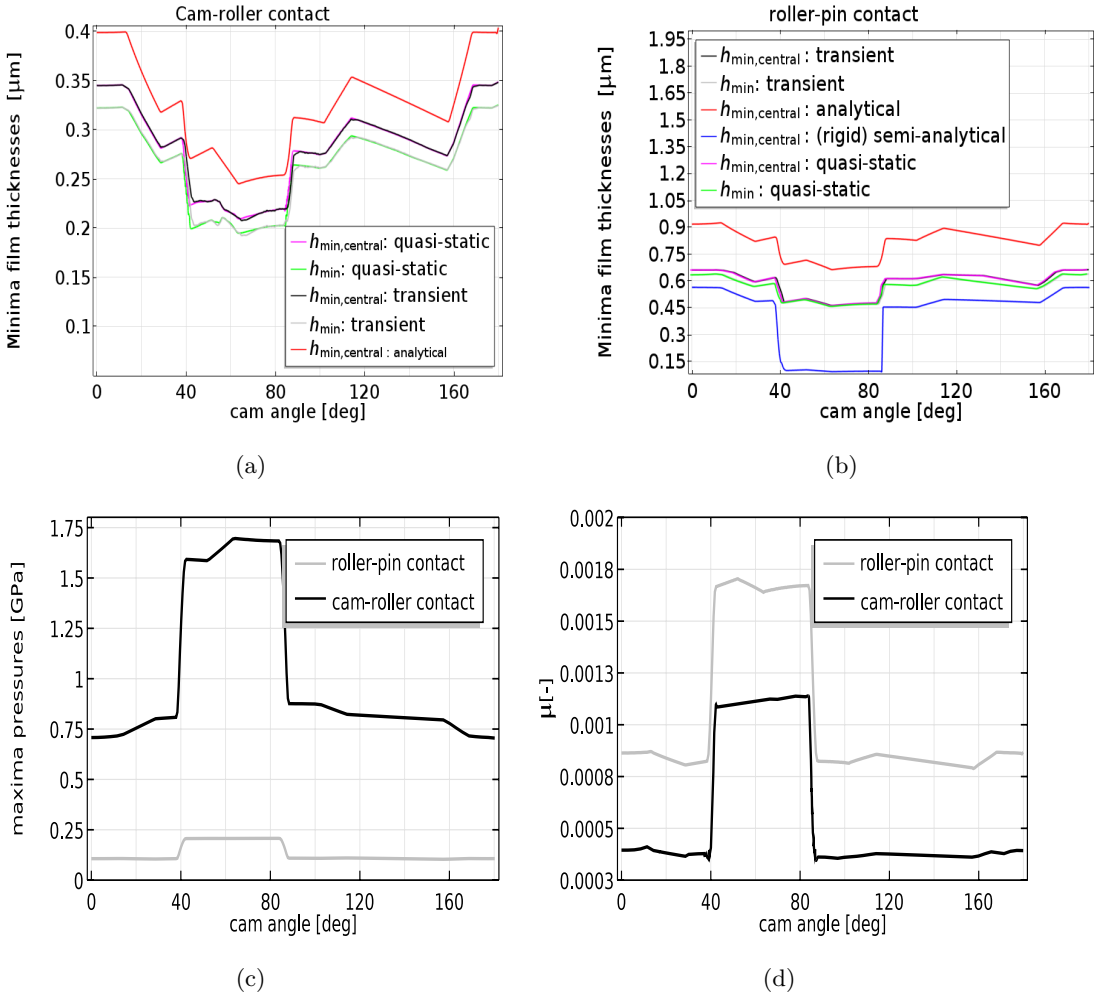

FIGURE 3.9: Evolution of a) minima film thicknesses for cam-roller contact, b) minima film thicknesses for roller-pin contact, c) maxima pressures, and d) friction coefficients.

Figure 3.9(a) shows the evolution of minimum film thickness as a function of the cam angle. Again, note that $h_{\text{min,central}}$ is the central plane ($y = 0$) minimum film thickness, while h_{min} is absolute minimum film thickness which usually occurs at the rear of the contact where axial surface profiling starts.

Again, one may observe the "dips" in the profiles at a cam angle of 40°- 90°cam angle due to the sudden increase in contact force. Figure 3.9(a) also compares the results for a full transient solution with those obtained using quasi-static analysis, i.e. without squeeze motion effect $\frac{\partial h\rho}{\partial t} = 0$. It can be concluded that transient effects, in this case squeeze film motion, are negligible as a minimal phase lag between the solutions is observed. Figure 3.9(a) also shows the evolution of the minimum film thickness obtained using the Dowson-Higginson [18] film thickness equation for an infinite line contact. It is clear that the analytical solution significantly overestimates $h_{\text{min,central}}$ as it does not account for side leakage.

Similar observations are made for the roller-pin contact (see Figure 3.9(b), i.e. quasi-static analysis yields fairly accurate results as squeeze film motion effects appear to be negligible. For the sake of comparison Figure 3.9(b) also the depicts the results obtained using the semi-analytical model, based on rigid surfaces, as was done in section 3.3.2. It is clear that, especially in the high contact force regions, the minimum film thickness is highly underestimated as elastic deformation is disregarded in this model. The result for the evolution of $h_{\text{min,central}}$, after applying the Dowson-Higginson [18] film thickness equation for infinite line contacts, for the roller-pin contact is depicted in Figure 3.9(b). As is the case for the cam-roller contact, the minimum film thickness is significantly overestimated as side leakage is disregarded.

As can be deduced from Figure 3.9(c), the maximum pressure for the cam-roller contact cycles between 0.5-1.8 GPa, while the roller-pin contact experiences significantly lower pressures (ranging between 0.1-0.25 GPa). The latter is due to the fact that the roller-pin contact is a conformal contact and thus has a much larger contact area.

The friction coefficients for cam-roller and roller-pin contacts are depicted in Figure 3.9(d). As can be seen, very low values of friction coefficients are achieved. For the cam-roller contact this appears to be caused by the fact that i) this analysis is based on smooth surfaces (no asperity interaction considered) and ii) negligible sliding is predicted, meaning that rolling friction is dominant here and sliding friction is negligible.

The range of values for the roller-pin friction coefficient are of the same magnitude as those measured by Lee and Patterson [50]. An increase in friction coefficient is noticed in the nose region. This increase is caused mainly by an increase in viscosity (piezoviscous effect). Furthermore, it is also worth pointing out here that consideration of elastic deformation in the roller-pin contact decreases the friction coefficient. This is because including elastic deformation results in a larger contact area, and thus in lower pressure. This causes a relative decrease in viscosity and therefore sliding friction.

Similarly to the analysis carried out in section 3.3.2 negligible sliding at the cam-roller contact was detected.

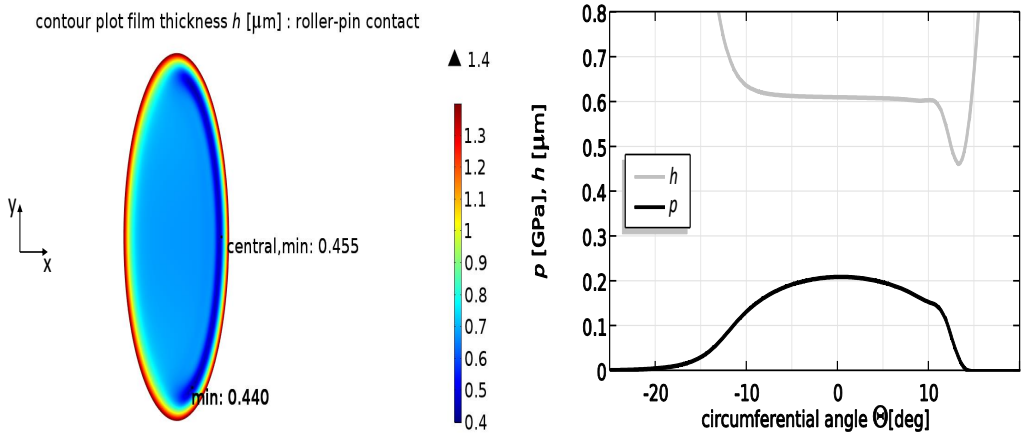

(a) Contour plot of the film thickness distribution illustrating the formation of side lobes.

(b) Pressure and film thickness distribution along circumferential coordinate Θ.

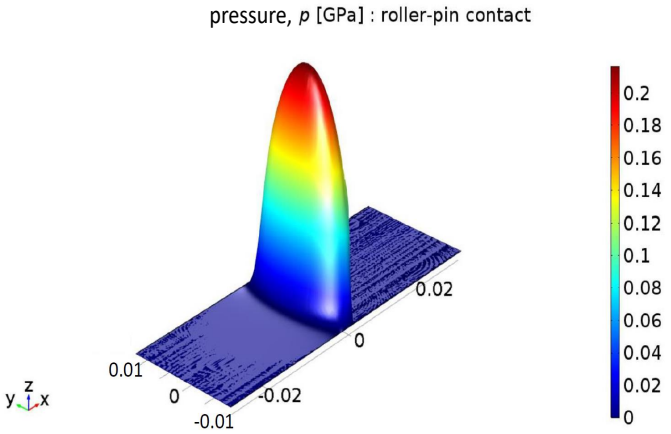

(c) Height expression of the pressure distribution. Dimensional Cartesian space coordinates are used here and $x = R_{\text{pin}}\Theta$.

FIGURE 3.10: Evaluation of pressure and film thickness distribution for the roller-pin contact. The operating conditions correspond to those at 64° cam angle, which lies in the cam's nose region.

Another important finding for the roller-pin contact was that, due to axial crowning of the pin, the contact footprint has an elliptical shape, which is clearly visible at high loads. This can be seen from Figure 3.10(a) which shows the contour plot of the film thickness distribution for 64° cam angle, from which it can be deduced that side lobes are formed where minimum film thickness h_{min} occurs (see Nijenbanning et al. [60]). Figure 3.10(b) presents the pressure and film thickness distribution for the roller-pin contact at the central ($y = 0$) plane. It can readily be observed that the pressure and film thickness distribution inhibit typical EHL characteristics, i.e. a Hertzian parabolic type pressure curve and film thickness distribution which is uniform in the centre of the

contact and has a local restriction $h_{\text{min,central}}$ at the outlet of the contact. These results are in line with those reported by O'Donoghue et al [61] for elastic journal bearings. An important remark to make here is that although the roller-pin contact may be conformal in nature, it exhibits similar tribological behaviour to the non-conformal finite length line contacts for the range of loads considered. In fact the (unintentional) crowning of the pin appears to be beneficial as a straight pin might induce edge loading, i.e. for the crowned pin the maximum pressure is located at the centre (see Figure 3.10(c)).

3.4 Mixed lubrication solutions

The results in section 3.3.3, pertaining to the evolution of film thickness for a cam rotational velocity of $\omega_c = 950$RPM, suggested that both cam-roller and roller-pin contact might be operating in the mixed lubrication regime. This hypothesis is based on a composite R_q of 0.2μm, which is typical for a run-in cam-roller follower contact [6]. For the current application ω_c ranges between approximately 400 and 1300 RPM. From the latter it is obvious that for the low to moderate range of cam rotational velocities both cam-roller and roller-pin operate in the mixed lubrication regime. This is of course an incentive to expand the general cam-roller lubrication model, described in section 3.3, to include surface roughness effects, i.e. to develop a mixed lubrication model.

There are two types of general approach to the calculation of the friction in mixed lubricated contacts. The first is the rough-EHL theory-based models and the second is the load-sharing concept-based models [70, 53].

In the rough-EHL models the lubricant flow and surface deformation are solved numerically by means of a discretized rough surface in both the solid deflection and Reynolds equations [83, 24]. These models are thought to be more accurate, however there are still issues/problems in the "thin film lubrication regime", such as accuracy, convergence, mesh size dependence and the film collapse criterion [82, 38, 57, 84].

The aforementioned issues do not apply to load-sharing based models, as first introduced by Johnson [40]. Load-sharing models are known for their robustness and simple methodology for friction estimation. In fact, this approach splits the problem into a separate smooth surface EHL and dry rough contact problem. The contact intensity is governed by the proportionality of loads carried by lubricant film and asperity contacts (see eq. 2.5). The dry rough contact and smooth surface EHL solver are linked through the film thickness. Since then, this approach has been adopted and refined in many other studies [31, 58, 9, 2], which have demonstrated a reliable approach in friction prediction. The mixed friction coefficient is simply calculated using eq. 2.6.

In this thesis the load-sharing concept has been adopted for mixed friction calculations. The algorithm adopted here relies on a FEM-based smooth surface EHL solver and

boundary element method (BEM)-based dry rough contact solver, which are linked through the film thickness.

In section 3.3 a smooth surface finite line contact EHL model was presented. In this section, however, the exact axial shape of the interacting solids has not been taken into account so as to reduce the required computational effort and complexity. Instead, the pressure distribution in the axial direction is assumed to be uniform. This simplifies the problem to an "infinite" line contact problem, i.e. a 2D problem. The models which are used here are described in detail in Papers D and E.

In this section the roller-pin contact friction coefficient $\mu_{\mathrm{r-p}}$ is used as an input parameter in order to asses its influence on the cam-roller lubrication performance. While section 3.4.1 focuses on improving mixed friction predictions in the high SRR domain by means of a mixed thermo-elastohydrodynamic model, section 3.4.2 focuses on the low SRR domain by including stick-slip transitions on asperity scale.

The reference operating conditions applying to this section, which by the way are almost the same as those given in Table 3.1, are listed in Table 3.4. From the results obtained in sections 3.3.2 and 3.3.3 it is interesting to assess the influence of roller-pin friction coefficient $\mu_{\mathrm{r-p}}$ on the lubrication performance of two specific cam angles, namely 0° and 63.5°. The choice of the aforementioned cam angles relies on the reasoning that at 0° cam angle the highest roller slip occurs (see Figure 3.7(b)), and at 63.5° cam angle both maximum pressure and minimum film thickness occur (see Figures 3.9(a) and 3.9(c)). The kinematic parameters corresponding to these cam angles are given in Table 3.5.

TABLE 3.5: Reference operating conditions for $\theta = 0°$ and $\theta = 63.5°$.

θ	F [N]	R_x [m]	U_{c} [m/s]
0°	2250	0.0152	4.62
63.5°	12500	0.0105	3.98

3.4.1 Influence of roller-pin contact friction level

Coming back to the cam-roller contact analysis, it has been shown in section 3.3.3 that when the lubrication conditions in the roller-pin contact are favourable, i.e. low coefficient of friction, roller slippage is negligible. This indicates that the risk of, for example, scuffing, which is a thermally driven process, would also be minimal. The solution for the friction coefficient and film thickness in the roller-pin contact, shown in section 3.3.3, is based on a smooth surface EHL assumption, i.e. full film lubrication regime. Lubrication conditions at the cam-roller contact may change when the roller-pin contact operates in the mixed of boundary lubrication regime. This may occur at lower cam rotational velocities, insufficient oil supply, misalignment, higher surface roughness and suchlike.

TABLE 3.4: Reference operating conditions and geometrical parameters for cam-roller follower lubrication analysis. Note that both cam and roller share the same mechanical and thermal properties.

Parameter	Value	Unit
ω_{c}	950	rev/min
ν	0.3	-
ρ_0	870	kg/m^3
$\rho_{\mathrm{c/r}}$	7850	kg/m^3
α	1.84E-8	Pa^{-1}
β	0.032	K^{-1}
β_T	0.00065	K^{-1}
η_0	0.013	Pa·s
τ_0	3.5	MPa·s
R_{f}	0.018	m
R_{pin}	0.0091	m
L	0.021	m
T_0	77	°C
k	0.13	W/mK
$k_{\mathrm{c/r}}$	46	W/mK
c	1970	J/kg$K$
$c_{\mathrm{c/r}}$	450	J/kg·K
μ_{a}	0.1	-
$p_{\mathrm{a,lim}}$	6	GPa

In order to systematically study the influence of the lubrication performance at the cam-roller contact as a function of the lubrication conditions in the roller-pin contact, the friction coefficient at the roller-pin contact was assumed. To be more specific, $\mu_{\mathrm{c-r}}$ in eq. 3.1 is calculated using the mixed lubrication model, while $\mu_{\mathrm{r-p}}$ is an input parameter. This assessment should provide insight in terms of the "sensitivity" of cam-roller contact lubrication as a function of the lubrication regime which the roller-pin contact operates in.

The coefficient of friction of the roller-pin contact is varied from levels corresponding to full film lubrication to values corresponding to boundary lubrication. This basically means that the resisting torque in eq. 3.1 is increased, which obviously should result in higher roller slippage or sliding velocities at the cam-roller contact. For the results presented in section 3.3.2 and 3.3.3 negligible sliding at cam-roller contact was predicted, justifying the assumption of Newtonian and isothermal conditions in model development. However, for the assessment of increasing $\mu_{\mathrm{r-p}}$ (and thus higher sliding velocities), non-Newtonian and thermal effects can no longer be disregarded and should be included in the model. Therefore, the mixed lubrication model for the cam-roller contact developed takes into account thermal, non-Newtonian and surface roughness effects using measured surface topography, i.e. a mixed thermo-elastohydrodynamic (TEHL) model. As mentioned earlier, for these calculations the mixed-TEHL model relies on the infinite line contact approach in order to reduce complexity and computational effort. The model is described

in detail in Paper D.

In the current study inertia effects (2nd term on the RHS of eq. 3.1) are assumed to negligible as compared to the resisting torque due to roller-pin contact friction. The aforementioned assumption rests on the chosen cam rotational velocity and increasing values of $\mu_{\mathrm{r-p}}$ by which the inertia torque becomes less pronounced. This assumption was crosschecked and was shown to be a realistic assumption for the given operating conditions. The torque balance of eq. 3.1 now reduces to:

$$\underbrace{\mu_{\mathrm{c-r}} R_{\mathrm{f}} F}_{\text{tractive torque}} = \underbrace{\mu_{\mathrm{r-p}} R_{\mathrm{pin}} F}_{\text{resisting torque}} \tag{3.6}$$

From eq. 3.6, ω_{r} is solely governed by the tractive and resisting torque. This, together with the concluding remark in section 3.3.3 that squeeze film motion is negligible justifies the assumption of a quasi-static analysis for studying the effect of roller-pin contact friction on cam-roller lubrication.

In the smooth surface infinite line contact EHL model the non-Newtonian behaviour of the lubricant is simulated using the Eyring model [25], while the Roelands model [65] is adopted to simulate the dependence of viscosity on temperature and pressure.

A BEM-based dry rough contact solver, as described in the work of Akchurin et al. [2], is used to calculate the local dry/solid contact pressures of a representative section of the real measured surface topography. The dry rough contact solver is based on a linear elastic-perfectly plastic material model. The cam-roller contact studied here is highly loaded, meaning that an almost uniform film thickness distribution is generated within the contact zone, i.e. the deformed gap height is almost uniform. Taking advantage of this, one may pre-calculate the asperity contact force $F_{\mathrm{a,L_xL_y}}$ (of contact calculation domain which has the dimensions $L_x L_y$) as a function of the separation distance h_{s}, assuming nominally flat surfaces in contact. The film thickness h is related to the separating distance h_{s} through the condition of volume conservation. This is imaginable as the film thickness h can theoretically be zero, while the separating distance h_{s} cannot. Volume conservation means that the total lubricant volume between the smooth surfaces should be equal to the volume occupied by the pockets formed by the non-contacting parts between the rough surfaces. The aforementioned has been taken into account in the model in this thesis. So, for nominally flat surfaces in contact one may establish a contact "stiffness curve", relating h and $F_{\mathrm{a,L_xL_y}}$, for a series of h values. Averaging the normal asperity contact force $F_{\mathrm{a,L_xL_y}}$ over the contact calculation domain $L_x \times L_y$ results in an auxiliary contact pressure $\bar{p}_{\mathrm{a}} = \frac{F_{\mathrm{a,L_xL_y}}}{L_x L_y}$. Finally, a pre-calculated relationship (for the specific contact pair) can be established:

$$\bar{p}_{\mathrm{a}}(x) = f[h(x)] \tag{3.7}$$

Figure 3.11 depicts the pre-calculated "$h - \bar{p}_{\mathrm{a}}$ curve", as is called throughout this thesis, for the cam-roller contact analysis. The curve basically represents the influence of the measured surface roughness. As a reference point the cam-roller contact conditions at 0°, which is on the base circle region, are studied. The kinematic parameters, F, R_x and U_{c} (corresponding to 0° cam angle) are given in Table 3.5.

A parametric analysis is performed in which the roller-pin contact friction coefficient $\mu_{\mathrm{r-p}}$ is increased. Simulations are stopped whenever an SRR of 2 is attained. A SRR of 2 means that a simple sliding situation has been reached. The results of the mixed-TEHL model were compared with those obtained, assuming Newtonian and isothermal conditions. The results are shown in Figure 3.12.

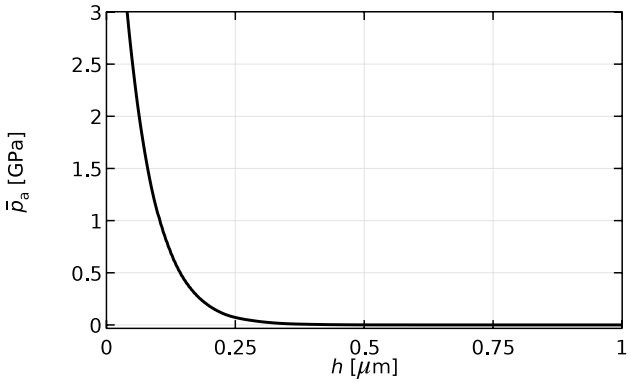

FIGURE 3.11: Surface roughness influence curve "$h - \bar{p}_{\mathrm{a}}$", used for cam-roller contact analysis.

Figure 3.12(a) shows that for both *non-Newtonian + thermal* and *Newtonian + isothermal* models an increase in SRR is observed for increasing values of $\mu_{\mathrm{r-p}}$. This is due to the fact that sliding velocity at the cam-roller contact has to increase to compensate for an increase of $\mu_{\mathrm{r-p}}$. Another observation is that a dramatic increase in the SRR is observed when *non-Newtonian + thermal* effects are taken into account. It is worth mentioning that both non-Newtonian and thermal effects contribute to viscosity reduction in a non-linear fashion. In fact, a clear deviation between the two models is observed from a $\mu_{\mathrm{r-p}}$ value of approximately 0.0175. The initiation of this deviation is governed by the non-Newtonian effect, in this case related to the characteristic shear stress τ_0 for the Eyring type lubricant. For the considered application a larger value of τ_0 would shift the starting point of non-Newtonian effect to a higher value of $\mu_{\mathrm{r-p}}$.

The main conclusion which can be drawn here is that non-Newtonian and thermal effects cause a significant decrease in traction. As a result, the sliding velocity has to increase to compensate for this additional "loss" of traction. Note that an *increase* in sliding velocity means a *decrease* in sum velocity, as the roller angular velocity decreases. As the film thickness h is a strong function of the sum velocity, its decrease using the *non-Newtonian + thermal* model is much more amplified than the *Newtonian + isothermal* model (see

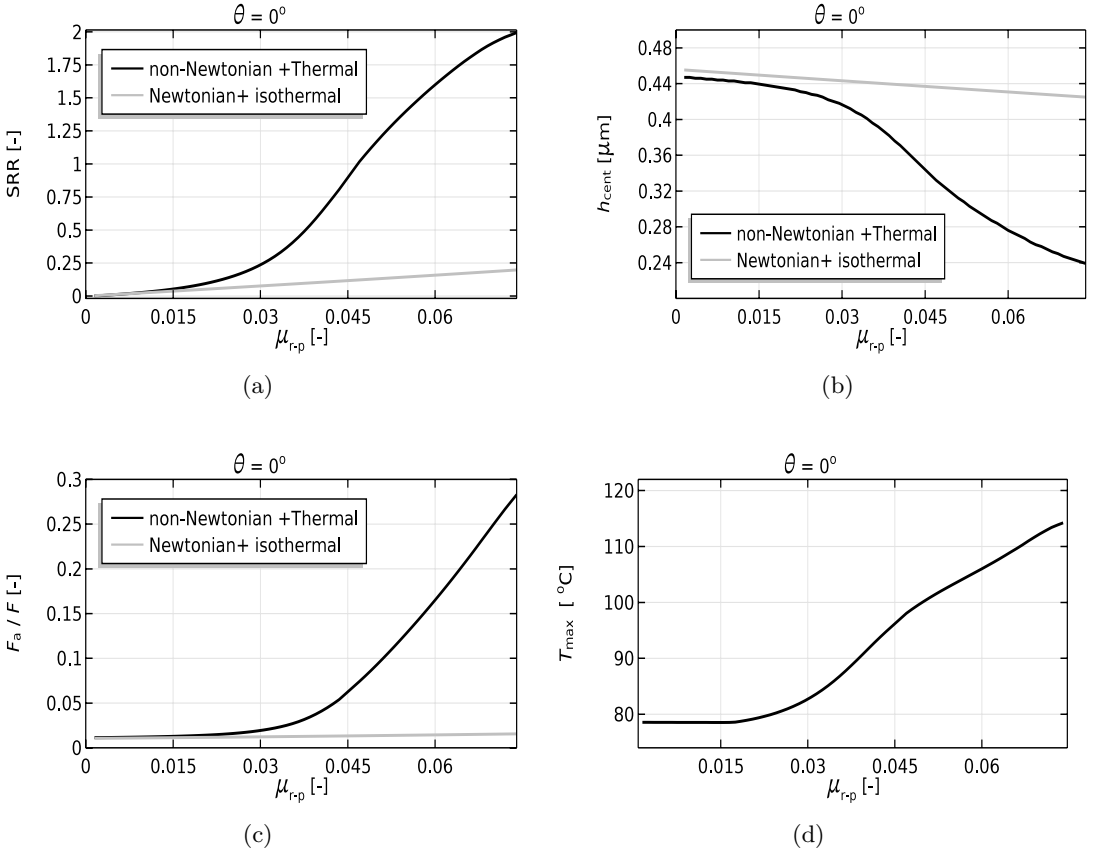

FIGURE 3.12: Variation of crucial design variables such as a) the SRR, b) central film thickness h_{cent} c) asperity load ratio F_{a}/F and d) maximum contact temperature $T_{\max}$, as a function of the roller-pin friction coefficient $\mu_{\text{r-p}}$. Results are presented for 0° cam angle.

Figure 3.12(b)).

Because of the dramatic decrease of film thickness using the *non-Newtonian + thermal* model, the fraction of load carried by asperities F_{a}/F significantly increases when compared with the *Newtonian + isothermal* model. This is clearly visible in Figure 3.12(c). In fact one may observe that, after $\mu_{\text{r-p}} \approx 0.0175$, the lubrication mode using the *non-Newtonian + thermal* model rapidly shifts from the full film regime to the mixed lubrication regime.

Finally Figure 3.12(d), which plots the variation of maximum temperature, speaks for itself: the combination of high sliding velocities and increasing friction coefficient results in an increase in heat generation.

3.4.2 Influence of stick-slip transitions at cam-roller contact

In section 3.4.1 the influence of roller-pin friction on cam-roller contact lubrication performance was assessed by means of a mixed-TEHL model.

The model was validated using published experimental data from Johnson and Spence [41]. As not all operating conditions were available in the paper of Johnson and Spence [41], "translated" data as provided by Gelinck [30] was used as input for the model. More details on this can be found in Paper D.

The mixed-TEHL model predictions were compared with measured Stribeck and traction curves (see Figure 3.13). From Figure 3.13 it is clear that overall good agreement is obtained between model predictions and experiments. However, there is some discrepancy in the low SRR domain (SRR $< 4\%$) of the traction curves (see Figure 3.13(b)). It can be seen that the traction curves obtained from the model start from a non-zero value. This is due to the fact that the asperity traction coefficient μ_a (see eq. 2.7) is not assumed to be a function of the SRR, which is the case in practice. In the case of pure rolling the traction coefficient would theoretically be zero.

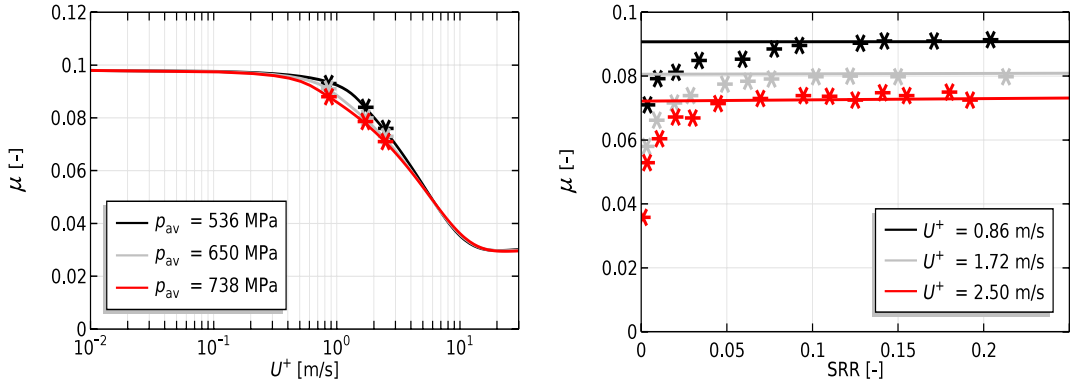

(a) (b)

FIGURE 3.13: Comparison model predictions and experiments [41, 30] for a) Stribeck curves and b) traction curves.

The sliding velocity at cam-roller contact, and thus also the SRR, is strongly governed by the contact force. For the considered application of fuel injection cam-roller follower units the SRR reaches values up to $10^{-6} - 10^{-5}$ in the nose region where the contact forces are the highest. However, this is not directly visible from Figure 3.7(b).

In rolling contact problems the SRR is often referred to as the creep ratio, which is a term more widely used in vehicle dynamics [86]. Due to the existence of a finite value of the SRR rather than a zero value (such as for the cam-roller contact), the contact area is divided into micro-stick and slip zones, which are exposed to combined normal and tangential loading. A stick zone can be defined as two contacting elements or group of elements that have no relative velocity with respect to each other as they travel through the contact. In slip regions the aforementioned condition does not hold.

When a tangential force F_x is transmitted to the contact the contacting elements deform (elastically). The tangential force, which is related to the SRR, also causes a type

of tangential displacement $\delta_x(x)$ throughout the contact. A slip element exists when the elastic deformation cannot support the displacement, i.e. the maximum tangential deformation is restricted when an upper limit of shear traction has been reached. A sticking element is thus defined as when the acting shear stress over that element is less than the limiting shear stress. The most convenient way of defining the upper limit of shear traction is according to the Coulomb friction theory (see eq. 2.7), i.e. the maximum (localized) shear traction is the product of normal pressure and a Coulomb friction coefficient $\mu_{\mathrm{a,lim}}$. In equation form this yields:

$$q_{i,\mathrm{lim}} = \mu_{\mathrm{a,lim}} p_{\mathrm{a,i}} \tag{3.8}$$

$\mu_{\mathrm{a,lim}}$ is the *sliding* boundary friction coefficient, which should be determined experimentally [52]. Its typical value is usually in the order of 0.1-0.13.

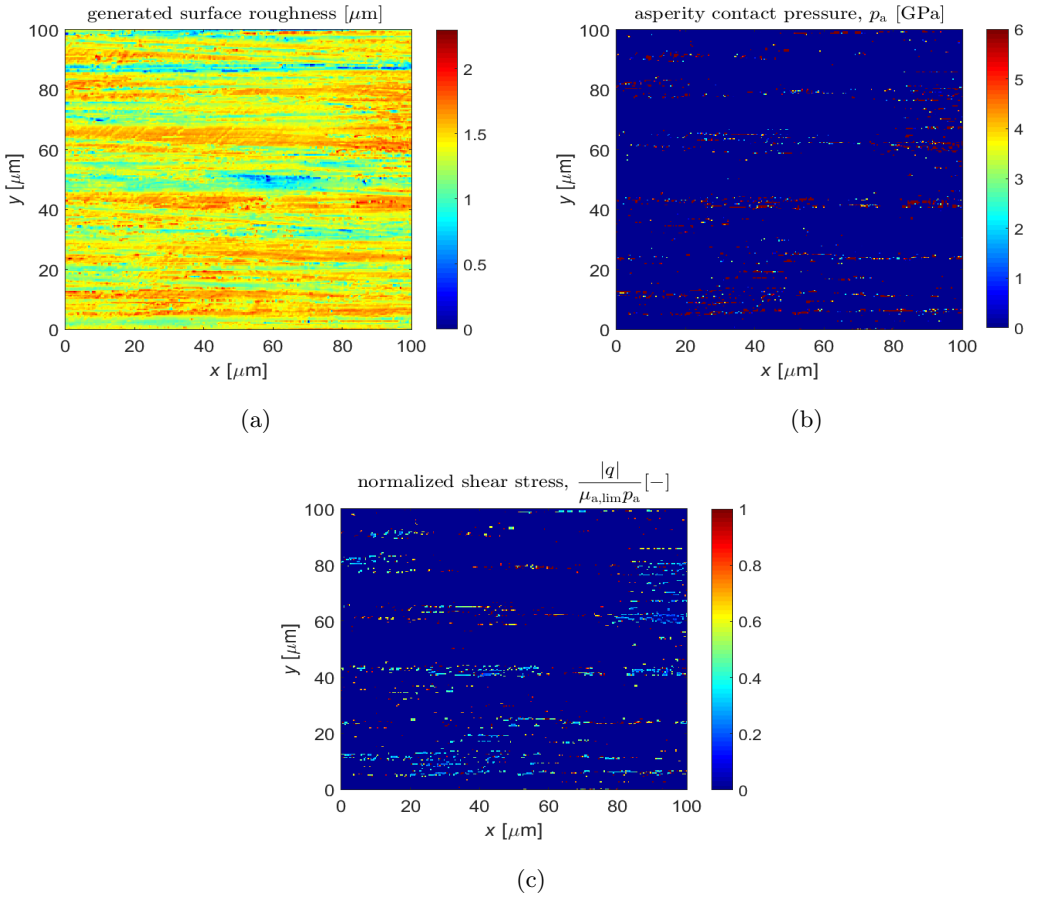

FIGURE 3.14: An impression of a) surface roughness, which is exposed to a combined normal and tangential load, and its resulting b) normal asperity contact pressure distribution and c) normalized shear stress distribution.

So, the moment the shear stress of an asperity (q_{i} in eq. 2.7) exceeds this upper limit, the shear stress magnitude over the asperity is set equal to the upper limit, i.e. $q_{\mathrm{i}} = q_{i,\mathrm{lim}}$

if $q_{\mathrm{i}} > \mu_{\mathrm{a,lim}} p_{\mathrm{a,i}}$.

Figure 3.14(a) shows an example of a combined surface roughness for two nominally flat surfaces in contact. The combined surface roughness is the summation of the two surface roughness height profiles. If these two rough surfaces, which are in contact, are exposed to a combined normal and tangential load, the resulting normal contact pressure distribution may look like the depiction in Figure 3.14(b). The hardness of the material, beyond which yielding is initiated, is 6 GPa. Hence, the allowable local pressures within the contact are therefore confined to 6 GPa for the ideal elastic-perfectly plastic material model chosen here. If the applied tangential load (or SRR) is not large enough to make the entire contact area slip, the contact zone will be composed of stick and slip elements. Figure 3.14(c) depicts the normalized shear stress distribution for the given example. Note that when $\frac{|q|}{\mu_{\mathrm{a,lim}} p_{\mathrm{a}}} = 1$, the element is in the slip "mode", while for $0 < \frac{|q|}{\mu_{\mathrm{a,lim}} p_{\mathrm{a}}} < 1$ the element is defined to be in the stick "mode". Gross sliding occurs at the moment when a sufficiently large SRR (and thus large tangential force) makes the entire contact area slip, i.e when the stick area disappears. The aforementioned behaviour is depicted in Figure 2.3.

Coming back to cam-roller follower contact modelling, the possibility exists that the stick-slip status of the cam-roller contact under such small SRRs ($10^{-6} - 10^{-5}$) has not yet reached the status of gross sliding, i.e. some contacting asperities may still be in the stick mode. Predicting the mixed frictional force for the cam-roller contact using a *sliding* boundary friction coefficient $\mu_{\mathrm{a,lim}}$, might therefore (largely) overestimate the friction force.

In order to improve mixed-friction predictions in the low SRR domain, the mixed-lubrication model presented in section 3.4.1 was expanded by taking into account the stick-slip status on the asperity scale and its influence on the mixed friction coefficient $\mu_{\mathrm{c-r}}$. However, in order to reduce complexity, isothermal conditions were assumed in the model. This assumption is justified here as the sliding velocities considered are very low and so is the expected heat generation. The complete mixed-lubrication model is composed of a smooth surface EHL model and a dry (rough) contact model. The former calculates the hydrodynamic pressure build-up and the film thickness in the contact, while the latter calculates the asperity pressure and shear stress distribution. The contact model is based on the boundary element method and takes advantage of a half-space approximation. Part of the dry contact model, which calculates asperity shear stress distribution is called the stick-slip model, while the other part that calculates the normal contact pressure is called the normal contact model. The normal contact model is the same as that employed in section 3.4.1. The BEM-based stick-slip model, as described in the work of Bazrafshan et al. [7], was employed here to calculate the asperity shear stress distribution. The complete (mixed-lubrication) model is described in detail in Paper E.

Asperity level stick-slip transitions have been analysed in a similar way to the analysis for the normal contact pressure distribution, based on the $\bar{p}_{\mathrm{a}}(x) = f[h(x)]$ relation eq. 3.7. Assuming nominally flat surfaces in contact, for an imposed film thickness h and tangential load F_x, the tangential displacement δ_x can be calculated for contact calculation domain $L_x \times L_y$. The film thickness h corresponds to a normal load $F_{\mathrm{a,L_xL_y}}$. Analogous to auxiliary/averaged contact pressure $\bar{p}_{\mathrm{a}}$, an auxiliary asperity friction coefficient $\mu_{\mathrm{a}}(x)$ can be derived as follows:

$$\mu_{\mathrm{a}} = \frac{|\bar{q}|}{\bar{p}_{\mathrm{a}}} \tag{3.9}$$

where $|\bar{q}| = \frac{F_x}{L_x L_y}$. So, taking the normal pressure distribution from the normal contact model as an input for the stick-slip model, and additionally imposing load F_x as input, results in a value of δ_x and an auxiliary asperity friction coefficient μ_{a}. In equation form this yields:

$$\mu_{\mathrm{a}}(x) = f[h(x), \delta_x(x)] \tag{3.10}$$

Given the roughness of the cam-roller pair, a 3D map can be constructed for μ_{a} as a function of different combinations of δ_x and h. The map is presented in Figure 3.15. This map, likewise the "$h - \bar{p}_{\mathrm{a}}$ curve" always holds for the specific rough contact pair. Note that the asperity friction coefficient transition map Figure 3.15 and the "$h - \bar{p}_{\mathrm{a}}$ curve" Figure 3.11 are mutually dependent. For the current analysis the boundary lubrication coefficient $\mu_{\mathrm{a,lim}} = 0.12$.

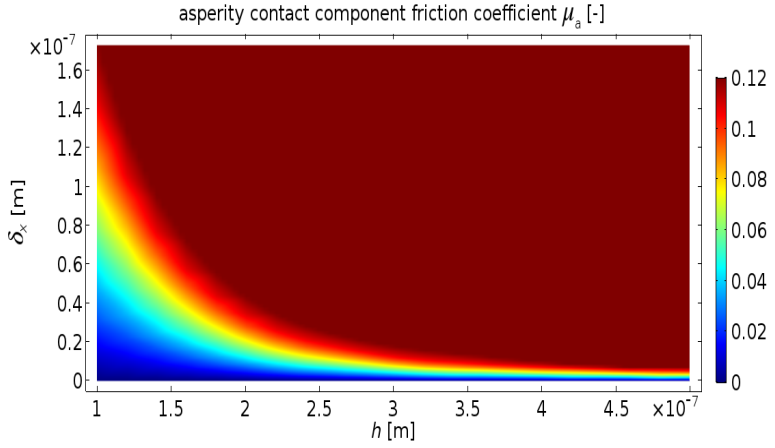

FIGURE 3.15: a) Calculated 3D-map for the asperity contact friction coefficient μ_{a} as a function of the film thickness h and tangential displacement δ_x.

One can directly observe the major characteristics of this asperity friction transition map. To elaborate somewhat, for a decreasing film thickness (thus for increasing normal contact loads) the distance δ_x increases before gross sliding takes place. This is expected since with increasing normal loads the asperity contact area increases, so that a larger

pre-sliding distance δ_x is required.
The SRR is related to the tangential force F_x, which in turn determines the tangential displacement δ_x which varies through the contact as follows:

$$\delta_x(x) = \text{SRR} \cdot (x - x_{\text{inlet}}) \tag{3.11}$$

where x_{inlet} denotes the denotes the inlet position of the lubricated contact zone. The derivation of eq. 3.11 is explained in Paper E.
From Figure 3.15 a direct link can be made between $\delta_x(x)$ and SRR as these are related through eq. 3.11. In fact, the behaviour of μ_{a} versus SRR is similar to μ_{a} versus δ_x.

The influence of roller-pin contact friction coefficient on cam-roller lubrication is analysed in a similar way to that performed in section 3.4.1. The modelling approach also relies on the quasi-steady behaviour. In fact, squeeze film motion effects are ignored $\frac{\partial h\rho}{\partial t} = 0$. In this study only conditions where SRR $< 3\%$ are considered. Hence, ω_{r} can be estimated assuming pure rolling conditions and $\dot{\omega}_{\text{r}}$ (see eq. 3.1) can directly be obtained from graphical differentiation of ω_{r} (with respect to time).
Simulations are carried out in which the roller-pin friction coefficient $\mu_{\text{r-p}}$ is increased from a value of 0.001 and are stopped whenever a SRR of 3% is reached. The operating conditions are listed in Table 3.4. Additionally, the kinematic parameters correspond to the nose region of the cam, i.e. 63.5°, and are given in Table 3.5. Again, for the current analysis isothermal conditions are assumed.
Figure 3.16 provides the relation between increasing values of $\mu_{\text{r-p}}$ and SRR. In this Figure the stick-slip results, meaning a variable asperity friction coefficient according to Figure 3.15, are compared with those obtained by assuming the asperity friction coefficient $\mu_{\text{a}}(x)$ to be a constant and equal to $\mu_{\text{a}} = \mu_{\text{a,lim}} = 0.12$, i.e. assuming gross sliding.
Note that an increase in $\mu_{\text{r-p}}$ means that the cam roller friction coefficient $\mu_{\text{c-r}}$ automatically needs to increase proportionally (see eq. 3.6). Consequently, the sliding velocity or SRR needs to increase in order to compensate for this. Note that SRR and δ_x are mutually dependent through eq. 3.6 altogether with Figure 3.15. In fact, an increase in $\mu_{\text{r-p}}$ indirectly means an increase in $\delta_x(x)$, which is linked to μ_{a} through Figure 3.15. For the nose position the central film thickness is approximately 0.27μm. So, for the initial values of $\mu_{\text{r-p}}$, the combination of h and $\delta_x(x)$ (see Figure 3.16) reveals that the gross sliding inception has not occurred yet, i.e. some asperities are still in the stick mode. Hence, the $\mu_{\text{a}}(x) < 0.12$.

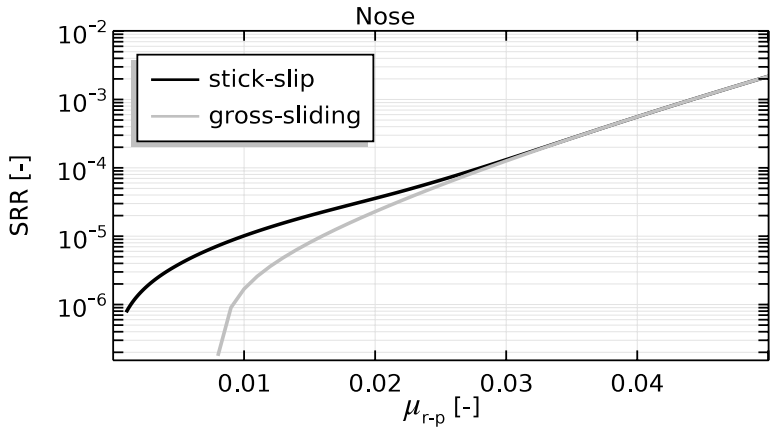

FIGURE 3.16: Influence of $\mu_{\mathrm{r-p}}$ on lubrication conditions at nose position.

As $\mu_{\mathrm{r-p}}$ is increased, SRR increases further, and so does $\delta_x\,(x)$, up to the inception of gross sliding. Consequently μ_{a} will approach the full sliding value $\mu_{\mathrm{a,lim}}$. This explains the unification of the curves depicted in Figure 3.16. The discrepancy between the results obtained, especially for low values of $\mu_{\mathrm{r-p}}$, is large. This is expected since the stick-slip behaviour of asperities results in less traction at the cam-roller contact and hence a lower value of $\mu_{\mathrm{c-r}}$ for the same SRR.
Furthermore, there are two import features which can be deduced from Figure 3.16 regarding the starting points of the curves, namely:

- Simulations were carried out with a starting value of $\mu_{\mathrm{r-p}} = 0.001$, and gradually increased. However, if one takes a close look at Figure 3.16, it is clear that under the assumption of gross sliding the value of $\mu_{\mathrm{r-p}} = 0.001$ is never attained for the gross sliding case. This can be explained as follows: the analysis here is carried out such that the shape of the film thickness/separating distance is hardly affected, i.e. the sum velocity is rather constant during the parametric analysis. This implies that the load carried by the asperities is also hardly affected (see Figure 3.11). Now as explained earlier, for a given $\mu_{\mathrm{r-p}}$ the only thing which may be affected is the sliding velocity. If one assumes gross sliding, i.e. $\mu_{\mathrm{a}}\,(x)$, the asperity contact contribution to the torque balance remains unchanged. Furthermore, if the specified $\mu_{\mathrm{r-p}}$ is so small that the tractive torque due to asperity interaction on its own is already greater than the resisting torques, it means from a numerical perspective that the sliding velocity has to increase in a negative way to satisfy the torque balance by means of the hydrodynamic shear stress. To be more specific, $U_{\mathrm{r}} > U_{\mathrm{c}}$, meaning that the roller is driving the cam, which is unrealistic. Hence, in the simulations $\mu_{\mathrm{r-p}}$ is only considered from the point when SRR > 0. This explains the discrepancy between the starting points of the curves depicted in

Figure 3.16. This simply means that, under the assumption of a constant asperity contact friction coefficient, for the current operating conditions a minimum/starting value of $\mu_{\mathrm{r-p}} \approx 0.008$ for roller-pin traction would be required in order to let the cam drive the roller.

- The second feature of Figure 3.16 is that when $\mu_{\mathrm{a}} = \mu_{\mathrm{a,lim}} = 0.12$ (gross-sliding) is assumed, the overall $\mu_{\mathrm{c-r}}$ is also overestimated, which ensues logically from an overestimation in tractive torque. An increase in tractive torque means a decrease in sliding velocity. This is also the reason why the minimum value of $\mu_{\mathrm{r-p}} \approx 0.008$ is coupled with a smaller value of SRR than in the curve obtained considering stick-slip transitions.

Chapter 4

Conclusions, discussion and recommendations

4.1 Conclusions

This thesis studies the lubrication performance of the coupled cam-roller and roller-pin contact of a heavily loaded cam-roller follower component. The roller is profiled in axial direction to reduce edge loading. In order to study the effect of axial roller profiling, first a (3D) steady-state smooth surface finite line contact EHL model was developed in which the influence of load, velocity and material properties on pressure and film thickness was studied. It was found that unlike traditional EHL solutions (infinite line and elliptical contacts), the maximum pressure and minimum film thickness in the contact are highly affected by variations in load. The model was validated with benchmark results found in past literature. Good agreement was found between the results from the developed model and results from published literature.

The previously developed smooth surface finite line contact EHL model was then expanded to capture transient variations such as those occurring in the real cam-follower application. In this model roller slippage was taken into account and the roller-pin contact was modelled under the assumption of rigid surfaces. The results in terms of film thickness and pressure were compared with those obtained using traditional analytical solutions. It was found that i) both cam-roller and roller-pin contact operate in the mixed lubrication regime from low to moderately high cam rotational velocities, ii) analytical film thickness formulas for infinite line contacts overestimate the film thickness in the contact as they do not account for side leakage, and iii) roller axial profiling may significantly enhance the maximum pressure and minimum film thickness values, albeit at the cost of higher power losses due to enlargement of the effective lubricated area.

Furthermore, the finite line contact cam-follower lubrication model was expanded to take into account the elastic deformation in the roller-pin contact model. It was found that elastic deformation in the roller-pin contact is beneficial in terms of film thickness and pressure. Furthermore, it was found that the roller-pin contact behaves as a concentrated conformal contact, as it exhibits similar characteristics to finite line contacts (for the load range considered).

Next, the influence of the roller-pin friction coefficient on cam-roller contact lubrication performance was studied. To this end, a steady-state mixed-TEHL model was developed for the cam-roller contact. The model relied on the infinite line contact approach. It was found that for the increasing friction levels in the roller-pin contact the sliding at the cam-roller contact increases. Consequently, thermal and non-Newtonian effects can no longer be disregarded. In fact, it was found that thermal and non-Newtonian effects reduce traction. In essence, this means that the sliding at the cam-roller contact increases and surface roughness effects become more pronounced, i.e. mixed lubrication becomes important. This indicates that the risk on scuffing would increase due to for instance high sliding and significant asperity contact. Also, results highlight the importance of the roller-pin contact as this appears to be critical contact in the cam-roller follower component. The mixed-TEHL model was validated with published measurements found in the literature, in which good agreement was found for the results corresponding to the high SRR domain.

Finally, in order to improve the accuracy in terms of friction force, in the low SRR domain, the influence of stick-slip transitions on asperity scale were included in the model. The main findings are that stick-slip transitions (or variable asperity contact friction coefficient) are of crucial importance in regions of the cam where the acting contact forces are very high. Assuming a constant asperity contact friction coefficient (or assuming that the inception of gross sliding has already occurred) in highly loaded regions may lead to large overestimation in the minimum required cam-roller contact friction coefficient in order to keep the roller rolling.

4.2 Discussion

Based on the approach and findings in this thesis, a few points are worth discussing further.

From the results, as shown in section 3.4.1, it is clear that (the onset of) roller slippage is strongly governed by the rheology of the lubricant. Accurate description of the rheology of the lubricant is thus important in order to get more accurate estimations of the film thickness and frictional force. In order to improve the model output accuracy

in terms of film thickness and frictional force, the rheology of the lubricant can be described using much more advanced rheological models (see for instance [81, 34, 62]). The Roelands viscosity-temperature-pressure relationship, despite still being used widely due to its simplicity, is rather outdated. It is worth mentioning that any other constitutive rheological equation describing the lubricant behaviour can be implemented in the current model without affecting the general model structure.

Additionally, in the current analysis the disturbance of interacting asperities on the lubricant flow, i.e. micro-EHL effects, were not considered. The assumption behind this was that the surfaces were ground in rolling direction. It is commonly known that inclusion of micro-EHL effects (the build-up of an EHL film at the asperity tip as opposed to dry or quasi-dry Coulombic sliding) leads to a decrease in asperity friction [68, 52]. For instance, cams could be textured to benefit from micro-EHL effects as these may realize an increase in film thickness and decrease in friction. The influence of micro-EHL effects on friction prediction in the cam-roller contact could be investigated in the future.

In this thesis the boundary lubrication coefficient was assumed to be known and constant for the high slide-to-roll ratio domain. For most boundary layers the shear stress increases with pressure in a linear manner. However, the variation of the coefficient of friction ($\mu_a = \frac{q}{p_a}$) on asperity scale (due to non-linear shear stress-pressure relation or temperature effects) may give a variation in the macroscopic boundary lubrication coefficient of friction (see for instance [27, 12]). This, of course, depends on the chemical composition of the boundary layer. The tribo-chemistry and tribo-film formation of boundary layers is not considered here.

The output of this model provides regions with a potential chance of scuffing in terms of generated heatat the macroscopic level. However, scuffing typically indicates a breakdown of the boundary layer and thus promoting metal-to-metal contact. This entails exceeding a certain critical temperature (on asperity scale) [10]. In order to quantitatively predict the onset of scuffing, detailed micro-scale temperature calculations are required, also for mixed lubrication conditions. Nevertheless, the output of the mixed-lubrication model presented in this thesis certainly indicates the regions that are potentially at risk of scuffing.

Another point which can be addressed here is that for the mixed-lubrication simulations quasi-static conditions were assumed and, in line with this, roller inertia effects could be ignored. It should be stressed that this assumption is valid for the case analysed in this thesis, because the cam's lateral shape and chosen cam rotational velocity allowed this. To elaborate somewhat: from the cam surface velocity profile (Figure 3.1), which corresponds to a cam rotational velocity of 950 RPM, one may observe that this profile is a rather evenly distributed or has minimal fluctuations throughout the cam's periphery. This indicates that the roller angular acceleration – and thus also roller inertia torque – will be minimal for a cam rotational velocity of 950 RPM. Of course, for higher cam

rotational velocities the fluctuations in cam surface velocity profile will be higher and inertia effects will be more significant. Also, for other types of cam shape roller both inertia effects and transient (squeeze film motion) effects may be very important. In this thesis the primary reason behind the parametric analysis (as carried out in section 3.4.1) was to have an indication when the "system fails", i.e. when the sudden/rapid increase in SRR is noticed. It is expected that in reality a (sudden) increase in roller-pin friction will cause higher roller slippage, and at the same time will induce a higher roller deceleration. This means that a (sudden) increase in roller-pin friction might lead to a much higher roller slippage due to simultaneous increase of roller inertia torque and resisting torque at the roller-pin contact.
This work has highlighted the importance of the roller-pin contact as this contact appears to be the critical one in the cam-roller follower system unit. Therefore, it is necessary to obtain more in-depth knowledge concerning the tribological behaviour of this contact.

4.3 Recommendations

Concrete recommendations for future studies can be summed-up as follows:

- Theoretical work:
  - *Roller-pin contact modelling.*
    This work has highlighted the importance of the roller-pin contact as this contact appears to be the critical one in the cam-roller follower component. Therefore it is strongly suggested that a detailed transient mixed- lubrication model for the roller-pin contact should be developed in order to better assess the coupled tribological behaviour of both contacts. The roller-pin contact is a self-lubricated hydrodynamic bearing, i.e. lubricant supply to the contact occurs through the sides and is thus driven by a pressure difference. Hence, a suitable cavitation model should also be adopted so as to accurately simulate side inflow, starvation, the cavitated region, film reformation and non-submerged situations.
  - *Model usage for other application.*
    The model developed in this thesis was applied to analyse the lubrication conditions in the cam-roller contact. With regard to model applicability it is worth mentioning that a similar approach as followed in this thesis could be followed to analyse the tribological behaviour of other dynamic (non-conformal) EHL contacts such as gears and roller bearings. This model would form a good basis for this.

- Experimental validation:
  - *The general **steady-state** mixed-TEHL model.*
    A complete validation of the mixed-lubrication model ranging from the full-film regime to the boundary lubrication regime, also for different slip ratios. This should be done for a rheologically well defined lubricant. A lot of published measurement data pertaining to mixed lubricated line contacts exists. However, the (raw) roughness data is often not provided. This leaves the recommendation for further experimental validation of the mixed-lubrication model presented herein. This is possible by measuring the friction on a two-disc machine experimental setup. Accurate measurement of traction at the (very) low SRR domain may be problematic for very smooth surfaces. In order to validate the model friction predictions in the low SRR domain one could, for instance, increase the surface roughness. This would increase the critical SRR before gross-sliding takes place. By doing so, a larger part of the SRR domain where stick-slip transitions are important can be validated accurately. If the surface roughness is increased, the running-in behaviour of the interacting surfaces will also be different. Care should be taken to ensure that the experiments are performed using run-in surfaces.
  - *The **coupled** cam-roller, roller-pin contact lubrication model.*
    The coupled cam-roller, roller-pin contact lubrication model should be validated, preferably in terms of roller slippage, on a full-scale valve train test rig. In these tests it is required to monitor the cam and roller rotational velocities. Experimental studies in the past utilized – depending on the setup – either optical scanners [5], Hall effect sensors [20] or magnetoresistive sensors [44] in order to monitor the roller rotational velocity. Once the roller rotational velocity is measured, and synchronized with the lift event of the cam, the slippage can be calculated by subtracting the measured roller rotational velocity from the roller rotational velocity on the basis of the no-slip condition.

Bibliography

[1] M. Abdullah, S. Shah, M. Bhutta, R. Mufti, M. Khurram, M. Najeeb, W. Arshad, and K. Ogawa. Benefits of wonder process craft on engine valve train performance. *Proceedings of the Institution of Mechanical Engineers, Part D: Journal of Automobile Engineering*, Epub March 12, 2018. DOI:10.1177/0954407018760935.

[2] A. Akchurin, R. Bosman, P. Lugt, and M. van Drogen. On a model for the prediction of the friction coefficient in mixed lubrication based on a load-sharing concept with measured surface roughness. *Tribology Letters*, 59(1):19, 2015.

[3] B. Andersson. Paper xviii (iii) Company perspectives in vehicle tribology-Volvo. *Tribology Series*, 18:503–506, 1991.

[4] S. Bair and W. Winer. Shear strength measurements of lubricants at high pressure. *Journal of Lubrication Technology*, 101(3):251–257, 1979.

[5] S. Bair and W. Winer. Paper vi (v) a technique for measuring roller follower skidding on automotive camshafts. *Tribology Series*, 18:157–162, 1991.

[6] A. Ball, D. Dowson, and C. Taylor. Cam and follower design. *Tribology Series*, 14:111–130, 1989.

[7] M. Bazrafshan, M. de Rooij, and D. Schipper. On the role of adhesion and roughness in stick-slip transition at the contact of two bodies: A numerical study. *Tribology International*, 121:381–388, 2018.

[8] M. Björling. *Friction in Elastohydrodynamic Lubrication*. PhD thesis, Luleå University of Technology, Luleå, Sweden, 2014.

[9] L. Bobach, R. Beilicke, D. Bartel, and L. Deters. Thermal elastohydrodynamic simulation of involute spur gears incorporating mixed friction. *Tribology International*, 48:191–206, 2012.

[10] R. Bosman and D. Schipper. On the transition from mild to severe wear of lubricated, concentrated contacts: the IRG (OECD) transition diagram. *Wear*, 269(7-8):581–589, 2010.

[11] P. Carreau. Rheological equations from molecular network theories. *Transactions of the Society of Rheology*, 16(1):99–127, 1972.

[12] L. Chang and Y. Jeng. A mathematical model for the mixed lubrication of non-conformable contacts with asperity friction, plastic deformation, flash temperature, and tribo-chemistry. *Journal of Tribology*, 136(2):022301, 2014.

[13] Y. Chiu. Lubrication and slippage in roller finger follower systems in engine valve trains. *Tribology transactions*, 35(2):261–268, 1992.

[14] M. Colechin, C. Stone, and H. Leonard. Analysis of roller-follower valve gear. Technical report, SAE Technical Paper 930692, 1993.

[15] DAF Trucks. Daf mediabank, http://www.daf.nl/nl-nl/news-and-media/daf-imagebank, Retrieved: 4-10-2018.

[16] D. Dowson, P. Harrison, C. Taylor, and G. Zhu. Experimental observation of lubricant film state between a cam and bucket follower using the electrical resistivity technique. In *Proceedings of the Japan International Tribology Conference*, pages 119–124, 1990.

[17] D. Dowson and G. Higginson. A numerical solution to the elasto-hydrodynamic problem. *Journal of Mechanical Engineering Science*, 1(1):6–15, 1959.

[18] D. Dowson and G. Higginson. *Elasto-hydrodynamic lubrication: the fundamentals of roller and gear lubrication*, volume 23. Pergamon Press, Oxford, United Kngdom, 1966.

[19] D. Dowson, G. Higginson, and A. Whitaker. Elasto-hydrodynamic lubrication: A survey of isothermal solutions. *Journal of Mechanical Engineering Science*, 4(2):121–126, 1962.

[20] P. Duffy. An experimental investigation of sliding at cam to roller tappet contacts. Technical report, SAE Technical Paper 930691, 1993.

[21] European Union. Paris agreement, https://ec.europa.eu/clima/policies/international/negotiations/paris, Retrieved: 25-05-2018.

[22] European Union. Reducing CO2 emissions from heavy-duty vehicles, https://ec.europa.eu/clima/policies/transport/vehicles/heavy, Retrieved: 25-05-2018.

[23] H. Evans and R. Snidle. The isothermal elastohydrodynamic lubrication of spheres. *Journal of Tribology*, 103(4):547–557, 1981.

[24] H. Evans, R. Snidle, and K. Sharif. Deterministic mixed lubrication modelling using roughness measurements in gear applications. *Tribology International*, 42(10):1406–1417, 2009.

[25] H. Eyring. Viscosity, plasticity, and diffusion as examples of absolute reaction rates. *The Journal of Chemical Physics*, 4(4):283–291, 1936.

[26] B. Fantino, J. Frene, and J. Du Parquet. Elastic connecting-rod bearing with piezoviscous lubricant: Analysis of the steady-state characteristics. *ASME. Journal of Lubrication Technology*, 101:190–197, 1979.

[27] I. Faraon. *Mixed lubricated line contacts*. PhD Thesis, University of Twente, The Netherlands, 2005.

[28] I. Faraon and D. Schipper. Stribeck curve for starved line contacts. *Journal of Tribology*, 129(1):181–187, 2007.

[29] B. Gecim. Lubrication and fatigue analysis of a cam and roller follower. *Tribology Series*, 14:91–100, 1989.

[30] E. Gelinck. *Mixed lubrication of line contacts*. PhD Thesis, University of Twente, The Netherlands, 1998.

[31] E. Gelinck and D. Schipper. Calculation of Stribeck curves for line contacts. *Tribology International*, 33(3):175–181, 2000.

[32] R. Gohar and A. Cameron. The mapping of elastohydrodynamic contacts. *ASLE Transactions*, 10(3):215–225, 1967.

[33] W. Habchi. *A Full-system Finite Element Approach to Elastohydrodynamic Lubrication Problems*. PhD thesis, L 'Institut National des Sciences Appliquées de Lyon, France, 2008.

[34] W. Habchi, S. Bair, F. Qureshi, and M. Covitch. A film thickness correction formula for double-newtonian shear-thinning in rolling ehl circular contacts. *Tribology Letters*, 50(1):59–66, 2013.

[35] B. Hamrock and D. Dowson. Isothermal elastohydrodynamic lubrication of point contacts: Part i - theoretical formulation. *Journal of Tribology*, 98(2):223–228, 1976.

[36] B. Hamrock and D. Dowson. Isothermal elastohydrodynamic lubrication of point contacts: Part iii - fully flooded results. *Journal of Tribology*, 99(2):264–275, 1977.

[37] B. Hamrock, S. Schmid, and B. Jacobson. *Fundamentals of fluid film lubrication*. CRC press, Boca Raton, 2004.

[38] M. Holmes, H. Evans, and R. Snidle. Discussion. *Tribology Transactions*, 46(2):282–288, 2003.

[39] F. Ji and C. Taylor. A tribological study of roller follower valve trains. part 1: A theoretical study with a numerical lubrication model considering possible sliding. *Tribology Series*, 34:489–499, 1998.

[40] K. Johnson, J. Greenwood, and S. Poon. A simple theory of asperity contact in elastohydro-dynamic lubrication. *Wear*, 19(1):91–108, 1972.

[41] K. Johnson and D. Spence. Determination of gear tooth friction by disc machine. *Tribology International*, 24(5):269–275, 1991.

[42] Kams Inc. Visual dynamics of camshaft and valve train motion. url: http://kams.publishpath.com/visual-dynamics-of-camshaft-motion, Retrieved: 04-09-2018.

[43] D. Karupannasamy, J. Hol, M. de Rooij, T. Meinders, and D. Schipper. Modelling mixed lubrication for deep drawing processes. *Wear*, 294:296–304, 2012.

[44] M. Khurram, R. Mufti, R. Zahid, N. Afzal, and M. Bhutta. Experimental measurement of roller slip in end-pivoted roller follower valve train. *Proceedings of the Institution of Mechanical Engineers, Part J: Journal of Engineering Tribology*, 229(9):1047–1055, 2015.

[45] M. Khurram, R. Mufti, R. Zahid, N. Afzal, M. Bhutta, and M. Khan. Effect of lubricant chemistry on the performance of end pivoted roller follower valve train. *Tribology International*, 93:717–722, 2016.

[46] Y. Kondo, T. Koyama, and S. Sasaki. Tribological properties of ionic liquids. In *Ionic liquids-New aspects for the future*, chapter 5, pages 127–141. InTech, 2013.

[47] P. Kundu and I. Cohen. *Fluid mechanics*. New York: Elsevier, 4 edition, 2008.

[48] M. Kushwaha and H. Rahnejat. Transient elastohydrodynamic lubrication of finite line conjunction of cam to follower concentrated contact. *Journal of Physics D: Applied Physics*, 35(21):2872, 2002.

[49] M. Kushwaha, H. Rahnejat, and R. Gohar. Aligned and misaligned contacts of rollers to races in elastohydrodynamic finite line conjunctions. *Proceedings of the Institution of Mechanical Engineers, Part C: Journal of Mechanical Engineering Science*, 216(11):1051–1070, 2002.

[50] J. Lee and D. Patterson. Analysis of cam/roller follower friction and slippage in valve train systems. Technical report, SAE Technical Paper 951039, 1995.

[51] P. Lindholm, C. Spiegelberg, S. Andersson, and S. Björklund. Contact conditions in a cam and roller contact. In *World Tribology Congress WTC2001*, page 4, 2001.

[52] Q. Liu, W. T. Napel, J. Tripp, P. Lugt, and R. Meeuwenoord. Friction in highly loaded mixed lubricated point contacts. *Tribology transactions*, 52(3):360–369, 2009.

[53] P. Lugt and G. Morales-Espejel. A review of elasto-hydrodynamic lubrication theory. *Tribology Transactions*, 54(3):470–496, 2011.

[54] J. Matthews and F. Sadeghi. Kinematics and lubrication of camshaft roller follower mechanisms. *Tribology Transactions*, 39(2):425–433, 1996.

[55] S. Messe and A. Lubrecht. Transient elastohydrodynamic analysis of an overhead cam/tappet contact. *Proceedings of the Institution of Mechanical Engineers, Part J: Journal of Engineering Tribology*, 214(5):415–425, 2000.

[56] H. Moes. Lubrication and beyond. *UT lecture notes*, Code 115531, University of Twente, Enschede, The Netherlands, 2000.

[57] G. Morales-Espejel, M. Dumont, P. Lugt, and A. Olver. A limiting solution for the dependence of film thickness on velocity in ehl contacts with very thin films. *Tribology Transactions*, 48(3):317–327, 2005.

[58] G. Morales-Espejel, A. Wemekamp, and A. Félix-Quiñonez. Micro-geometry effects on the sliding friction transition in elastohydrodynamic lubrication. *Proceedings of the Institution of Mechanical Engineers, Part J: Journal of Engineering Tribology*, 224(7):621–637, 2010.

[59] A. Mostofi and R. Gohar. Elastohydrodynamic lubrication of finite line contacts. *Journal of Tribology*, 105(4):598–604, 1983.

[60] G. Nijenbanning, C. Venner, and H. Moes. Film thickness in elastohydrodynamically lubricated elliptic contacts. *Wear*, 176(2):217–229, 1994.

[61] J. O'Donoghue, D. Brighton, and C. Hooke. The effect of elastic distortions on journal bearing performance. *Journal of Lubrication Technology*, 89(4):409–415, 1967.

[62] L. Paouris, R. Rahmani, S. Theodossiades, H. Rahnejat, G. Hunt, and W. Barton. An analytical approach for prediction of elastohydrodynamic friction with inlet shear heating and starvation. *Tribology Letters*, 64(1):10, 2016.

[63] T.-J. Park and K.-W. Kim. Elastohydrodynamic lubrication of a finite line contact. *Wear*, 223(1):102–109, 1998.

[64] A. Petrusevich. Fundamental conclusions from the contact-hydrodynamic theory of lubrication. *Izv. Akad. Nauk SSR (OTN)*, 2:209–233, 1951.

[65] C. Roelands. *Correlational aspects of the viscosity-temperature-pressure relationship of lubricating oils*. PhD thesis, TU Delft, Delft University of Technology, The Netherlands, 1966.

[66] L. San Andres. Approximate design of statically loaded cylindrical journal bearings. *Journal of tribology*, 111(2):390–393, 1989.

[67] M. Shirzadegan, A. Almqvist, and R. Larsson. Fully coupled EHL model for simulation of finite length line cam-roller follower contacts. *Tribology International*, 103:584–598, 2016.

[68] J. Sloetjes. *Micro-elasthohydrodynamic lubrication in concentrated sliding contacts*. PhD thesis, University of Twente, Enschede, The Netherlands, 2006.

[69] F. Smith. Lubricant behavior in concentrated contact - some rheological problems. *ASLE Transactions*, 3(1):18–25, 1960.

[70] H. Spikes. Mixed lubrication - an overview. *Lubrication Science*, 9(3):221–253, 1997.

[71] R. Stribeck. Characteristics of plain and roller bearings. *Zeit. VDI*, 46:1341, 1902.

[72] R. Stribeck. Die wesentlichen eigenschaften der gleit-und rollenlager [the key qualities of sliding and roller bearings]. *Zeitschrift des Vereines Deutscher Ingenieure*, 46(38):1432–1437, 1902.

[73] A. Torabi, S. Akbarzadeh, and M. Salimpour. Comparison of tribological performance of roller follower and flat follower under mixed elastohydrodynamic lubrication regime. *Proceedings of the Institution of Mechanical Engineers, Part J: Journal of Engineering Tribology*, 231(8):986–996, 2017.

[74] A. Turturro, R. Rahmani, H. Rahnejat, C. Delprete, and L. Magro. Assessment of friction for cam-roller follower valve train system subjected to mixed non-newtonian regime of lubrication. In *ASME 2012 Internal Combustion Engine Division Spring Technical Conference*, pages 917–923. American Society of Mechanical Engineers, 2012.

[75] M. Umar, R. Mufti, and M. Khurram. Effect of flash temperature on engine valve train friction. *Tribology International*, 118:170–179, 2017.

[76] C. Venner. *Multilevel solution of the EHL line and point contact problems*. PhD thesis, University of Twente, Enschede, The Netherlands, 1991.

[77] J. Wang, C. Venner, and A. Lubrecht. Influence of surface waviness on the thermal elastohydrodynamic lubrication of an eccentric-tappet pair. *Journal of Tribology*, 135(2):021001–021001–11, 2013.

[78] J. Williams. *Engineering Tribology.* Cambridge University Press. DOI:10.1017/CBO9780511805905, 2005.

[79] D. Wymer and A. Cameron. EHL lubrication of a line contact. part 1: optical analysis of a roller bearing. *Proc. Instn. Mech. Engrs*, 188, 1974.

[80] D. Wymer and A. Cameron. Elastohydrodynamic lubrication of a line contact. *Proceedings of the Institution of Mechanical Engineers*, 188(1):221–238, 1974.

[81] S. Yasutomi, S. Bair, and W. Winer. An application of a free volume model to lubricant rheology idependence of viscosity on temperature and pressure. *Journal of Tribology*, 106(2):291–302, 1984.

[82] D. Zhu. Elastohydrodynamic lubrication in extended parameter ranges - part ii: Load effect. *Tribology Transactions*, 45(4):549–555, 2002.

[83] D. Zhu and Y.-Z. Hu. A computer program package for the prediction of EHL and mixed lubrication characteristics, friction, subsurface stresses and flash temperatures based on measured 3D surface roughness. *Tribology Transactions*, 44(3):383–390, 2001.

[84] D. Zhu, Y. Liu, and Q. Wang. On the numerical accuracy of rough surface EHL solution. *Tribology Transactions*, 57(4):570–580, 2014.

[85] G. Zhu. *A theoretical and experimental study of the tribology of a cam and follower.* PhD thesis, The University of Leeds, Leeds, The United Kingdom, 1988.

[86] Y. Zhu and U. Olofsson. An adhesion model for wheel–rail contact at the micro level using measured 3D surfaces. *Wear*, 314(1-2):162–170, 2014.

PART B

Paper A

Elastohydrodynamic lubrication of coated finite line contacts

S.S. Alakhramsing[1], M.B. de Rooij[1], D.J. Schipper[1] and M. van Drogen[2]

Proceedings of the Institution of Mechanical Engineers, Part J: Journal of Engineering Tribology, 232 (9), 1077-1092, 2018.
DOI:10.1177/1350650117705037

[1]Faculty of Engineering Technology, University of Twente, P.O. Box 217, 7500 AE Enschede, The Netherlands
[2]Central Laboratory Metals, DAF Trucks N.V., P.O. Box 90065, 5600 PT Eindhoven, The Netherlands

Nomenclature

h film thickness (m)

H dimensionless film thickness, $H = \frac{hR_x}{a^2}$

h_0 rigid body displacement (m)

H_0 dimensionless rigid body displacement, $H_0 = \frac{h_0 R_x}{a^2}$

a Hertzian contact half-width, $a = \sqrt{\frac{8FR_x}{\pi LE'}}$ (m)

R_x roller radius (m)

R_d roller dub-off radius (m)

l_s roller straight length (m)

F applied load (N)

h_e element size

L roller axial length (m)

p pressure (Pa)

p_h Hertzian pressure $p_\mathrm{h} = \frac{2F}{\pi La}$ (Pa)

P dimensionless pressure, $P = \frac{p}{p_\mathrm{h}}$

E' reduced elasticity modulus, $E' = \frac{2}{\frac{1-{\nu_{\mathrm{s},1}}^2}{E_{\mathrm{s},1}} + \frac{1-{\nu_{\mathrm{s},2}}^2}{E_{\mathrm{s},2}}}$ (Pa)

k equivalent diffusion coefficient (-)

k_AD artificial diffusion coefficient (-)

Pe element Peclet number (-)

x, y, z spatial coordinates (m)

X, Y, Z dimensionless spatial coordinates, $X = \frac{x}{a}$, $Y = \frac{y}{2L}$, $Z = \begin{cases} \frac{z}{t_c}\text{: for coating} \\ \frac{z}{a}\text{: for substrate} \end{cases}$

u_d, v_d, w_d x, y and z-components of the solid's elastic deformation field (m)

U_d, V_d, W_d dimensionless x, y and z-components of the solid's elastic deformation field, $U_d = \frac{u_d R_x}{a^2}$, $V_d = \frac{v_d R_x}{a^2}$, $W_d = \frac{w_d R_x}{a^2}$

u_1 surface velocity of body 1 (m/s)

u_2 surface velocity of body 2 (m/s)

u_m lubricant mean entrainment velocity $u_m = \frac{u_1+u_2}{2}$ (m/s)

E_c coating's Young's modulus of elasticity (Pa)

E_s substrate's Young's modulus of elasticity (Pa)

$E_{c,eq}$ coating's equivalent Young's modulus of elasticity (Pa)

$E_{s,eq}$ substrate's equivalent Young's modulus of elasticity (Pa)

$\tilde{E}_{c,eq}$ dimensionless coating's equivalent Young's modulus of elasticity

$\tilde{E}_{s,eq}$ dimensionless substrate's equivalent Young's modulus of elasticity

ν_c coating's Poisson ratio (-)

ν_s substrate's Poisson ratio (-)

$\nu_{c,eq}$ coating's equivalent Poisson ratio (-)

$\nu_{s,eq}$ substrate's equivalent Poisson ratio (-)

Ω computational domain

Ω_f contact boundary

Ω_D bottom boundary

Ω_s symmetry boundary

$\partial\Omega_f$ contact boundary's edges

α pressure-viscosity coefficient (GPa^{-1})

η lubricant viscosity (Pa·s)

η_0 lubricant reference viscosity (Pa·s)

$\tilde{\eta}$ lubricant dimensionless viscosity, $\tilde{\eta} = \frac{\eta}{\eta_0}$

ρ lubricant density (kg/m^3)

ρ_0 lubricant reference density (kg/m^3)

$\tilde{\rho}$ lubricant dimensionless viscosity, $\tilde{\rho} = \frac{\rho}{\rho_0}$

U dimensionless speed parameter, $U = \frac{2\eta_0 u_\mathrm{m}}{E' R_x}$

G dimensionless material property parameter $G = \alpha_\mathrm{B} E'$

W dimensionless load parameter, $W = \frac{F/L}{E' R_x}$

α_AD upwind function (-)

Abreviations and Subscripts

FEM finite element method

AD artificial diffusion

EHL elastohydrodynamic lubrication

c coating

s substrate

eq equivalent

Elastohydrodynamic lubrication of coated finite line contacts

Abstract

In this work a finite element-based model is presented that simulates elastohydrodynamic lubrication in coated finite line contacts. Using this model the film thickness and pressure distributions, between a straight roller with rounded edges on a plate, were analysed. The model was successfully validated against representative results reported in literature. Parameter studies were conducted to study the influence of varying operating conditions, axial surface profile parameters and coating mechanical properties on the overall EHL behaviour of the contact. It was found that in contrast with typical EHL behaviour the maximum pressure and minimum film thickness, which are located at the rear of the contact, are largely influenced by variations in load. Results also reveal that axial surface profile parameters and coating mechanical properties may act as amplifiers to the effect of load on pressure and film thickness distribution and can thus, if smartly chosen, significantly enhance lubrication performance.

Keywords: EHL, finite line contacts, coatings

1 Introduction

From past literature, dedicated to elastohydrodynamic lubrication (EHL), one may retrieve that a lot of work has been done on elliptical point and infinite line contact problems. In the latter a uniform pressure distribution in axial direction is assumed. However, significantly less work has been done on finite line contact problems despite the high importance of the topic. Due to the finite lengths of components high stresses are generated towards the extremities of the contact, often referred as edge loading. Typical examples include cam-roller followers pairs, rolling element bearings, gear teeth

etc. Axial surface profiling of components is therefore often utilized to minimize edge loading.

Depending on the type of surface profiling, the pressure and film thickness distribution may deviate significantly from that predicted using the infinitely long line contact assumption. The foundation of these observations were laid by experiments performed in 1967-1974 by Gohar and Cameron [11], and Wymer and Cameron [23]. In the latter they measured the film thickness distribution for tapered rollers on a glass plate using optical interferometry. They were able to show that film shapes near the ends were very different from those at the central plane. Moreover, the absolute minimum film thickness always occurred near the extremities of the roller. The minimum film thickness and maximum pressure are crucial design parameters as they significantly affect wear and fatigue and thus ultimately the service life of the component.

Mostofi and Gohar [16] were one of the first to present a numerical solution to the finite line contact EHL problem. The type of rollers used were those with a straight length and rounded edges. However, the numerical results near the position were profiling starts were physically inconsistent. Using the same profiled rollers as in [16], Park and Kim [18] obtained improved contour plots for the pressure and film thickness distribution using an improved numerical scheme as described in [17]. They also concluded that the maximum pressure and minimum film thickness always occur near the position were the profiling starts.

The aforementioned numerical studies were rather limited to low or moderate loads. Extension to higher loads were made by Kushuwaha et al. [15].

Shirzadegan et al. [20] recently presented a finite element-based model applicable to finite line contacts. The model developed in [20] is an extension of the pioneering work of Habchi et al.[13] and can easily cope with highly loaded situations by means of numerical stabilization. In [20] different types of axial profiling were considered, i.e. rounded edges, logarithmic and crowing, and their influence on lubricant performance.

The aforementioned studies serve sufficient knowledge to perform more in-depth investigations in order to gain a fundamental understanding into the design limits of finite line contact problems. In most practical engineering applications operating conditions, such as entrainment velocity, radii of curvature and load, vary with time. It is therefore important that the axial surface profile shape should suffice over the full range of operating conditions. Moreover, nowadays an increasing trend in the use of surface coatings in lubricated contacts is observed and from past studies (see for instance [2], [8], [9] and [12]) one may conclude that smart use of surface coatings can significantly enhance lubrication performance. However, according to the authors knowledge past studies, concerning lubricated coated contacts, are rather limited to infinite line contacts and circular contacts.

Therefore this paper presents a finite element method (FEM)-based finite line contact

model that includes the possibility of having a coating on interacting solids. In this work the lubricated conjunction of an axially surface profiled roller on a plate is analysed. The numerical predictions are first quantitatively validated with benchmark results found in literature. Furthermore, the influence of operating conditions, roller profiling and coating mechanical properties on the tribological behaviour of the contact, are investigated.

2 Mathematical model

The model presented herein is similar to the circular coated contact model presented by Habchi [12], but then slightly modified in order to simulate finite line contacts. Furthermore, isothermal conditions are assumed to simplify the analysis. The model relies on a full system finite element resolution of the EHL governing equations, which are the Reynolds, linear elasticity and the load balance equations.

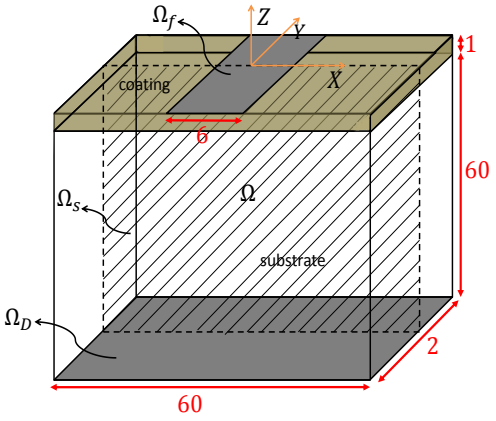

FIGURE 1: Equivalent geometry for EHL analysis of the finite line coated contact problem. Note that the dimensions are exaggerated for the sake of clarity.

The equivalent computational domain Ω, for the EHL problem, is presented in Figure 1 where above the substrate a coating is present with a unit dimensionless thickness. Furthermore, both coating and substrate share a dimensionless axial length of two. The aforementioned geometrical dimensions, for both coating and substrate, are irrespective of the actual coating thickness t_c and axial length L due to unique definitions of Y and Z (see nomenclature). As suggested in [13], a dimensionless thickness of 60 for the substrate is sufficient to approximate a half-space for calculation of elastic displacement field. The two-dimensional Reynolds equation should be solved for the pressure distribution on computational boundary Ω_f, representing the geometrical contact region. The geometrical dimensions for Ω_f are $-4.5 \leq X \leq 1.5$ and $-1 \leq Y \leq 0$ to satisfy zero pressure boundary conditions at the borders [15]. Note that in order to reduce computational effort the advantage of symmetry around boundary Ω_s, which lies in the XZ-plane, has

been taken.

The Reynolds equation, which is a convection-diffusion type equation, is strongly convection dominated in highly loaded situations and will thus exhibit superious oscillations in the solution when solved using a typical Galerkin formulation [1].

The inconsistent (non-residual based) artificial diffusion (AD) method is one of the oldest and simplest methods as it directly adds an artificial diffusion term to the Reynolds equation in regions where the solution is strongly convection dominated. In [13] it was shown that the solution was not significantly affected with the use of isotropic artificial diffusion. Hence, in this work the inconsistent AD stabilization technique is used. The slightly modified Reynolds equation can now be written as follows:

$$\frac{\partial}{\partial X}\left(\left(-\frac{\tilde{\rho}H^3}{\tilde{\eta}\lambda}+k_{\mathrm{AD},X}\right)\frac{\partial P}{\partial X}+H\tilde{\rho}\right)+\frac{\partial}{\partial Y}\left(\left(-\frac{a^2}{(2L)^2}\frac{\tilde{\rho}H^3}{\tilde{\eta}\lambda}+k_{\mathrm{AD},Y}\right)\frac{\partial P}{\partial Y}\right)=0 \quad (1)$$

where the dimensionless speed parameter λ is defined as $\lambda=\frac{12u_{\mathrm{m}}\eta_0 R_x^2}{a^3 p_{\mathrm{h}}}$, $k_{\mathrm{AD},X}$ and $k_{\mathrm{AD},Y}$ are the artificial diffusion coefficients. a and L are the Hertzian contact width and roller axial length respectively. The variation of viscosity $\tilde{\eta}$ with pressure is simulated using Roelands viscosity-pressure relation [19], while the density $\tilde{\rho}$ of lubricant is assumed to be dependent on pressure according to the Dowson-Higginson density-pressure relation [7].

The free boundary cavitation problem, that arises at the exit of the lubricated contact, is treated according to the penalty formulation of Wu [21]. This method adds an additional (penalty) term to the Reynolds equation that only acts in the negative pressure zones. The penalty term enforces the arising negative pressure in the solution towards zero. It is important to note that the equivalent diffusion tensor $\{k_X, k_Y\}=\left\{\frac{\tilde{\rho}H^3}{\tilde{\eta}\lambda}, \frac{a^2}{(2L)^2}\frac{\tilde{\rho}H^3}{\tilde{\eta}\lambda}\right\}$ of eq. 1 is anisotropic due to different definitions of X and Y. The stabilizing terms will therefore have to be amended for the anisotropic nature accordingly. For this reason $k_{\mathrm{AD},X}$ and $k_{\mathrm{AD},Y}$ are defined separately and constructed in the following manner [1]:

$$\begin{bmatrix} k_{\mathrm{AD},X} \\ k_{\mathrm{AD},Y} \end{bmatrix} = \alpha_0 \alpha_{\mathrm{AD}} h_e \left|u\right| \begin{bmatrix} \rho_{\mathrm{AD},X} \\ \rho_{\mathrm{AD},Y} \end{bmatrix} \quad (2)$$

where $\{\rho_{\mathrm{AD},X},\ \rho_{\mathrm{AD},Y}\}$ are tuning parameters, h_e is a typical element size and $u=H\frac{\partial\tilde{\rho}}{\partial P}$ is the equivalent convection coefficient. The constant α_0 and upwind function α_{AD} are defined as follows [13]:

$$\alpha_0 = \frac{1}{2l} \quad (3a)$$

$$\alpha_{\mathrm{AD}} = \coth\left(Pe_{\mathrm{mean}}\right) - {}^{1}/_{Pe_{\mathrm{mean}}} \quad (3b)$$

where l is the interpolation order. The mean diffusion coefficient k_{mean} and scaled cell Peclet number Pe_{mean} (according to the formulation in [10]) are computed as follows:

$$k_{\text{mean}} = \left(\frac{1}{k_X} + \frac{1}{k_Y} \right)^{-1} \tag{4a}$$

$$Pe_{\text{mean}} = \frac{u h_e}{2 k_{\text{mean}} l} \tag{4b}$$

As can be extracted from Eq. 2, the only difference between the definitions of $k_{\text{AD},X}$ and $k_{\text{AD},Y}$ lies in the choice of tuning parameters $\rho_{\text{AD},X}$ and $\rho_{\text{AD},Y}$. The tuning parameters should be minimal just to suppress the generated oscillations and not so large to introduce excessive damping.

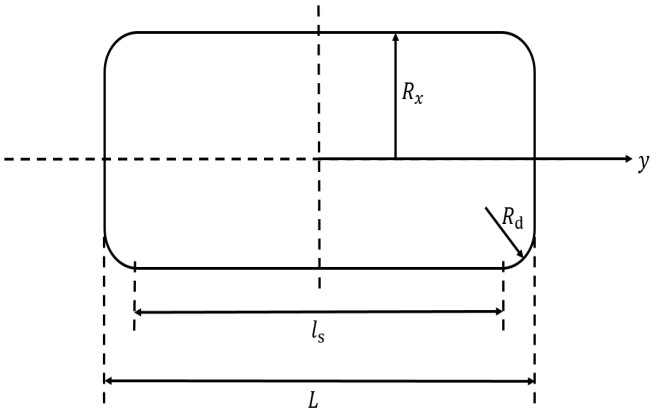

FIGURE 2: Schematic of considered roller axial profile.

The EHL film thickness expression H for a straight cylindrical roller with axial dub-off profiling (see Figure 2) can simply be written as [18]:

$$H(X,Y) = H_0 + \frac{X^2}{2} + \frac{L^2 R_x}{4a^2} \frac{(Y + Y_{\text{d}})^2}{2R_{\text{d}}} (Y < -Y_{\text{d}}) + \frac{L^2 R_x}{4a^2} \frac{(Y - Y_{\text{d}})^2}{2R_{\text{d}}} (Y > Y_{\text{d}}) - W_{\text{d}}(X,Y) \tag{5}$$

where H_0 is the rigid body displacement and W_{d} is the contribution due to elastic deformation. The second term in eq. 5 represents the static separation due to the geometry of the roller in undeformed state. Note that $Y_{\text{d}} = \frac{l_{\text{s}}}{L}$, is the dimensionless axial position where axial profiling starts, R_{d} is the round corner radius and l_{s} is the straight roller length. $(Y < -Y_{\text{d}})$ and $(Y > Y_{\text{d}})$ are Boolean functions, equal to one if true and zero if not true.

The conservation law states that the applied load should be balanced by the hydrodynamically generated force. Assuming that acceleration forces are negligible, the following

load equation should hold for the contact:

$$\int_{\Omega_f} P\left(X,Y\right) d\Omega = \frac{1}{2}\pi \tag{6}$$

Note that eq. 6 already takes into account symmetrical boundary conditions at plane Ω_s. Eq. 6 is balanced by iteratively adjusting H_0 until the Reynolds equation, i.e. the pressure solution, converges.

For the elasticity problem three assumptions are made, namely:

- both substrates are coated
- the substrates of both interacting bodies share similar mechanical properties, i.e. $E_{s,1} = E_{s,2} = E_s$ and $\nu_{s,1} = \nu_{s,2} = \nu_s$
- the coating materials on both substrates also share similar mechanical properties, i.e. i.e. $E_{c,1} = E_{c,2} = E_c$ and $\nu_{c,1} = \nu_{c,2} = \nu_c$

where subscripts "s" and "c" denote substrate and coating respectively. Note that the aforementioned assumptions are purely made here to simplify the analysis. Extension to other problems, such as usage of different coating and/or substrate materials, can straightforwardly be taken in to account.

For the elastic deformation calculation we again make use of an equivalent elastic model, see [13] for more details. In the equivalent elastic model one of the interacting bodies, thus substrate with coating, is rigid while the other body has equivalent material properties to compensate for the total elastic deformation. As both substrates and coatings share similar mechanical properties, the equivalent dimensionless material properties for substrate ($\tilde{E}_{s,eq}$,$\nu_{s,eq}$) and coating ($\tilde{E}_{c,eq}$,$\nu_{c,eq}$) simplify to:

$$\begin{cases} \tilde{E}_{s,eq} & = \frac{E_s}{2}\frac{a}{Rp_h} \\ \nu_{s,eq} & = \nu_s \end{cases} \quad \text{for the substrate} \tag{7a}$$

$$\begin{cases} \tilde{E}_{c,eq} & = \frac{E_c}{2}\frac{a}{Rp_h} \\ \nu_{c,eq} & = \nu_c \end{cases} \quad \text{for the coating} \tag{7b}$$

In the current case, since the two substrates and coatings are made of the same material it means that the use of the equivalent material properties defined in eq. 7 leads to a total elastic deflection that is twice that of each solid body (substrate + coating) taken individually.

In fact, now two interdependent sets of the system of 3D elasticity equations need to be solved to calculate the elastic displacement field in both coating and substrate. The 3D elasticity equations are applied to dimensionless domain Ω to compute the total

elastic deformation. The sets of equations described by eqns. 8 and 9 describe the elastic deformation of substrate and coating respectively. For the substrate we get:

$$\begin{aligned}
&\zeta\frac{\partial}{\partial X}\left[\left(\tilde{\lambda}_\mathrm{s}+2\tilde{\mu}_\mathrm{s}\right)\frac{\partial U_\mathrm{d}}{\partial X}+\psi\tilde{\lambda}_\mathrm{s}\frac{\partial V_\mathrm{d}}{\partial Y}+\tilde{\lambda}_\mathrm{s}\frac{\partial W_\mathrm{d}}{\partial Z}\right]+\psi\zeta\frac{\partial}{\partial Y}\left[\tilde{\mu}_\mathrm{s}\left(\psi\frac{\partial U_\mathrm{d}}{\partial Y}+\frac{\partial V_\mathrm{d}}{\partial X}\right)\right]\\
&\qquad+\zeta\frac{\partial}{\partial Z}\left[\tilde{\mu}_\mathrm{s}\left(\frac{\partial U_\mathrm{d}}{\partial Z}+\frac{\partial W_\mathrm{d}}{\partial X}\right)\right]=0,\\
&\zeta\frac{\partial}{\partial X}\left[\tilde{\mu}_\mathrm{s}\left(\psi\frac{\partial U_\mathrm{d}}{\partial Y}+\frac{\partial V_\mathrm{d}}{\partial X}\right)\right]+\zeta\psi\frac{\partial}{\partial Y}\left[\tilde{\lambda}_\mathrm{s}\frac{\partial U_\mathrm{d}}{\partial X}+\psi\left(\tilde{\lambda}_\mathrm{s}+2\tilde{\mu}_\mathrm{s}\right)\frac{\partial V_\mathrm{d}}{\partial Y}+\tilde{\lambda}_\mathrm{s}\frac{\partial W_\mathrm{d}}{\partial Z}\right]\\
&\qquad+\zeta\frac{\partial}{\partial Z}\left[\tilde{\mu}_\mathrm{s}\left(\frac{\partial V_\mathrm{d}}{\partial Z}+\psi\frac{\partial W_\mathrm{d}}{\partial Y}\right)\right]=0,\\
&\zeta\frac{\partial}{\partial X}\left[\tilde{\mu}_\mathrm{s}\left(\frac{\partial U_\mathrm{d}}{\partial Z}+\frac{\partial W_\mathrm{d}}{\partial X}\right)\right]+\zeta\psi\frac{\partial}{\partial Y}\left[\tilde{\mu}_\mathrm{s}\left(\frac{\partial V_\mathrm{d}}{\partial Z}+\psi\frac{\partial W_\mathrm{d}}{\partial Y}\right)\right]\\
&\qquad+\zeta\frac{\partial}{\partial Z}\left[\tilde{\lambda}_\mathrm{s}\frac{\partial U_\mathrm{d}}{\partial X}+\psi\tilde{\lambda}_\mathrm{s}\frac{\partial V_\mathrm{d}}{\partial Y}+\left(\tilde{\lambda}_\mathrm{s}+2\tilde{\mu}_\mathrm{s}\right)\frac{\partial W_\mathrm{d}}{\partial Z}\right]=0
\end{aligned}\tag{8}$$

And for the coating:

$$\begin{aligned}
&\frac{\partial}{\partial X}\left[\left(\tilde{\lambda}_\mathrm{c}+2\tilde{\mu}_\mathrm{c}\right)\frac{\partial U_\mathrm{d}}{\partial X}+\psi\tilde{\lambda}_\mathrm{c}\frac{\partial V_\mathrm{d}}{\partial Y}+\zeta\tilde{\lambda}_\mathrm{c}\frac{\partial W_\mathrm{d}}{\partial Z}\right]+\psi\frac{\partial}{\partial Y}\left[\tilde{\mu}_\mathrm{c}\left(\psi\frac{\partial U_\mathrm{d}}{\partial Y}+\frac{\partial V_\mathrm{d}}{\partial X}\right)\right]\\
&\qquad+\zeta\frac{\partial}{\partial Z}\left[\tilde{\mu}_\mathrm{c}\left(\zeta\frac{\partial U_\mathrm{d}}{\partial Z}+\frac{\partial W_\mathrm{d}}{\partial X}\right)\right]=0,\\
&\frac{\partial}{\partial X}\left[\tilde{\mu}_\mathrm{c}\left(\psi\frac{\partial U_\mathrm{d}}{\partial Y}+\frac{\partial V_\mathrm{d}}{\partial X}\right)\right]+\psi\frac{\partial}{\partial Y}\left[\tilde{\lambda}_\mathrm{c}\frac{\partial U_\mathrm{d}}{\partial X}+\psi\left(\tilde{\lambda}_\mathrm{c}+2\tilde{\mu}_\mathrm{c}\right)\frac{\partial V_\mathrm{d}}{\partial Y}+\tilde{\lambda}_\mathrm{c}\zeta\frac{\partial W_\mathrm{d}}{\partial Z}\right]\\
&\qquad+\zeta\frac{\partial}{\partial Z}\left[\tilde{\mu}_\mathrm{c}\left(\zeta\frac{\partial V_\mathrm{d}}{\partial Z}+\psi\frac{\partial W_\mathrm{d}}{\partial Y}\right)\right]=0,\\
&\frac{\partial}{\partial X}\left[\tilde{\mu}_\mathrm{c}\left(\zeta\frac{\partial U_\mathrm{d}}{\partial Z}+\frac{\partial W_\mathrm{d}}{\partial X}\right)\right]+\psi\frac{\partial}{\partial Y}\left[\tilde{\mu}_\mathrm{c}\left(\zeta\frac{\partial V_\mathrm{d}}{\partial Z}+\psi\frac{\partial W_\mathrm{d}}{\partial Y}\right)\right]\\
&\qquad+\zeta\frac{\partial}{\partial Z}\left[\tilde{\lambda}_\mathrm{c}\frac{\partial U_\mathrm{d}}{\partial X}+\psi\tilde{\lambda}_\mathrm{c}\frac{\partial V_\mathrm{d}}{\partial Y}+\zeta\left(\tilde{\lambda}_\mathrm{c}+2\tilde{\mu}_\mathrm{c}\right)\frac{\partial W_\mathrm{d}}{\partial Z}\right]=0
\end{aligned}\tag{9}$$

where $\{U_\mathrm{d}, V_\mathrm{d}, W_\mathrm{d}\}$ are the X, Y and Z-components of the solid's elastic displacement field, $\psi=\frac{a}{2L}$ and $\zeta=\frac{a}{t_\mathrm{c}}$. Eqns. 8 and 9 are derived analogously to the elasticity equations presented in [12]. The dimensionless (equivalent) Lamé's coefficients for substrate and coating are calculated as follows:

$$\begin{cases}\tilde{\mu}_\mathrm{s}=\frac{\tilde{E}_\mathrm{s,eq}}{2(1+\nu_\mathrm{s,eq})}\\ \tilde{\lambda}_\mathrm{s}=\frac{\nu_\mathrm{s,eq}\tilde{E}_\mathrm{s,eq}}{(1-2\nu_\mathrm{s,eq})(1+\nu_\mathrm{s,eq})}\end{cases}\quad\text{for the substrate}\tag{10a}$$

$$\begin{cases}\tilde{\mu}_\mathrm{c}=\frac{\tilde{E}_\mathrm{c,eq}}{2(1+\nu_\mathrm{c,eq})}\\ \tilde{\lambda}_\mathrm{c}=\frac{\nu_\mathrm{c,eq}\tilde{E}_\mathrm{c,eq}}{(1-2\nu_\mathrm{c,eq})(1+\nu_\mathrm{c,eq})}\end{cases}\quad\text{for the coating}\tag{10b}$$

where the material properties ($\tilde{E}_\mathrm{s,eq}$,$\nu_\mathrm{s,eq}$) and ($\tilde{E}_\mathrm{c,eq}$,$\nu_\mathrm{c,eq}$) are evaluated by means of equations 7a and 7b respectively.

In order to obtain a unique solution for the EHL problem, proper boundary conditions (BCs) need to be imposed. These are summarized as follows:
For the Reynolds equation:

$$\begin{cases} P = 0 & \text{on } \partial\Omega_f \\ \nabla P \cdot \mathrm{n} = 0 & \text{on } \Omega_s \end{cases} \tag{11}$$

For the elastic model:

$$\begin{cases} U_\mathrm{d} = V_\mathrm{d} = W_\mathrm{d} = 0 & \text{on } \Omega_D \\ \sigma_n = \sigma_{ZZ} = & \\ \quad \zeta \left[\tilde{\lambda}_\mathrm{c} \dfrac{\partial U_\mathrm{d}}{\partial X} + \psi \tilde{\lambda}_\mathrm{c} \dfrac{\partial V_\mathrm{d}}{\partial Y} + \left(\tilde{\lambda}_\mathrm{c} + 2\tilde{\mu}_\mathrm{c} \right) \zeta \dfrac{\partial W_\mathrm{d}}{\partial Z} \right] = -P & \\ \quad \text{on } \Omega_f & \\ V_\mathrm{d} = 0 & \text{on } \Omega_s \\ \sigma_n = 0 & \text{elsewhere} \end{cases} \tag{12}$$

Additionally, a continuity BC on the common boundary of coating and substrate is imposed.

3 Results

Summarizing, the complete model consists of the modified Reynolds eq. 1, the load balance eq. 6, two sets of interdependent elasticity equations for substrate and coating eqns. 8 and 9, and their respective boundary conditions equations 11 and 12.
The dry dimensionless Hertzian pressure profile was taken as initial guess for the pressure distribution, while for the elastic displacement field the solution corresponding to the dry Hertzian contact was taken as initial guess. The load balance eq. 6, which is associated with the unknown H_0, is added to the complete system of equations formed by eqns. 1 and 8 and 9.
The developed model is solved using the FEM with a general purpose finite element analysis software [5]. The resulting system of non-linear equations is solved using a monolithic approach where all the dependent variables$(P, U_\mathrm{d}, V_\mathrm{d}, W_\mathrm{d}, H_0)$ are collected in one vector of unknowns and simultaneously solved using a modified Newton-Raphson iteration scheme. For specific numerical details, concerning the weak coupling resolution of the Reynolds and elasticity equations, the reader is referred to [13] as only the main features of the model are recalled here.
Lagrange quintic elements were used for the hydrodynamic part, while quadratic elements

were used for the elastic part. A custom tailored mesh, similar to that detailed in [12], was deployed to reach an optimum combination between accuracy and calculation speed. The maximum element size in the contact zone in X-direction was chosen smaller than 0.06 while for Y-direction the maximum element size was chosen to be smaller than 0.03. This, because steeper gradients are expected in Y-direction. The element size was allowed to increase gradually as the distance from the contact boundary increased. The aforementioned corresponds to the usage of approximately 350000 degrees of freedom for the uncoated case and approximately 400000 degrees of freedom for the coated case. Converged solutions to relative errors ranging between $10^{-3} - 10^{-4}$ are typically reached within 12 iterations, corresponding to a computation time of approximately 2 minutes on an Intel(R) Xenon(R) CPU E5-2640 processor. Much less iterations (2-5) are required when calculations are continued from a previously obtained solution with a somewhat different set of input parameters.

The results herein are presented in twofold. The first part of the results corresponds to uncoated contacts, while the second part discusses results corresponding to coated contacts. Note that the particular case when the Young's moduli of coating and substrate are identical, i.e. E_c=E_s, corresponds to an uncoated contact.

3.1 Uncoated case

3.1.1 Influence of numerical stabilization on overall solution

The tuning factors [$\rho_{AD,X}$, $\rho_{AD,Y}$] are chosen different due to anisotropic nature of the diffusion tensor $\{k_X, k_Y\}$ of eq. 1. In fact, in terms of the amount of artificial diffusion added for streamline stabilization the effect is similar to that described in [13] and therefore not detailed here, i.e small deviations around the pressure spike are observed and the minimum film thickness is not significantly effected. It is thus safe to choose $\rho_{AD,X}$ smaller than 0.5.

It is widely known, for infinite line and point contacts, that with increasing loads the Petrusevich pressure spike(s) shift more towards the exit of the lubricated contact and becomes smaller in magnitude at the same time. The maximum pressure then occurs at the centre of the contact and is approximately the same as the maximum dry Hertzian contact pressure p_h. However, for the finite line contact the maximum pressure P_{max} and minimum film thickness H_{min} occur near the edges of the contact. Therefore the amount of artificial diffusion in crosswind direction needs to be chosen carefully as this also is the direction that causes the anisotropic nature of the diffusion tensor.

TABLE 1: Reference operating conditions and geometrical parameters for a straight roller with rounded edges.

Parameter	**Value**	**Unit**
F	3150	N
E_{s}	210	GPa
ν_{s}	0.3	-
E_{c}	210	GPa
ν_{c}	0.3	-
α	1.89E-8	Pa^{-1}
η_0	0.013	Pa·s
U_{m}	1	m/s
R_x	0.008	m
L	0.01	m
R_{d}	0.127	m
l_{s}	0.0085	m
U	7.3891E-12	-
W	1.7904E-4	-
G	4150	-
p_{h}	1.17	GPa

Figure 3 shows the pressure distribution for a straight roller with rounded edges with and without stabilization. The operating conditions and roller profiling geometrical parameters are given in Table 1. Note that the Young's moduli of coating and substrate are identical, i.e. E_{c}=E_{s}, which corresponds to an uncoated contact. As can be retrieved from Figure 3, the pressure distribution without crosswind stabilization is not smooth whereas with crosswind stabilization a smooth solution is obtained.

From "numerical experiments" we ascertained that the influence of crosswind artificial diffusion on the absolute minimum film thickness is much more amplified when compared to the influence of streamline artificial diffusion. This is mainly due to the fact that axial pressure gradients $\frac{\partial P}{\partial Y}$ are affected in a much more amplified fashion with crosswind diffusion due to the anisotropic nature of the diffusion tensor. This is also the reason why crosswind diffusion has a greater influence on the absolute minimum film thickness H_{min} as compared to the central plane minimum film thickness $H_{\mathrm{min,central}}$, which seems to remain unaffected (see Figure 4(a)). The exact value for H_{min} corresponds to a value of $\rho_{\mathrm{AD},Y} = 0$, but then the solution for pressure distribution is not smooth. This can be extracted from Figure 4(b) in which the pressure and film thickness distributions are plotted along the line $X = 0$. Note that the absolute maximum pressure P_{max} and the maximum pressure at the central plane $P_{\mathrm{max,central}}$ are negligibly affected by the introduced amount of crosswind diffusion (see Figure 4(c)). Nevertheless, from "numerical experiments" we conclude that, as a rule of thumb, $\rho_{\mathrm{AD,Y}}$ should always be

chosen smaller than 0.1.

The present authors also attempted to implement more consistent (residual based) stabilizing methods, such as described in references [4] and [6], to stabilize the solution in crosswind direction. These include shock-capturing techniques which aim to eliminate effects such as overshoots and undershoots close to discontinuities. Unfortunately, these techniques make the system of equations more non-linear and consequently induce convergence issues. This is of course an incentive for more detailed investigation into the implementation of more consistent techniques for the "anisotropic convection-dominated convection diffusion problem".

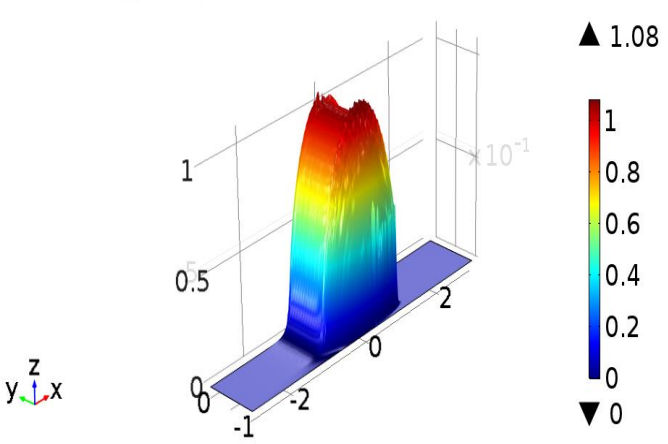

(a)

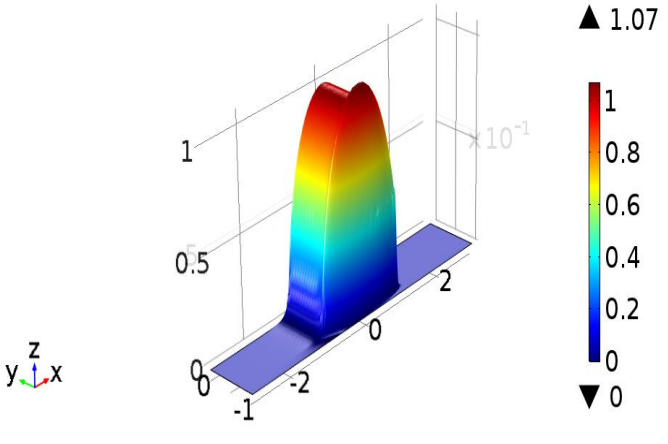

(b)

FIGURE 3: The pressure distribution a) with crosswind stabilization and b) without crosswind stabilization.

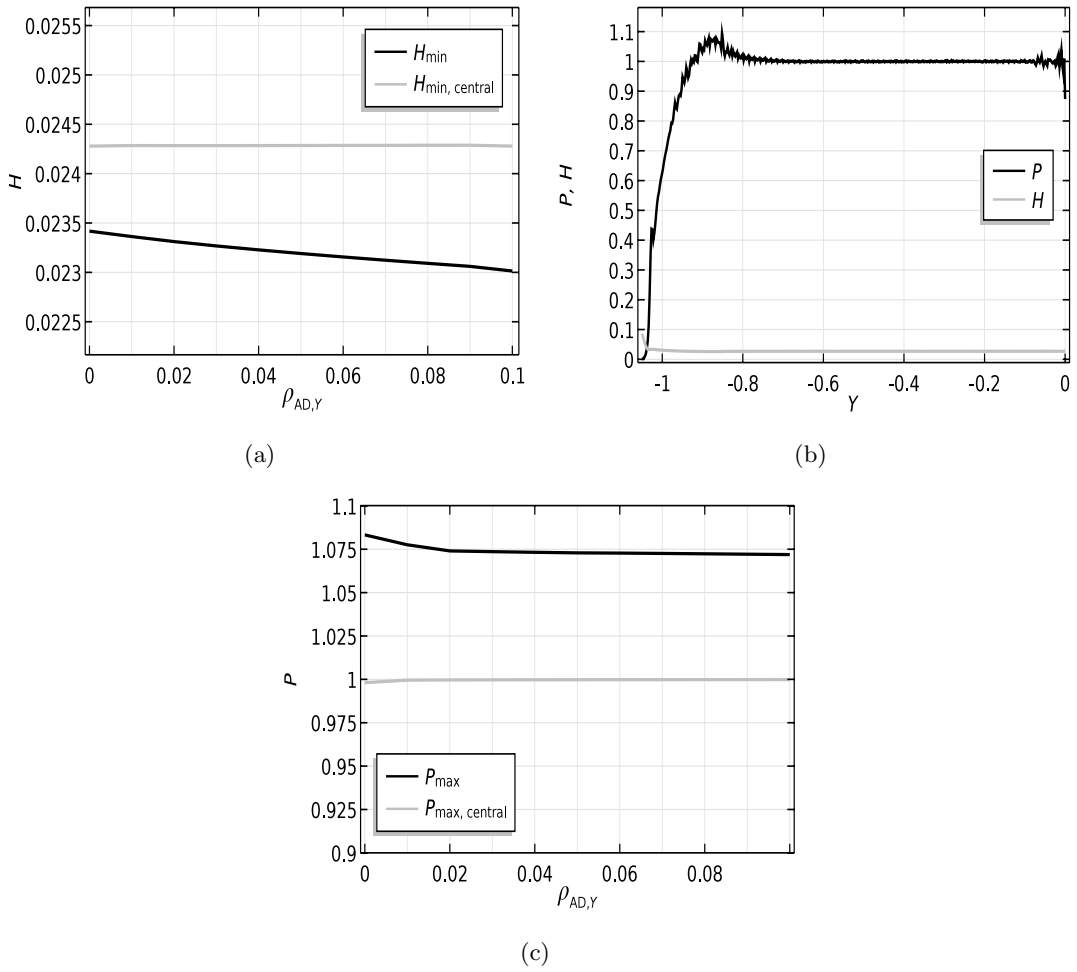

FIGURE 4: Influence of crosswind stabilization on a) minima film thicknesses and b) on axial pressure and film thickness distributions and c) maxima pressures.

3.1.2 Quantitative validation

Park and Kim [18] have presented benchmark results for an uncoated straight roller (with straight length l_s) with rounded edges (with dub-off radius R_d). They also compared their results qualitatively with experimental results obtained using optical interferometry [22]. The operating conditions and roller profile parameters are given in Table 2.

Note that the presented coated finite line contact model herein can be numerically validated with the results presented in ref.[18] if the material properties of coating and substrate are set to be the same (see Table 2).

In ref. [18] a slightly different definition for the load parameter ($W_{\text{Kim}} = \frac{F}{E' R_x^2}$) is used than what is "usual" for infinite line contacts ($W = \frac{F/L}{E' R_x}$). The axial length L is not given in ref. [18], but can somehow be estimated. In the present analysis the axial length L was estimated on the basis of the contact footprint length, i.e. for an equivalent infinite line contact problem the load acting over the unit footprint length can be used as input

data [14]. In ref.[18] the profiling starts at a position of y_d=0.7 x R_x from the central plane, meaning that for the infinite analysis $L = l_s$ =2 x 0.7 x R_x would be used as input data. This statement does not always hold as for higher loads situations the lubricated contact footprint length becomes larger. This will be shown in the next sub-section. For dry contact analysis the footprint length is usually taken to be the same as the straight roller length l_s. However, for a lubricated contact the pressure distribution is slightly extended [15]. For this reason the axial length here is assumed to be a factor of 1.07 times larger than the contact dry footprint length in ref.[18], i.e. L =2 x 0.7 x R_x x 1.07

TABLE 2: Operating conditions for reference case. Partly adapted from [18].

Parameter	**Value**	**Unit**
F	570.24	N
E_s	200	GPa
ν_s	0.3	-
E_c	200	GPa
ν_c	0.3	-
α	1.364E-8	Pa^{-1}
η_0	0.0528	Pa·s
U_m	1	m/s
R_x	0.012	m
L	2 x 0.7 x R_x x 1.07	m
R_d	0.3 x R_x	m
y_d	0.7 x R_x	m
l_s	2 x y_d	m
U	2E-11	-
$W_{Kim} = \frac{F}{E' R_x^2}$	1.8E-5	-
G	3000	-
p_h	0.304	GPa

Comparisons are made according to different sections of the contact. These correspond to the streamline and axial sections through the maximum pressure and absolute minimum film thickness. The sections are defined as shown in Figure 5.

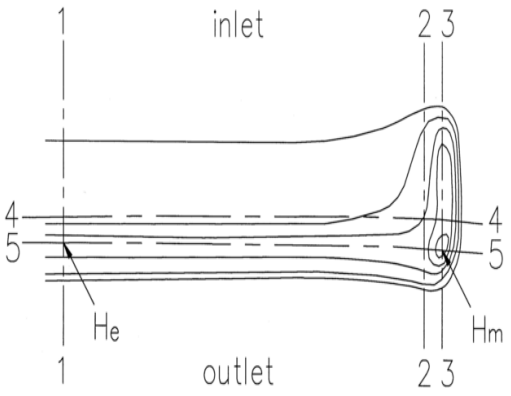

FIGURE 5: Definition of sections through lubricated contact. Reproduced from reference [18].

Section 1-1 is the central line in streamline direction (plotted against $Y = 0$) where the minimum film thickness $H_{\text{min,central}}$ occurs. Section 2-2 and 3-3 correspond to contour sections where the absolute maximum pressure P_{max} and the absolute minimum film thickness H_{min} occur respectively. Section 4-4 and 5-5 are contour sections in transverse direction where the absolute maximum pressure and absolute minimum film thickness occur respectively.

Figure 6 presents the zoomed-in contour plots for pressure and film thickness. Note that different dimensionless variables are used for the sake of comparison. It is clear that the maximum pressure and minimum film thickness occur near the region where profiling starts (thus near a dimensionless position of $y/R_x = -0.7$).

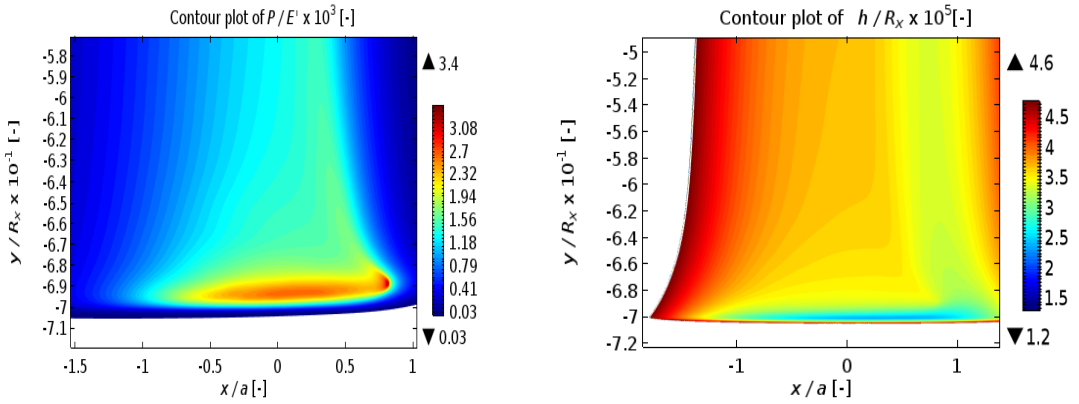

(a) (b)

FIGURE 6: Zoomed-in contour plots of a) the film thickness and b) pressure distribution at the rear of the contact. Note that different dimensionless variables have been used for the sake of comparison.

In fact the secondary pressure peak occurs near the side constriction and rear exit of the lubricated contact area. Flow continuity demands that the pressure gradients should be coupled with local restrictions of minima film thickness. Hence, the secondary pressure peaks near the side constriction also inhibit lubricant flow in their vicinity. Consequently small islands (iso-film thickness contours) are formed at the rear of the contact. These are commonly referred as end closure films in literature [15].
It can readily be concluded from the figures that traditional EHL infinite line contact solutions do not reveal the tribological behaviour at the extremities of the contact in terms of pressure and film thickness distributions. These findings are in line with previous studies (see for instance [15, 18, 3]).
In Figure 7 the results for pressure and film thickness distributions are presented according to the defined sections in Figure 5. The results are to be compared with those reported in [18]. Overall good agreement is obtained for the results obtained using the current approach. The minimum film thickness and maximum pressure and their positions are accurately predicted. In Figure 7(e) there is some minor difference in obtained axial pressure distribution for section 4-4, although the maximum pressure is accurately predicted. This is mainly due to the assumed axial length as earlier discussed. The assumed axial length might shift the location of maximum pressure a little, which in turn may lead to this discrepancy.

3.1.3 Parameter study

It is of interest to see how the finite line contact responds to varying operating conditions such as load, speed and material properties. The dimensionless parameters of the aforementioned operating conditions are represented by the load parameter W, speed parameter U and material property parameter G. The operating conditions for the current cases are detailed in Table 1.

Figure 8 shows how the pressure and film thickness distribution (plotted along $X = 0$ and $Y = 0$) vary as a function of these three parameters, while keeping two constant at a time. Variation of W, U and G all result to some minor variation around the pressure spike along the central plane and/or central film thickness variation. These variations are much more explainable from traditional EHL solutions for line and/or elliptical contacts. The most remarkable observation is that the pressure and film thickness distribution, especially at the side extremities, are highly affected by varying loads. To be more specific, the variation in pressure distribution at the extremities seems to be highly amplified with increasing load in the sense that the secondary pressure peak smears out and the covered (lubricated) axial length becomes larger. These results are in line with previous theoretical and experimental findings [22] and [18].

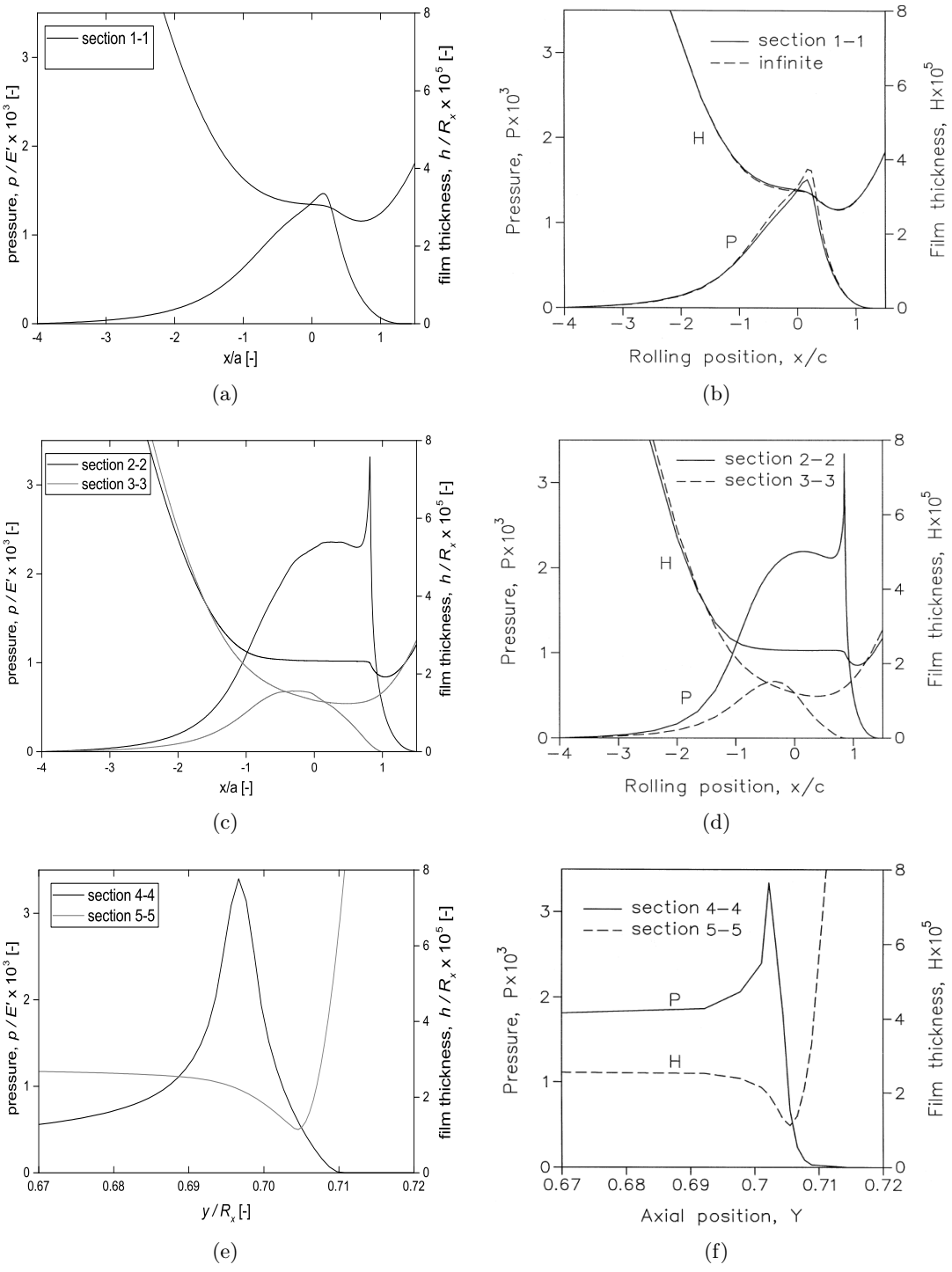

FIGURE 7: Results for pressure and film thickness profiles, for the different sections, using the current approach (left column). Note that here $H = \frac{h}{R_x}$ and $P = \frac{p}{E'}$. The figures are to be compared with those reproduced from Park and Kim [18] (right column).

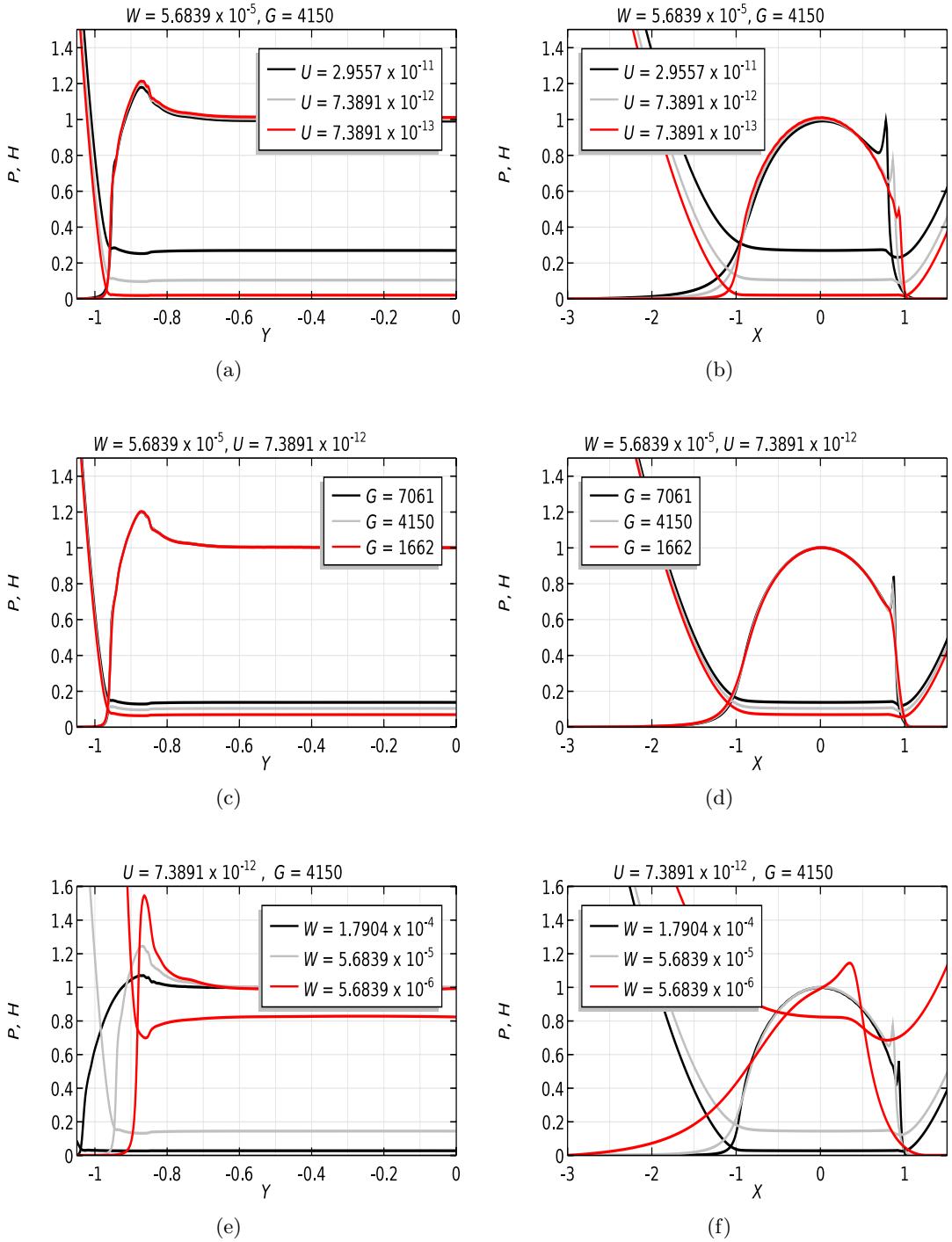

FIGURE 8: Influence of varying operating conditions such as speed, elasticity and contact load on streamline and axial pressure shapes.

To make things more clear, Figure 9 plots the variation $H_{\text{min}}/H_{\text{min,central}}$ as function of W, U and G from which it is clear that the absolute minimum film thickness is highly affected by variations in load. Especially from low to moderate loads this phenomenon is much more visible. For variations in U and G the ratio $H_{\text{min}}/H_{\text{min,central}}$ seems to remain constant. Note that the behaviour of $H_{\text{min,central}}$ is much more explainable using traditional EHL solutions for infinite line contacts [18]. It is therefore much more interesting to study the behaviour of ratio $H_{\text{min}}/H_{\text{min,central}}$ from a designers perspective. In practice one would like to maximize the value of $H_{\text{min}}/H_{\text{min,central}}$ as $H_{\text{min,central}}$ can fairly be estimated using the infinite line contact assumption. This would drastically decrease computational overhead.

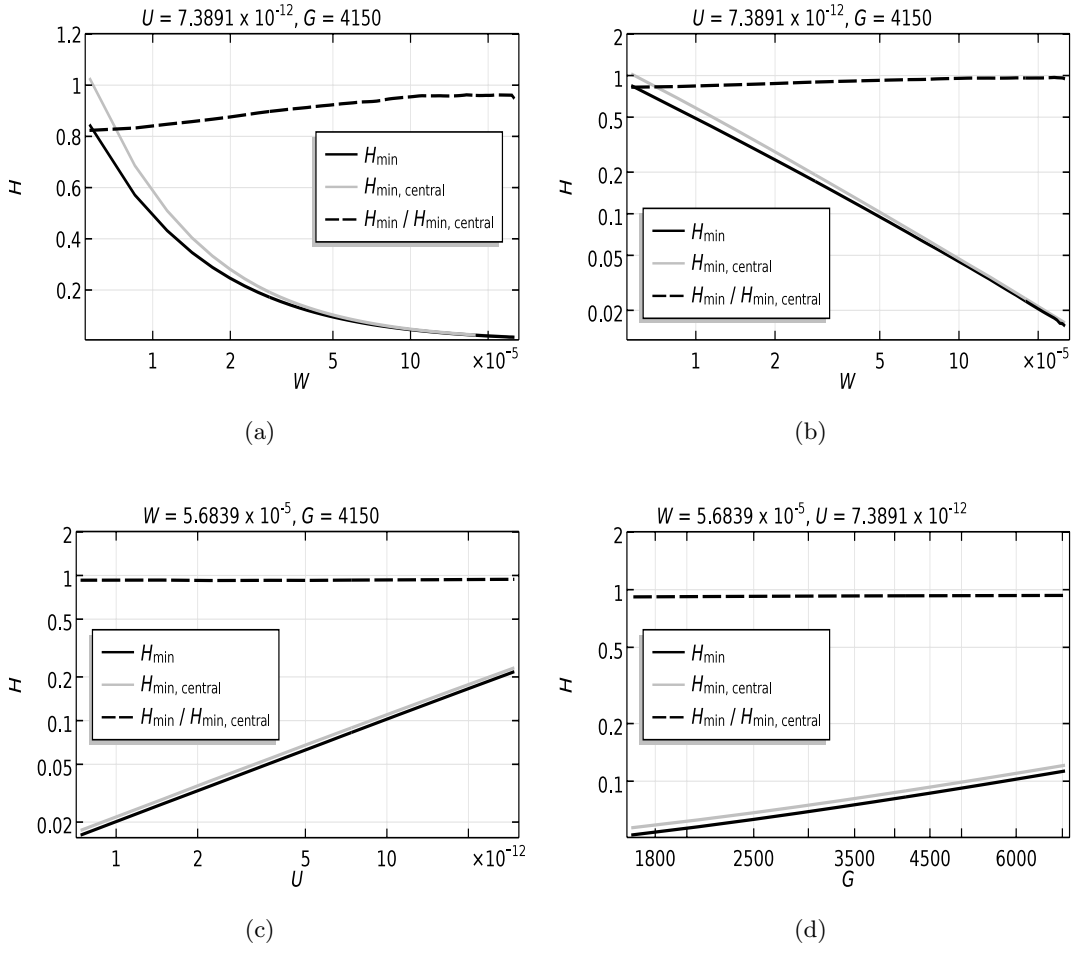

FIGURE 9: Variation of H_{min}, $H_{\text{min,central}}$ and ratio $H_{\text{min}}/H_{\text{min,central}}$ with dimensionless speed, material and load parameters while keeping two fixed at a time. The minimum film thickness H_{min} seems to behave different with increasing load.

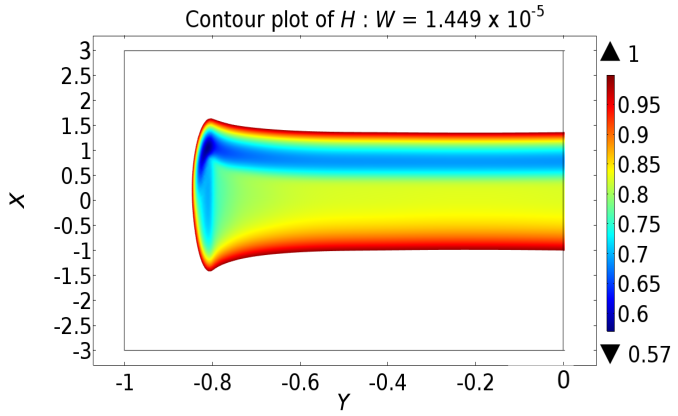

(a)

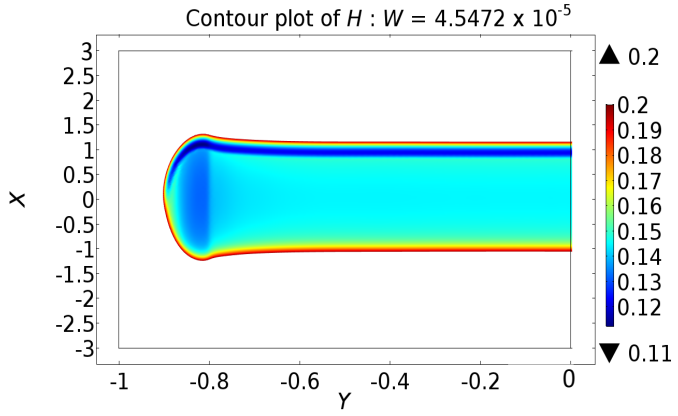

(b)

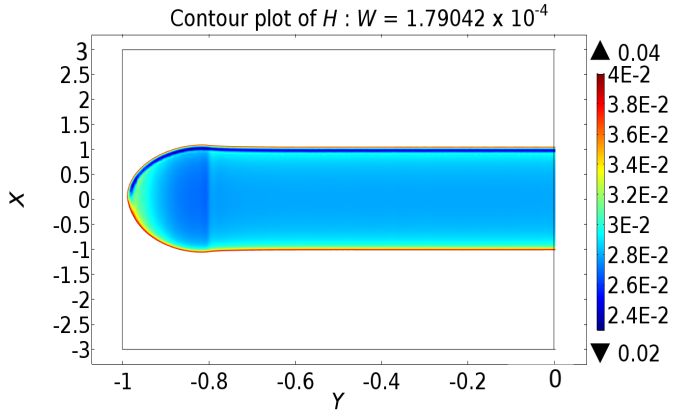

(c)

FIGURE 10: Contour plots of film thickness H for increasing values of dimensionless load parameter W showing how the position of minimum film thickness shifts as the contact centre flattens.

Figure 10 plots the contours of the film thickness for increasing loads. It can be seen that for all conditions $H_{\min}$ occurs at the rear of the contact and that for increasing loads the lubricated area extends (also see Figure 8(e)). Also note that also, similar

as for elliptical contacts, with increasing load the contact centre gets more flattened and the end closure films (small islands of minimum film thickness) become smaller. Consequently, the ratio $H_{\text{min}}/H_{\text{min,central}}$ also increases as can be seen from Figure 9(a). This however also depends on the axial profile itself, i.e. the straight roller length and dub-off radius as will be explained now.

So, apart from varying operating conditions it is also interesting to take a look at the influence of geometrical parameters on the pressure and film thickness distributions. In fact, for the axial profile of the roller one may vary the straight roller length and dub-off radius to optimize the pressure distribution, i.e. to make it more uniform by reducing edge stress concentrations and consequently increase $H_{\text{min}}/H_{\text{min,central}}$.

Figure 11 presents the variations of pressure and film thickness profiles as a function of the dub-off radius R_{d}. From Figure 11(a) it is clear that a higher relief radius smears out the secondary pressure peak, resulting to a larger contact area. Furthermore, the ratio $H_{\text{min}}/H_{\text{min,central}}$ seems to increase with increasing R_{d}. The aforementioned, is amplified with increasing loads. One would then think that choosing a larger R_{d} results in a more uniform the pressure profile and thus a better design. However, there seems to be an optimum range for minimum film thickness vs dub-off radius mapped against the range of loads. In fact, for a too large R_{d} the ratio $H_{\text{min}}/H_{\text{min,central}}$ starts to decrease after a certain applied load. This is mainly due to the fact that there is no space available for the pressure profile to extend as a zero boundary condition is imposed at the extremities. Consequently, the pressure gradient $\frac{dP}{dY}$ at the extremities increases and thus H_{min} decreases (see Figure 11(b)).

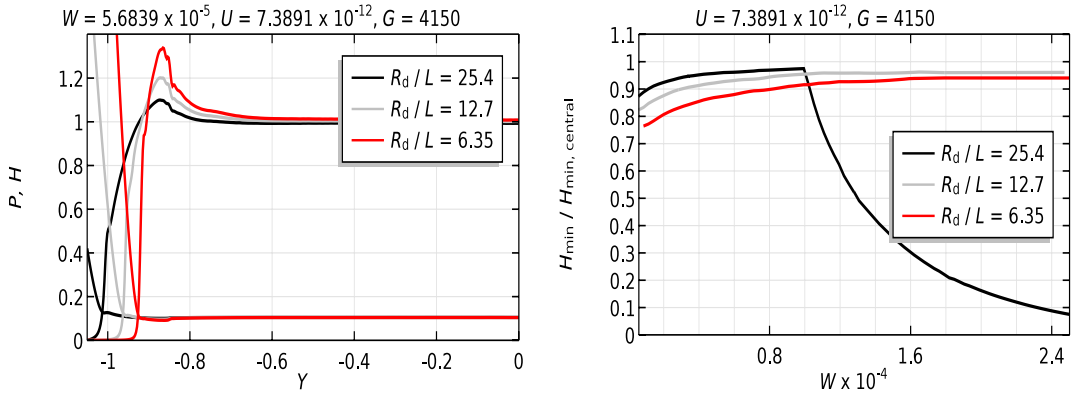

(a) (b)

FIGURE 11: Influence of round corner radius on a) pressure and film thickness distributions and b) minima film thicknesses.

A similar statement can be made about variations in the straight length of the roller (see Figure 12(a)). There is an optimum range for choosing an appropriate straight

roller length as a too large value for Y_d results to a decrease of $H_{min}/H_{min,central}$ with increasing loads (see Figure 12(b)). If a too small value for Y_d is chosen, the contact area is reduced and the maximum pressure consequently increases.

All these findings make it really hard to develop a robust correlation between absolute minimum film thickness and operating conditions, as axial profile design parameters play an equally important role. In fact, a good understanding of finite line contact behaviour as a basis will lead to a better design of mechanical components in terms of film thickness and pressure distributions, and as a result, increase in service life.

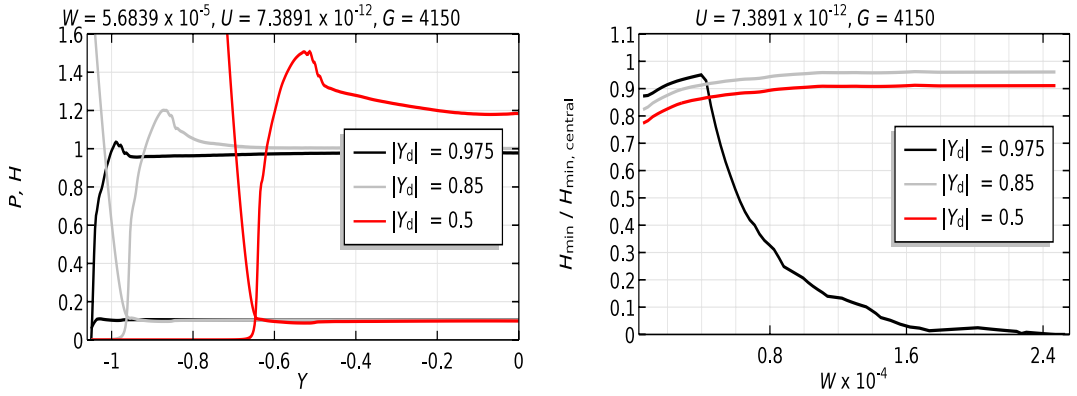

(a) (b)

FIGURE 12: Influence of roller straight length on a) pressure and film thickness shape and b) minima film thicknesses.

3.2 Coated case

The influence of mechanical properties, in terms of coating stiffness and thickness, on the overall EHL behaviour of a finite line contact will be discussed in this section. The reference operating conditions for the present results are identical to those presented in Table 1. In addition the coating thickness t_c and Young's modulus E_c will subsequently be defined for the cases studied. Substrate mechanical properties are kept fixed and are given in Table 1.

In Figures 13(a) and13(b) the influence of coating stiffness on the pressure and film thickness distribution, is illustrated. Note that the case when E_c=210GPa (grey line), corresponds to the uncoated contact case.

One can directly observe that with increasing stiffness of the coating the maximum pressure increases, while the contact width decreases. Furthermore the pressure spike at the central plane and the secondary pressure peak at the rear of the contact increase in magnitude with increasing coating hardness. It seems obvious that with stiffer coatings higher pressures are expected, and to compensate for this (with fixed applied load) the

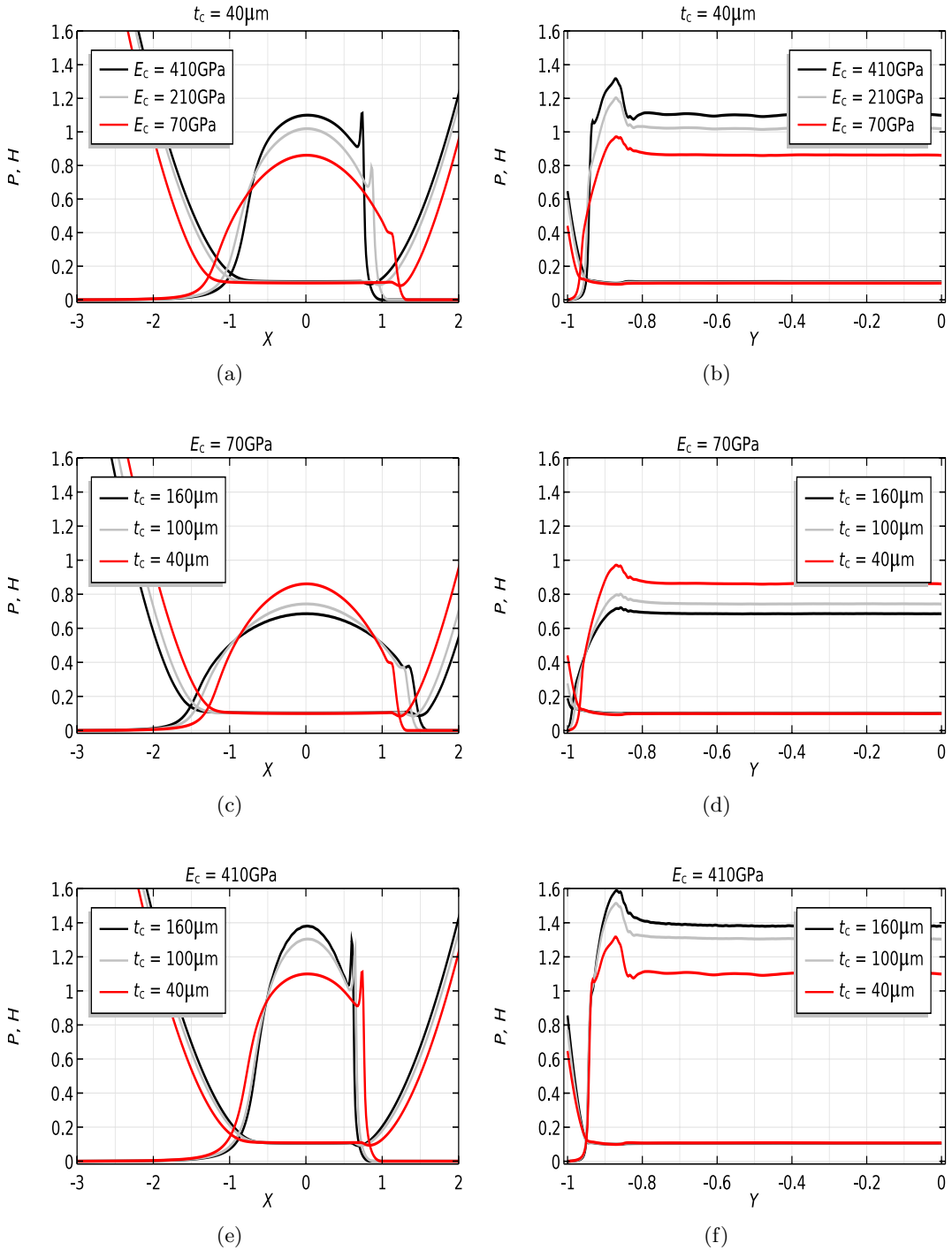

FIGURE 13: Influence of coating elasticity E_c and thickness t_c on pressure and film thickness distribution. The graphs are plotted on lines $Y = 0$ (left column) and $X = 0$ (right column). The contact area increases for softer coatings. This phenomenon is amplified with coating thickness. Exact the opposite occurs for stiffer coatings with increasing coating thickness.

contact area has to decrease. Taking a more detailed look at the behaviour of minima film thicknesses, H_{min} and $H_{\text{min,central}}$ depicted in Figure 14(c), it is clear that over the whole range of coating stiffness the minimum film thickness increase slightly (less than 10%) with increasing coating stiffness. Obviously, stiffer coatings mean less deformation and thus slight increase in minimum film thickness.

Now taking a look at Figures 13(c)-13(f) we see that the aforementioned phenomena, i.e. higher pressure with increasing coating elasticity, are amplified with increasing coating thickness. To be more specific, we see that for elastic coatings (E_{c} =70GPa) the maximum pressure is further reduced with increasing coating thickness (see Figures 13(c) and 13(d)), while for stiff coatings (E_{c} =410GPa) the maximum pressure is further increased with increasing coating thickness (see Figures 13(e) and 13(f)). To elaborate a bit on this, if we have a really elastic coating, for example E_{c}=70GPa, and we decrease the thickness of this coating, the influence of the stiff substrate (E_{s}=210GPa) increases. This means that there will be less deformation, i.e. the contact area decreases, thus the pressure will increase. Exactly the opposite occurs when considering a very stiff coating (e.g.E_{c} =410GPa).

In line with previous findings, for coated contacts we also see that for more elastic coatings the lubricated contact area is increased. This effect is further amplified with increasing coating thickness. The same also applies for increasing contact force, i.e. the lubricated contact area is also expanded with increasing load. Careful attention should be paid when dealing with elastic and thick coatings and high loads, in terms of minimum film thickness H_{min}, as all three aforementioned factors lead to an increase in contact area. From Figure 14(b) it is clear that at relatively high loads the ratio $H_{\text{min}}/H_{\text{min,central}}$ dramatically decreases. This is mainly due to the fact that at the rear of the contact the pressure distribution does not have sufficient space to expand, and thus the secondary pressure peak again grows in magnitude. Consequently, pressure gradients at the extremities increase and thus will the minimum film thickness H_{min} decrease. The influence of coating thickness, for elastic and stiff coatings, on H_{min} and $H_{\text{min,central}}$, are depicted in Figure 14(a). At first sight it can readily be concluded that the trends of minimum film thicknesses, for soft and stiff coatings respectively, are opposite. In fact, for soft coatings the minimum film thicknesses increase with increasing coating thickness, while for hard coatings the minimum film thicknesses slightly decrease with increasing coating thickness. This behaviour is not as expected as we saw that the minimum film thicknesses increased with increasing coating stiffness (refer to Figure 14(c) again). One would expect that for example, given coating which is harder than the substrate, the minimum film thickness would increase if the coating thickness is increased. Again, as can be extracted from Figure 14(a), this is not true due to the fact that when coating thickness is increased the behaviour of the minima film thicknesses are more likely governed by the pressure gradients ($\frac{dP}{dX}$ and $\frac{dP}{dY}$) at the exits as per flow continuity

demand. Meaning that for hard coatings the pressure gradients increase with increasing coating thickness, resulting to a decrease in film thickness. Similarly, for more elastic coatings the pressure gradients decrease with increasing coating thickness resulting to an increase in minimum film thicknesses.

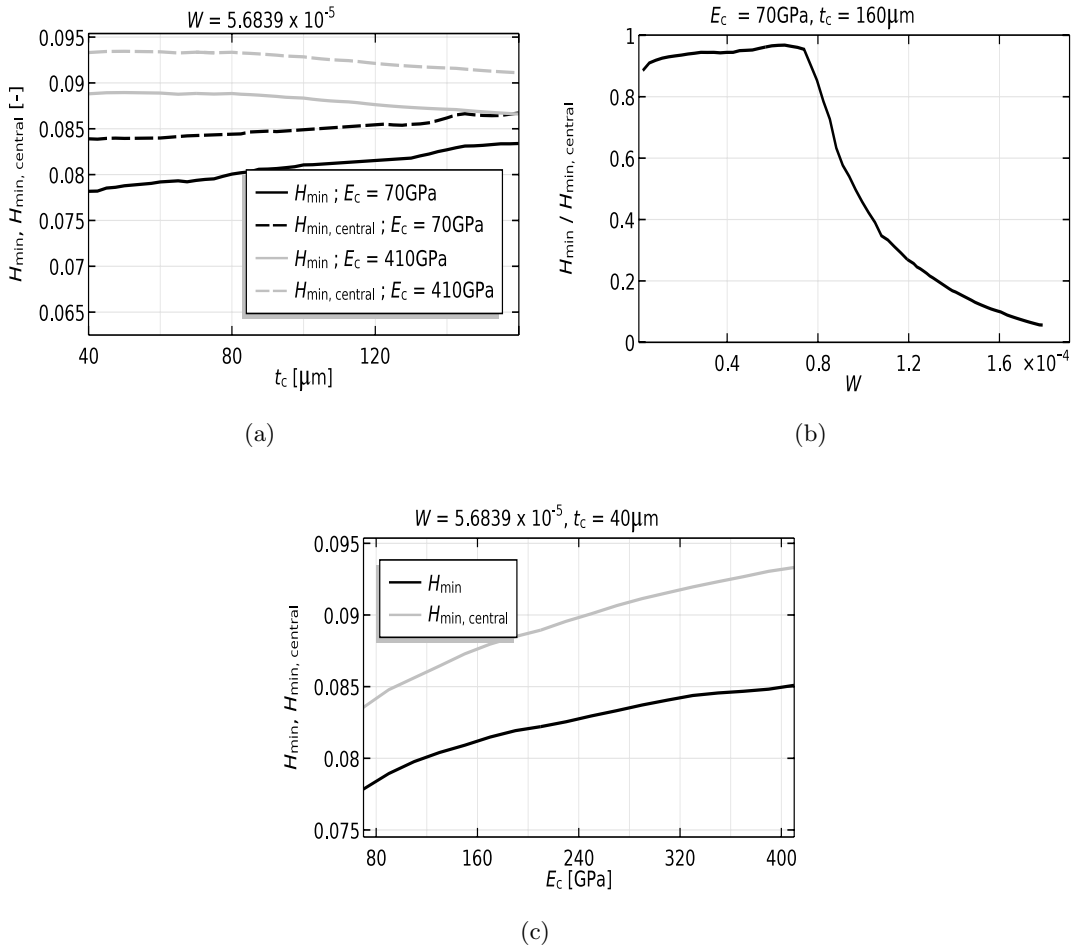

FIGURE 14: Influence of a) coating thickness t_c, b) dimensionless load parameter $\bar{W}$ and c) coating elasticity on minima film thicknesses.

4 Conclusions

In the present work a FEM-based coated finite line contact model was developed. The lubricated conjunction between a roller with rounded edges on a plate was analysed. The developed model was quantitatively validated by means of representative results reported in literature. Good agreement between the results was obtained.
Parameter studies were carried out to investigate the influence of operating conditions, geometrical parameters (of axial surface profile) and coating mechanical properties on the overall EHL behaviour of the contact. In line with previously reported findings, it

is shown that the pressure and film thickness distributions for finite line contacts vary significantly different with applied load as compared to infinite line contact models. At increasing loads the pressure distribution becomes more uniform in axial direction as long as there is space available for contact area expansion. When no space is left to compensate for higher loads, the secondary pressure peak at the extremities grows again and hence the absolute minimum film thickness decreases as per flow continuity demand. Large round corner radii, large straight roller lengths, too elastic and thick coatings, all amplify the effect of increasing loads, i.e. the pressure profile expands in all cases to compensate for the applied load. When no space is left to compensate for higher loads, the secondary pressure peak at the extremities grows again and hence the absolute minimum film thickness decreases.
All these findings make it really hard to develop a robust correlation between absolute minimum film thickness, maximum pressure and operating conditions, as coating and axial profile geometrical parameters play an equally important role. The present results certainly contribute to a better understanding of lubricated and coated finite line contacts. This model can effectively be used for improved designs of finite line contact applications in terms of film thickness and pressure distributions, and thus ultimately, contributing to longer service life of the components.

Acknowledgements

This research was carried out under project number F21.1.13502 in the framework of the Partnership Program of the Materials innovation institute M2i (www.m2i.nl) and the Netherlands Organization for Scientific Research (www.nwo.nl).

References

[1] S. Alakhramsing, R. van Ostayen, and R. Eling. Thermo-hydrodynamic analysis of a plain journal bearing on the basis of a new mass conserving cavitation algorithm. *Lubricants*, 3(2):256–280, 2015.

[2] A. Bennett and G. Higginson. Hydrodynamic lubrication of soft solids. *Journal of Mechanical Engineering Science*, 12(3):218–222, 1970.

[3] S. Chippa and M. Sarangi. Elastohydrodynamically lubricated finite line contact with couple stress fluids. *Tribology International*, 67:11–20, 2013.

[4] R. Codina. A discontinuity-capturing crosswind-dissipation for the finite element solution of the convection-diffusion equation. *Computer Methods in Applied Mechanics and Engineering*, 110(3):325–342, 1993.

[5] COMSOL multiphysics. Comsol multiphysics modeling guide. *COMSOL Inc.*, www.comsol.com. (accessed 3 April 2017).

[6] E. Do Carmo and A. Galeão. Feedback petrov-galerkin methods for convection-dominated problems. *Computer Methods in Applied Mechanics and Engineering*, 88(1):1–16, 1991.

[7] D. Dowson and G. Higginson. *Elasto-hydrodynamic lubrication: the fundamentals of roller and gear lubrication*, volume 23. Pergamon Press, Oxford, United Kingdom, 1966.

[8] A. Elsharkawy and B. Hamrock. EHL of coated surfaces: Part I: Newtonian results. *Journal of Tribology*, 116(1):29–36, 1994.

[9] A. Elsharkawy, M. Holmes, H. Evans, and R. Snidle. Micro-elastohydrodynamic lubrication of coated cylinders using coupled differential deflection method. *Proceedings of the Institution of Mechanical Engineers, Part J: Journal of Engineering Tribology*, 220(1):29–41, 2006.

[10] A. Galeão, R. Almeida, S. Malta, and A. Loula. Finite element analysis of convection dominated reaction–diffusion problems. *Applied Numerical Mathematics*, 48(2):205–222, 2004.

[11] R. Gohar and A. Cameron. The mapping of elastohydrodynamic contacts. *ASLE Transactions*, 10(3):215–225, 1967.

[12] W. Habchi. A numerical model for the solution of thermal elastohydrodynamic lubrication in coated circular contacts. *Tribology International*, 73:57–68, 2014.

[13] W. Habchi, D. Eyheramendy, P. Vergne, and G. Morales-Espejel. A full-system approach of the elastohydrodynamic line/point contact problem. *Journal of Tribology*, 130(2):021501, 2008.

[14] M. Heydari and R. Gohar. The influence of axial profile on pressure distribution in radially loaded rollers. *Journal of Mechanical Engineering Science*, 21(6):381–388, 1979.

[15] M. Kushwaha, H. Rahnejat, and R. Gohar. Aligned and misaligned contacts of rollers to races in elastohydrodynamic finite line conjunctions. *Proceedings of the Institution of Mechanical Engineers, Part C: Journal of Mechanical Engineering Science*, 216(11):1051–1070, 2002.

[16] A. Mostofi and R. Gohar. Elastohydrodynamic lubrication of finite line contacts. *Journal of Tribology*, 105(4):598–604, 1983.

[17] T.-J. Park and K.-W. Kim. A numerical analysis of the elastohydrodynamic lubrication of elliptical contacts. *Wear*, 136(2):299–312, 1990.

[18] T.-J. Park and K.-W. Kim. Elastohydrodynamic lubrication of a finite line contact. *Wear*, 223(1):102–109, 1998.

[19] C. Roelands. *Correlational aspects of the viscosity-temperature-pressure relationship of lubricating oils*. PhD thesis, Delft University of Technology, Delft, The Netherlands, 1966.

[20] M. Shirzadegan, A. Almqvist, and R. Larsson. Fully coupled EHL model for simulation of finite length line cam-roller follower contacts. *Tribology International*, 103:584–598, 2016.

[21] S. Wu. A penalty formulation and numerical approximation of the reynolds-hertz problem of elastohydrodynamic lubrication. *International Journal of Engineering Science*, 24(6):1001–1013, 1986.

[22] D. Wymer and A. Cameron. EHL lubrication of a line contact. Part 1: Optical analysis of a roller bearing. *Proc. Instn. Mech. Engrs*, 188, 1974.

[23] D. Wymer and A. Cameron. Elastohydrodynamic lubrication of a line contact. *Proceedings of the Institution of Mechanical Engineers*, 188(1):221–238, 1974.

Paper B

Lubrication and frictional analysis of cam-roller follower mechanisms

S.S. Alakhramsing[1], M.B. de Rooij[1], M. van Drogen[2] and D.J. Schipper[1]

Proceedings of the Institution of Mechanical Engineers, Part J: Journal of Engineering Tribology, 232 (3), 347-363, 2018.
DOI:10.1177/1350650117718083

[1]Faculty of Engineering Technology, University of Twente, P.O. Box 217, 7500 AE Enschede, The Netherlands
[2]Central Laboratory Metals, DAF Trucks N.V., P.O. Box 90065, 5600 PT Eindhoven, The Netherlands

Nomenclature

a Hertzian contact half-width (m)

A roller crowning curvature (m)

C radial clearance (m)

C_U dimensionless variation of mean entrainment velocity

C_F dimensionless variation of contact force

C_R dimensionless variation of reduced radius of curvature

D pin diameter (m)

D_{plunger} plunger diameter (m)

e roller eccentricity (m)

E_{eq} equivalent Young's modulus of elasticity (Pa)

$\tilde{E}_{\text{eq}}$ dimensionless equivalent Young's modulus of elasticity (-)

E' reduced elasticity modulus (Pa)

f kinematic coefficient (m)

F force (N)

g axial surface profile function (m)

G dimensionless axial surface profile function

h film thickness (m)

H dimensionless film thickness

h_0 rigid body displacement (m)

H_0 dimensionless rigid body displacement

I roller inertia (kg.m^2)

k_s spring stiffness (N/m)

l vertical displacement of follower (m)

L roller axial length (m)

L_s roller straight length (m)

m mass (kg)

p pressure (Pa)

P dimensionless pressure

p_h Hertzian pressure (Pa)

q horizontal offset of reciprocating follower (m)

R_x reduced radius of curvature (m)

R_pin pin radius (m)

R_f outer radius roller (m)

R_b base circle radius (m)

R_1 length of vector $\overrightarrow{R}_1$ (m)

S Sommerfeld number(-)

u, v, w x, y and z-components of the solid's elastic deformation field (m)

U, V, W dimensionless x, y and z-components of the solid's elastic deformation field

U_cam cam surface velocity (m/s)

U_roller roller surface velocity (m/s)

U_m lubricant mean entrainment velocity (m/s)

x, y, z spatial coordinates (m)

X, Y, Z dimensionless spatial coordinates

$x_\mathrm{fc}, y_\mathrm{fc}$ relative coordinates of follower centre (m)

$X_\mathrm{fc}, Y_\mathrm{fc}$ global coordinates of follower centre (m)

$x_\mathrm{c}, y_\mathrm{c}$ relative coordinates of point of contact (m)

X_c, Y_c global coordinates of point of contact (m)

z_d roller crown drop (m)

α pressure-viscosity coefficient (GPa^{-1})

η lubricant viscosity (Pa·s)

η_0 lubricant reference viscosity (Pa·s)

$\tilde{\eta}$ lubricant dimensionless viscosity

θ cam angle (rad)

θ_p pressure angle (rad)

μ_1 friction coefficient cam-roller interface(-)

μ_2 friction coefficient roller-pin interface(-)

μ_0 limiting traction coefficient of lubricant

ρ lubricant density (kg/m^3)

ρ_0 lubricant reference density (kg/m^3)

$\tilde{\rho}$ lubricant dimensionless viscosity

ν Poisson ratio (-)

ν_{eq} equivalent Poisson ratio (-)

ϕ_1 direction of vector $\overrightarrow{R}_1$ (rad)

ω rotational speed (rad/s)

Ω computational domain

Ω_f contact boundary

Ω_D bottom boundary

Ω_s symmetry boundary

Subscripts

eq equivalent

f follower

fc follower centre

FIP fuel injection pump

min minimum

r rolling

ref reference

s sliding

t tappet

v valve train

Lubrication and frictional analysis of cam-roller follower mechanisms

Abstract

In this work a full numerical solution to the cam-roller follower lubricated contact is provided. The general framework of this model is based on a model describing the kinematics, a finite length line contact isothermal-EHL model for the cam-roller contact and a semi-analytical lubrication model for the roller-pin bearing. These models are interlinked via an improved roller-pin friction model. For the numerical study a cam-roller follower pair, as part of the fuel injection system in Diesel engines, was analysed. The results, including the evolution of power losses, minimum film thickness and maximum pressures, are compared with analytical solutions corresponding to infinite line contact models. Main findings of this work are that for accurate prediction of crucial performance indicators such as minimum film thickness, maximum pressure and power losses a finite length line contact analysis is necessary due to non-typical EHL characteristics of the pressure and film thickness distributions. Furthermore, due to the high contact forces associated with cam-roller pairs as part of fuel injection units, rolling friction is the dominant power loss contributor as roller slippage appears to be negligible. Finally, the influence of the different roller axial surface profiles on minimum film thickness, maximum pressure and power loss is shown to be significant. In fact, due to larger contact area the maximum pressure can be reduced and the minimum film thickness can be increased significantly, however at the cost of higher power losses.

Keywords: EHL, cam-roller, finite line contacts, roller slippage

1 Introduction

Design of the injection cams in heavy duty Diesel engines is from a tribological perspective one the most challenging technical tasks as these components are subjected to instantaneous heavily loaded pressures from the fuel injector. Lubrication is of significant importance to reduce friction and wear. Apart from the high fluctuating loads, varying radius of curvature and lubricant entrainment speed make the tribological design even more challenging.

The preference of roller followers over sliding followers is more often made by engine manufactures due to reduced friction losses and occurrence of wear [19]. As reported by Lee and Patterson [17], the problem of wear on the interacting surfaces still remains if slip occurs. Furthermore, accurate estimation of friction losses depends to a large extend on the sliding velocity. In contrast to a cam and sliding follower, the slide-to-roll ratio (SRR) for the cam and roller follower is additionally also dependent on the lubricant rheology and friction at the roller-pin interface. Most previous studies assumed pure rolling conditions (see for instance [10, 18, 2]), i.e. the cam and roller surface speed are assumed to be equal. One may only find a few published studies on the lubrication analysis of the cam and roller follower contact that consider the possibility of roller slippage along the cam surface. Chiu [1] and later Ji and Taylor [13] developed a theoretical roller friction model from which they concluded that slippage exists, especially at high cam rotational speeds due to large inertia forces. The occurrence of roller slippage has also been proven experimentally [14].

Axial surface profiling of the rollers is often utilized to minimize stress concentrations that are generated at the extremities of the contact. It has been proven both theoretically and experimentally that the maximum pressure and minimum film thickness occur near the regions where axial profiling starts [29, 20, 16]. Disregarding axial surface profiling, as assumed in traditional infinite line contact models, may lead to inaccurate estimation of crucial lubrication performance indicators such as the minimum film thickness and maximum pressure. Consequently, frictional losses may also deviate significantly from reality as these are dependent on the film thickness and pressure distribution.

Finite line contact models would therefore be more appropriate to describe the EHL behaviour of the contact. Finite line contact problems of cam and flat faced follower conjunctions have been studied in the past, see for instance [15, 26]. Shirzadegan et al. [25] studied the finite line contact problem of a cam-roller follower. However, roller slippage was disregarded in their analysis and no results concerning the working frictional losses at the lubricated interfaces were presented. Turtorro et al. [27] also presented a cam-roller lubrication model which allows for roller slippage, however their solution for

the lubricant film thickness is obtained using analytical expressions rather than solving the Reynolds equations.

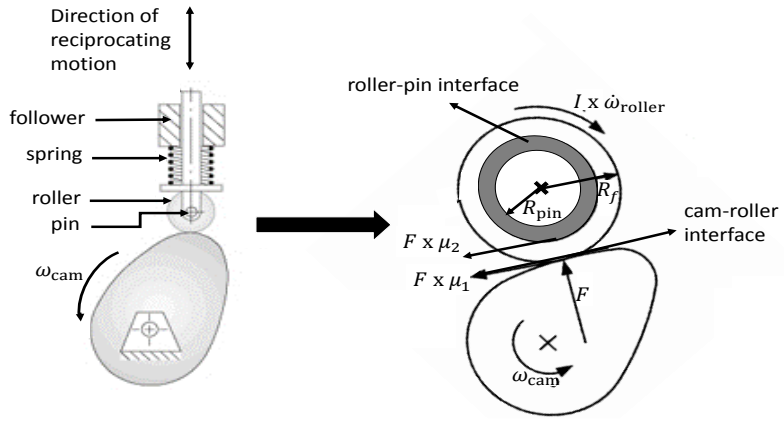

FIGURE 1: Cam and roller follower configuration with an emphasis on frictional forces acting at the cam-roller and roller-pin interface.

From the previously mentioned studies it may be concluded that up till date a limited number of studies concerning the lubrication analysis of cam-roller followers based on a full numerical solution, i.e. taking into account non-typical EHL characteristics of the finite length line contact and possible roller slippage, have been presented. However, the approach followed in the aforementioned studies can be applied to perform more in-depth investigations into the frictional behaviour of cam-roller follower mechanisms. Therefore in this paper a FEM-based lubrication model, applicable to any cam-roller follower system, is developed. In the present study we assume that thermal effects are insignificant and therefore isothermal conditions are assumed. The finite line contact EHL model is similar to the one presented in [25], which efficiently takes care of roller axial surface profiling. An improved roller friction model, to determine roller slippage, is presented. In contrast to previous models, the presented roller friction model also takes into account the film thickness distribution in the roller-pin bearing. For the numerical analysis, a cam-roller follower unit as part of the fuel injection equipment of a Diesel engine, was considered. The results analysed, are the evolution of the minimum film thickness, maximum pressure, individual frictional losses and roller slippage along the cam surface. Furthermore, the influence of different roller axial surface profiles on the aforementioned variables is analysed.

2 Mathematical model

The type of configuration considered in this work is that of a cam and reciprocating roller follower, in which the roller is free to rotate due to traction enforced by the cam. The roller is supported by a "low-friction" hydrodynamic bearing. The considered configuration, with an emphasis on the working frictional forces at the lubricated interfaces, is presented in Figure 1. The lubricated interfaces in the configuration are separately defined as cam-roller interface and roller-pin interface for the sake of distinctness.
In the first part of this section a kinematic analysis for the considered configuration is presented. The kinematic analysis provides input, in terms of reduced radius of curvature, entrainment velocity and normal contact force variations, that enters the EHL calculations. The second part presents the governing EHL equations to describe the tribological behaviour in the cam-roller contact. The third part provides details concerning the individual evaluation of frictional losses, due to hydrodynamic rolling and sliding at cam-roller and roller-pin interfaces. Finally, the last part of this section treats the roller slippage calculation.

2.1 Kinematic analysis

The kinematic model adopted in this work stems from Matthews et al. [18] who developed a general procedure to derive the variations in reduced radius of curvature and entrainment velocity for several types of cam-follower configurations. For this reason only the main equations are presented and for details the reader is referred to [18]. Figure 2 shows the cam and reciprocating follower configuration along with nomenclature, coordinate system and angles.

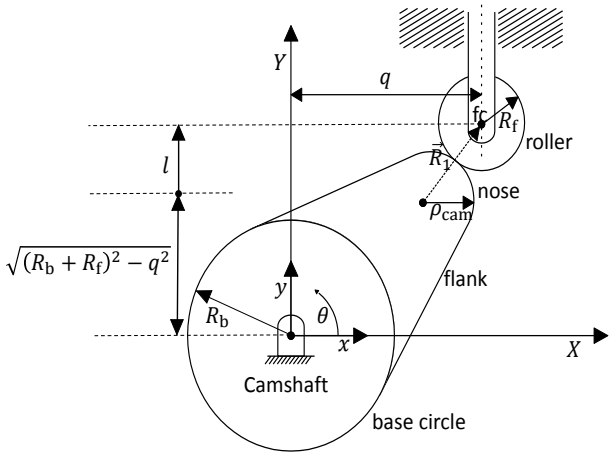

FIGURE 2: Cam and roller follower configuration with specification of coordinate system and nomenclature.

The kinematic analysis of the cam and reciprocating roller follower mechanism requires the lift curve $l(\theta)$, outer radius of roller R_f and global position of cam and follower as input. Note that subscripts "f " and "fc" denote follower and follower centre respectively. The lift curve $l(\theta)$ illustrates the vertical displacement of the roller follower centre as depicted in Figure 2.

With global position (X, Y) is meant the centre position of cam and follower in a coordinate system where the origin is fixed to the ground. However, commonly a relative coordinate system (x, y), where the coordinate system is fixed to the camshaft, is used to derive the instantaneous radius of curvature. Transformation from the global coordinate system to the relative coordinate system, or vice versa, can be made using:

$$\begin{bmatrix} x \\ y \end{bmatrix} = \begin{bmatrix} \cos\theta & \sin\theta \\ -\sin\theta & \cos\theta \end{bmatrix} \begin{bmatrix} X \\ Y \end{bmatrix} \tag{1a}$$

$$\begin{bmatrix} X \\ Y \end{bmatrix} = \begin{bmatrix} \cos\theta & -\sin\theta \\ \sin\theta & \cos\theta \end{bmatrix} \begin{bmatrix} x \\ y \end{bmatrix} \tag{1b}$$

Note that angles are measured positive in counterclockwise direction. As mentioned earlier the lift curve $l(\theta)$ is needed as input for derivation [1] of the kinematic variations. In the equations presented hereafter, the angle (θ) after the dependent variables are omitted for the sake of brevity.

The global coordinates of the roller follower centre (X_{fc},Y_{fc}) are given as:

$$\begin{cases} X_{\mathrm{fc}} = q \\ Y_{\mathrm{fc}} = \sqrt{(R_{\mathrm{b}} + R_{\mathrm{f}})^2 - q^2} + l \end{cases} \tag{2}$$

where R_{b} is the base circle radius and q is the horizontal offset of reciprocating follower.

Calculation of cam radius of curvature

From mathematics we know that the radius of curvature ρ at a certain point, that moves along a path in the relative frame (x, y), can be computed as follows:

$$\rho = \frac{f^3}{f_y f'_x - f_x f'_y} \tag{3}$$

[1] The lift curve $l(\theta)$ and fuel pressure $P_{\mathrm{fuel}}(\theta)$ profile are specified in n data points. These data points are (usually) measured values with increments of a specified angle (usually less than one degree cam angle). The smaller this increment the higher the resolution of the profile and hence accuracy of solution. The n data points are spline-interpolated with respect to cam angle, i.e. the discrete displacement profile is interpolated to obtain a third-order piecewise continuous polynomial fit for displacement versus cam angle. The derivatives of this polynomial fit will give the velocity and acceleration profiles. A similar procedure was applied to deduce the contact force profile.

where the kinematic coefficients f, f_x, f_y, $f_x^{'}$ and $f_y^{'}$ are calculated as follows:

$$\begin{cases} f_x = \dfrac{dx}{d\theta} = \dfrac{dX}{d\theta}\cos\theta - X\sin\theta + \dfrac{dY}{d\theta}\sin\theta + Y\cos\theta \\ f_y = \dfrac{dy}{d\theta} = -\dfrac{dX}{d\theta}\sin\theta - X\cos\theta + \dfrac{dY}{d\theta}\cos\theta - Y\sin\theta \\ f_x^{'} = \dfrac{d^2x}{d\theta^2} = \dfrac{d^2X}{d\theta^2}\cos\theta + \dfrac{d^2Y}{d\theta^2}\sin\theta - 2\dfrac{dX}{d\theta}\sin\theta \\ \qquad\qquad + 2\dfrac{dY}{d\theta}\cos\theta - X\cos\theta - Y\sin\theta \\ f_y^{'} = \dfrac{d^2y}{d\theta^2} = -\dfrac{d^2X}{d\theta^2}\sin\theta + \dfrac{d^2Y}{d\theta^2}\cos\theta - 2\dfrac{dX}{d\theta}\cos\theta \\ \qquad\qquad - 2\dfrac{dY}{d\theta}\sin\theta + X\sin\theta - Y\cos\theta \\ f = \sqrt{f_x^2 + f_y^2} \end{cases} \tag{4}$$

Now, substituting the expressions for the roller follower centre (eq. 2) for the above defined kinematic coefficients, and then again substituting in the expression for calculation of the radius of curvature eq. 3 gives the instantaneous cam radius of curvature:

$$\rho_{\text{cam}} = \frac{f_{\text{fc}}^3}{f_{y,\text{fc}} f_{x,\text{fc}}^{'} - f_{x,\text{fc}} f_{y,\text{fc}}^{'}} - R_f \tag{5}$$

The equivalent radius of curvature R_x that enters the EHL calculations is then calculated as follows:

$$R_x = \left(\frac{1}{\rho_{\text{cam}}} + \frac{1}{R_{\text{f}}}\right)^{-1} \tag{6}$$

Calculation of cam surface velocity

The mean entraining velocity of lubricant, that enters the EHL calculations is calculated as follows:

$$U_{\text{m}} = \frac{U_{\text{cam}} + U_{\text{roller}}}{2} \tag{7}$$

where the surface velocities of cam U_{cam} needs to be evaluated from the kinematic analysis and is dependent on the cam radius of curvature ρ_{cam} and cam rotational speed ω_{cam}. The roller follower surface velocity U_{roller} depends on traction caused by the cam. The calculation of U_{roller} is treated in the next subsection.

Vector $\overrightarrow{R}_1$, in Figure 2, can be interpreted as an imaginary link between the point of contact (X_{c},Y_{c}) and centre of the roller follower (X_{fc},Y_{fc}). At this point it is worth noting that vector $\overrightarrow{R}_1$ always passes the point of contact and therefore the point of contact itself has no relative motion to vector $\overrightarrow{R}_1$. Therefore the velocity of a point on the cam surface, relative to the point of contact is actually equal to the velocity of that same

point relative to vector $\overrightarrow{R}_1$. In equation form this yields:

$$U_{\text{cam}} = \rho_{\text{cam}}\,\omega_{\text{cam}}\,(1 - h_1) \tag{8}$$

where the kinematic coefficient h_1 denotes the variation of the direction of vector $\overrightarrow{R}_1$ and is thus computed as follows:

$$h_1 = \frac{d\phi_1}{d\theta} \tag{9}$$

where the direction of vector $\overrightarrow{R}_1$, ϕ_1, is computed as follows:

$$\phi_1 = \tan\left(\frac{Y_{\text{fc}} - Y_{\text{c}}}{X_{\text{fc}} - X_{\text{c}}}\right)^{-1} \tag{10}$$

The point of contact (x_{c},y_{c}), in the relative coordinate system, is given by:

$$\begin{cases} x_{\text{c}} = x_{\text{fc}} + R_f \dfrac{f_{y,\text{fc}}}{f_{\text{fc}}} \\ y_{\text{c}} = y_{\text{fc}} - R_f \dfrac{f_{x,\text{fc}}}{f_{\text{fc}}} \end{cases} \tag{11}$$

where relative coordinates $(x_{\text{fc}}, y_{\text{fc}})$ are deduced by transforming the global coordinates $(X_{\text{fc}}, Y_{\text{fc}})$ according to eq. 1a. The global coordinates of the point of contact $(X_{\text{c}}, Y_{\text{c}})$ can then be obtained by transforming eq. 11 by means of eq. 1b.
Similar to eq. 8, the roller surface speed can be computed as follows:

$$U_{\text{roller}} = -R_f\,\omega_{\text{cam}}\left(\frac{\omega_{\text{roller}}}{\omega_{\text{cam}}} - h_1\right) \tag{12}$$

The calculation of the angular velocity of the roller ω_{roller} will be treated later on in this section.

Calculation of normal contact force

The contact force associated with the cam-follower pair is typically the resultant of inertia forces, caused by moving parts, and the spring force. In the present work we consider the operating conditions of cam-roller follower pairs in fuel injection pumps (FIP) of heavy duty Diesel engines. These pumps are used to generate high fuel pressures for injection. So, in addition to inertia and spring forces, the injection force acting on the plunger also needs to be considered.
In order to simplify the analysis a few realistic assumptions are made. These are: i) the complete tappet including roller, pin, spring, plunger etc. is considered as a single moving mass, ii) each individual component is considered as a single lumped mass, iii) the rotational velocity of the pump is constant and is also not affected by fluctuations of

engine strokes, iv) the moving mass of the spring is assumed to be a third of its mass [30], v) the spring stiffness is linear and finally, vi) there is no offset and/or eccentricity of the cam to the centre of the roller.
With these simplifications the total acting force is computed as follows:

$$F_{\text{total}} = \underbrace{F_{\text{FIP}}}_{\text{hydraulic force}} + \underbrace{F_0}_{\text{pre-load}} + \underbrace{F_{\text{s}}}_{\text{spring force}} + \underbrace{F_{\text{i}}}_{\text{inertia force}} \tag{13}$$

where the individual forces are calculated as:

$$\begin{cases} F_{\text{FIP}} = \frac{P_{\text{fuel}}}{A_{\text{plunger}}} = \frac{4P_{\text{fuel}}}{\pi D^2_{\text{plunger}}} \\ F_0 = \text{constant} \\ F_{\text{s}} = k_{\text{s}} l \\ F_{\text{i}} = m_{\text{eq}} \omega^2_{\text{cam}} \frac{d^2 l}{d\theta^2} = \left(\frac{m_{\text{s}}}{3} + m_{\text{T}} + m_{\text{v}}\right) \omega^2_{\text{cam}} \frac{d^2 l}{d\theta^2} \end{cases} \tag{14}$$

where k_{s}, D_{plunger}, m_{s}, m_{T}, m_{v} are the spring stiffness, plunger diameter, spring mass, tappet mass and valve train mass respectively.
For the cam and roller follower configuration the pressure angle θ_P is an important design parameter as it limits the steepness of the cam in the design process. The pressure angle is defined as the angle between the direction of axis transmission and direction of motion of the follower. The pressure angle is calculated as follows:

$$\theta_P = \tan\left(\frac{X_{\text{fc}} - X_{\text{c}}}{Y_{\text{fc}} - Y_{\text{c}}}\right)^{-1} \tag{15}$$

The actual acting normal contact force, that enters the EHL calculations, is then computed as follows:

$$F = F_{\text{total}} \cos\theta_P \tag{16}$$

2.2 Governing EHL equations for cam-roller contact

As mentioned earlier, the EHL model here is similar to that presented by Shirzadegan et al. [25]. The model leans on a full-system finite element resolution of the EHL equations. In this work only the main equations are recalled and for more details the reader is referred to [25]. All EHL equations are presented in dimensionless form. Hence, the

following (dimensionless) variables and parameters are introduced:

$$
\begin{aligned}
X &= \frac{x}{a_{\mathrm{ref}}} & Y &= \frac{y}{2L} & Z &= \frac{z}{a_{\mathrm{ref}}} & P &= \frac{p}{p_{\mathrm{h}}} \\
\tilde{\eta} &= \frac{\eta}{\eta_0} & \tilde{\rho} &= \frac{\rho}{\rho_0} & H &= \frac{hR_{\mathrm{ref}}}{a_{\mathrm{ref}}^2} & H_0 &= \frac{h_0 R_{\mathrm{ref}}}{a_{\mathrm{ref}}^2} \\
C_R(\theta) &= \frac{R_x(\theta)}{R_{\mathrm{ref}}} & C_U(\theta) &= \frac{U_{\mathrm{m}}(\theta)}{U_{\mathrm{ref}}} & C_F(\theta) &= \frac{F(\theta)}{F_{\mathrm{ref}}} & U &= \frac{uR_{\mathrm{ref}}}{a_{\mathrm{ref}}^2} \\
V &= \frac{vR_{\mathrm{ref}}}{a_{\mathrm{ref}}^2} & W &= \frac{wR_{\mathrm{ref}}}{a_{\mathrm{ref}}^2} & G &= \frac{gR_{\mathrm{ref}}}{a_{\mathrm{ref}}^2}
\end{aligned}
\tag{17}
$$

with Hertzian parameters defined as follows:

$$
\begin{aligned}
p_{\mathrm{h}} &= \frac{2F_{\mathrm{ref}}}{\pi L a_{\mathrm{ref}}} & a_{\mathrm{ref}} &= \sqrt{\frac{8F_{\mathrm{ref}}R_{\mathrm{ref}}}{\pi L E'}} \\
E' &= \frac{2}{\frac{1-\nu_{\mathrm{cam}}^2}{E_{\mathrm{cam}}} + \frac{1-\nu_{\mathrm{roller}}^2}{E_{\mathrm{roller}}}}
\end{aligned}
\tag{18}
$$

where the subscript "ref" denotes the reference operating conditions. Figure 3 gives the equivalent computational domain for the finite line contact problem. Ω denotes the finite elastic domain for calculation of the displacement fields. The dimensions of 60 x 60 x 2 are chosen in such a way to mimic a half-space for calculation of the elastic displacement field. Boundary Ω_f, with dimensions of $-4.5 \leq X \leq 1.5$ and $-1 \leq Y \leq 1$, stands for the fluid film domain used to solve for the pressure distribution by means of the Reynolds equation. Finally, Ω_D denotes the bottom boundary of the finite elastic domain.

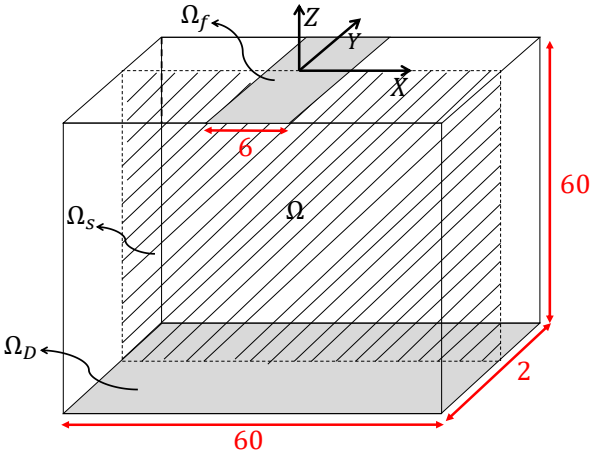

FIGURE 3: Equivalent geometry for EHL analysis of the finite line contact problem. Note that the dimensions are exaggerated for the sake of clarity.

Reynolds equation

The dimensionless Reynolds equation is written as follows:

$$\frac{\partial}{\partial X}\left(-\frac{\tilde{\rho}H^3}{\tilde{\eta}\lambda}\frac{\partial P}{\partial X}+C_U(\theta)H\tilde{\rho}\right)+\frac{\partial}{\partial Y}\left(-\frac{a_{\mathrm{ref}}^2}{(2L)^2}\frac{\tilde{\rho}H^3}{\tilde{\eta}\lambda}\frac{\partial P}{\partial Y}\right)+\frac{a_{\mathrm{ref}}\omega_{\mathrm{cam}}}{U_{\mathrm{ref}}}\frac{\partial H\tilde{\rho}}{\partial\theta}=0 \quad (19)$$

where, $\lambda=\frac{12U_{\mathrm{ref}}\eta_0R_x^2}{a^3p_{\mathrm{h}}}$ is the dimensionless speed parameter, and $\tilde{\rho}$ and $\tilde{\eta}$ are the dimensionless density and viscosity respectively. $C_U(\theta)$ represents the variation of the mean entrainment velocity U_{m} (see eq. 7). Variation of viscosity and density with pressure are modelled according to the Roelands [23] and Dowson-Higginson [7] equations respectively. The free boundary cavitation problem, arising at the exit of the lubricated contact, is treated according to the penalty formulation of Wu [28]. In the latter an auxiliary/penalty term is added to the Reynolds equation to force all negative pressure to zero. It should be mentioned that this term has no influence on regions where $P\geq 0$ and thus consistency of eq. 19 is preserved. Wu [28] also showed that the so-called Reynolds boundary conditions, i.e. $\nabla P\cdot\overrightarrow{n}_c=0$ on the cavitation boundary, is automatically satisfied with this approach. $\overrightarrow{n}_c$ is the outlet normal vector to the cavitation boundary.

A combination of non-residual and residual based "artificial diffusion" terms, as detailed in [12], were added to the weak formulation of eq. 19 in order to stabilize the solution at high loads.

Finally, it is assumed that the inlet of the contact is fully flooded and the surface roughness is small enough to be disregarded (smooth surfaces are assumed).

Film thickness expression

The film thickness expression H for a general finite line contact problem may be written as follows:

$$H\left(X,Y,\theta\right)=H_0\left(\theta\right)+\frac{X^2}{2C_R(\theta)}+G(Y,\theta)-W\left(X,Y,\theta\right) \quad (20)$$

where H_0 is the rigid body displacement and W is the contribution due to elastic deformation. $C_R(\theta)$ denotes the dimensionless variation of the reduced radius of curvature R_x (see eq. 6). $G(Y,\theta)$ can be any function to approximate the dimensionless geometrical variation of the axial surface profile. Numerical studies in the past, aiming to reduce edge effects due to the finite length, showed that the most favourable effect with respect to edge stress concentration reduction is obtained when the generatrix of the finite line contact corresponds to a logarithmic function. In the present study the logarithmic expression, as proposed by Fujiwara and Kawase [9] is adopted, and is written as follows:

$$g(y,\theta)=-A\ln\left\{1-\left[1-\exp\left(\frac{-\mathrm{z_m}}{\mathrm{A}}\right)\right]\left(\frac{2y-L_{\mathrm{s}}}{L-L_{\mathrm{s}}}\right)^2\right\} \quad (21)$$

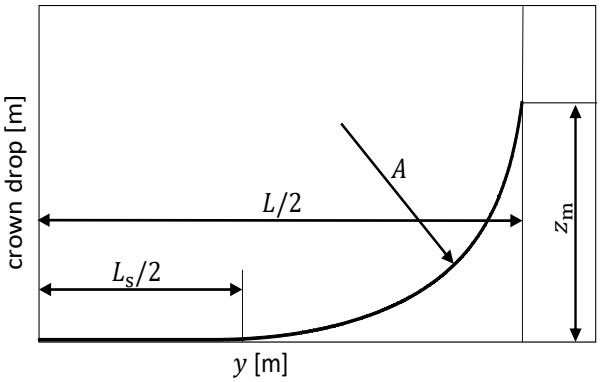

FIGURE 4: Roller axial profiling utilizing a logarithmic shape with defined design parameters straight length L_s, crown drop z_m and crowning curvature A.

Eq. 21 corresponds to Figure 4 in which A represents the degree of crowning curvature, z_m is the crown drop at the extremities and L_s is the straight roller length. These three parameters provide more flexibility in roller design. Note also that $g(y, \theta)$ is only valid for $\frac{L_s}{2} \leq y \leq \frac{L}{2}$, otherwise zero.

Load balance

H_0 is obtained by satisfying the conservation law that states that the applied load should be balanced by the hydrodynamically generated force. In equation form this can be written as follows:

$$\int_{\Omega_f} P\,(X, Y, \theta)\, d\Omega = \pi C_F(\theta) \tag{22}$$

where Ω_f denotes the fluid film domain (see Figure 3) and $C_F(\theta)$ stands for the dimensionless variation of contact force F (see eq. 16). Finally, if symmetry is used (with symmetrical plane Ω_s) the dimensionless pressure P should be multiplied by a factor of 2.

Calculation of elastic deformation

For the elastic deformation calculation we make use of the equivalent elasticity property as described in [12], i.e. two contacting material properties (E_1, ν_1) and (E_2, ν_2) can be reduced to a single component with equivalent material properties (E_{eq}, ν_{eq}). In fact, the (dimensionless) equivalent material properties are calculated as follows [12]:

$$\tilde{E}_{eq} = \frac{E_1^2 E_2 (1+\nu_2)^2 + E_2^2 E_1 (1+\nu_1)^2}{\left[E_1\,(1+\nu_2) + E_2\,(1+\nu_1)\right]^2} \frac{a_{ref}}{R_{ref} p_h} \tag{23a}$$

$$\nu_{eq} = \frac{E_1 \nu_2\,(1+\nu_2) + E_2 \nu_1\,(1+\nu_1)}{E_1\,(1+\nu_2) + E_1\,(1+\nu_2)} \tag{23b}$$

From eq. 24 it follows that the dimensionless (equivalent) Lamé's coefficients $\tilde{\mu}$ and $\tilde{\lambda}$ are respectively calculated as follows:

$$\tilde{\mu} = \frac{\tilde{E}_{\mathrm{eq}}}{2\left(1+\nu_{\mathrm{eq}}\right)} \tag{24a}$$

$$\tilde{\lambda} = \frac{\nu_{\mathrm{eq}\tilde{\mathrm{E}}_{\mathrm{eq}}}}{\left(1-2\nu_{\mathrm{eq}}\right)\left(1+\nu_{\mathrm{eq}}\right)} \tag{24b}$$

where ($\tilde{E}_{\mathrm{eq}}$,ν_{eq}) are calculated by means of eq. 23. The 3D-elasticity equations are applied to the dimensionless domain Ω to compute the total elastic deformation. The following system of equations is derived for calculation of the elastic displacement field [25]:

$$\begin{aligned}
&\frac{\partial}{\partial X}\left[\left(\tilde{\lambda}+2\tilde{\mu}\right)\frac{\partial U}{\partial X}+\psi\tilde{\lambda}\frac{\partial V}{\partial Y}+\tilde{\lambda}\frac{\partial W}{\partial Z}\right] \\
&\qquad +\psi\frac{\partial}{\partial Y}\left[\tilde{\mu}\left(\psi\frac{\partial U}{\partial Y}+\frac{\partial V}{\partial X}\right)\right]+\frac{\partial}{\partial Z}\left[\tilde{\mu}\left(\frac{\partial U}{\partial Z}+\frac{\partial W}{\partial X}\right)\right]=0, \\
&\frac{\partial}{\partial X}\left[\tilde{\mu}\left(\psi\frac{\partial U}{\partial Y}+\frac{\partial V}{\partial X}\right)\right]+\psi\frac{\partial}{\partial Y}\left[\tilde{\lambda}\frac{\partial U}{\partial X}+\psi\left(\tilde{\lambda}+2\tilde{\mu}\right)\frac{\partial V}{\partial Y}+\tilde{\lambda}\frac{\partial W}{\partial Z}\right] \\
&\qquad +\frac{\partial}{\partial Z}\left[\tilde{\mu}\left(\frac{\partial V}{\partial Z}+\psi\frac{\partial W}{\partial Y}\right)\right]=0, \\
&\frac{\partial}{\partial X}\left[\tilde{\mu}\left(\frac{\partial U}{\partial Z}+\frac{\partial W}{\partial X}\right)\right]+\psi\frac{\partial}{\partial Y}\left[\tilde{\mu}\left(\frac{\partial V}{\partial Z}+\psi\frac{\partial W}{\partial Y}\right)\right] \\
&\qquad +\frac{\partial}{\partial Z}\left[\tilde{\lambda}\frac{\partial U}{\partial X}+\psi\tilde{\lambda}\frac{\partial V}{\partial Y}+\left(\tilde{\lambda}+2\tilde{\mu}\right)\frac{\partial W}{\partial Z}\right]=0
\end{aligned} \tag{25}$$

where $\psi = a_{\mathrm{ref}}/2L$.

Boundary conditions

In order to obtain a unique solution for the EHL problem, proper boundary conditions (BCs) need to be imposed.
For the Reynolds equation these are summarized as follows:

$$\begin{cases} P=0 & \text{on } \partial\Omega_f \\ \nabla P\cdot \mathrm{n}=0 & \text{on } \Omega_s \end{cases} \tag{26}$$

Note that for the present analysis the advantage of symmetry of the problem (around symmetrical plane Ω_s) has been taken in order to reduce the computation effort required.

For the elastic model the BCs are summarized as follows:

$$\begin{cases} U_k = U = V = W = 0 \qquad \text{on } \Omega_D \\ \sigma_n = \sigma_{ZZ} = \\ \quad \left[\tilde{\lambda}\dfrac{\partial U}{\partial X} + \psi\tilde{\lambda}\dfrac{\partial V}{\partial Y} + \left(\tilde{\lambda} + 2\tilde{\mu}\right)\dfrac{\partial W}{\partial Z}\right] = -P \ \text{ on } \Omega_f \\ U_k \cdot n = V = 0 \qquad \text{on } \Omega_s \\ \sigma_n = 0 \qquad \text{elsewhere} \end{cases} \tag{27}$$

2.3 Friction loss evaluation

The three most important friction related issues in a cam and roller follower configuration, assuming perfectly smooth surfaces, are: i) occurrence of roller slippage, resulting in high friction, ii) the EHL rolling friction that becomes increasingly important for lower degrees of slide-to-roll ratios, and iii) roller-pin bearing friction. The three aforementioned friction contributors are inter-related.

The total frictional force, acting at the cam-roller interface, consists thus of a sliding and rolling component which are calculated as follows:

$$F_s = \frac{2L\eta_0 R_{\text{ref}}}{a_{\text{ref}}} \int_{\Omega_f} \frac{\tilde{\eta}\left(U_{\text{roller}} - U_{\text{cam}}\right)}{H} d\Omega \tag{28a}$$

$$F_r = \frac{2La_{\text{ref}}^2 p_h}{R_{\text{ref}}} \int_{\Omega_f} \frac{H}{2}\frac{\partial P}{\partial X} d\Omega \tag{28b}$$

where F_s and F_r denote the sliding and rolling friction respectively. Note the direction of the sliding frictional force F_s coincides with the direction of the sliding velocity $(U_{\text{roller}} - U_{\text{cam}})$. U_{cam} and U_{roller} are evaluated according to eq. 8 and 12 respectively. The friction coefficient μ_1, acting at the roller outer surface, can thus be computed as follows:

$$\mu_1 = \frac{F_{\text{s}} + F_{\text{r}}}{F} \tag{29}$$

In the present analysis the roller-pin is modelled as a full film bearing. High pressures are not expected (due to large contact area) and therefore the viscosity-pressure dependence is neglected here. According to references [15, 8] squeeze film effects are important in cases when the the lubricant entrainment velocity profile inhibits points of flow reversal. For the both cam-roller and roller-pin contact this is not the case (see Figure 7). Hence, for the roller-pin contact squeeze film effects are neglected and quasi-static behaviour is assumed instead (see Figure 9(a) which justifies this assumption). The film thickness distribution for the roller bearing with a certain eccentricity e from the central position,

can be approximated as follows:

$$h_{\text{roller}-\text{pin}} = C\,(1 - n\cos\phi) \tag{30}$$

where C is the radial clearance between roller and pin and $n = \frac{e}{C}$ is the dimensionless eccentricity. The angle ϕ is the circumferential coordinate defined as starting from the minimum film thickness $h_{\text{min,roller}-\text{pin}}$ of the roller-pin bearing (see Figure 5).

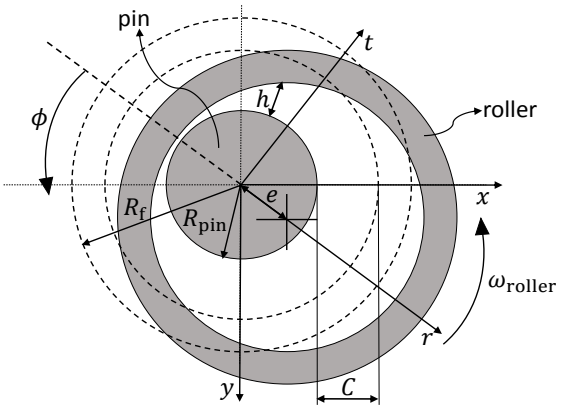

FIGURE 5: Schematic view of a cylindrical journal bearing with fixed coordinate system (x, y) and moving coordinate system (r, t).

For journal bearings of finite length the pressure gradients in both directions need to be considered. As such, there is no analytical solution to the Reynolds equation. Several approximate solutions are reported in literature, which are based on asymptotic solutions obtained using the long bearing (Sommerfeld) and short bearing (Ocvirk) solutions. San Andres [24] derived an approximate analytical solution that gives good results for finite length bearings. This approach gives the following approximate solution for calculating the Sommerfeld number S:

$$\begin{aligned}
S &= \frac{F}{\eta_0 \omega_{\text{roller}} L R_{\text{pin}}} \left(\frac{C}{R_{\text{pin}}}\right)^2 = \sqrt{fr^2 + ft^2} \\
fr &= Zr\, fr_\infty \qquad & fr_\infty &= \frac{-12n^2}{(2+n^2)\,\gamma^2} \\
ft &= Zt\, ft_\infty \qquad & ft_\infty &= \frac{6\pi n}{(2+n^2)\,\gamma} \\
Zt &= 1 - \frac{\tanh\left(\lambda t L/D\right)}{\lambda t L/D} \qquad & Zr &= 1 - \frac{\tanh\left(\lambda r L/D\right)}{\lambda r L/D} \\
\lambda t &= (\lambda s - \lambda m)\, e^{-L/D} + \lambda m \qquad & \lambda r &= \sqrt{2}\lambda t \\
\lambda s &= \sqrt{\frac{2+n^2}{2\gamma^2}} \qquad & \lambda m &= \sqrt{\frac{2\,(2+n^2)\,(1+\gamma)}{4\gamma^2 + 4\gamma - \gamma n^2}} \\
\gamma &= \sqrt{(1-n^2)}
\end{aligned} \tag{31}$$

where, $D = 2R_{\text{pin}}$ is the pin diameter, $fr = Fr/C$ and $ft = Ft/C$ are the dimensionless radial and tangential fluid film forces respectively. Zr and Zt are axial correction functions, used to correct for the radial and tangential fluid film forces respectively. In Figure 5 the moving radial and tangential coordinate system are represented by axes r and t respectively. These are conveniently defined here as the fluid film reaction forces, given by eq. 31, are defined in the moving coordinate system. Note that the radial axis always joins the roller and pin centre points.

It is worth mentioning that the analytical expressions in eq. 31 also take into account the side leakage from the bearing (for more details the reader is asked to refer to [24]). The bearing friction coefficient μ_2, defined at the roller inner surface, and attitude angle β are calculated as follows [24]:

$$\begin{aligned} \mu_2 &= \left(\frac{2\pi}{S\sqrt{1-n^2}} + \frac{n}{2}\sin(\beta)\right)\left(\frac{C}{R}\right) \\ \beta &= a\tan(-ft/fr) \end{aligned} \tag{32}$$

The individual (absolute) instantaneous power losses (in Watts) at the cam-roller and roller-pin contact are respectively computed as follows:

$$\text{cam} - \text{roller sliding power loss} = F_s\left|U_{\text{cam}} - U_{\text{roller}}\right| \tag{33a}$$

$$\text{cam} - \text{roller rolling power loss} = F_r\left|U_{\text{cam}} + U_{\text{roller}}\right| \tag{33b}$$

$$\text{roller} - \text{pin power loss} = \mu_2 F R_{\text{pin}}\omega_{\text{cam}}\left|\frac{\omega_{\text{roller}}}{\omega_{\text{cam}}} - h_1\right| \tag{33c}$$

The calculation of ω_{roller} is treated in the next subsection.

2.4 Determination of roller slippage

The rotational speed of the roller follower is primarily determined by the driving/tractive torque at the cam-roller interface. Sliding friction acting on the inner wall of the roller resists or tries to slow down the motion of the roller. The roller on itself rotates about its own axis and thus has an angular acceleration. This consequently induces an angular moment of the roller, which is defined as the product of the angular acceleration and mass moment of inertia of the roller.

The roller rotational speed is obtained by balancing the tractive torque (acting at the outer surface of roller) with the combined torques due to roller-pin friction and roller inertia force, by iteratively adjusting the roller rotational speed. In equation form this

yields:

$$\underbrace{\mu_1 R_f F}_{\text{tractive torque}} = \underbrace{\mu_2 R_{\text{pin}} F}_{\text{resisting torque}} + \underbrace{I\,\dot{\omega}_{\text{roller}}}_{\text{inertia torque}} \tag{34}$$

where friction coefficients μ_1 and μ_2 are computed by means of eqns. 29 and 32 respectively. $I = 0.5 m_{\text{roller}} \left(R_{\text{pin}}^2 + R_f^2\right)$, denotes the mass moment of inertia of the roller. ω_{roller} is adjusted by means of an iterative procedure to satisfy eq. 34.

Note that in this analysis the frictional torque, due to sliding friction at the end of the roller, has been disregarded as it is assumed that its contribution to the overall resisting torque is small.

From eq.34 it can readily be deduced that if the RHS of the equation is larger than the LHS, it means that the rolling requirement cannot be satisfied and consequently slip will occur. This may be the situation, for example, at higher rotational speeds where inertia forces are high.

Another situation that might increase the possibility of roller slip is when the limiting traction coefficient μ_0, governed by cam-roller lubrication conditions, is exceeded. For full film lubrication μ_0 is typically governed by the type of lubricant used, mean contact pressure and sum velocity. In this analysis however, μ_0 is assumed to be constant for the sake of simplicity. If the friction coefficient at the cam-roller interface is found to be larger than μ_0 then maximum friction cannot satisfy the pure rolling condition and roller slip will occur.

2.5 Overall numerical procedure

The complete system of equations is formed by the Reynolds equation 19 and elasticity equation 25 with their respective boundary conditions as given by eqns. 26 and 27 respectively. Additionally three other equations are added to the complete systems of equations, namely: i) the load balance equation 22 associated with unknown H_0, ii) the roller slip equation 34 associated with unknown ω_{roller}, and iii) eq. 31 to calculate the roller eccentricity associated with unknown n.

The model developed here is solved using the FEM with a multiphysics finite element analysis software COMSOL [3]. The problem is formulated as a set of strongly coupled non-linear partial differential equations. The resulting system of non-linear equations is solved using a monolithic approach where all the dependent variables $P, U, V, W, H_0, \omega_{\text{roller}}, n$ are collected in one vector of unknowns and simultaneously solved using a Newton-Raphson algorithm. For details concerning the fully-coupled numerical procedure, the reader is asked to read reference [12] as only the main features are recalled in this work.

A custom tailored mesh, similar to [12], was employed for the present calculations. For the elastic part Lagrange quadratic elements were used, while for the hydrodynamic part

Lagrange quintic elements were used. The aforementioned tailored mesh corresponds to approximately 300000 degrees of freedom.

For steady-state simulations converged solutions to relative errors ranging between $10^{-3} - 10^{-4}$ are reached within 10 iterations. This corresponds to a computation time of approximately 1.5 minutes on an Intel(R) Core(TM)i7-2600 processor. Realistic initial guesses, as detailed in [25], for pressure and H_0 are to be chosen to reduce to the number of iterations required for converged solutions.

For the transient calculations a steady state solution was fed as initial guess. Furthermore, a dimensionless time-step $\Delta\theta$ of 0.01 was chosen for the base circle region for the calculations. For remaining regions, where steep kinematic variations occur, a smaller time-step was chosen. The computation time for simulation of the full cam's lateral surface (360°) is approximately 28 hours.

3 Results

In this section a comprehensive analysis, for the cam and roller follower, is performed and results are presented. The configuration parameters and reference operating conditions are given in Table 1.

A height expression of the pressure distribution, for the given reference operating conditions, is shown in Figure 6. Traditional characteristics are observed as for finite line contact solutions, i.e. a secondary pressure peak is observed at the rear of the contact. Near the occurrence of this secondary pressure peak, the absolute minimum film thickness is located (see for instance [22]).

TABLE 1: Reference operating conditions and geometrical parameters for cam roller follower analysis.

Parameter	**Value**	**Unit**
E'	220	GPa
ν_{eq}	0.3	-
α	1.78E-8	Pa^{-1}
η_0	0.01	Pa·s
R_{b}	0.035	m
R_{f}	0.018	m
R_{pin}	0.0095	m
C	74	μm
L	0.021	m
d_{plunger}	0.0082	m
k_{s}	40	kN/m
m_{eq}	0.55	kg
m_{roller}	0.11	kg
F_0	500	N
A	17	μm
L_{s}	0.007	m
z_{m}	50	μm
q	0	m
μ_0	0.07	-

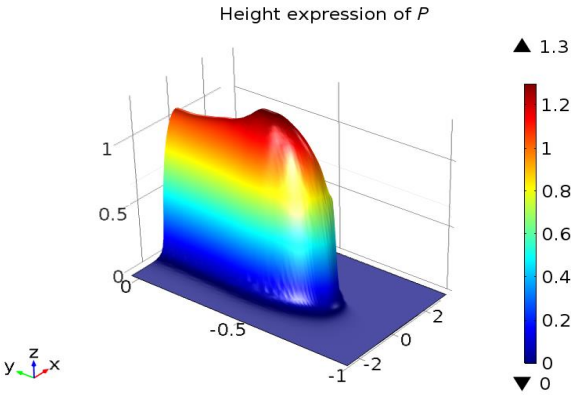

FIGURE 6: The pressure distribution for the roller with logarithmic axial profile, viewed from the rear of the contact. Furthermore, $F = 7$ kN, $U_{\mathrm{m}} = 4.2$ m/s and $p_{\mathrm{h}} = 1.05$ GPa. Note that the dimensions of the contact domain are exaggerated here for the sake of clarity.

3.1 Transient analysis

Kinematic variations

The kinematic variations, such as for contact force, cam surface speed and radius of curvature are required as an input for the EHL calculations. The kinematic model, as presented earlier, was therefore used to derive profiles for $R_x(\theta)$, $U_{\text{cam}}(\theta)$ and $F(\theta)$. In order to derive these profiles, the lift-curve $l(\theta)$ and fuel injection force force $F_{\text{FIP}}(\theta)$ are required. Profiles for $l(\theta)$ and $F_{\text{FIP}}(\theta)$ are presented in Figure 7. The derived profile for the cam surface velocity $U_{\text{cam}}(\theta)$ is also provided in the same figure.

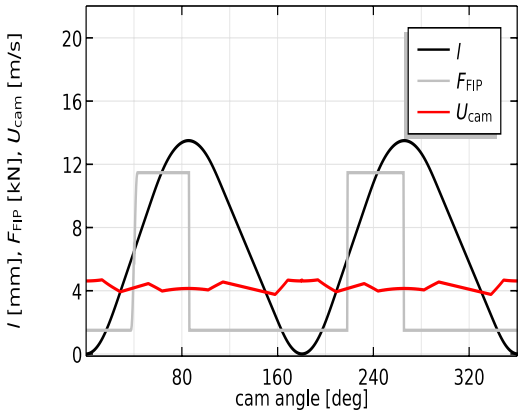

FIGURE 7: Variation of pumping load F_{FIP}, lift S and cam surface speed U_{cam} as function of cam angle θ.

Looking at the lift-curve it can readily be extracted that the considered cam has two lobes/noses, hence two periods of rise and dwell. Furthermore it is clear that the lift-curve (and hence cam surface speed) and load profile are symmetrical about 180° cam angle. The profile for the radius of curvature $R_x(\theta)$ can be obtained once $l(\theta)$ is known. The profile for the cam radius of curvature is not shown here, however the plot for the cam surface velocity is given in Figure 7 for a cam rotational speed of 950 rpm. It can be concluded that the cam surface velocity is fairly constant (with minor variations) over the whole cam's lateral profile.

The contact force at the cam/roller interface is dominated by the fuel pressure (F_{FIP} varies from 1 kN to 12 kN). In fact a software determines how many grams of fuel are needed per pump stroke, and it activates the pump at a certain cam angle. The pumping action continues till the top of the cam (maximum lift and maximum hydraulic force $F_{\text{FIP,max}}$), but once on the top the pumping motion will go back to zero and the pressure drops. So the starting angle varies, and the end angle is always at the top of the cam or centre of the nose region. The activation and de-activation of the pumping action occur quite abruptly as can be observed from Figure 7.

Common rail fuel injection systems are nowadays commonly used. In this system a common rail, connected to the individual fuel injectors, is utilized in which fuel is kept under constant pressure providing better fuel atomization. In real life there is a complex mapping of common rail pressure vs engine rpm and engine torque. A change in common rail pressure will directly influence the pump load. For the present analysis a worst case scenario was extracted from the complex (software-based) mapping of F_{FIP} vs cam speed. This "worst case scenario" mapping corresponds to Figure 8, which depicts the maximum hydraulic force $F_{\mathrm{FIP,max}}$ that can occur at a certain cam speed.

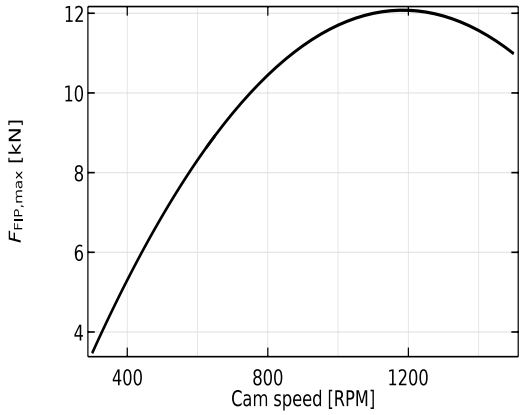

FIGURE 8: Mapping of maximum pumping load $F_{\mathrm{FIP,max}}$ against cam rotational speed.

The final contact force profile $F_{\mathrm{total}}(\theta)$ can easily be derived if $l(\theta)$ and $F_{\mathrm{FIP}}(\theta)$ are known, and is not plotted here. It should be stated however, that the spring and inertia forces appear to be almost negligible compared to the forces arising due to fuel injection pressure.

Results

The results hereafter are presented for cam angle intervals of 0°-180°, as the cam shape is symmetrical about 180° cam angle. In fact the solution from 0°-180° is identical to that for 180°-360°. Furthermore, the cam speed is kept fixed at 950RPM.
The degree of separation between surfaces, defined as specific film thickness, has a very strong influence on the type and amount of wear. Figure 9(a) provides the variation of the absolute and central minimum film thicknesses, h_{min} and $h_{\mathrm{min,central}}$ respectively, over the cam's lateral surface. Note that $h_{\mathrm{min,central}}$ is the minimum film thickness on the $Y = 0$ plane, while h_{min} occurs at the rear of the contact (near the region where axial profiling starts).

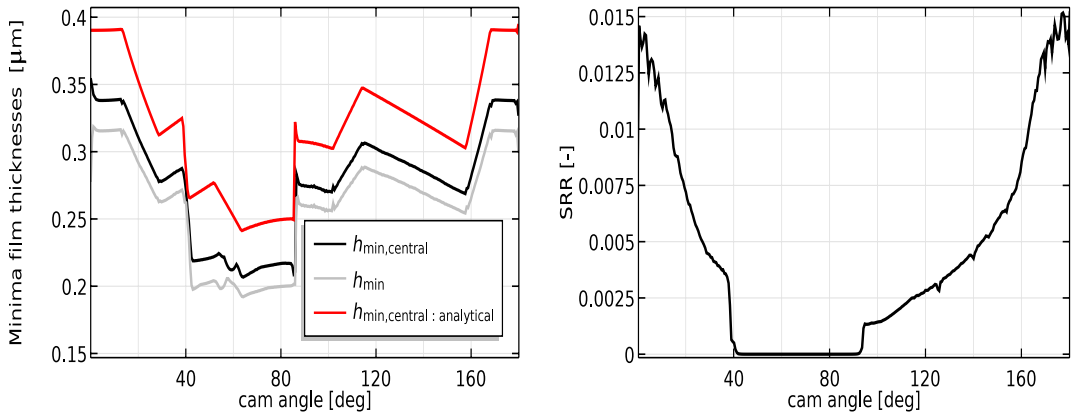

(a) (b)

FIGURE 9: Evolution of a) minima film thicknesses and b) slide-to-roll ratio SRR as function of cam angle. Notice the abrupt variations in the overall solution between 40°-90° cam angle, due to sudden activation of pumping action.

Overall a fairly constant film thickness is predicted as compared to the flat faced followers due to rolling motion of the follower. The "dips" in the film thickness profile (between 40°-90°) are due to a rapid increase of the contact force (1 kN to 12 kN), i.e. the contact force remains approximately constant at a value around $F_{\mathrm{FIP,max}}$, while the cam surface speed also remain constant approximately. The numerically calculated minima film thicknesses are compared against that predicted using the Dowson-Higginson film thickness equation for classical ("infinite") line contacts [6]. As expected, the analytical solution overestimates $h_{\mathrm{min,central}}$ as side-leakage is neglected in this approximation. Note that the analytical calculation also assumes "pure rolling conditions". Assuming a composite surface roughness of 0.2μm of the opposing surfaces, it can be concluded that the cam/roller contacts operates in the mixed lubrication regime (i.e. $\frac{h_{\mathrm{avg}}}{\sigma} < 3$).
Comparing the solutions for the analytically and numerically calculated minima film thicknesses it can also be extracted that transient effects are negligible, i.e. minimum phase lag, due to squeeze-film motion, is observed between the solutions. This observation is in line with previous findings [25]. Squeeze-film damping is mainly observed for cam-follower configurations in which the lubricant entrainment velocity profile inhibits points of flow reversal, see for instance [8].
Furthermore, due to large contact forces involved negligible slippage occurs. It is evident from Figure 9(b) that the SRR remains less than 1.5% over the full cycle. For the present analysis it was found that the friction coefficient at cam-roller interface μ_1 was less than the limiting traction coefficient μ_0. Therefore there is a very small difference between U_{cam} and U_{roller}. Again, the "dips" are due to rapid increase in contact force, i.e. the value of SRR is largest at base circle positions where the contact force is lowest.

From Figure 9(b) it can also be concluded that the sliding velocity is so small that it is important to include rolling traction when evaluating power losses.

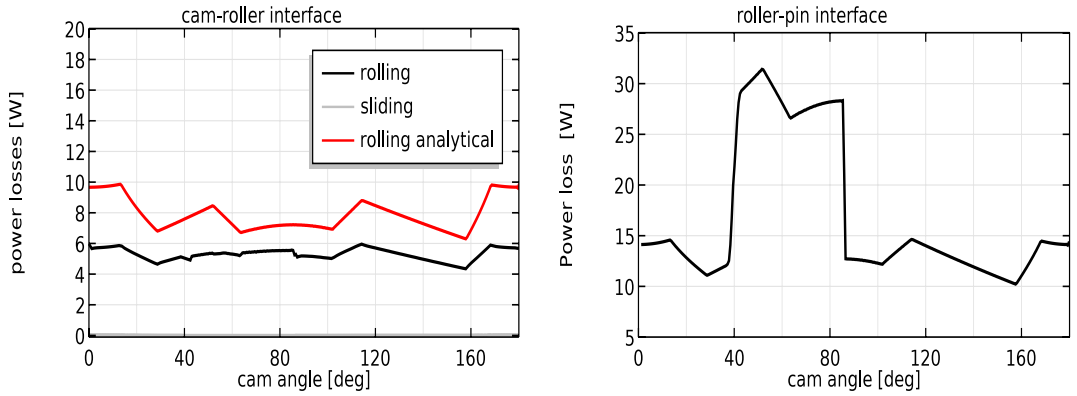

(a) (b)

FIGURE 10: Evolution of individual power losses (due to rolling and sliding friction) for a) cam-roller interface and b) roller-pin interface.

For a special case of pure rolling conditions, i.e. $U_{\text{cam}} = U_{\text{roller}}$, Crecilius et al. [4] developed an analytical expression for calculation of the hydrodynamic rolling friction. The expression takes into account an exponential dependence of viscosity on pressure and reduces for fully flooded conditions to the following equation:

$$F_{r,\text{analytical}} = \frac{4.485 L R_x (2\eta_0 \alpha U_{\text{cam}}/R_x)^{0.67}}{2\alpha} \tag{35}$$

Note that for pure rolling conditions the sum velocity is $2U_{\text{cam}}$. Also note that eq. 35 consistently agrees with previous findings by Crook [5] in the sense that F_r is proportional with the film thickness (which for EHL is proportional to the sum velocity) and negligibly dependent on the normal contact force.

Figure 10(a) presents the individual contributions of rolling and sliding traction on the power losses for the cam-roller interface (refer to eqns. 33a and 33b). As can be extracted from the aforementioned figure, sliding power loss is negligible (almost zero) when compared to rolling power losses, which varies around 5.5W over the full cam periphery. The analytical solution for rolling power loss (eq. 35 multiplied with the sum velocity) is also plotted in the same Figure. As can be observed, the analytical solution overestimates the power loss as this method overestimates the contact area, i.e. for the finite line contact problem it is known that depending on applied load and axial design parameters the contact area may increase or decrease, while in the analytical approximation the full axial length of the roller is used as contact area (see eq. 35). It is clear that rolling friction plays an important role in accurate power loss estimations.

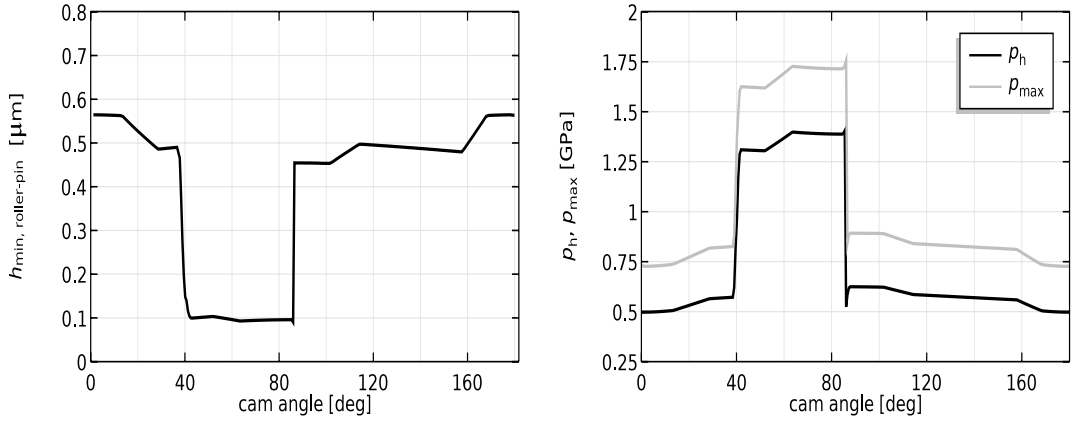

(a) (b)

FIGURE 11: Evolution of a) minimum film thickness for roller-pin interface and b) maximum pressures for cam-roller interface as a function of cam angle. Notice the abrupt variations in the overall solution between 40°-90° cam angle, due to sudden activation of pumping action.

Figure 10(b) plots the evolution of the power loss for the roller-pin interface (refer to eq. 33c). Due to the high contact loads the total bearing losses reach peak values up-to 30W around the nose region. The sudden rise in frictional losses in the bearing can be attributed to the abrupt variation in contact force. This causes, likewise to cam-roller interface, a "dip" in the minimum film thickness profile of roller-pin bearing (see Figure 11(a)). However, for the roller-pin bearing this effect is much more amplified as the eccentricity is directly dependent on contact force (see eq. 31).

When considering the variation of minimum film thickness at the roller/pin interface, as presented in Figure 11(a), it can be concluded that a poor film thickness of approximately 0.1μm is predicted around the nose region. This indicates that, assuming a composite roughness of 0.2μm, the roller-pin bearing operates in mixed or even boundary lubrication regime. The semi-analytical lubrication model for the roller-pin interface does not include deformation of solids which might enhance film thickness distribution. Furthermore, in this simplistic analysis for the roller-pin interface it is assumed that surfaces are perfectly smooth, meaning that in the practical case frictional losses will be higher and consequently will induce higher roller slippage. Accurate calculation of the film thickness distribution in the roller-bin bearing is thus extremely important and should be investigated in more detail in future work. The present work however, certainly emphasizes on the importance of accurate friction calculation in the roller-pin bearing as this contact is equally important as the cam-roller contact, but often weakly included in previous roller friction models [1, 13].

Finally, the maximum pressure variation is presented in Figure 11(b). The maximum pressure cycles between 0.5 GPa and 1.8 GPa. The maximum Hertzian pressure p_h for

a traditional "infinite" line contact model is also plotted in the same figure. It is clear that the Hertzian analytical solution significantly underestimates the maximum pressure, which for the finite line contact is located near the rear of the contact (secondary pressure peak).
From the aforementioned comparisons between analytical and numerical predictions it is clear that usage of traditional analytical tools (applicable to infinite line contacts) may lead to significant deviations from actual solutions. The analytical solutions however, can be used as a first estimation for preliminary designs. For accurate predictions numerical studies are inevitable.

3.2 Parameter study: Variation of cam rotational speed

It is of interest to analyse the behaviour of the minima film thicknesses and other performance indicators over the full range of cam rotational speeds. As earlier mentioned, the maximum fuel injection force is also mapped against cam speed (see Figure 8).
From the results obtained from the transient analysis, presented in the previous section, we could also observe that the worst operating conditions are expected in the nose region of the cam, i.e. power losses, minima film thicknesses and maximum pressures reach their peak values in the nose region. We also saw that the aforementioned performance indicators also remain fairly constant in the nose region because of the contact load that remains almost constant between $40°-90°$ cam angle. Therefore for the parameter study, concerning variation of cam speed, any position in the nose region can be chosen. To be more specific, any position on the nose between the fixed margin of $40°-90°$ cam angle can be chosen to examine the variation of crucial tribo-performance indicators.
Figure 12(a) presents the evolution of minima film thicknesses, for cam-roller and roller-pin contact, with increasing cam speed for at a fixed cam angle of $68°$. For cam-roller contact it can be seen that the minimum film thickness increases with increasing cam speed even-though the contact force on nose region also increases with increasing cam speed. The effect of contact force, seems to be less dominant as compared to sum velocity, which is analogously explainable from traditional infinite line contact EHL solutions.
For the roller-pin contact the minimum film thickness decreases from low to moderate cam speeds and then again increases from moderate to higher cam speeds. This trend can analogously be explained from the variation of the (inverse) Sommerfeld number with increasing cam speeds, which follows the same trend (see Figure 12(b)).
The variation of individual power losses for cam-roller and roller-pin interface are plotted in Figures 12(d) and 12(e) respectively. For the cam-roller interface we see that the sliding power loss, which is mainly governed by the contact force, remains negligible for the full range of cam speeds, i.e the contact force increases with cam speed and hence the

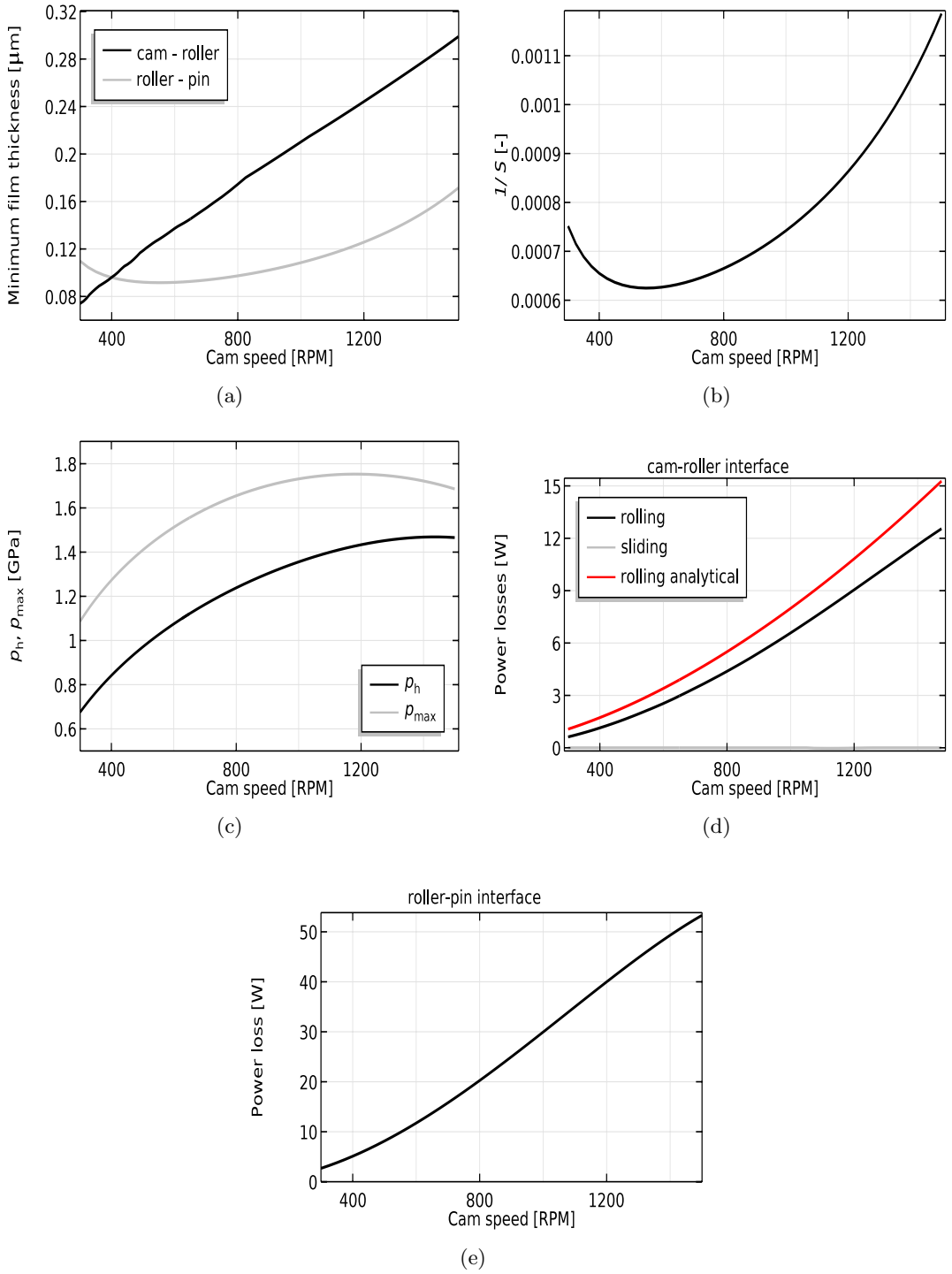

FIGURE 12: Variation of crucial design variables such as a) minima film thicknesses, b) (inverse) Sommerfeld number c) maximum pressure and d-e) power losses with cam rotational speed.

sliding speed remains minimal. Furthermore, rolling power loss increases with increasing cam speed mainly due to the fact that the sum velocity increases (refer to eq. 33b), and hence the film thickness increases. The analytical method overestimates the rolling power loss due to overestimation of contact area. For the roller-pin interface an increase power loss is observed with increase in cam speed. This increase is mainly due to the fact that the sliding speed increases and hence viscous shear in this contact increases accordingly. Finally, an increase in maximum pressure is observed with increasing cam speed (see Figure 12(c)). This is mainly due to the mapping of $F_{\mathrm{FIP,max}}$ against cam speed (see Figure 8). It is no surprise that the maximum pressure will behave similarly as $F_{\mathrm{FIP,max}}$. Also note that the analytical approximation using the Hertzian theory for line contacts underestimates the maximum pressure over the full range of cam rotational speeds.

3.3 Influence of different axial surface profiles

From the results obtained from the transient analysis it can be extracted that for the considered cam-roller configuration, any position on the nose between the fixed margin of $40°-90°$ cam angle can be chosen to examine the variation of crucial tribo-performance indicators. It would be of interest to study the effect of different axial profile designs on crucial cam-roller contact performance indicators, such as minimum film thickness, maximum pressure and rolling power loss. The axial profile can be optimized for a certain operating point, to obtain a more uniform axial pressure distribution. Note that for the considered operating conditions, roller slippage around nose region was found to be negligible. Also note that the choice of different roller axial shapes does not influence the results from the semi-analytical lubrication model for the roller-pin contact, as the film thickness is directly correlated with the applied load.

For the present study three different roller axial surface logarithmic profiles are considered. Table 2 presents the design parameters corresponding to the three different logarithmic profiles (see Figure 13(a)). Note that design 1 is similar to that (given in Table 1), used for the cam-roller analysis. For the present study the cam angle was fixed at 68°.

	L_{s} (mm)	A (μm)	z_{m} (μm)
design 1	7	17	50
design 2	4	100	100
design 3	11	10	10

TABLE 2: Considered logarithmic axial surface profiles.

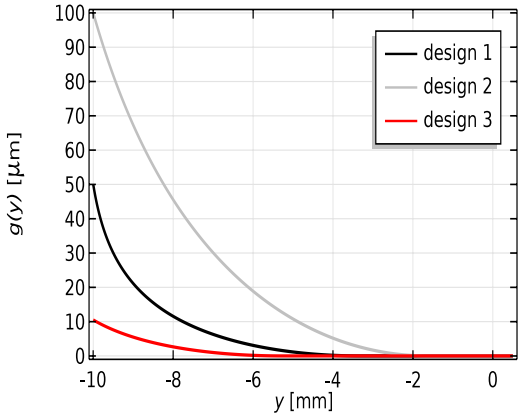

(a) Different considered designs for logarithmic axial surface profiling.

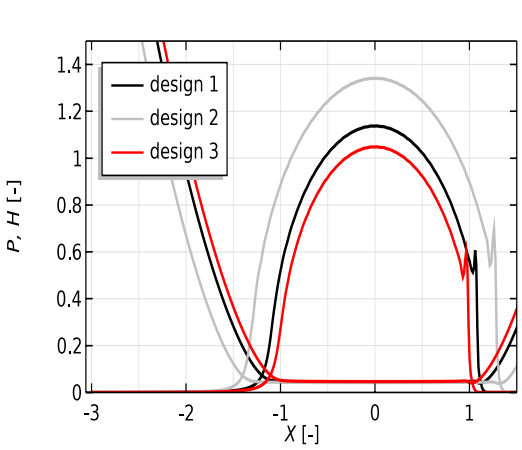

(b) Influence of different logarithmic axial surface profiles on pressure and film thickness distributions, plotted along line $Y = 0$.

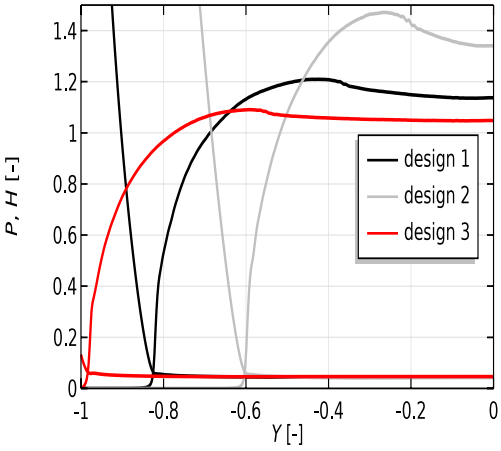

(c) Influence of different logarithmic axial surface profiles on pressure and film thickness distributions, plotted along line $X = 0$.

FIGURE 13: Influence of a) considered roller axial surface profiles on b) streamline and c) axial pressure and film thickness distributions.

Figures 13(b) and 13(c) present the dimensionless pressure and film thickness distributions along the lines $Y = 0$ and $X = 0$ respectively. It can readily be extracted that the most uniform pressure distribution is obtained for design 3. In fact, for design 3 the transverse lubricant flow experiences significantly less geometric discontinuity near the region where axial profiles starts. Consequently, the pressure profile inhibits less steep gradients at the rear of the contact and thus covers more area to carry the applied load. For this reason the minimum film thickness increases and maximum pressure decreases when compared to reference design 1 (see Table 3). However, due tot the fact that the covered contact area increases, the power losses also increase for design 3.

Exact the opposite is observed for design 2, i.e. due to larger geometric discontinuity the maximum pressure increases and minimum film thickness decreases. However, due

to decrease in covered contact area the power loss decreases. It is clear from the case studies that maximum pressure and minimum film thickness values are improved at the cost higher power losses.

	$h_{\min}$ (μm)	$p_{\max}$ (GPa)	power loss (W)
design 1	0.202	1.68	5.75
design 2	0.175	2.01	4.37
design 3	0.211	1.51	7.10

TABLE 3: Influence of considered axial surface profile design on crucial performance indicators around nose region.

4 Conclusions

A finite line contact EHL model, was utilized to analyse cam-roller follower lubrication conditions. A detailed kinematic analysis was presented to derive variations of load, speed and radius of curvature with respect to cam angle. The model includes an improved (semi-analytical) roller friction model, which takes into account the roller-pin film thickness distribution. Therefore, friction losses are more accurately estimated and consequently the roller slippage prediction is also improved.

For the numerical analysis a cam and logarithmically profiled roller follower were simulated. The cam-follower pair was assumed to be part of the fuel injection equipment in heavy duty Diesel engines.

It was found that friction losses in the roller-pin contact are highest due to high contact forces (and thus low film thickness) and sliding speeds. The importance of more accurate friction models for the roller-pin contact is highlighted here as this the contact associated with highest power losses and lowest minimum film thickness.

For the cam-roller contact it can be concluded that rolling friction is the most important power loss contributor as roller slippage was found to be negligible for the load range considered. The results in terms of friction losses, minimum film thickness and maximum pressure were compared with quasi-statistic analytical solutions corresponding to infinite line contact models. The importance of considering a finite line contact model, instead of an infinite line contact, was clearly emphasized, i.e. traditional line contact model significantly underestimates the maximum pressure and overestimates the minimum film thickness. Also, power loss estimation using the analytical approach may deviate significantly when compared with actual power losses due to overestimation of contact area.

An important observation that was made is that transient effects are negligible, therefore the quasi-static analysis should also suffice to study lubrication conditions for the

cam-roller pair.

Different roller axial profiles were considered to study their influence on crucial performance indicators around the nose region. It was found that maximum pressure and minimum film thickness values can be improved significantly, however at the cost of higher power losses. Therefore, suitable optimization routines need to be utilized in order to reach an optimum combination between friction losses, maximum pressure and minimum film thickness.

Computational times for simulating cam-roller follower lubrication, with usage of the current model, are found to be reasonable. Moreover, the developed model demonstrated the ability to cope with abrupt changes in operating conditions in which the load suddenly increases and decreases. Therefore this model can certainly be used to study the influence of modifications in cam and/or roller shape design, on the overall efficiency of the cam-follower unit.

The present study focuses on lubrication conditions in a highly loaded cam-roller follower pair in which sliding is found to be insignificant. However, for example in lightly to moderately loaded cam-roller contacts, where relatively high sliding speeds might occur, extension of the model to non-Newtonian and thermal effects might be important. Also, more extensive rheological formulations (see for instance [11, 21]) should then be used. The aforementioned aspects are suggested for future work.

Acknowledgements

This research was carried out under project number F21.1.13502 in the framework of the Partnership Program of the Materials innovation institute M2i (www.m2i.nl) and the Netherlands Organization for Scientific Research (www.nwo.nl).

References

[1] Y. Chiu. Lubrication and slippage in roller finger follower systems in engine valve trains. *Tribology transactions*, 35(2):261–268, 1992.

[2] M. Colechin, C. Stone, and H. Leonard. Analysis of roller-follower valve gear. Technical report, SAE Technical Paper 930692, 1993.

[3] COMSOL multiphysics. Comsol multiphysics modeling guide. *COMSOL Inc.*, www.comsol.com. (accessed 3 April 2017).

[4] W. Crecelius and J. Pirvics. Computer program operation manual on shaberth. a computer program for the analysis of the steady state and transient thermal performance of shaft-bearing systems. Technical report, DTIC Document, 1976.

[5] A. Crook. The lubrication of rollers iv. measurements of friction and effective viscosity. *Philosophical Transactions of the Royal Society of London A: Mathematical, Physical and Engineering Sciences*, 255(1056):281–312, 1963.

[6] D. Dowson and G. Higginson. A numerical solution to the elasto-hydrodynamic problem. *Journal of Mechanical Engineering Science*, 1(1):6–15, 1959.

[7] D. Dowson and G. Higginson. *Elasto-hydrodynamic lubrication: the fundamentals of roller and gear lubrication*, volume 23. Pergamon Press, Oxford, United Kingdom, 1966.

[8] D. Dowson, C. Taylor, and G. Zhu. A transient elastohydrodynamic lubrication analysis of a cam and follower. *Journal of Physics D: Applied Physics*, 25(1A):A313, 1992.

[9] H. Fujiwara and T. Kawase. Logarithmic profiles of rollers in roller bearings and optimization of the profiles. *NTN Technical Review*, 75:140–148, 2007.

[10] B. Gecim. Lubrication and fatigue analysis of a cam and roller follower. *Tribology Series*, 14:91–100, 1989.

[11] W. Habchi, S. Bair, F. Qureshi, and M. Covitch. A film thickness correction formula for double-newtonian shear-thinning in rolling ehl circular contacts. *Tribology Letters*, 50(1):59–66, 2013.

[12] W. Habchi, D. Eyheramendy, P. Vergne, and G. Morales-Espejel. A full-system approach of the elastohydrodynamic line/point contact problem. *Journal of Tribology*, 130(2):021501, 2008.

[13] F. Ji and C. Taylor. A tribological study of roller follower valve trains. part 1: A theoretical study with a numerical lubrication model considering possible sliding. *Tribology Series*, 34:489–499, 1998.

[14] M. Khurram, R. Mufti, R. Zahid, N. Afzal, and U. Bhutta. Experimental measurement of roller slip in end-pivoted roller follower valve train. *Proceedings of the Institution of Mechanical Engineers, Part J: Journal of Engineering Tribology*, 229(9):1047–1055, 2015.

[15] M. Kushwaha and H. Rahnejat. Transient elastohydrodynamic lubrication of finite line conjunction of cam to follower concentrated contact. *Journal of Physics D: Applied Physics*, 35(21):2872, 2002.

[16] M. Kushwaha, H. Rahnejat, and R. Gohar. Aligned and misaligned contacts of rollers to races in elastohydrodynamic finite line conjunctions. *Proceedings of the Institution of Mechanical Engineers, Part C: Journal of Mechanical Engineering Science*, 216(11):1051–1070, 2002.

[17] J. Lee and D. Patterson. Analysis of cam/roller follower friction and slippage in valve train systems. Technical report, SAE Technical Paper 951039, 1995.

[18] J. Matthews and F. Sadeghi. Kinematics and lubrication of camshaft roller follower mechanisms. *Tribology Transactions*, 39(2):425–433, 1996.

[19] N. Miyamura. Fuel saving in internal-combustion engines. *Journal of Japanese Society of Tribologists*, 36(11):855–859, 1991.

[20] A. Mostofi and R. Gohar. Elastohydrodynamic lubrication of finite line contacts. *Journal of Tribology*, 105(4):598–604, 1983.

[21] L. Paouris, R. Rahmani, S. Theodossiades, H. Rahnejat, G. Hunt, and W. Barton. An analytical approach for prediction of elastohydrodynamic friction with inlet shear heating and starvation. *Tribology Letters*, 64(1):10, 2016.

[22] T.-J. Park and K.-W. Kim. Elastohydrodynamic lubrication of a finite line contact. *Wear*, 223(1):102–109, 1998.

[23] C. Roelands. *Correlational aspects of the viscosity-temperature-pressure relationship of lubricating oils*. PhD thesis, Delft University of Technology, Delft, The Netherlands, 1966.

[24] L. San Andres. Approximate design of statically loaded cylindrical journal bearings. *Journal of Tribology*, 111(2):390–393, 1989.

[25] M. Shirzadegan, A. Almqvist, and R. Larsson. Fully coupled EHL model for simulation of finite length line cam-roller follower contacts. *Tribology International*, 103:584–598, 2016.

[26] M. Teodorescu, M. Kushwaha, H. Rahnejat, and S. Rothberg. Multi-physics analysis of valve train systems: from system level to microscale interactions. *Proceedings of the Institution of Mechanical Engineers, Part K: Journal of Multi-body Dynamics*, 221(3):349–361, 2007.

[27] A. Turturro, R. Rahmani, H. Rahnejat, C. Delprete, and L. Magro. Assessment of friction for cam-roller follower valve train system subjected to mixed non-newtonian regime of lubrication. In *ASME 2012 Internal Combustion Engine Division Spring Technical Conference*, pages 917–923. American Society of Mechanical Engineers, 2012.

[28] S. Wu. A penalty formulation and numerical approximation of the reynolds-hertz problem of elastohydrodynamic lubrication. *International Journal of Engineering Science*, 24(6):1001–1013, 1986.

[29] D. Wymer and A. Cameron. Elastohydrodynamic lubrication of a line contact. *Proceedings of the Institution of Mechanical Engineers*, 188(1):221–238, 1974.

[30] G. Zhu and C. M. Taylor. *Tribological analysis and design of a modern automobile cam and follower*, volume 4. John Wiley & Sons, 2001.

Paper C

A full numerical solution to the coupled cam–roller and roller–pin contact in heavily loaded cam–roller follower mechanisms

S.S. Alakhramsing[1], M.B. de Rooij[1], M. van Drogen[2] and D.J. Schipper[1]

Proceedings of the Institution of Mechanical Engineers, Part J: Journal of Engineering Tribology, 232 (10), 1273-1284, 2018.
DOI:10.1177/1350650117746899

[1]Faculty of Engineering Technology, University of Twente, P.O. Box 217, 7500 AE Enschede, The Netherlands
[2]Central Laboratory Metals, DAF Trucks N.V., P.O. Box 90065, 5600 PT Eindhoven, The Netherlands

Nomenclature

a Hertzian contact half-width (m)

A roller crowning curvature (m)

C radial clearance (m)

C_U dimensionless variation of cam surface velocity

C_F dimensionless variation of contact force

C_R dimensionless variation of reduced radius of curvature

D pin diameter (m)

e roller eccentricity (m)

E' reduced elasticity modulus (Pa)

F force (N)

g axial surface profile function (m)

G dimensionless axial surface profile function

h film thickness (m)

H dimensionless film thickness

h_0 rigid body displacement (m)

H_0 dimensionless rigid body displacement

I roller inertia (kg.m^2)

L roller axial length (m)

L_s roller straight length (m)

m mass (kg)

p pressure (Pa)

P dimensionless pressure

p_{h} Hertzian pressure (Pa)

R_x reduced radius of curvature (m)

R_y crowning curvature curvature (m)

R_{pin} pin radius (m)

R_{f} outer radius roller (m)

U_{cam} cam surface velocity (m/s)

U_{roller} roller surface velocity (m/s)

U_{m} lubricant mean entrainment velocity (m/s)

x, y, z spatial coordinates (m)

X, Y, Z dimensionless spatial coordinates

$\bar{x}, \bar{y}$ global coordinates

z_{d} roller crown drop (m)

α pressure-viscosity coefficient (GPa^{-1})

η lubricant viscosity (Pa·s)

η_0 lubricant reference viscosity (Pa·s)

$\tilde{\eta}$ lubricant dimensionless viscosity

Θ circumferential coordinate (rad)

θ cam angle (rad)

θ cam angle (rad)

δ z-component of elastic displacement field (m)

$\tilde{\delta}$ dimensionless Z-component of elastic displacement field

$\mu_{\mathrm{cam-roller}}$ friction coefficient cam-roller contact (-)

$\mu_{\mathrm{roller-pin}}$ friction coefficient roller-pin contact (-)

ν Poisson ratio (-)

ρ lubricant density (kg/m^3)

ρ_0 lubricant reference density (kg/m^3)

$\tilde{\rho}$ lubricant dimensionless viscosity

ω rotational speed (rad/s)

Ω computational domain

Ω_f contact boundary

Ω_D contact boundary

Ω_s symmetry boundary

Subscripts

cent central

f follower

min minimum

r radial

ref reference

A full numerical solution to the coupled cam–roller and roller–pin contact in heavily loaded cam–roller follower mechanisms

Abstract

In cam-roller follower units two lubricated contacts may be distinguished, namely the cam-roller contact and roller-pin contact. The former is a non-conformal contact while the latter is conformal contact. In an earlier work a detailed transient finite line contact EHL model for the cam-roller contact was developed. In this work a detailed transient EHL model for the roller-pin contact is developed and coupled to the earlier developed cam-roller contact EHL model via a roller friction model. For the transient analysis a heavily loaded cam-roller follower unit is analysed. It is shown that likewise the cam-roller contact, the roller-pin contact also inhibits typical finite line contact EHL characteristics at high loads. The importance of including elastic deformation for analysing lubrication conditions in the roller-pin contact is highlighted here, as it significantly enhances the film thickness and friction coefficient. Other main findings are that for heavily loaded cam-roller follower units, as studied in this work, transient effects and roller slippage are negligible, and the roller-pin contact is associated with the highest power losses. Finally, due to the non-typical EHL characteristics of both cam-roller and roller-pin contact numerical analysis becomes inevitable for the evaluation of the film thicknesses, power losses and maximum pressures.

Keywords: EHL, cam-roller, roller-pin, finite line contacts, roller slip

1 Introduction

Cam-roller follower mechanisms as part of fuel injection units in heavy duty Diesel engines are subjected to very high fluctuating loads coming from the fuel injector. Apart from the high fluctuating contact forces, varying radius of curvature and lubricant entertainment velocity make the tribological design of these components even more challenging. The lubricant entrainment speed of the cam-roller contact on itself is a function of geometrical configuration, cam rotational velocity and roller angular speed.

Two lubricated contacts may be distinguished when considering a cam-roller follower unit, namely the cam-roller contact and roller-pin contact (see Figure 1). The former is a non-conformal contact while the latter is conformal contact. The roller angular speed is a function of the working frictional forces at the cam-roller and roller-pin contact and inertia torque caused by angular acceleration of the roller itself. Roller slip is defined as the difference between the cam and roller surface velocities at the point of contact.

Khurram et al. [11] proved the existence of roller slip experimentally. Lee and Patterson [12] showed that the problem of wear on the interacting surfaces still occurs if slip is present.

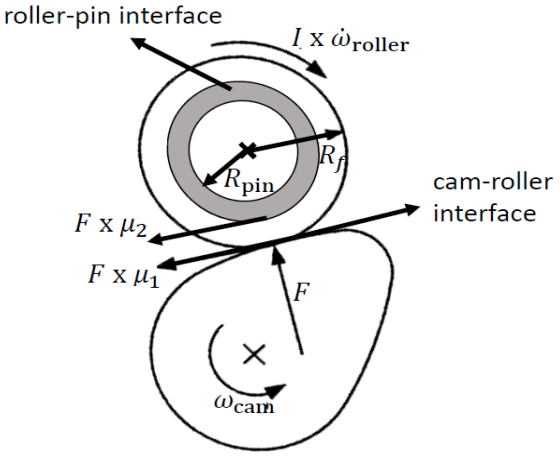

FIGURE 1: Cam-roller follower configuration showing the frictional forces acting at the cam-roller and roller-pin contact.

Previously developed cam-roller follower lubrication models (see for instance [3, 10, 18]), which include the possibility of roller slippage, all rely on (semi)-analytical formulations for the film thickness distribution in the cam-roller contact. In those studies the frictional forces working at the roller-pin contact were also estimated using simple analytical formulas or were considered to be constant throughout the whole operating range.

Recently Alakhramsing et al. [2] presented a finite element method (FEM)-based cam-roller lubrication model taking into account axial surface profiling of the roller and also allowing for roller slip. The importance of taking into account axial surface profiling

into EHL models has been shown by a number of published studies (see for instance [20, 17, 1]).

The general framework of the model developed in [2] relies on a finite length line contact EHL model for the cam-roller contact and semi-analytical lubrication model for the roller-pin contact. The roller-pin contact was modelled as a full film journal bearing. The basis of the semi-analytical model used for the roller-pin contact relies on the assumption that the interacting surfaces are rigid and that the lubricant has an isoviscous behaviour. It is expected that under the extremely high contact forces (ranging from 2kN to 15 kN), which are also directly transmitted to the roller-pin contact, the "rigid surfaces" assumption might not be accurate. It is therefore important to include elastic deformation of the roller and pin into the analysis. As shown in past studies, see for example [15, 7], the rigid hydrodynamic solution for journal bearings might significantly overestimate the maximum pressure and underestimate the minimum film thickness.

Therefore, in this paper we present full transient numerical EHL solutions for both cam-roller and roller-pin contact. Both EHL models for cam-roller and roller-pin contact are interlinked via a roller friction model, which predicts possible roller slippage. It is expected that with this model the estimation of important design variables for both cam-roller and roller-pin contact (such as minimum film thicknesses, maximum pressures and friction losses) are significantly improved and thus leading to a better understanding of the tribological behaviour of the cam-roller follower unit. Typical simulation results analysed in this work are the evolution of the minimum film thickness, maximum pressure, individual frictional losses and roller slippage along the cam surface.

2 Mathematical model

The complete mathematical model consists of two FEM-based EHL models corresponding to the cam-roller and roller-pin contact, which are interlinked through the torque balance applied to the roller. Furthermore, it is assumed that thermal effects are insignificant and thus isothermal conditions are assumed.

The first part of the mathematical model, which applies to the cam-roller contact is similar to the full transient EHL solution presented by Alakhramsing et al. [2]. Hence, in this paper only the main features corresponding to the cam-roller contact are recalled and for further details the reader is asked to refer to Alakhramsing et al. [2].

The second part of the mathematical model corresponds to the conformal roller-pin contact and relies on a full transient EHL solution for elastic bearings.

Finally, in the last part of this mathematical section the coupling between the two aforementioned EHL models is explained.

2.1 Cam-roller contact EHL model

The typical governing EHL equations which apply to the cam-roller contact consist are the Reynolds equation, the load balance equation and the 3D-linear elasticity equations. All governing EHL equations for the cam-roller contact are presented in non-dimensional form. Hence, the following dimensionless variables are introduced:

$$
\begin{aligned}
X &= \frac{x}{a_{\mathrm{ref}}} & Y &= \frac{y}{2L} & Z &= \frac{z}{a_{\mathrm{ref}}} \\
P &= \frac{p}{p_{\mathrm{h}}} & \tilde{\eta} &= \frac{\eta}{\eta_0} & \tilde{\rho} &= \frac{\rho}{\rho_0} \\
H &= \frac{hR_{\mathrm{ref}}}{a_{\mathrm{ref}}^2} & H_0 &= \frac{h_0 R_{\mathrm{ref}}}{a_{\mathrm{ref}}^2} & C_R(\theta) &= \frac{R_x(\theta)}{R_{\mathrm{ref}}} \\
C_U(\theta) &= \frac{U_{\mathrm{cam}}(\theta)}{U_{\mathrm{ref}}} & C_F(\theta) &= \frac{F(\theta)}{F_{\mathrm{ref}}} & G &= \frac{gR_{\mathrm{ref}}}{a_{\mathrm{ref}}^2} \\
\tilde{\delta} &= \frac{\delta R_{\mathrm{ref}}}{a_{\mathrm{ref}}^2} & \theta &= \omega_{\mathrm{cam}} t
\end{aligned}
\tag{1}
$$

with Hertzian parameters defined as follows:

$$
\begin{aligned}
p_{\mathrm{h}} &= \frac{2F_{\mathrm{ref}}}{\pi L a_{\mathrm{ref}}} & a_{\mathrm{ref}} &= \sqrt{\frac{8F_{\mathrm{ref}}R_{\mathrm{ref}}}{\pi L E'}} \\
E' &= \frac{2}{\frac{1-\nu_{\mathrm{cam}}^2}{E_{\mathrm{cam}}} + \frac{1-\nu_{\mathrm{roller}}^2}{E_{\mathrm{roller}}}}
\end{aligned}
\tag{2}
$$

where the subscript "ref" denotes the reference operating conditions.

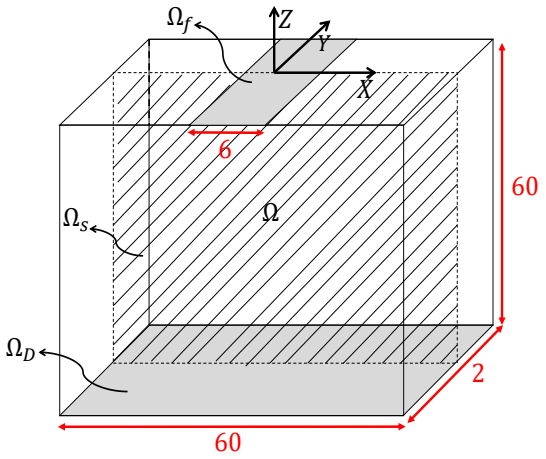

FIGURE 2: Equivalent geometry for EHL analysis of the finite line contact problem. Dimensions are exaggerated for the sake of clarity.

Figure 2 presents the equivalent EHL computational domain Ω for the cam-roller contact. Instead of calculating the elastic deformation twice for the two semi-infinite bodies,

an equivalent elastic domain Ω (with equivalent mechanical properties) is chosen for calculation of the combined elastic displacement field $\tilde{\delta}$ (see reference [9] for more details). The dimensionless side length of 60 for the elastic domain Ω is chosen in such a way so that the zero displacement boundary condition, imposed on bottom boundary Ω_{D}, holds [9]. Ω_{f} denotes the fluid domain on which the Reynolds equation is solved and has dimensions of $-4.5 \leq X \leq 1.5$ and $-1 \leq Y \leq 1$. In the present study the advantage of symmetry (around symmetrical plane Ω_{s}) has been taken in order to reduce the computational power required. The dimensionless transient Reynolds equation, which governs the pressure distribution in the contact, is written as follows:

$$\frac{\partial}{\partial X}\left(-\frac{\tilde{\rho}H^3}{\tilde{\eta}\lambda}\frac{\partial P}{\partial X}+\left(\frac{U_{\mathrm{roller}}(\theta)}{2U_{\mathrm{ref}}}+\frac{C_U(\theta)}{2}\right)H\tilde{\rho}\right) + \frac{\partial}{\partial Y}\left(-\frac{a_{\mathrm{ref}}^2}{(2L)^2}\frac{\tilde{\rho}H^3}{\tilde{\eta}\lambda}\frac{\partial P}{\partial Y}\right)+\frac{a_{\mathrm{ref}}\omega_{\mathrm{cam}}}{U_{\mathrm{ref}}}\frac{\partial H\tilde{\rho}}{\partial\theta}=0 \quad (3)$$

where, $\lambda = \frac{12U_{\mathrm{ref}}\eta_0 R_{\mathrm{ref}}^2}{a^3 p_{\mathrm{h}}}$ is the dimensionless speed parameter, and $\tilde{\eta}$ and $\tilde{\rho}$ are the dimensionless viscosity and density of lubricant respectively. $\theta = \omega_{\mathrm{cam}}t$ is the cam angle and ω_{cam} is the cam rotational speed. $C_U(\theta)$ represents the variation of the cam surface velocity U_{cam}. Note that U_{cam} and U_{roller} are parallel to the X-axis, which is why the wedge term in Y-direction in the Reynolds equation is nil. Eq. 3 includes the following features/assumptions:

- Compressibility and piezoviscous behaviour of the lubricant are modelled using the Dowson-Higginson [5] and Roelands [16] relations respectively.
- The free boundary problem arising at the outlet of the contact is treated using the penalty formulation of Wu [19]
- Suitable numerical stabilization techniques, as detailed in [9], are utilized in order to stabilize the solution at high loads.
- Fully flooded conditions are assumed at the inlet of the contact and opposing surfaces are assumed to be smooth.

The film thickness for the cam-roller contact, at any cam angle θ, can be described using the following expression

$$H\left(X,Y,\theta\right) = H_0\left(\theta\right) + \frac{X^2}{2C_R(\theta)} + G(Y,\theta) - \tilde{\delta}\left(X,Y,\theta\right) \quad (4)$$

where H_0 is the rigid body displacement and $\tilde{\delta}$ is the combined elastic deformation, of which the calculation is based on a 3D-elasticity matrix [2]. $C_R(\theta)$ denotes the

dimensionless variation of the reduced radius of curvature $R_x = \left(\frac{1}{\rho_{\text{cam}}} + \frac{1}{R_{\text{f}}}\right)^{-1}$. ρ_{cam} is the cam radius of curvature. $G(Y, \theta)$ is a dimensionless function that represents the axial surface profile of the roller. The roller, considered in this study, has a logarithmic axial shape which is described using the following equation [8]:

$$g(y,\theta) = -A \ln\left\{1 - \left[1 - \exp\left(\frac{-\mathrm{z_m}}{\mathrm{A}}\right)\right]\left(\frac{2y - L_{\text{s}}}{L - L_{\text{s}}}\right)^2\right\} \tag{5}$$

where A represents the degree of crowning curvature, z_{m} is the crown drop at the extremities and L_{s} is the straight roller length. Please note that here only the positive Y-part of the solid domain has been retained to account for the problem symmetry. Furthermore, $g(y, \theta)$ is only valid for $\frac{L_{\text{s}}}{2} \leq y \leq \frac{L}{2}$, otherwise zero.
The rigid body displacement H_0 is obtained by satisfying the load balance. In equation form this yields:

$$\int_{\Omega_f} 2P\left(X, Y, \theta\right) dX = \pi C_F(\theta) \tag{6}$$

where $C_F(\theta)$ denotes the dimensionless variation of contact force F. Note that the pressure P in eq. 6 is multiplied with a factor of 2 in order to account for the symmetry of the problem. The boundary conditions for the complete cam-roller EHL model are summarized as follows [17]:

- The pressure at the borders of the fluid flow domain Ω_f equals zero.
- Symmetrical boundary conditions are imposed at plane Ω_{s} for the elastic and hydrodynamic problem.
- A zero displacement condition is imposed at bottom boundary Ω_{D}
- For the elastic part a pressure boundary condition is imposed on the fluid flow domain Ω_f.
- On all remaining boundaries zero stress conditions are imposed.

Finally, the friction coefficient $\mu_{\text{cam-roller}}$ defined at the cam-roller contact is calculated as follows:

$$\mu_{\text{cam-roller}} = \frac{2L\eta_0 R_{\text{ref}}}{a_{\text{ref}} F} \int_{\Omega_f} \frac{\tilde{\eta}\left(U_{\text{roller}} - U_{\text{cam}}\right)}{H} + \frac{2La_{\text{ref}}^2 p_h}{R_{\text{ref}} F} \int_{\Omega_f} \frac{H}{2} \frac{\partial P}{\partial X} d\Omega \tag{7}$$

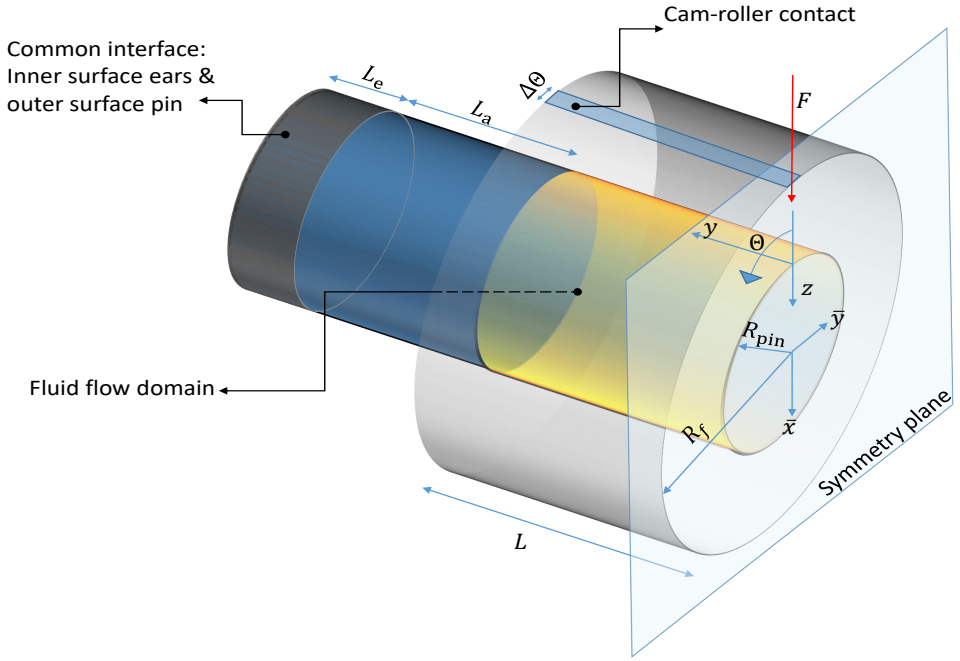

FIGURE 4: Roller-pin contact computational domain. Dimensions are exaggerated for the sake of clarity.

2.2 Roller-pin contact EHL model

Figure 3 shows the configuration of the roller-pin bearing. The roller is free to rotate and the pin is fixed to the tappet around the inner circumference of the so-called "ears" of the tappet. In between the roller and the ears of the tappet a small clearance is kept in order to allow the roller to freely rotate and also to allow lubricant to reach the roller-pin interface through the sides of the contact.

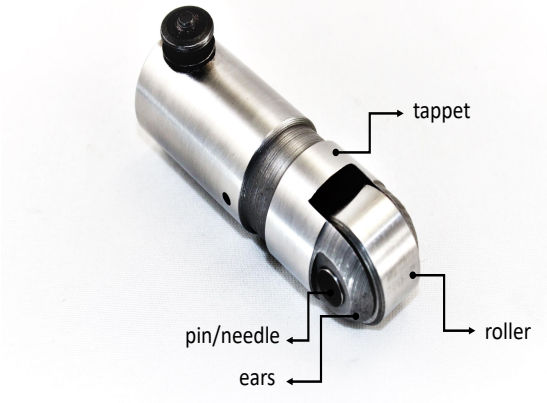

FIGURE 3: Example of a cam-roller follower unit.

Figure 4 shows the deduced computational domain for the roller-pin EHL model shown

in Figure 3. As can be extracted from this figure the advantage of symmetry has been taken at the $y = 0$ plane. Unlike for the cam-roller contact, the governing equations for the roller-pin contact, are solved in dimensional form.

The pin is slightly crowned in axial direction in order to reduce edge stress concentrations, while the roller inner surface is assumed to be perfectly straight. The film thickness distribution for the roller-pin contact, which can be described in similar manner as for an elastic journal bearing, is written as follows:

$$h = C - e_{\bar{x}} \cos\Theta - e_{\bar{y}} \sin\Theta + \frac{y^2}{2R_y} + \partial_{\mathrm{r}} \tag{8}$$

where C is the nominal radial clearance, R_y is the crowing curvature of the pin, $e_{\bar{x}}$ and $e_{\bar{y}}$ are the global $\bar{x}$ and $\bar{y}$ components of the roller eccentricity (see Figure 5) and $\partial_{\mathrm{r}} = \delta_{\mathrm{roller}} + \delta_{\mathrm{pin}}$ is the combined radial elastic deformation of roller and pin. Unlike for rigid bearings, the dimensionless eccentricity $\epsilon = \frac{e}{C}$ is allowed to be greater than one when elastic deformation is taken into account [15].

Note that, unlike for the cam-roller contact, the elastic deflections for roller and pin are individually calculated and summed up for evaluation of the film thickness. $\Theta = \phi + \varphi$ is the circumferential coordinate. φ is the roller attitude angle, i.e. $e_x = e\cos\varphi$ and $e_y = e\sin\varphi$. The angle ϕ is the circumferential coordinate defined as starting from the minimum film thickness $h_{\mathrm{min,roller-pin}}$ of the roller-pin bearing (see Figure 5).

The Reynolds equation, which governs the pressure distribution in the roller-pin contact, is written as follows:

$$-\frac{1}{R_{\mathrm{pin}}^2}\frac{\partial}{\partial\Theta}\left(\frac{\rho h^3}{12\eta}\frac{\partial p}{\partial\Theta}\right) - \frac{\partial}{\partial y}\left(\frac{\rho h^3}{12\eta}\frac{\partial p}{\partial\Theta}\right) + \frac{U_{\mathrm{roller}}}{2R_f}\frac{\partial}{\partial\Theta}(\rho h) + \omega_{\mathrm{cam}}\frac{\partial}{\partial\theta}(\rho h) = 0 \tag{9}$$

Note that U_{roller} is the outer roller surface velocity, while $\frac{R_{\mathrm{pin}}U_{\mathrm{roller}}}{R_f}$ is the inner roller surface velocity.

Similar to the cam-roller contact, variation of viscosity and density with pressure is simulated using the Roelands [16] and Dowson-Higginson [5] rheological expressions. The cavitation problem within the lubricated contact is treated according to the penalty formulation of Wu [19].

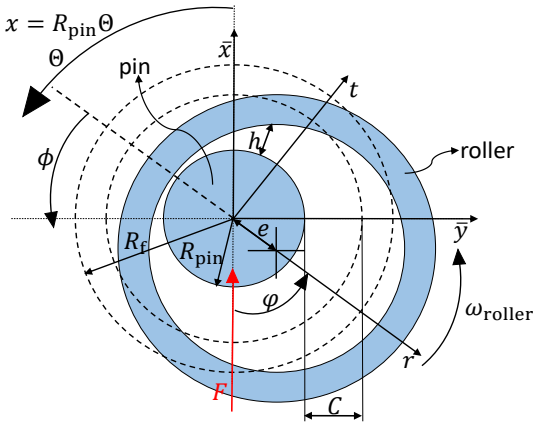

FIGURE 5: Schematic view of a cylindrical journal bearing with fixed coordinate system (x, y) and moving coordinate system (r, t).

In the present analysis we align the x-axis of the (x, y) coordinate system at all times with force vector $F(\theta)$, which acts at the cam-roller contact (see Figure 5). The eccentricity components (e_x, e_y) are obtained by satisfying the equations of motion:

$$m_{\text{roller}}\omega_{\text{cam}}^2 \begin{bmatrix} \ddot{e}_{\bar{x}} \\ \ddot{e}_{\bar{y}} \end{bmatrix} = \begin{bmatrix} F_x \\ F_y \end{bmatrix} - \begin{bmatrix} F \\ 0 \end{bmatrix} \tag{10}$$

where the fluid film reaction forces are defined as follows:

$$\begin{bmatrix} F_x \\ F_y \end{bmatrix} = \int_{-L/2}^{L/2} \int_{0}^{2\pi} p(\Theta, y, \theta) \begin{bmatrix} \cos\Theta \\ \sin\Theta \end{bmatrix} R_{\text{pin}} \cdot d\Theta dy \tag{11}$$

Note that due to the unique definition of coordinate system (x, y) the y-component of the applied load F is zero at all times. The radial displacement ∂_{r}, which is caused by the lubricant pressure build up in the contact, is evaluated using a full deformation model based on a 3D-elasticity matrix [4].
The boundary conditions for the complete roller-pin EHL model are summarized as follows:

- The pressure is continuous and periodic in circumferential direction Θ.
- A zero pressure condition is imposed at the (side) borders of the fluid film domain in order to simulate fully submerged conditions.
- A zero displacement condition is imposed at the common interface between the pin and inner surface of the ears of the tappet.
- For the elastic part a pressure boundary condition is imposed on the outer surface of the pin and inner surface of the roller on the lubricant flow domain.

- The centre of contact between the cam and roller always lies on the x-axis of the roller-pin model. The most accurate way to describe the boundary condition at the outer surface of the roller, where cam-roller contact occurs, would be by prescribing the displacement field which is calculated from the cam-roller contact EHL model. However, from our simulations we observed that similar results are obtained if a zero displacement condition is imposed on the outer contact domain. Of course, the size of the contact domain itself varies for different cam angles (due to varying operating conditions). Nevertheless, based on dry Hertzian analysis an estimation of the range in which the contact area varies can be made. For the cases studied, the contact width varies between 0.3mm to 0.6mm. Due to the considerably large thickness of the roller, the displacement fields of cam-roller and roller-pin contact are not at all influenced by each other. So, for the current analysis a fixed outer roller boundary has been used at all cam angles on which a zero displacement condition has been imposed.
- On all remaining boundaries zero stress conditions are imposed.

Finally, the friction coefficient $\mu_{\text{roller}-\text{pin}}$ defined at the roller-pin contact is calculated as follows:

$$\mu_{\text{roller}-\text{pin}} = \int_{-L/2}^{L/2} \int_{0}^{2\pi} -\frac{h}{2FR_{\text{pin}}} \frac{dp}{d\Theta} + \eta \frac{R_f}{FR_{\text{pin}}} \frac{U_{\text{roller}}}{h} R_{\text{pin}} \cdot d\Theta dy \tag{12}$$

Note that in the current analysis friction evaluation is based on isothermal and Newtonian assumptions. Extension of the model to capture non-Newtonian and thermal effects is suggested for future work.

2.3 Coupling of cam-roller and roller pin contact

As mentioned earlier, the cam-roller and roller-pin contact are coupled through the global torque balance applied to the roller. The global torque balance, used for calculation of roller rotational speed ω_{roller} yields [10]:

$$\underbrace{\mu_{\text{cam}-\text{roller}} R_f F}_{\text{tractive torque}} = \underbrace{\mu_{\text{roller}-\text{pin}} R_{\text{pin}} F}_{\text{resisting torque}} + \underbrace{I\omega_{\text{cam}}\, \dot{\omega}_{\text{roller}}}_{\text{inertia torque}} \tag{13}$$

where $I = 0.5 m_{\text{roller}} \left(R_{\text{pin}}^2 + R_f^2 \right)$ is the mass moment inertia of the roller and friction coefficients $\mu_{\text{cam}-\text{roller}}$ and $\mu_{\text{roller}-\text{pin}}$ are calculated by means of eqns. 25 and 12 respectively. When the RHS of eq. 13 increases, the sliding velocity at the cam-roller contact consequently also needs to increase to satisfy the torque balance, i.e. the LHS needs to increase. This is also known as the "self-correcting action" [10].

2.4 Overall numerical procedure

The complete models thus consists of two sub-EHL models corresponding to cam-roller and roller-pin contact. The governing equations for both models include the Reynolds equations and the 3D-linear elasticity equations with their associated BC's. Additionally, for the cam-roller EHL model the load balance (with unknown H_0) is added to the system of equations, while for the roller-pin EHL model the equations of motion (with unknown eccentricity components e_x and e_y) are added to the system of equations.
The two sub-models are interlinked via the global torque balance, which determines the roller angular velocity ω_{roller}.
The complete model is solved using a finite element analysis software package [4]. In fact, the problem is formulated a set of strongly coupled partial differential equations. After finite element discretization, the resulting set of non-linear equations is solved using a monolithic approach in which all dependent variables

$$\left(\left\{P, \tilde{\delta}, H_0\right\}_{\text{cam}-\text{roller}}, \{p, \delta, e_x, e_y\}_{\text{roller}-\text{pin}}, \omega_{\text{roller}}\right)$$

are collected in one vector of unknowns and simultaneously solved using a damped Newton-Raphson iteration scheme.
From a numerical perspective the weak form finite element formulation of the governing EHL equations of both sub-models are similar, except from the fact that the computational domains are different. Therefore for numerical details pertaining the fully-coupled approach the reader is referred to [9] as only the main features are recalled here.
A similar customized element size distribution, as detailed in [9], was employed for the equivalent EHL computational domain for the cam-roller contact.
For the roller-pin contact a similar strategy was followed, i.e. in the pressure build-up region a dense element distribution was chosen which was allowed to decrease gradually as the distance from the fluid film boundary increased.
For the both models Lagrange quintic elements were used for the hydrodynamic part while for the elastic part Lagrange quadratic elements were used. The aforementioned custom tailored meshes for cam-roller and roller-pin EHL models correspond to approximately 350,000 degrees of freedom in total.
Steady-state solutions were fed as initial guess for the transient calculations. Steady-state solutions are reached within 11 iterations, corresponding to relative errors between $10^{-3} - 10^{-4}$ and calculation times ranging from 1.5-2 minutes on a computer with an Intel(R) Core(TM)i7-2600 processor.
For the transient calculations a dimensionless time step $\Delta\theta$ of 0.01 was chosen. In regions where abrupt kinematic variations occur smaller time step sizes where chosen.

3 Results

In this section a comprehensive transient analysis, for the considered cam and roller follower, is performed and the results are presented. The analysed cam-roller follower unit is part of a fuel injection pump unit of a heavy duty Diesel engine. The operating conditions considered here are similar to those presented in Alakhramsing et al. [2] and correspond to a cam rotational speed of 950 RPM. The configuration parameters and reference operating conditions are given in Table 1.

TABLE 1: Reference operating conditions and geometrical parameters for cam roller follower analysis. Adopted from Alakhramsing et al. [2].

Parameter	**Value**	**Unit**
E'	220	GPa
ν	0.3	-
α	1.78E-8	Pa^{-1}
η_0	0.01	Pa·s
R_f	0.018	m
R_pin	0.0095	m
C	74	μm
L	0.021	m
R_y	4.5	m
m_roller	0.11	kg
A	17	μm
L_s	0.007	m
z_m	50	μm
R_ref	0.015	m
U_ref	4.2	m/s
F_ref	2250	N

Figure 6 presents the dimensionless variation of the cam surface speed, load and reduced radius of curvature for the cam-roller contact. As explained in reference [2] the profile for the contact force inhibits abrupt variations, ranging from 2kN to 13kN, which are due to sudden activation and de-activation of pumping action. Furthermore, the cam surface speed and reduced radius of curvature are fairly constant (with minor variations) throughout the cam's lateral profile. Note that the variations of $C_R(\theta)$, $C_U(\theta)$ and $C_F(\theta)$ are identical for $0^\circ - 180^\circ$ and $180^\circ - 360^\circ$ cam angle. Therefore, in this work results are only presented for $0^\circ - 180^\circ$ cam angle.

Figures 7 and 8(a) depict height expressions for the pressure distributions in the cam-roller and roller-pin contact at 64° cam angle (cam's nose region), where the tribological conditions are worst. In both aforementioned figures traditional characteristics corresponding

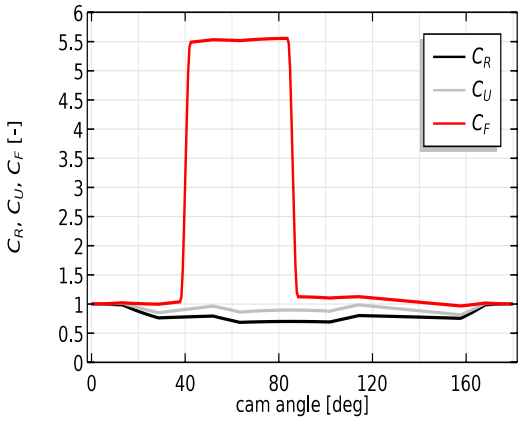

FIGURE 6: Variation of the dimensionless reduced radius $C_R(\theta)$, cam surface speed $C_U(\theta)$ and contact force $C_F(\theta)$ as a function of cam angle θ.

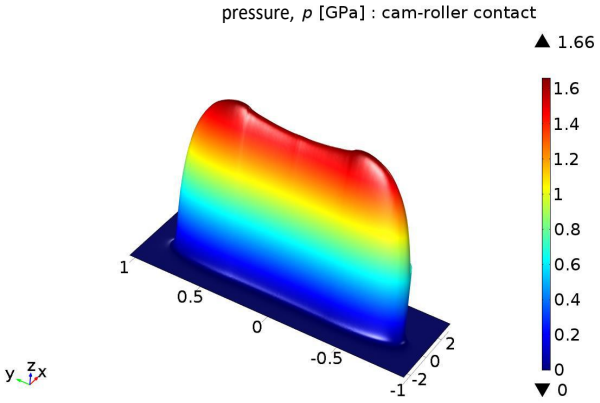

FIGURE 7: The pressure distribution for the cam-roller contact at 64° cam angle. Note that here dimensionless space coordinates (X, Y), as given in eq. 1, are used. Furthermore, the dimensions are exaggerated for the sake of clarity.

to finite line contact solutions are observed. To be more specific, for the cam-roller contact, which has a logarithmically shaped roller, typical secondary pressure peaks are observed at the sides of the contact. Near the occurrence of the secondary pressure peak, the absolute minimum film thickness $h_{\min}$ is located.

For the roller-pin contact, which has a axially crowned pin, the maximum pressure is located in the central plane ($Y = 0$). Due to axial crowning of the pin, the contact footprint has an elliptic shape. Figure 8(c) shows the contour plot of the film thickness distribution for 64° cam angle, from which can be extracted that side lobes are formed where minimum film thickness $h_{\min}$ occurs (see Nijenbanning et al. [14]).

Figure 8(b) presents the pressure and film thickness distribution for the roller-pin contact at the $Y = 0$ plane. It can readily be observed that the pressure and film thickness distribution inhibit typical EHL characteristics, i.e. a Hertzian parabolic type pressure curve and film thickness distribution which is uniform in the centre of the contact and has a local restriction $h_{\min,\text{central}}$ at the outlet of the contact. Similar findings were reported

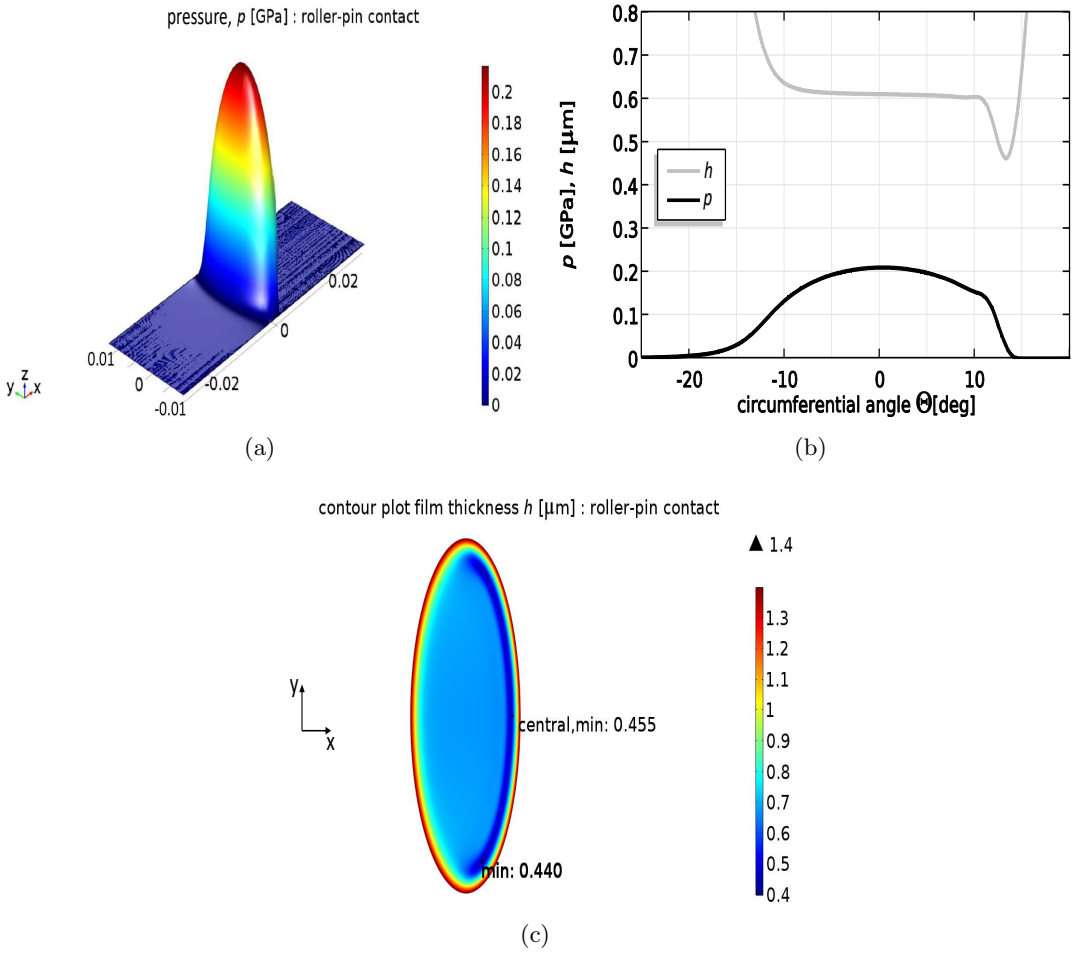

FIGURE 8: Evaluation of pressure and film thickness distribution for the roller-pin contact. The operating conditions correspond to those at 64° cam angle, which lies in the cam's nose region.a)The pressure distribution. Space coordinates are dimensional here, b)Pressure and film thickness distribution along line $Y = 0$. c) Contour plot of the film thickness distribution illustrating the formation of side lobes.

by O'Donoghue et al. [15] for elastic journal bearings with high eccentricity ratios. An important remark to make here is that the roller-pin contact, may be conformal in nature, but has a similar tribological behaviour as non-conformal finite length line contacts for the range of loads considered. In line with this finding, the importance of axial surface profiling of the pin is highlighted here as an axially straight pin might induce edge loading.

Figure 9(a) shows the evolution of minima film thickness as a function of the cam angle. Again, note that $h_{\text{min,central}}$ is the central plane ($Y = 0$) minimum film thickness, while h_{min} is absolute minimum film thickness which usually occurs at the rear of the contact where axial surface profiling starts [1].

At a first glance one may observe the "dips" in the profiles between $40° - 90°$ cam angle. These are mainly due to the sudden increase in contact force, as the cam surface speed

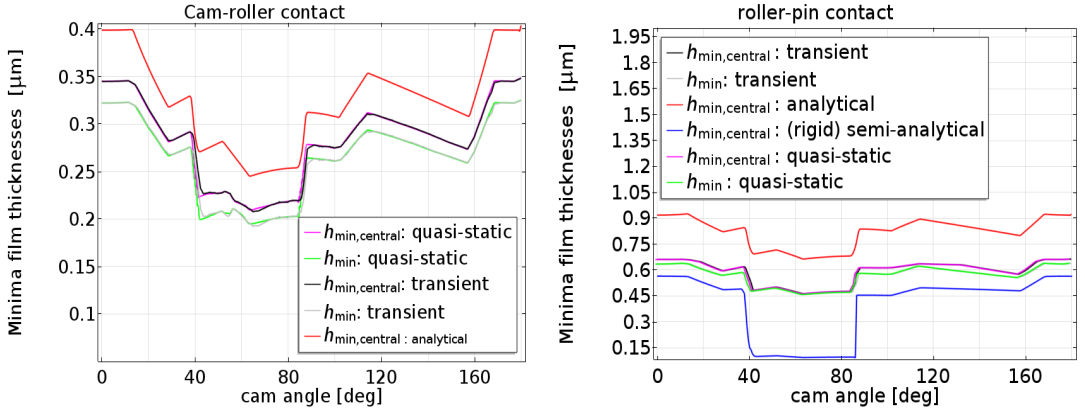

FIGURE 9: Evolution of minima film thicknesses for a) cam-roller contact and b) roller-pin contact.

and radius of curvature are fairly constant. Figure 9(a) also compares the results for a full transient solution with those obtained using quasi-static analysis. It can be concluded that transient effects, in this case squeeze film motion, are negligible as a minimal phase lag between the solutions is observed. These findings are in line with past studies [6, 13] from which may be concluded that squeeze film effects are mainly important in cases where the entrainment velocity profile inhibits points of flow reversal, i.e. the entrainment velocity profiles passes a zero value. Figure 9(a) also shows the evolution of the minimum film thickness obtained using the Dowson-Higginson [5] film thickness equation for infinite line contact. It is clear that the analytical solution significantly overestimates $h_{\text{min,central}}$ as it does not account for side leakage.

Similar observations are made for the roller-pin contact (see Figure 9(b)), i.e. quasi-static analysis yields fairly accurate results as squeeze film motion effects appear to be negligible. For the sake of comparison Figure 9(b) also the depicts the results obtained using the semi-analytical model, based on rigid surfaces, as used by Alakhramsing et al. [2]. It is clear that, especially in the high contact force regions, the minimum film thickness is highly underestimated as elastic deformation is disregarded in this model. In fact, for the rigid surface semi-analytical model, the dimensionless eccentricity ratio $\epsilon = \frac{e}{C}$ is not allowed to be larger than one, which leads to calculation of very small film thicknesses. It is apparent from Figure 14 that the dimensionless eccentricity ratio is larger than one throughout the whole operating range. This also highlights the importance of taking into account elastic deformation of roller and pin in the analysis. Finally, if closely noticed, one may observe that the ratio $h_{\text{min}}/h_{\text{min,central}}$ increases in the cam's nose region. This is mainly due to the fact that with formation of side-lobes, where h_{min} occurs, the ratio $h_{\text{min}}/h_{\text{min,central}}$ is load dependent (see for instance Nijenbanning et al. [14] and Alakhramsing et al. [1]).

From Figure 8(b) it can be extracted that the pressure and film thickness distribution in the highly loaded roller-pin contact, which is a conformal contact, inhibits typical EHL features for concentrated non-conformal contacts. The conformal contact in this case may be described by a cylinder with radius R_{pin} in a hollow outer cylinder with inner radius $R_{\text{pin}} + C$. For conformal contacts the reduced radius of curvature can be calculated provided that the radius of curvature of the (concave) outer cylinder radius is taken as negative. For the case considered (see Table 1) this would be approximately 1m. The result for the evolution of $h_{\text{min,central}}$, after applying the Dowson-Higginson [5] film thickness equation for infinite line contacts, for the roller-pin contact is depicted in Figure 9(b). Similar as for the cam-roller contact, the minimum film thickness is significantly overestimated due to non-typical EHL characteristics of finite length line contacts.

Figure 10 presents the evolution of the maximum pressures corresponding to the cam-roller and roller-pin contact. As can be seen, the maximum pressure for the cam-roller contact cycles between 0.65-1.75 GPa, while the roller-pin contact experiences significantly lower pressures (ranging between 0.1-0.25 GPa). The difference in experienced pressure between cam-roller and roller-pin contact is due to the difference in contact area. As a matter of fact, the contact width for the cam-roller contact varies between 0.2mmm-0.6mm, corresponding to base circle and nose regions, respectively. For the roller-pin contact the contact width varies between 3.8mm-5.8mm, corresponding to base circle and nose regions, respectively.

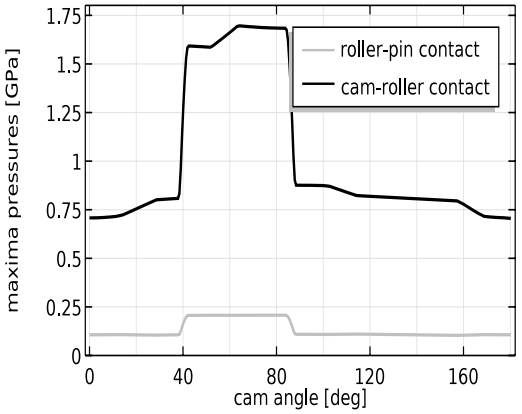

FIGURE 10: Evolution of the maximum pressures, corresponding to the cam-roller and roller-pin contact, as a function of cam angle θ.

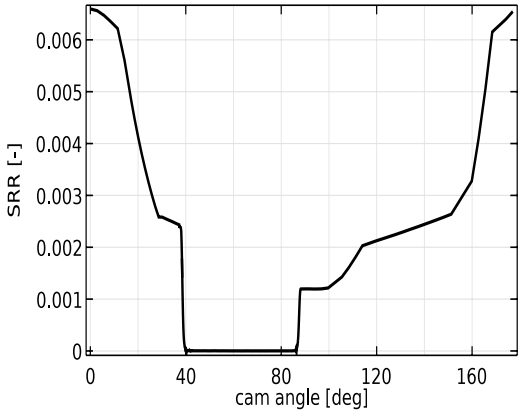

FIGURE 11: Evolution of the SRR, corresponding to the cam-roller contact, as a function of cam angle θ.

In general, for both contacts the tribological conditions are worst in the cam's nose region, i.e. both minimum film thickness and maximum pressure occur between $40° - 90°$ cam angle.

The evolution of the slide-to-roll ratio $\text{SRR} = \frac{U_{\text{cam}} - U_{\text{roller}}}{0.5(U_{\text{cam}} + U_{\text{roller}})}$, for the cam-roller contact, is depicted in Figure 11. SSR is lowest in the nose region, due to large contact forces, and highest in the base circle regions. Nevertheless, roller slip is negligible throughout the whole cam's lateral surface due to overall high contact forces and due to the fact that the limiting traction coefficient μ_{lim} is never exceeded.

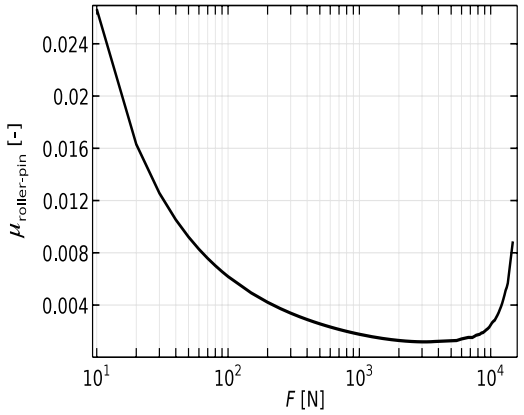

FIGURE 12: Variation of roller-pin contact friction coefficient $\mu_{\text{roller-pin}}$ as a function of applied load F. U_{roller} is kept fixed at 4.2m/s.

The friction coefficients for cam-roller and roller-pin contact are depicted in Figure 13 from which it can be noticed that very low values of friction coefficients are achieved. The range of values for the roller-pin friction coefficient are of the same magnitude as those measured by Lee and Patterson [12]. An increase in friction coefficient is noticed in the nose region. This increase is mainly caused due to a substantial increase in viscosity.

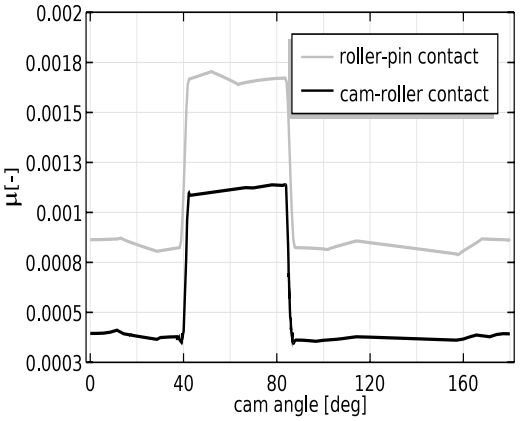

FIGURE 13: Evolution of friction coefficients $\mu_{\text{cam}-\text{roller}}$ and $\mu_{\text{roller}-\text{pin}}$ as a function of cam angle θ.

Assuming a composite surface roughness of 0.2μm, it can be inferred that the cam-roller contact operates in the mixed lubrication regime, i.e. $\frac{h}{\sigma} < 3$. This means that the friction coefficient for the cam-roller contact would be higher and the values depicted in Figure 13 should be seen as a minimum. On the other hand, whether the cam-roller contact operates in mixed or full-film regime should not have a large influence on the tribological behaviour of the roller-pin contact as operating in mixed lubrication regime of the cam-roller contact will only enhance traction, resulting to less slip. Extension to a mixed lubrication model for both cam-roller and roller-pin contact is suggested for future work.

Except from the fact that elastic deformation of roller and pin enhance the film thickness distribution, it is also worth noting that the friction coefficient is also significantly improved for the load range considered. This can be retrieved from Figure 12, which presents $\mu_{\text{roller}-\text{pin}}$ as a function of contact force F (and assuming U_{roller} to be constant). In fact, the $\mu_{\text{roller}-\text{pin}}$ is in its optimal range for the load range (2kN-13kN) considered. It is obvious that when elastic deformation is considered the contact area increases. Consequently, the hydrodynamic pressure decreases and thus also the sliding frictional force (which is viscosity dependent) decreases. The trend of $\mu_{\text{roller}-\text{pin}}$ can be explained as follows. When elastic deformation is insignificant, $\mu_{\text{roller}-\text{pin}}$ is inversely proportional to the Sommerfeld number $S = \frac{F}{\eta_0 \omega_{\text{roller}} L R_{\text{pin}}} \left(\frac{C}{R_{\text{pin}}}\right)^2$ (see for instance reference [2]), i.e. $\mu_{\text{roller}-\text{pin}} \sim 1/S$. So, in hydrodynamic lubrication (HL) $\mu_{\text{roller}-\text{pin}}$ decreases with increasing loads until the moment when elastic deformation becomes important, i.e. the elastohydrodynamic lubrication (EHL) regime is attained. In pure EHL conditions $\mu_{\text{roller}-\text{pin}}$ will increase with increasing loads. So, the load range in which the roller-pin contact operates can be seen as a transition zone from HL to EHL conditions. It is clear from Figure 12 that for loads higher than 10 kN approximately $\mu_{\text{roller}-\text{pin}}$ starts

increasing again. Meaning that for this case pure EHL conditions are achieved for loads higher than 10 kN approximately.

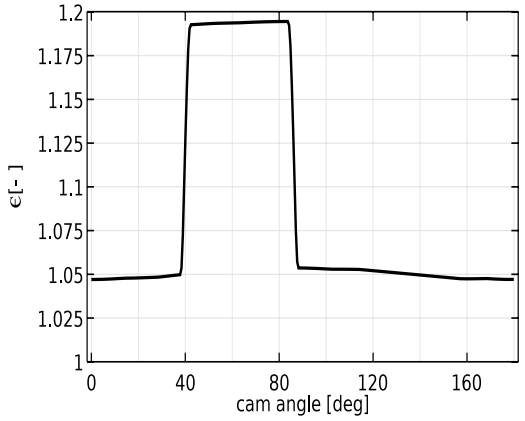

FIGURE 14: Evolution of the dimensionless eccentricity ratio ϵ, corresponding to the roller-pin contact, as a function of cam angle θ.

The power losses corresponding to cam-roller and roller-pin contact are shown in Figure 15. As reported in earlier work Alakhramsing et al. [2], rolling friction losses play a dominant role as roller slip appears to be negligible. Also note that the rolling power losses are proportional to the sum velocity and almost independent on contact force. This is also why the total power losses for the cam-roller contact cycles is around 6W with minor variations.

The power losses for the roller-pin contact, obtained using the full transient analysis, are compared with those obtained using the rigid semi-analytical model as used by Alakhramsing et al. [2]. For the roller-pin contact, which is a sliding contact, the power losses are proportional to the sliding speed. In the base circle regions the semi-analytical model, which does not include elastic deformation, overestimates the power losses as the contact area is overestimated and the film thickness is under estimated. Furthermore, in the nose region the semi-analytical model underestimates the power losses as the semi-analytical model assumes isoviscous behaviour, i.e. the viscosity increases significantly in the cam's nose region.

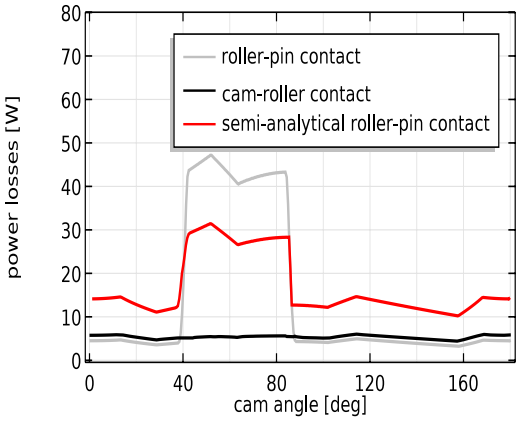

FIGURE 15: Evolution of the individual power losses, corresponding to the cam-roller and roller-pin contact, as a function of cam angle θ.

4 Conclusions

A multyphysics model, enabling coupled transient EHL simulations of cam-roller and roller-pin contact in cam-roller follower mechanisms, has been developed. For the transient analysis a heavily loaded cam-roller follower unit, as part of a heavy duty Diesel engine, was considered.

It has been shown that likewise the cam-roller contact, the roller-pin contact also inhibits typical finite line contact EHL characteristics at high loads. Coming on to the nature of finite line contacts, the importance of axial profiling for the roller-pin contact is highlighted here as edge loading is reduced.

Another important contribution made in this work is that is has been shown that elastic deformation of roller and pin significantly enhance the film thickness distribution in the roller-pin contact. Also, prediction of other crucial performance indicators such as maximum pressure and power losses as significantly improved when compared to the models assuming rigid surfaces.

Finally, for heavily loaded cam-roller followers, as studied in this work, it can be concluded that: i) transient effects are negligible and quasi-static analysis yields sufficiently accurate results, ii) roller slip is negligible due to high contact forces and pure rolling may be assumed, iii) highest power losses are associated with the roller-pin contact due to simple sliding and relatively larger contact area as compared to the cam-roller contact and, iv) due to the non-typical EHL characteristics of both cam-roller and roller-pin contact numerical analysis becomes inevitable for evaluation of crucial tribological performance indicators.

Due to the finite line contact nature of the roller-pin contact axial surface profiling seems to be a promising way to optimize the tribological performance of this contact. Extension of the model to other features, such as mixed lubrication, non-Newtonian, and optimizing

routines, is suggested for future work.

Acknowledgements

This research was carried out under project number F21.1.13502 in the framework of the Partnership Program of the Materials innovation institute M2i (www.m2i.nl) and the Netherlands Organization for Scientific Research (www.nwo.nl).

References

[1] S. Alakhramsing, M. de Rooij, D. Schipper, and M. van Drogen. Elastohydrodynamic lubrication of coated finite line contacts. *Proceedings of the Institution of Mechanical Engineers, Part J: Journal of Engineering Tribology*, 232(9):1077–1092, 2018.

[2] S. Alakhramsing, M. de Rooij, D. Schipper, and M. van Drogen. Lubrication and frictional analysis of cam–roller follower mechanisms. *Proceedings of the Institution of Mechanical Engineers, Part J: Journal of Engineering Tribology*, 232(3):347–363, 2018.

[3] Y. Chiu. Lubrication and slippage in roller finger follower systems in engine valve trains. *Tribology Transactions*, 35(2):261–268, 1992.

[4] COMSOL multiphysics. Comsol multiphysics modeling guide. *COMSOL Inc.*, www.comsol.com. (accessed 3 April 2017).

[5] D. Dowson and G. Higginson. *Elasto-hydrodynamic lubrication: the fundamentals of roller and gear lubrication*, volume 23. Pergamon Press, Oxford, United Kingdom, 1966.

[6] D. Dowson, C. Taylor, and G. Zhu. A transient elastohydrodynamic lubrication analysis of a cam and follower. *Journal of Physics D: Applied Physics*, 25(1A):A313, 1992.

[7] B. Fantino, J. Frene, and J. Du Parquet. Elastic connecting-rod bearing with piezoviscous lubricant: Analysis of the steady-state characteristics. *ASME. Journal of Lubrication Technology*, 101:190–197, 1979.

[8] H. Fujiwara and T. Kawase. Logarithmic profiles of rollers in roller bearings and optimization of the profiles. *NTN Technical Review*, 75:140–148, 2007.

[9] W. Habchi, D. Eyheramendy, P. Vergne, and G. Morales-Espejel. A full-system approach of the elastohydrodynamic line/point contact problem. *Journal of Tribology*, 130(2):021501, 2008.

[10] F. Ji and C. Taylor. A tribological study of roller follower valve trains. part 1: A theoretical study with a numerical lubrication model considering possible sliding. *Tribology Series*, 34:489–499, 1998.

[11] M. Khurram, R. Mufti, R. Zahid, N. Afzal, and U. Bhutta. Experimental measurement of roller slip in end-pivoted roller follower valve train. *Proceedings of the Institution of Mechanical Engineers, Part J: Journal of Engineering Tribology*, 229(9):1047–1055, 2015.

[12] J. Lee and D. Patterson. Analysis of cam/roller follower friction and slippage in valve train systems. Technical report, SAE Technical Paper 951039, 1995.

[13] S. Messe and A. Lubrecht. Transient elastohydrodynamic analysis of an overhead cam/tappet contact. *Proceedings of the Institution of Mechanical Engineers, Part J: Journal of Engineering Tribology*, 214(5):415–425, 2000.

[14] G. Nijenbanning, C. Venner, and H. Moes. Film thickness in elastohydrodynamically lubricated elliptic contacts. *Wear*, 176(2):217–229, 1994.

[15] J. O'Donoghue, D. Brighton, and C. Hooke. The effect of elastic distortions on journal bearing performance. *Journal of Lubrication Technology*, 89(4):409–415, 1967.

[16] C. Roelands. *Correlational aspects of the viscosity-temperature-pressure relationship of lubricating oils*. PhD thesis, Delft University of Technology, Delft, The Netherlands, 1966.

[17] M. Shirzadegan, A. Almqvist, and R. Larsson. Fully coupled EHL model for simulation of finite length line cam-roller follower contacts. *Tribology International*, 103:584–598, 2016.

[18] A. Turturro, R. Rahmani, H. Rahnejat, C. Delprete, and L. Magro. Assessment of friction for cam-roller follower valve train system subjected to mixed non-newtonian regime of lubrication. In *ASME 2012 Internal Combustion Engine Division Spring Technical Conference*, pages 917–923. American Society of Mechanical Engineers, 2012.

[19] S. Wu. A penalty formulation and numerical approximation of the reynolds-hertz problem of elastohydrodynamic lubrication. *International Journal of Engineering Science*, 24(6):1001–1013, 1986.

[20] D. Wymer and A. Cameron. Elastohydrodynamic lubrication of a line contact. *Proceedings of the Institution of Mechanical Engineers*, 188(1):221–238, 1974.

Paper D

A mixed-TEHL analysis of cam-roller contacts considering roller slip: on the influence of roller-pin contact friction

S.S. Alakhramsing[1], M.B. de Rooij[1], A. Akchurin[1] D.J. Schipper[1] and M. van Drogen[2]

ASME Journal of Tribology, 141 (1), 011503-011503-15, 2019.
DOI:10.1115/1.4040979

[1]Faculty of Engineering Technology, University of Twente, P.O. Box 217, 7500 AE Enschede, The Netherlands
[2]Central Laboratory Metals, DAF Trucks N.V., P.O. Box 90065, 5600 PT Eindhoven, The Netherlands

Nomenclature

a Hertzian contact half-width $= \sqrt{\frac{8FR_x}{\pi LE'}}$ (m)

c lubricant heat capacity (J/kg·K)

c_c cam material heat capacity (J/kg·K)

c_r roller material heat capacity (J/kg·K)

E' reduced elasticity modulus $= \frac{2}{\frac{1-\nu_\mathrm{c}^2}{E_\mathrm{c}}+\frac{1-\nu_\mathrm{r}^2}{E_\mathrm{r}}}$ (Pa)

f coefficient of friction (-)

F force (N)

F_a asperity friction force (N)

F_h hydrodynamic friction force (N)

h film thickness (m)

H dimensionless film thickness

h_0 rigid body displacement (m)

H_0 dimensionless rigid body displacement

k lubricant thermal conductivity (W/m·K)

k_c cam material heat capacity (W/m·K)

k_r roller material heat capacity (W/m·K)

L axial length (m)

p total pressure (Pa)

P dimensionless total pressure

p_h hydrodynamic pressure (Pa)

P dimensionless hydrodynamic pressure

$\bar{p}_{\mathrm{a}}$ asperity mean contact pressure (Pa)

$\bar{P}_{\mathrm{a}}$ dimensionless asperity mean contact pressure

p_{av} average Hertzian pressure $= \frac{F}{2aL}$ (Pa)

p_{Hertz} Hertzian pressure $= \frac{2F}{\pi La}$ (Pa)

R_x reduced radius of curvature (m)

R_{pin} pin radius (m)

R_{f} outer radius roller (m)

SRR slide-to-roll ratio

T temperature (K)

T_0 ambient temperature (K)

u, w x, z components of elastic displacement field (m)

U, W dimensionless X, Z components of elastic displacement field

u_{c} cam surface velocity (m/s)

u_{r} roller surface velocity (m/s)

u_{m} lubricant mean entrainment velocity (m/s)

x, y, z spatial coordinates (m)

X, Y, Z dimensionless spatial coordinates

α pressure-viscosity coefficient (GPa^{-1})

μ lubricant viscosity (Pa·s)

μ_0 lubricant reference viscosity (Pa·s)

η generalized Newtonian viscosity (Pa·s)

$\bar{\eta}$ dimensionless generalized Newtonian viscosity

θ cam angle (rad)

τ shear stress (MPa)

τ_0 characteristic Eyring shear stress (MPa)

ρ lubricant density (kg/m^3)

$\bar{\rho}$ dimensionless lubricant density

ρ_0 lubricant reference density (kg/m^3)

ρ_c cam material density (kg/m^3)

ρ_r roller material density (kg/m^3)

$\bar{\rho}$ lubricant dimensionless viscosity

ω rotational speed (rad/s)

Ω computational domain

$\partial\Omega_f$ contact boundary

$\partial\Omega_d$ bottom boundary

Subscripts

a asperity

c cam

cent central

f follower

h hydrodynamic

min minimum

r roller

A mixed-TEHL analysis of cam-roller contacts considering roller slip: on the influence of roller-pin contact friction

Abstract

In this work a mixed lubrication model, applicable to cam-roller contacts, is presented. The model takes into account non-Newtonian, thermal effects and variable roller angular velocity. Mixed lubrication is analysed using the load sharing concept, using measured surface roughness. Using the model a quasi-static analysis for a heavily loaded cam-roller follower contact is carried out. The results show that when the lubrication conditions in the roller-pin contact are satisfactory, i.e. low friction levels, then the nearly "pure rolling" condition at the cam-roller contact is maintained and lubrication performance is also satisfactory. Moreover, non-Newtonian and thermal effects are then negligible. Furthermore, the influence of roller-pin friction coefficient on the overall tribological behaviour of the cam-roller contact is investigated. In this part a parametric study is carried out in which the friction coefficient in the roller-pin contact is varied from values corresponding to full film lubrication to values corresponding to boundary lubrication. Main findings are that at increasing friction levels in the roller-pin contact there is a sudden increase in the slide-to-roll ratio (SRR) in the cam-roller contact. The value of the roller-pin friction coefficient at which this sudden increase in SRR is noticed depends on the contact force, the non-Newtonian characteristics and viscosity-pressure dependence. For roller-pin friction coefficient values higher than this critical value, inclusion of non-Newtonian and thermal effects becomes highly important. Furthermore, after this critical level of roller-pin friction, the lubrication regime rapidly shifts from full film to mixed lubrication. Based on the findings in this work the importance of ensuring

adequate lubrication in the roller-pin contact is highlighted as this appears to be the critical contact in the cam-follower unit.

Keywords: EHL, cam-roller, roller-pin, mixed lubrication, roller slip

1 Introduction

Cam-roller followers as part of valve-train mechanisms in internal combustion engines are of crucial importance. Anderson [7] reported that the valve train mechanism accounts for 6-10% of the internal friction losses, which is significant. However, fluctuating contact forces, varying radius of curvature and lubricant entrainment velocity make the tribological design of cam-roller followers units very challenging.

Two lubricated contacts may be distinguished within the cam-roller follower unit namely, the roller-pin contact and the cam-roller contact. The former is a conformal contact, while the latter is a non-conformal contact. The roller is allowed to freely rotate along its axis. The roller rotational velocity is governed by the torque balance applied on the roller itself (see Figure 1).

The roller-pin contact ideally functions as a hydrodynamic journal bearing favouring low friction levels. The intention is to keep the friction levels in the roller-pin contact as low as possible to allow a low resisting torque and hence less sliding at the cam-roller contact. The latter is often referred as roller slip in literature.

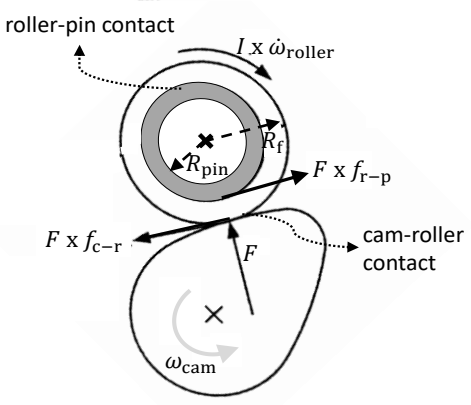

FIGURE 1: Cam-roller follower configuration showing the frictional forces acting at the cam-roller and roller-pin contact.

Note that the lubricant entrainment speed of the cam-roller contact on itself is a function of geometrical configuration, cam rotational velocity and roller angular speed. This means that the tribological behaviour of the cam-roller contact is strongly affected by

lubrication performance in the roller-pin contact. In past literature one can find a few studies, which have dealt with this subject.

Duffy [18] and Khurram et al. [31] have proven the occurrence of roller slippage experimentally. Lee and Patterson [32] have reported that the problem of wear still remains if roller slippage occurs.

Many other authors have tried to understand the tribological performance of the cam-roller contact theoretically. Chiu [15] and later Ji and Taylor [27] were the first ones to develop lubrication models that take into account possible sliding at the cam-roller contact. Both the aforementioned authors concluded that roller slip occurs at high cam rotational velocities due to simultaneous increase in roller angular momentum. Turturro et al. [46] presented a steady-state model for a non-Newtonian lubricant to investigate the effect of viscosity on the friction of the cam and roller follower. Torabi et al. [45] developed a mixed thermo-elastohydrodynamic lubrication (TEHL) numerical model and compared the tribological performance between the flat-faced and roller follower under similar operating conditions. The aforementioned authors showed that thermal effects and mixed lubrication generally affect the minimum film thickness and cannot be neglected. In an earlier work [4] the current authors developed a full numerical EHL model for both cam-roller and roller-pin contact. In that study a cam-roller follower unit as part of a fuel injection unit in a heavy duty Diesel engine, was analysed. The authors showed that squeeze-film motion effects are negligible and quasi-static analysis would yield sufficiently accurate results for highly loaded cam-roller follower contacts. The loads considered ranged between 2.5kN-15kN. Due to the all time high loads, inertia effect were comparably found to be negligible. It was also shown that extremely low levels of friction coefficient are achieved at the roller-pin contact when operating under ideal conditions (ranging between 0.001-0.003). The latter findings are also in line with experimental and theoretical results [27, 32].

As earlier mentioned, the friction coefficient acting at the roller-pin contact has a major influence on the tribological behaviour at the cam-roller contact. Notable is that the coupling between cam-roller contact and roller-pin contact has never been investigated systematically despite its high interdependency. All previously mentioned studies assumed ideal conditions at the roller-pin contact, i.e. a low friction coefficient.

This paper attempts to fill in the aforementioned gap by analysing the “sensitivity” of cam-roller lubrication performance as a function of the friction levels in the roller-pin contact. This assessment should provide useful insight into the coupled tribological behaviour of the two contacts. Lubrication performance at the roller-pin contact may strongly be deteriorated by external factors such as insufficient oil supply, misalignment, manufacturing errors etc. Detailed investigation into the external factors is beyond the scope of the present study. This is why the “sensitivity” of the cam-roller lubrication performance as function of the lubrication mode of the roller-pin contact is assessed here

by assuming a friction coefficient at the roller-pin contact. In order to accurately predict the frictional force at the cam-roller contact a mixed-thermo-elastohydrodynamic (TEHL) model is presented in this paper. The model efficiently takes into account thermal, non-Newtonian and surface roughness effects using measured surface topography.

2 Mathematical model

In this section the mathematical model, including the theory and governing equations, is described. In this study axial surface profiling of opposing surfaces is neglected in order to reduce the computational effort. In fact, the interacting solids are assumed to be perfectly straight in axial direction and also, the pressure distribution in axial direction is assumed to be uniform. This simplifies the problem to that of a classical line contact. Furthermore, as also indicated in the introduction section, a cam-roller follower unit as part of the fuel injection system in a heavy duty Diesel engine is studied in this paper. As motivated by Alakhramsing et al. [5], a quasi-static analysis is justified for the considered application. Therefore, the model described in this section relies on steady-state conditions.

The complete model consists of two sub-models, which are used to solve for the pressure and temperature distribution in the contact, respectively. The mixed-EHL model which governs the pressure distribution in the contact is based on the load-sharing concept as defined by Johnson [28]. The temperature distribution in the contact is governed by the energy equations, which are employed for the lubricant and bounding solids.

The thermal and mixed-EHL models are interlinked with each other through the rheological formulations of the lubricant.

The general modelling approach here resembles the non-Newtonian TEHL modelling approach, as introduced by Habchi et al. [25], for smooth surfaces. The model developed in reference [25] leans on a full-system finite element formulation of the governing TEHL equations. However, a few additions are made here to the TEHL model, to account for variable roller angular velocity and roughness effects. These will be treated throughout this mathematical section.

2.1 Mixed lubrication model

Following the load sharing concept of Johnson et al. [28], in the mixed lubrication regime the contact load is partly carried by the fluid film and partly by the interacting asperities. In equation form this yields:

$$F = \int_{\Omega} p \, d\Omega \; = \int_{\Omega} (p_{\mathrm{a}} + p_{\mathrm{h}}) \, d\Omega \tag{1}$$

where, p_{a} and p_{h} denote the pressure carried by asperities and fluid film respectively. p is the summation of the individual distributions of p_{a} and p_{h}. For the sake of clarity, p is called the total pressure in this work. Ω denotes the calculation domain. The cam-roller pairs considered here are grinded in rolling direction. Therefore, for the sake of simplicity, the influence of the surface roughness on fluid pressure and micro-EHL effects are assumed to be negligible in this work. In this work a separate dry rough contact model and smooth EHL model are used to evaluate p_{a} and p_{h} respectively. These two models are interlinked through the film thickness. Therefore these models will be described individually in the subsequent (sub-)sections. The algorithm of the load-sharing based model herein is similar to that which is described in the work of Masjedi and Khonsari [36].

2.1.1 Smooth EHL component

The finite element method (FEM)-based smooth line contact EHL model is governed by four main equations, namely: the generalized Reynolds equation, the linear elasticity equations, the load balance and the torque balance (which couples the cam-roller and roller-pin contact). All classical EHL equations are presented in dimensionless form. Hence, the following dimensionless variables are introduced:

$$\begin{aligned} X &= \frac{x}{a} \qquad Z = \frac{z}{a} \qquad P_{\mathrm{h}} = \frac{p_{\mathrm{h}}}{p_{\mathrm{Hertz}}} \qquad \bar{\eta} = \frac{\eta}{\mu_0} \qquad \bar{\rho} = \frac{\rho}{\rho_0} \\ H &= \frac{hR_x}{a^2} \quad H_0 = \frac{h_0 R_x}{a^2} \quad U = \frac{uR_x}{a^2} \quad W = \frac{WR_x}{a^2} \end{aligned} \tag{2}$$

where a and p_{Hertz} denote the dry Hertzian half-contact width and maximum Hertzian pressure respectively. The density ρ and generalized Newtonian viscosity η are allowed to vary in both x and z-direction, i.e. the lubricant properties are also allowed to vary across the film thickness (z-direction). $Z = 0$ and $Z = 1$ correspond to the roller and cam surfaces, respectively.

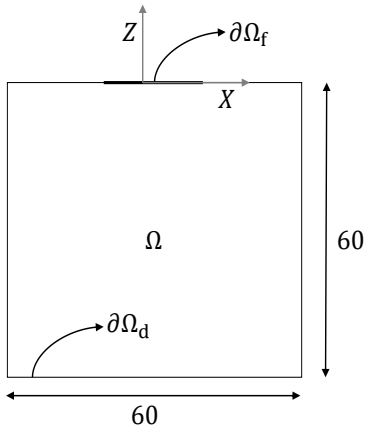

FIGURE 2: Equivalent geometry for EHL analysis of the infinite line contact problem. The dimensions are exaggerated for the sake of clarity.

Figure 2 shows the equivalent EHL computational domain Ω for the cam-roller contact. In the current approach the elastic deformation is not calculated using the traditional half-space approximation. Instead, the 2D linear elasticity equations with appropriate boundary conditions are employed on a finite computational domain to solve for the displacement field. In this model a finite elastic domain Ω (with equivalent mechanical properties) is used for calculation of the total elastic deformation. This avoids calculating the elastic deformation twice for the two structures and hence reduces the computational effort required. The dimensionless side lengths of 60 of elastic domain Ω are chosen in such a way to ensure that a zero elastic displacement field is attained in regions far away from contact zone $\partial\Omega_f$. In fact, in [25] the author showed that the side length of the finite structure should be at least 60 times the Hertzian half-contact width so that the elastic deformation would agree with the solution obtained by using the classical multilevel multi-integration (MLMI) method [12] applied to a half-space. Note that $\partial\Omega_f$ denotes the fluid film boundary on which the generalized-Reynolds equation is solved and has dimensions of $-4.5 \leq X \leq 1.5$, to ensure that the pressure is nil at the exit points of the boundary. $\partial\Omega_d$ denotes the bottom boundary, where the elastic displacement should be zero. As mentioned earlier, the calculation of the elastic displacement field is based on the 2D-linear elasticity equations which are written as follows [26]:

$$\begin{cases} -\frac{\partial}{\partial X}\left[C_1\frac{\partial U}{\partial X}+C_2\frac{\partial W}{\partial Z}\right]-\frac{\partial}{\partial Z}\left[C_3\left(\frac{\partial U}{\partial Z}+\frac{\partial W}{\partial X}\right)\right]=0 \\ \\ -\frac{\partial}{\partial X}\left[C_3\left(\frac{\partial U}{\partial Z}+\frac{\partial W}{\partial X}\right)\right]-\frac{\partial}{\partial Z}\left[C_2\frac{\partial U}{\partial X}+C_1\frac{\partial W}{\partial Z}\right]=0 \end{cases} \tag{3}$$

where U and W are the X and Z-components of the elastic displacement field respectively. The coefficients C_1, C_2 and C_3 are constants in the compliance matrix and can be

calculated as follows:

$$\begin{aligned} C_1 &= \frac{\tilde{E}_{\mathrm{eq}}\left(1-\nu_{\mathrm{eq}}\right)}{\left(1+\nu_{\mathrm{eq}}\right)\left(1-2\nu_{\mathrm{eq}}\right)} \\ C_2 &= \frac{\nu_{\mathrm{eq}}\tilde{E}_{\mathrm{eq}}}{\left(1+\nu_{\mathrm{eq}}\right)\left(1-2\nu_{\mathrm{eq}}\right)} \\ C_3 &= \frac{\tilde{E}_{\mathrm{eq}}}{2\left(1+\nu_{\mathrm{eq}}\right)} \end{aligned} \tag{4}$$

The (dimensionless) equivalent mechanical properties $\left(\tilde{E}_{\mathrm{eq}}, \nu_{\mathrm{eq}}\right)$ of elastic domain Ω are calculated as follows:

$$\begin{aligned} \tilde{E}_{\mathrm{eq}} &= \frac{E_{\mathrm{c}}^2 E_{\mathrm{r}}(1+\nu_{\mathrm{r}})^2 + E_{\mathrm{r}}^2 E_{\mathrm{c}}(1+\nu_{\mathrm{c}})^2}{\left[E_{\mathrm{c}}\left(1+\nu_{\mathrm{r}}\right)+E_{\mathrm{r}}\left(1+\nu_{\mathrm{c}}\right)\right]^2}\frac{a}{R_x p_{\mathrm{Hertz}}} \\ \nu_{\mathrm{eq}} &= \frac{E_{\mathrm{c}}\nu_{\mathrm{r}}\left(1+\nu_{\mathrm{r}}\right)+E_{\mathrm{r}}\nu_{\mathrm{c}}\left(1+\nu_{\mathrm{c}}\right)}{E_{\mathrm{c}}\left(1+\nu_{\mathrm{r}}\right)+E_{\mathrm{r}}\left(1+\nu_{\mathrm{c}}\right)} \end{aligned} \tag{5}$$

where subscripts "c" and "r" denote cam and roller respectively. The hydrodynamic pressure distribution in the contact is described using the generalized Reynolds equation for non-Newtonian thermal elastohydrodynamic lubrication, as given by Yang and Wen [39]:

$$\frac{\partial}{\partial X}\left(\bar{\varepsilon}\frac{\partial P_{\mathrm{h}}}{\partial X}\right)-\frac{\partial\left(\bar{\rho}^{*}H\right)}{\partial X}-\zeta P_{\mathrm{h}}^{-}=0 \tag{6}$$

where,

$\bar{\varepsilon}=\left(\frac{\bar{\rho}}{\bar{\eta}}\right)_e\frac{H^3}{\lambda}$ $\quad\left(\frac{\bar{\rho}}{\bar{\eta}}\right)_e=\frac{\bar{\eta}_e\overline{\rho'}_e}{\overline{\eta'}_e}-\overline{\rho''}_e$ $\quad\lambda=\frac{u_{\mathrm{m}}R_x^2\mu_{\mathrm{r}}}{a^3 p_{\mathrm{Hertz}}}$

$\mathrm{u_m}=\frac{u_{\mathrm{c}}+u_{\mathrm{r}}}{2}$ $\quad\bar{\rho}^{*}=\frac{\left[\bar{\eta}_e\overline{\rho'}_e(u_{\mathrm{c}}-u_{\mathrm{r}})+\bar{\rho}_e u_{\mathrm{c}}\right]}{u_{\mathrm{m}}}$

$\bar{\rho}_e=\int_0^1\bar{\rho}\,dZ$ $\quad\overline{\rho'}_e=\int_0^1\bar{\rho}\int_0^Z\frac{dZ'}{\bar{\eta}}\,dZ$

$\overline{\rho''}_e=\int_0^1\bar{\rho}\int_0^Z\frac{Z'dZ'}{\bar{\eta}}\,dZ$ $\quad\frac{1}{\bar{\eta}_e}=\int_0^1\frac{dZ}{\bar{\eta}}$

$\frac{1}{\overline{\eta'}_e}=\int_0^1\frac{ZdZ}{\bar{\eta}}$ $\quad R_x=\frac{1}{\frac{1}{R_{\mathrm{c}}}+\frac{1}{R_{\mathrm{f}}}}$

R_{c} and R_{f} are the cam radius of curvature and outer radius of the roller follower (see Figure 1). The outer roller surface velocity u_{r}, the calculation of which will be treated later, is an unknown variable that is dependent on the frictional forces working at the cam-roller and roller-pin contact. Note in eq. 6 both viscosity and density are allowed to vary across the film thickness through the integral terms defined.

In order to treat the free boundary problem (associated with the fluid film cavitation

phenomenon) arising at the outlet of the contact the penalty formulation of Wu [52] is utilized here. Using this formulation all negative pressures, arising at the exit of the lubricated contact, are penalized to zero by adding an penalty term. The penalty term is the last term on the LHS of eq. 6. P_{h}^{-} corresponds to the negative part of the pressure distribution and ζ is an arbitrary large number. Hence, only negative pressures are affected using this penalty term so that the consistency of eq. 6 is preserved. Wu [52] also showed that the Reynolds boundary condition $\nabla P_{\mathrm{h}} \cdot \overrightarrow{n}_c = 0$ is automatically satisfied using this approach. It is worth mentioning that the penalty formulation does not ensure mass conservation when film reformation occurs. However, this is not an issue here because such film reformation rarely affects the behaviour within concentrated contacts. Appropriate cavitation modelling approaches may for instance be found in references [10, 41]. Suitable numerical stabilization techniques, as detailed in [3], are utilized in order to stabilize the solution of eq. 6 at high loads. Finally, fully flooded conditions are assumed at the inlet of the contact.

The film thickness H of the cam-roller conjunction may be written as follows:

$$H\left(X\right) = H_0 + \frac{X^2}{2} - W\left(X\right) \tag{7}$$

where H_0 represents the rigid body displacement, which is an unknown associated with the load balance eq. 8 as defined by Johnson et al. [28] :

$$\int_{\partial\Omega_{\mathrm{f}}} P\left(X\right) dX = \int_{\partial\Omega_{\mathrm{f}}} P_{\mathrm{h}}\left(X\right) dX + \int_{\partial\Omega_{\mathrm{f}}} \bar{P}_{\mathrm{a}}\left(X\right) dX = \frac{\pi}{2} \tag{8}$$

where $\overline{P}_{\mathrm{a}}$ represents the dimensionless dry auxiliary contact pressure, the calculation of which, will be treated in the "Asperity contact component" section. The linear elasticity equations eq. 3 and generalized Reynolds equation eq. 6 are associated with the following boundary conditions respectively:

For the generalized Reynolds equation [25]:

$$P_{\mathrm{h}}\left(X = -4.5\right) = P_{\mathrm{h}}\left(X = 1.5\right) = 0 \quad \text{on} \quad \partial\Omega_{\mathrm{f}} \tag{9}$$

For the elastic model the BCs are summarized as follows:

$$\begin{cases} U = W = 0 & \text{on } \partial\Omega_{\mathrm{d}} \\ \tilde{\sigma}_n = \sigma_{ZZ} = C_2 \dfrac{\partial U}{\partial X} + C_1 \dfrac{\partial W}{\partial Z} = -P & \text{on } \partial\Omega_{\mathrm{f}} \\ \tilde{\sigma}_n = 0 & \text{elsewhere} \end{cases} \tag{10}$$

Please note that the total pressure P is used for the evaluation of the elastic deformation in eq. 10.

2.1.2 Asperity contact component

In order to calculate the proportion of the load carried by the asperities in the mixed lubrication model an approach, as introduced by Bobach et al. [11], is followed. This approach will be described briefly now.

In this study a boundary element method-based model of elastic/plastic solid body contact, as described in the work of Akchurin et al. [2], is used to calculate the local dry/solid contact pressures of a representative section of the real measured surface topography.

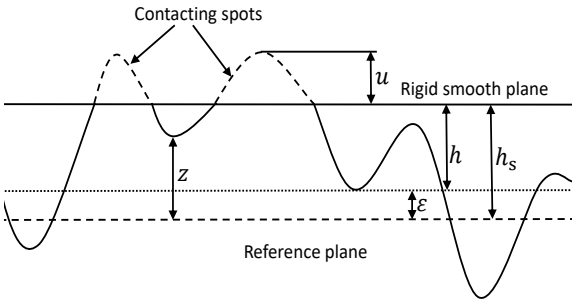

FIGURE 3: Schematic view of the surfaces which are in contact. $z(x, y)$ represents the surface roughness heights, h_s the separating distance and the deflection $u(x, y) = z(x, y) - h_s(x, y)$.

The model described in reference [2], and used here, is based upon the elastic half-space theory and includes a linear/elastic ideal/plastic material model. Hence, the allowable pressures within the contact are therefore a confined to a pressure $p_{a,lim}$ at which plastic flow occurs. $p_{a,lim}$ is an input parameter for the contact model and can be evaluated using micro-hardness measurements.

In the mixed lubrication model developed in the work of Akchurin et al. [2] a separation distance h_s is required to calculate the asperity contact pressure distribution p_a (see Figure 3). The separating distance h_s is related to the film thickness h through the condition of volume conservation, as defined by Johnson et al. [28]. To be more specific, h_s should fulfill the condition that the total lubricant volume between the smooth surfaces should be equal to the volume occupied by the pockets formed by the non-contacting parts between the rough surfaces. In fact, the separation distance h_s has the same shape as the film thickness h but with a constant offset ϵ so that volume conservation is preserved [2]. This can also be inferred from Figure 3.

The offset ϵ is obtained iteratively in the asperity contact model, by satisfying the following equation:

$$\int_A h(x, y)\, dA = \iint_{\tilde{A}} \left(h_s(x, y) - z(x, y) + u(x, y)\right) d\tilde{A} \tag{11}$$

where A is the total area and $\tilde{A}$ is the lubricated area. The set of equations, to be solved for the dry contact model are:

$$\begin{cases} u\left(x,y\right) = \dfrac{2}{\pi E'} \iint \dfrac{p_{\mathrm{a}}\left(x',y'\right)}{\sqrt{\left(x'-x\right)^2+\left(y'-y\right)^2}} dx'\, dy' \\ u\left(x,y\right) = z\left(x,y\right) - h_{\mathrm{s}}\left(x,y\right)\ ,\ \forall\, x,y\ \in A_{\mathrm{c}} \\ p_{\mathrm{a}}\left(x,y\right) > 0\ ,\ \forall\, x,y\ \in A_{\mathrm{c}} \\ p_{\mathrm{a}}\left(x,y\right) \leq p_{\mathrm{a,lim}} \end{cases} \tag{12}$$

For the dry contact model the unknowns are $p_{\mathrm{a}}\left(x,y\right)$ and A_{c}, whereas h_{s} is related to the film thickness according to eq. 11. The computational burden for the calculation of the integral in eq. 12 is decreased by employing the discrete fast Fourier transformation technique (DC-FFT) [34]. The foundation of the numerical solver is based on the conjugate gradient method [40]. For the current study periodic boundary conditions are specified at the edges of the contact model calculation domain, in order to calculate the representative section. If the dimensions of the dry contact model calculation domain are set to be L_x and L_y (for x and y-direction respectively), then one may define a mean contact pressure $\bar{p}_{\mathrm{a}}$ (over $L_x L_y$) as follows:

$$\bar{p}_{\mathrm{a}} = \frac{1}{L_x L_y} \int \int p_{\mathrm{a}}\left(x,y\right) dx\, dy \tag{13}$$

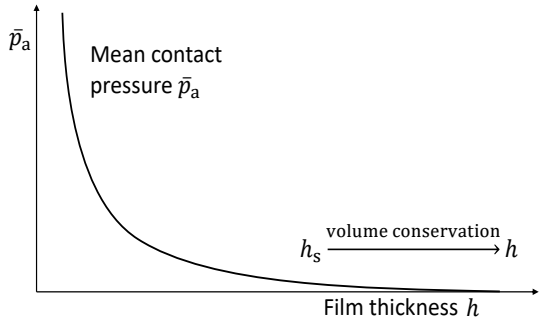

FIGURE 4: Relationship between the mean contact pressure $\bar{p}_{\mathrm{a}}$ and film thickness h.

One should not confuse $\bar{p}_{\mathrm{a}}$ with p_a as $\bar{p}_{\mathrm{a}}$ is not the actual asperity contact pressure. In fact, $\bar{p}_{\mathrm{a}}$ is an auxiliary pressure and is called the "mean contact pressure" in this work. Now a functional curve of $\bar{p}_{\mathrm{a}}$ versus h_s (and indirectly h) can be established (see Figure 4). So, basically we establish a pre-calculated relation between mean contact pressure $\bar{p}_{\mathrm{a}}$ and film thickness h by assuming nominally flat surfaces in contact, so that:

$$\bar{p}_{\mathrm{a}}\left(x\right) = f\left[h\left(x\right)\right] \tag{14}$$

Eq. 14 can interpreted as a relation indirectly describing the "contact stiffness", as $\bar{p}_{\mathrm{a}} L_x L_y$ is the applied contact force. The contact stiffness basically represents the influence of the measured surface roughness. For the sake of simplicity we call the curve depicted in Figure 4 as the "$h - \bar{p}_{\mathrm{a}}$ curve" throughout this paper. Note that eq. 14 can be used to evaluate any dry mean contact pressure for any film thickness in the actual mixed-TEHL model. The calculation of $\bar{p}_{\mathrm{a}}$ is done to scale-up the actual asperity contact pressure distribution p_a to the macro-scale to calculate the load carried by asperities -and ultimately- the mixed friction coefficient. The current method, as introduced by Bobach et al. [11], offers a more deterministic approach as compared to the load-sharing based statistical approach such as described in Masjedi and Khonsari [36, 37], as it uses measured surface roughness. Note that for usage in the load balance equation eq. 8 the dimensionless dry mean contact pressure $\bar{P}_{\mathrm{a}}$ is calculated as follows:

$$\bar{P}_{\mathrm{a}}(x) = \frac{\bar{p}_{\mathrm{a}}(x)}{p_{\mathrm{Hertz}}} \tag{15}$$

2.1.3 Calculation of roller surface velocity

The torque balance, which governs the roller surface velocity u_{r} is written as follows (see Figure 1):

$$\underbrace{f_{\mathrm{c-r}} R_{\mathrm{f}} F}_{\text{tractive torque}} = \underbrace{f_{\mathrm{r-p}} R_{\mathrm{pin}} F}_{\text{resisting torque}} + \underbrace{I\,\dot{\omega}_{\mathrm{r}}}_{\text{inertia torque}} \tag{16}$$

where subscripts "c-r" and "r-p" correspond to cam-roller and roller-pin contact, respectively.

In this study a cam-roller follower unit as part of a fuel injection unit in a heavy duty Diesel engine, is analysed. In fact, the contact forces which the cam-roller contact is subjected to, ranges between 2kN - 17kN. In this study we assume that the inertia torque (second term on RHS of eq. 16) is negligible as compared to the resisting torque caused by the frictional forces acting at the roller-pin contact (first term on RHS of eq. 16). Note that the inertia torque is significant at especially high cam rotational speeds. For the current study the cam rotational speeds are chosen such that the aforementioned assumption holds. Furthermore, one can also assume that under these high contact forces, in combination with increasing friction coefficient $f_{\mathrm{r-p}}$, the influence of the inertia torque becomes much less pronounced. Therefore, the roller rotational speed ω_{r} is solely governed by the tractive and resisting torques acting at the cam-roller and roller-pin contact, respectively. Hence, eq. 16 reduces to:

$$\underbrace{f_{\mathrm{c-r}} R_{\mathrm{f}} F}_{\text{tractive torque}} = \underbrace{f_{\mathrm{r-p}} R_{\mathrm{pin}} F}_{\text{resisting torque}} \tag{17}$$

Note that the friction coefficient $f_{\mathrm{c-r}}$ is defined at the roller surface, i.e. $f_{\mathrm{c-r}} = f_{\mathrm{c-r}}|_{Z=0}$. In this study the influence of the lubrication conditions at the roller-pin contact is studied, in terms of its friction coefficient $f_{\mathrm{r-p}}$, on the lubrication performance at the cam-roller contact. Hence, $f_{\mathrm{r-p}}$ is an input parameter. Calculation of the friction coefficient at the cam-roller contact $f_{\mathrm{c-r}}$ is treated in the next section.

2.2 Thermal analysis

As we assumed that the length of the contact in Y-direction is infinite, it is obvious that temperature variations in this direction can be neglected. To this end, the computational domain for the thermal part is two dimensional in the $XZ-$plane. Heat generation and heat flows through lubricant, asperities and bounding solids are taken into account here. Therefore, the computational domain here consists of three adjacent rectangular domains as is shown in Figure 5. For the thermal model slightly different normalizations for space coordinates are used:

$$X = \frac{x}{a} \quad Z = \begin{cases} z/h & : \text{for the lubricant} \\ z/a & : \text{for the solids} \end{cases} \tag{18}$$

Due to the definition of Z in eq. 18 a dimensionless geometrical domain of unity for the fluid film, irrespective of the actual thickness h, is attained. $Z = 0$ and $Z = 1$ correspond to the roller and cam surfaces, respectively. The chosen dimensionless depth of 3.15 for the bounding solids have been chosen on the basis of the works of Wang et al. [50] and Kaneta et al. [30] to ensure a zero temperature gradient in regions far a way from the contact zone Ω_{f}.

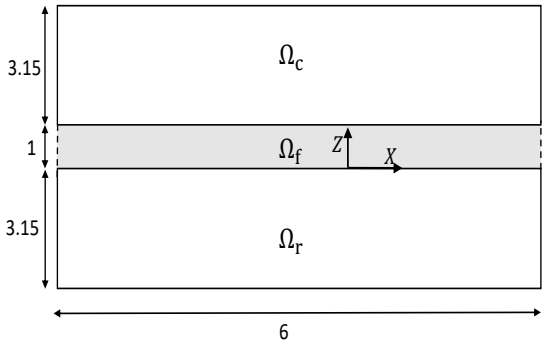

FIGURE 5: Computational domain for the thermal model.

Contrary to numerous publications devoted to the thermal EHL of smooth surfaces (see for instance, references [44, 43, 51, 16]), studies on the treatment of the thermal mixed EHL are relatively scarce, as pointed out by Masjedi and Khonsari [38]. However, with growing interest in the field of rough EHL in recent years, a few emerged studies also concentrated on the thermal effects in the mixed EHL (see for instance references [53, 54, 55, 48, 47, 33, 49]). Recently, Masjedi and Khonsari [37] developed a mixed-TEHL model and also validated it experimentally. The heat generation due to asperity contact was taken into account in the energy equation for the lubricant by means of an additional heat source term. Hence, the steady state two dimensional energy equation for the lubricant film and bounding solids can be written as follows [23]:

$$\begin{cases} \text{solid}: \text{cam} \\ -\frac{\partial}{\partial X}\left(\frac{k_\mathrm{c}}{a}\frac{\partial T}{\partial X}\right) - \frac{\partial}{\partial Z}\left(\frac{k_\mathrm{c}}{a}\frac{\partial T}{\partial Z}\right) + \rho_\mathrm{c} c_\mathrm{c} u_\mathrm{c}\frac{\partial T}{\partial X} = 0 \\ \\ \text{fluid}: \text{lubricant} \\ -\frac{\partial}{\partial X}\left(\frac{kH}{R_x}\frac{\partial T}{\partial X}\right) - \frac{\partial}{\partial Z}\left(\frac{kR_x}{Ha^2}\frac{\partial T}{\partial Z}\right) + \overline{\rho}\rho_0 c u_\mathrm{f}\frac{Ha}{R_x}\frac{\partial T}{\partial X} \\ = Q_\mathrm{comp} + Q_\mathrm{shear} + Q_\mathrm{a} \\ \\ \text{solid}: \text{roller} \\ -\frac{\partial}{\partial X}\left(\frac{k_\mathrm{r}}{a}\frac{\partial T}{\partial X}\right) - \frac{\partial}{\partial Z}\left(\frac{k_\mathrm{r}}{a}\frac{\partial T}{\partial Z}\right) + \rho_\mathrm{r} c_\mathrm{r} u_\mathrm{r}\frac{\partial T}{\partial X} = 0 \end{cases} \tag{19}$$

where

$$\begin{aligned} Q_\mathrm{comp} &= -\frac{T}{\overline{\rho}}\frac{\partial \overline{\rho}}{\partial T}\frac{p_\mathrm{Hertz} Ha}{R_x}\left(u_\mathrm{f}\frac{\partial P_\mathrm{h}}{\partial X}\right) \\ Q_\mathrm{shear} &= \frac{\overline{\eta}\mu_0 Ha^2}{R_x}\dot{\gamma}_{zx}^2 \\ Q_\mathrm{a} &= \frac{Ha^2}{R_x}\frac{dF_\mathrm{a}}{dV}\left|u_\mathrm{c} - u_\mathrm{r}\right| = \frac{Ha^2}{R_x}\frac{f_\mathrm{a}\bar{p}_\mathrm{a} dA}{dV}\left|u_\mathrm{c} - u_\mathrm{r}\right| \\ &= \frac{Ha^2}{R_x} f_\mathrm{a}\bar{p}_\mathrm{a}\left|u_\mathrm{c} - u_\mathrm{r}\right|\frac{dxdy}{h\,dxdy} = f_\mathrm{a}\bar{p}_\mathrm{a}\left|u_\mathrm{c} - u_\mathrm{r}\right| \end{aligned}$$

where Q_comp and Q_shear correspond to heat generation due to the lubricant compressive heating/cooling and shearing effects, respectively. Q_a corresponds to heat generation due to asperity interaction as given by Masjedi and Khonsari [37]. Note that Q_a uses mean contact pressure $\bar{p}_\mathrm{a}$, indicating that the actual (local) shear contribution of asperities has been scaled-up to the macro-scale.

In contrast to the mixed EHL component, which is implemented in the model in dimensionless form, the thermal part (eq. 19) is solved in dimensional form. As can be

observed in Eq. 19, heat convection across the lubricant film (Z-direction) is neglected due to its relatively small dimension compared to the other directions. See for instance the works of Guo et al. [24] and Cheng [14], which justify this assumption.

The lubricant film velocity field in x-direction u_f is written as follows [26]:

$$u_\mathrm{f} = u_\mathrm{r} + \frac{p_\mathrm{Hertz} H^2 a^3}{R_x^2 \mu_0} \frac{\partial P_\mathrm{h}}{\partial X} \left[\int_0^Z \frac{Z' dZ'}{\bar{\eta}} dZ - \frac{\bar{\eta}_e}{\bar{\eta}'_e} \int_0^Z \frac{dZ}{\bar{\eta}} \right] + \bar{\eta}_e \left(u_\mathrm{c} - u_\mathrm{r} \right) \int_0^Z \frac{dZ}{\bar{\eta}} \tag{20}$$

where, $\bar{\eta}_e$ and $\bar{\eta}'_e$ are defined in eq. 6. The shear rate through the film thickness can now be defined as [26]:

$$\dot{\gamma}_{zx} = \frac{\partial u_\mathrm{f}}{\partial z} = \frac{p_\mathrm{Hertz} Ha}{\mu_0 \bar{\eta} R_x} \frac{\partial P_\mathrm{h}}{\partial X} \left(Z - \frac{\bar{\eta}_e}{\bar{\eta}'_e} \right) + \frac{R_x}{Ha^2} \frac{\bar{\eta}_e}{\bar{\eta}} \left(u_\mathrm{c} - u_\mathrm{r} \right) \tag{21}$$

Finally, the shear stress through the lubricant film can simply be obtained as:

$$\tau_{zx} = \mu_0 \bar{\eta} \dot{\gamma}_{zx} \tag{22}$$

In order to obtain a unique and realistic solution for eq. 19 proper boundary conditions must be applied. These are summarized as follows:

$$\begin{cases} T\left(X = -4.5,\ -4.15 \leq Z \leq 0\right) = T_0 \\ T\left(X - 4.5,\ 1 \leq Z \leq 4.15\right) = T_0 \\ T\left(X,\ Z = -3.15\right) = T\left(X,\ Z = 4.15\right) = T_0 \\ T\left(X = -4.5,\ 0 \leq Z \leq 1\right) = T_0 \text{ where } u_\mathrm{f} \geq 0 \\ \frac{k_\mathrm{r}}{a} \frac{\partial T}{\partial Z}\big|_{Z=0^-} = \frac{k R_x}{Ha^2} \frac{\partial T}{\partial Z}\big|_{Z=0^+} \\ \frac{k_\mathrm{c}}{a} \frac{\partial T}{\partial Z}\big|_{Z=1^+} = \frac{k R_x}{Ha^2} \frac{\partial T}{\partial Z}\big|_{Z=1^-} \end{cases} \tag{23}$$

where T_0 is the ambient temperature. In the set of boundary conditions defined in eq. 23 one may note that temperature boundary conditions are imposed on the complete LHS of the computational domain shown in Figure 5. Due to the hyperbolic nature of eq. 19 only inlet boundary conditions are required. Moreover, in this work u_c and u_r are assumed to be positive. However, at the inlet of the fluid flow domain Ω_f a reversal flow may occur, leading to negative values of u_f. Hence, the ambient temperature boundary

condition is only needed for positive values of u_f. See the work of Habchi et al. [25] for more details. Finally, eq. 23 also specifies the associated heat flux continuity boundary conditions that are imposed at the solid-fluid interfaces.

For the friction calculations in the cam-roller analysis the following mixed friction coefficient $f_{\mathrm{c-r}}$ is defined at the roller surface ($Z = 0$),

$$f_{\mathrm{c-r}}|_{Z=0} = aL\frac{\int\limits_{\partial\Omega_\mathrm{f}} \tau_{zx}|_{Z=0}dX + f_\mathrm{a}\int\limits_{\partial\Omega_\mathrm{f}} \bar{p}_\mathrm{a}dX}{F} \tag{24}$$

where, L is the length of the contact in y-direction, τ_{zx} is calculated using eq. 22 and $\bar{p}_\mathrm{a}$ according to eq. 14. f_a is the boundary friction coefficient, which is an input parameter. f_a needs to be determined experimentally using a tribo-meter at very low speeds where the EHL film thickness is small compared to the composite surface roughness of the opposing surfaces (load carried by lubricant should be negligibly small.) The value of boundary friction coefficient reported in some studies is about 0.1-0.13 [21, 1, 37].

2.3 Fluid rheology

The density and viscosity are important variables to consider in the cam-roller lubrication analysis as they strongly influence the tribological performance of the conjunction. For variations in density $\bar{\rho}$ the Dowson-Higginson relation [17] is adopted:

$$\bar{\rho}\left(P_\mathrm{h}, T\right) = 1 + \frac{0.6\times10^{-9}P_\mathrm{h}p_\mathrm{Hertz}}{1+1.7\times10^{-9}P_\mathrm{h}p_\mathrm{Hertz}} - \beta_T\left(T - T_0\right) \tag{25}$$

where β_T is considered to be the thermal expansion coefficient of the lubricant. For the dependence of the generalized Newtonian viscosity $\bar{\eta}$ on shear stress the Eyring model [19] is adopted.

$$\frac{1}{\bar{\eta}\left(P_\mathrm{h}, T, \tau_e\right)} = \frac{1}{\bar{\mu}\left(P_\mathrm{h}, T\right)}\frac{\tau_0}{\tau_e}\sinh\left(\frac{\tau_e}{\tau_0}\right) \tag{26}$$

where $\tau_e = \sqrt{\tau_{xz}^2}$. Note that any other known non-Newtonian model, such as the Carreau model [13], Bair and Winer limiting shear stress model [9, 8] could be adopted without effecting the general modelling structure. For the sake of simplicity the dependence of viscosity $\bar{\mu}$ on pressure and temperature is determined using the Roelands equation [42]:

$$\bar{\mu}\left(P_\mathrm{h}, T\right) = \exp\left\{\left(\ln\left(\mu_0\right) + 9.67\right)\left[-1 + \left(1 + 5.1\times10^{-9}P_\mathrm{h}p_\mathrm{Hertz}\right)^{Z_0}\left(\frac{T-138}{T_0-138}\right)^{-S_0}\right]\right\} \tag{27}$$

where,

$$Z_0 = \frac{\alpha}{5.1 \times 10^{-9} \left(\ln\left(\mu_0\right) + 9.67\right)}$$
$$S_0 = \frac{\beta \left(T_0 - 138\right)}{\ln\left(\mu_0\right) + 9.67}$$

2.4 Overall numerical procedure

The complete mixed TEHL model for the cam-roller contact can be split-up in two finite element-based models, between which a global iteration scheme is established.
One model is associated with the calculation of the (hydrodynamic and asperity) pressure and film thickness distribution (described in subsection "Mixed lubrication model") and one model to solve the temperature distribution in the contact and bounding solids (described in section "Thermal analysis"). The global numerical procedure is described in the flowchart shown in Figure 6. The global numerical procedure for the TEHL model very much resembles the one developed by Habchi et al. [25], but is modified here to take into account the variable roller velocity u_r which is governed by the torque balance eq. 16. However, eq. 16 can be treated, likewise the load balance eq. 8, as an additional global equation to the complete system of equations so that the general modelling structure for the mixed-EHL part is still similar to the one developed in [25]. Note that in the simplified asperity contact modelling approach adopted here (subsection "Asperity contact component"), the mean contact pressure $\bar{P}_\mathrm{a}$ is a direct function of the film thickness H, and therefore the unknowns of the *mixed-lubrication model* are: $(P_\mathrm{h}, U, W, H_0, u_\mathrm{r})$.
The unknown variable associated with the *thermal model* is the temperature T.
Proper initial guesses, as detailed in reference [25], need to be chosen before launching the numerical loops, as shown in Figure 6.
The *mixed-lubrication model* and *thermal model* are individually and separately solved using the FEM where both problems are formulated as a set of strongly coupled non-linear partial differential equations. The resulting systems of non-linear equations is solved using a monolithic approach where for the *mixed-lubrication model* all the dependent variables $(P_\mathrm{h}, U, W, H_0, u_\mathrm{r})$, and for the *thermal model* the dependent variable (T), are collected in one vector of unknowns and simultaneously solved using a Newton-Raphson algorithm.
To clarify here, the Newton-Raphson algorithm is applied separately for solving each sub-model (that is *mixed-lubrication model* and *thermal model*) that compose the entire mixed-TEHL problem. For each sub-model convergence is achieved when relative tolerances in the order to $10^{-3} - 10^{-4}$ are reached. For specific numerical details concerning the weak finite element formulation of the governing equations, the reader is referred to [25]as only

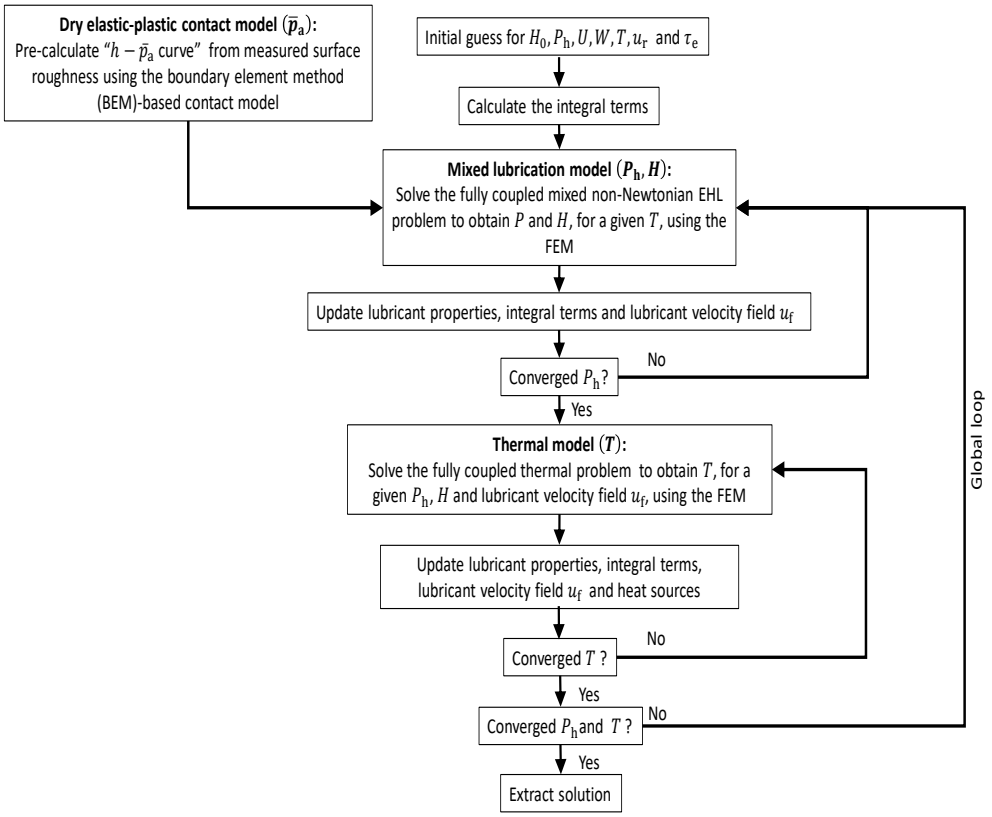

FIGURE 6: Numerical solution scheme for the cam-roller lubrication model.

the main features are recalled in this work.

As can be seen from Figure 6 the temperature solution is obtained from a given pressure distribution and vice-versa. Hence, a global algorithm, with respect to the coupled *mixed-lubrication model* and *thermal model*, is established to ensure overall convergence between the consecutive solutions of temperature and pressure distributions.

A similar customized element size distribution, as detailed in [35], was employed for the EHL and thermal computational domains. In fact, in the pressure build-up region a dense element size distribution was chosen which was allowed to decrease gradually as the distance from the fluid film boundary increased. The custom tailored mesh size distribution for the *mixed-lubrication model* corresponds to 50000 degrees of freedom, while for the *thermal model* 55000 degrees of freedom were used.

Steady-state solutions are usually reached within 20 global iterations, corresponding to global relative errors between $10^{-3} - 10^{-4}$.

3 Comparison with experiments

It would be interesting to compare the calculated mixed friction coefficient, using the current mixed-TEHL model, with published experimental data. This can be done using traction or Stribeck curves. Comparison of traction or Stribeck curves with published experiments is difficult due to the fact that i) frequently no data is available on the boundary friction coefficient f_{a} and ii) also the roughness data needed are frequently incomplete.

Johnson and Spence [29] measured traction curves using a two-disc machine. The purpose of their experiments was to simulate the contact between gear and teeth. Gelinck [20], who used the Greenwood and Williamson contact model [22] in his mixed-lubrication model, used the experimental data of Johnson and Spence [29] to validate his model. Assuming a Gaussian surface roughness distribution of the circumstantially grinded discs, Gelinck [20] estimated the (Greenwood and Williamson model) appropriate surface roughness parameters. The oil used in the experiments of Johnson and Spence [29] was the Shell Vitrea 68 oil. The operating conditions, given by Gelinck [20] can be found in Table 1. The dry contact model used in this work has been described previously in the "Asperity contact component" section. As in the current mixed-TEHL model an uncoupled approach is followed between the Smooth EHL component and the asperity contact component, the only output we need from the dry contact model is the "$h - \bar{p}_{\mathrm{a}}$ curve". The dry contact model used in this work is one which is well accepted [40] and has also been verified experimentally in previous work [2]. Hence, in order to compare the current approach with the experiments from Johnson and Spence [29], the "translated" $h - \bar{p}_{\mathrm{a}}$ curve from the work of Gelinck [20] has been used and is depicted in Figure 7.

In the traction experiments of Johnson and Spence [29], at high slip values, the coefficient of friction was found to be constant for circumstantially grinded discs. As suggested by Gelinck [20], the relevant values can then also be used to plot (part of) a Stribeck curve by assuming the sliding velocity to be equal to the sum velocity u^{+}.

Johnson and Spence [29] considered three levels of load along with three levels in sum velocity, which are given in Table 1. Consequently, nine data points could be used for the sake of comparison. The results are shown in Figure 8(a). Satisfactory agreement between the model and experiment is obtained.

Traction curves, corresponding to a load of 3062N, are compared in Figure 8(b). Overall, good agreement is obtained between model predictions and experiments, although there is some discrepancy in the low SRR domain. It can be seen that the traction curves obtained from the model start from a non-zero value. This is due to the fact that the asperity traction coefficient is not assumed to be a function of the SRR, which is the

TABLE 1: Experimental conditions experiment of Johnson and Spence [29], as given by Gelinck [20]. Subscripts 1 and 2 denote disc 1 and disc 2, respectively.

Parameter	**Value**	**Unit**
R_a	0.55	μm
E_1	210	GPa
E_2	210	GPa
ν_1	0.3	-
ν_2	0.3	-
ρ_0	870	kg/m^3
ρ_1	7850	kg/m^3
ρ_2	7850	kg/m^3
β	0.032	K^{-1}
β_T	0.00065	K^{-1}
R_x	19	mm
L	12.7	mm
α	1.94E-8	Pa^{-1}
μ_0	0.0374	Pa·s
τ_0	2.5	MPa·s
f_a	0.098	-
F	3062, 4500, 5800	N
p_{av}	536, 650, 738	MPa
u^+	0.86, 1.72, 250	m/s
T_0	50	°C
k	0.13	W/mK
k_1	46	W/mK
k_2	46	W/mK
c	1970	J/kg$K$
c_1	450	J/kg·K
c_2	450	J/kg·K

case in practice. In case of pure rolling the traction coefficient would theoretically be zero. This subject has been studied in previous work [6].

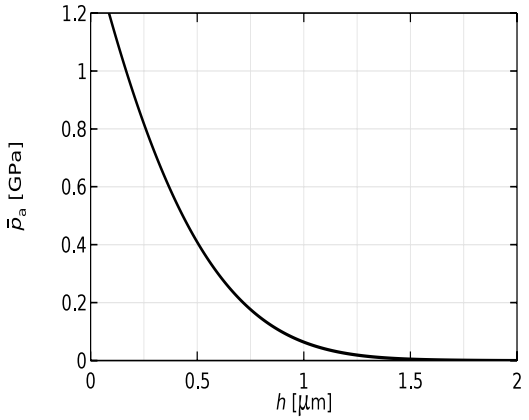

FIGURE 7: Surface roughness influence curve "$h - \bar{p}_a$ curve" calculated from the work of Gelinck [20].

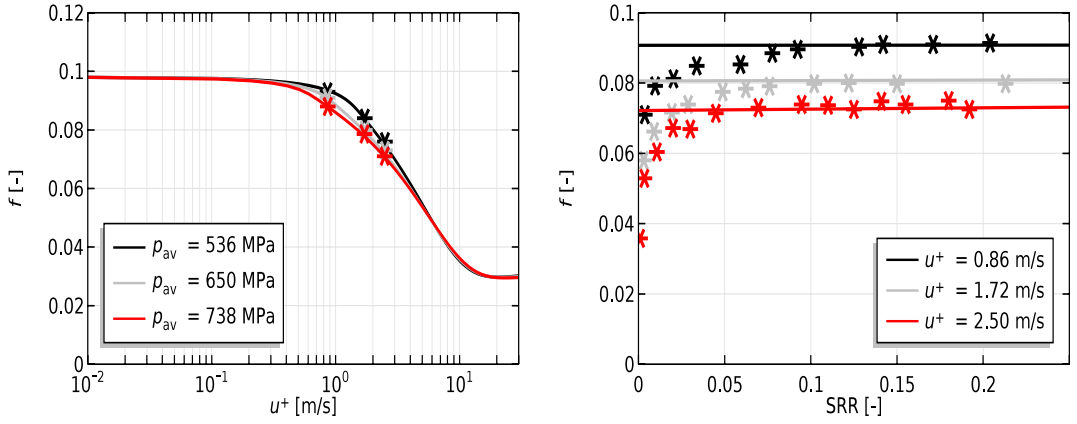

(a) (b)

FIGURE 8: Comparison model predictions and experiments [29, 20] for a) Stribeck curves and b) traction curves.

4 Results: Cam-roller follower analysis

The heavily loaded cam-roller follower unit, analysed in this study, is part of a fuel injection pump unit of a heavy duty Diesel engine of a truck. The lubricant and material properties, and geometrical parameters are listed in Table 2. The lubricant considered here is a 10W30 motor oil and its properties were provided by the oil supplier. The lift profile of the cam and reciprocating configuration considered, represents the vertical displacement of the roller follower centre. The variations of the lift, reduced radius of curvature R_x, cam surface velocity u_c and contact force F, as a function of the cam angle θ are depicted in Figure 9. The kinematic variations depicted in Figure 9 correspond to a cam rotational speed ω_c of 950 RPM. From the lift profile one may, for instance, deduce the region (e.g. range of cam angle) in which the nose of the cam is in contact with the roller. From Figure 9 it is clear that the centre of the nose region is defined at 90° cam angle, i.e. the highest vertical displacement. Regions corresponding to low values in lift or no lift at all are commonly called the flank/base circle regions.

TABLE 2: Reference operating conditions and geometrical parameters for cam-roller follower lubrication analysis.

Parameter	Value	Unit
ω_c	950	rev/min
E_c	200	GPa
E_r	200	GPa
ν_c	0.3	-
ν_r	0.3	-
ρ_0	870	kg/m^3
ρ_c	7850	kg/m^3
ρ_r	7850	kg/m^3
α	1.84E-8	Pa^{-1}
Z_0	0.68	-
β	0.032	K^{-1}
β_T	0.00065	K^{-1}
μ_0	0.013	Pa·s
τ_0	3.5	MPa·s
R_f	0.018	m
R_{pin}	0.0091	m
L	0.021	m
T_0	77	°C
k	0.13	W/mK
k_c	46	W/mK
k_r	46	W/mK
c	1970	J/kg$K$
c_c	450	J/kg·K
c_r	450	J/kg·K
f_a	0.1	-
f_{r-p}	0.0015	-
$p_{a,lim}$	6	GPa

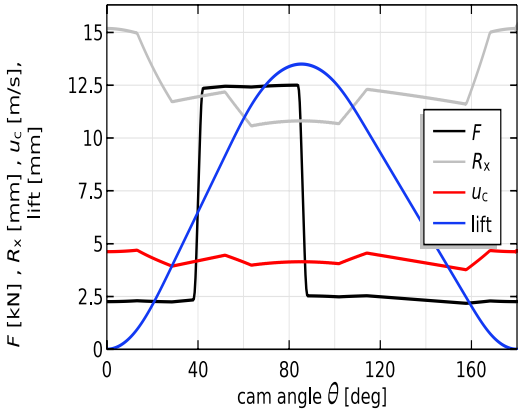

FIGURE 9: Variation of the lift, reduced radius of curvature R_x, cam surface speed u_c and contact force F as a function of cam angle θ.

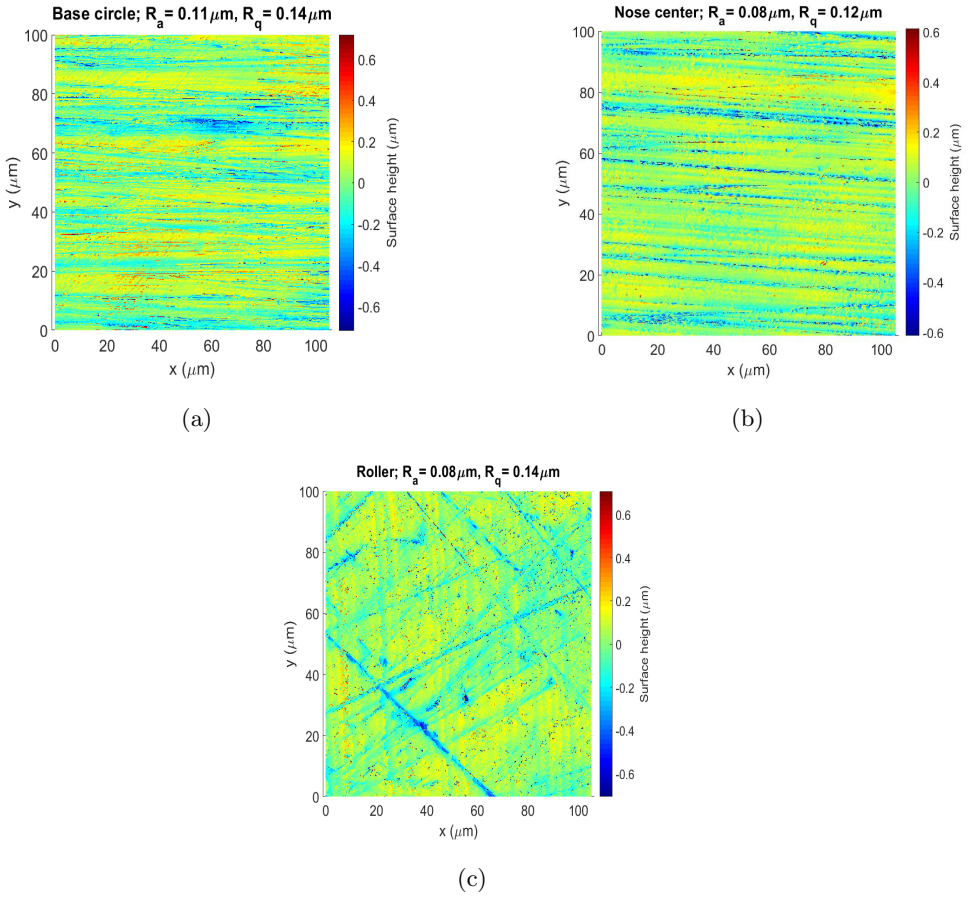

FIGURE 10: Measured surface roughness for a) base circle, b) nose centre and c) roller.

The cam shape is repeated after 180° cam angle, i.e the kinematic variations occurring in interval $0° - 180°$ cam angle are identical to those between $180° - 360°$ cam angle. Hence, Figure 9 only depicts the variations occurring between $0° - 180°$ cam angle. As can be observed from this Figure, the reduced radius of curvature and cam surface velocity are fairly constant (with minor variations) throughout the cam's lateral surface, whereas steep variations occur in the contact force profile.

The abrupt variations in the contact force profile are due to sudden activation and de-activation of pumping action within the fuel injection equipment (see reference [5] for more details). The highest contact forces occur partly on the flanks and partly on the nose region of the cam.

The surface roughness in the nose region of the cam differs from that of the flank/base circle region. In fact, as higher loads are expected in the nose region, a more precise surface finishing is applied to the nose region. For the present study the surface roughness is measured approximately at a cam angle of 0° (flank/base circle region) and at 90° (nose region). For the roller a randomly chosen area was used to measure the surface roughness. To give an indication, the R_a-values for the measured surface roughness of

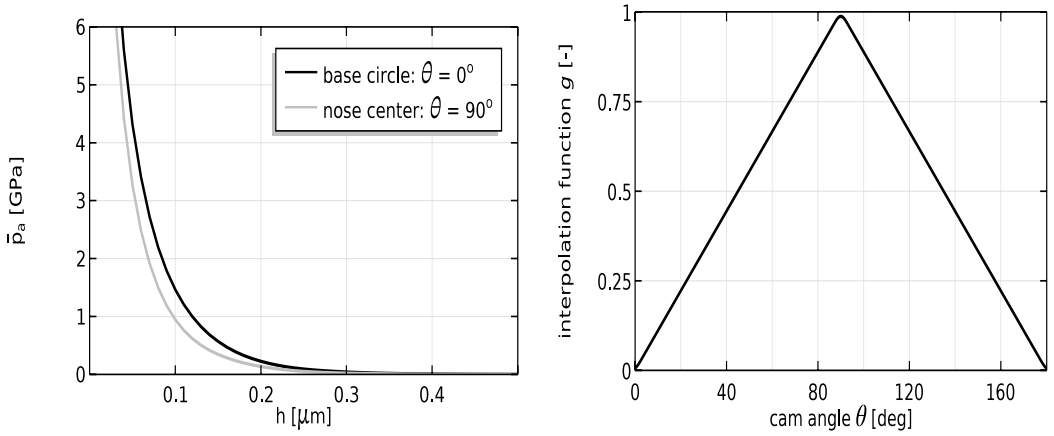

(a) (b)

FIGURE 11: a) Surface roughness influence curves "$h - \bar{p}_{\mathrm{a}}$ curves" and b) interpolation function g for the mapping of $h - \bar{p}_{\mathrm{a}}$ curves against cam angle.

base circle (0°) and nose (90°) positions are 0.11μm and 0.08μm, respectively. For the roller the surface roughness measurement yielded an R_a-value of 0.08μm. The measured surface roughness are given in Figure 10.

By means of the mathematical model described in subsection 2.1.2 "Asperity contact component" two "$h - \bar{p}_{\mathrm{a}}$ curves", corresponding to cam angles of 0° and 90° respectively, are deduced (see Figure 11(a)). Again, the $h - \bar{p}_{\mathrm{a}}$ curves provide the relationship between the film thickness h and mean contact pressure $\bar{p}_{\mathrm{a}}$. The computational grid size for the contact model contained $N_x \times N_y = 250 \times 250$ data points at intervals of 0.4μm (see reference [2] for more details on the contact model). A triangular shaped interpolation function $g(\theta)$ (see Figure 11(b)) is used to obtain a mapping between the "$h - \bar{p}_{\mathrm{a}}$ curve" and cam angle. In equation form this yields:

$$\begin{aligned} \bar{p}_{\mathrm{a}}(h,\theta) &= \bar{p}_{\mathrm{a}}(h,\theta = 0^\circ) \\ +g(\theta)\left(\bar{p}_{\mathrm{a}}(h,\theta = 90^\circ) - \bar{p}_{\mathrm{a}}(h,\theta = 0^\circ)\right) \end{aligned} \tag{28}$$

4.1 Full cam's lateral surface

A quasi-static analysis is carried out by means of the developed model in this work. For the current study the friction coefficient at the roller-pin contact $f_{\mathrm{r-p}}$ is kept fixed at all cam angles. Under ideal conditions the roller-pin contact should inhibit very low friction levels. So, a fixed value of $f_{\mathrm{r-p}} = 0.0015$ (as used in [27]) is chosen in this case.

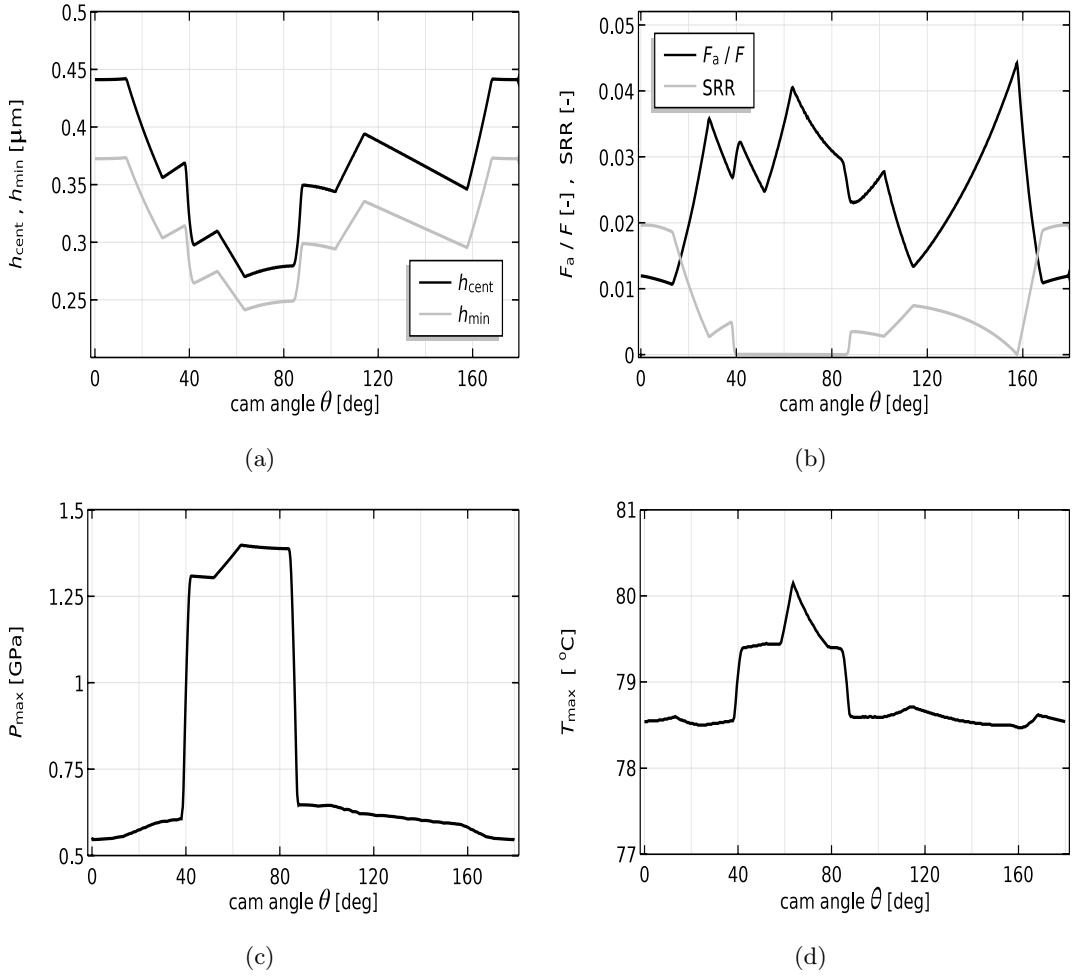

FIGURE 12: Evolution of crucial design variables such as a) film thicknesses h_{cent} and h_{min}, b) asperity load ratio F_{a}/F and SRR, c) maximum total pressure p_{max} and d) maximum contact temperature T_{max}, as a function of the cam angle θ.

Figure 12(a) presents the evolution of the central film thickness h_{cent} and minimum film thickness h_{min} as a function of the cam angle. Due to rolling motion of the follower overall a fairly constant film thickness is predicted when compared to conventional flat faced followers. The "dips" between $(40° - 90°)$ in the film thickness profiles, depicted in Figure 12(a), are due to the rapid increase in contact force. Note that the mean entrainment velocity remains approximately constant throughout the full cam's lateral surface. This evident from the relation between Figure 12(b), which shows the evolution of the slide-to-roll ratio $\left(\text{SRR} = \frac{U_{\text{c}}-U_{\text{r}}}{0.5(U_{\text{c}}+U_{\text{r}})}\right)$, and Figure 9. The SRR is negligible throughout the cam's lateral surface due to overall high contact forces, i.e. the SRR remains less than 2% over the full cycle. The highest roller slippage occurs on the base circle positions where the contact forces are the lowest. Figure 12(b) also depicts the variation of the proportion of the load carried by the asperities F_{a}/F. The F_{a}/F ratio directly depends on the film thickness and contact area. The load carried by the asperities is negligible for

the considered surfaces, as less than 5% of the load is carried by the asperities. Hence, it can be stated that under ideal conditions (for the considered cam rotational speed), the cam-roller contact operates in almost full film lubrication conditions.

Figure 12(c) presents the variation of total maximum contact pressure $p_{\max}$ as a function of the cam angle. The maximum pressure, which is almost directly proportional to the contact force F (as the cam radius of curvature $R_x(\theta)$ is fairly constant), cycles between 0.5 GPa and 1.5 GPa.

Figure 12(d) shows the evolution of the maximum contact temperature $T_{\max}$ as a function of the cam angle. Due to the almost "pure rolling" working conditions a very small temperature increase is noticed, i.e. a maximum temperature rise of approximately 3.5°C is noticed in the nose region. It is worth mentioning that due to negligible roller slippage heat is mainly generated due to compressive heating of lubricant and asperity frictional heating (even-though the asperities carry a very small fraction of the total load).

Finally, Figure 13 presents a snapshot of the asperity, hydrodynamic and total pressure distributions, together with the dimensionless film thickness distribution H at 63.5° cam angle. Note that at 63.5° cam angle both maximum pressure and minimum film thickness occur. It is evident from Figure 13 that for the considered operating conditions the asperity component pressure distribution is a small fraction of the total pressure distribution. Furthermore, when carefully looked, one may observe that still a substantial level of asperity interaction occurs near the outlet of the contact as the asperity mean contact pressure distribution spans out further than the hydrodynamic pressure distribution. This effect is amplified in more mixed lubrication conditions (see for instance reference [36]).

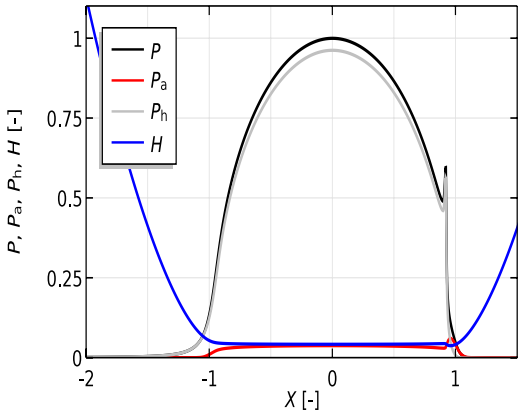

FIGURE 13: Snapshot of the asperity $\bar{P}_{\mathrm{a}}$, hydrodynamic P_{h} and total pressure P distributions, together with the dimensionless film thickness distribution H at 63.5° cam angle.

From the results obtained so far one may notice that when the roller-pin contact operates under ideal conditions, i.e. low friction levels, negligible roller slippage occurs and thus

leading to ideal operating conditions for the cam-roller contact. However, in practice still failures can occur in the cam-roller follower units. This may be a result of several factors. On the basis of the obtained results in this study, a most probable reason is poor lubrication conditions in the roller-pin contact. Due to, for example, insufficient supply of lubricant to the roller-pin contact or formation of wear particles the lubrication conditions at the roller-pin contact may deteriorate. It is therefore interesting to investigate the influence of roller-pin friction on the overall tribological behaviour of the cam-roller contact. The study is performed in the next section.

4.2 Parametric study: the influence of roller-pin friction

As mentioned earlier, it is interesting to assess the "sensitivity" of the cam-roller lubrication performance as function of the lubrication regime which the roller-pin contact operates in. The "sensitivity" of the cam-roller lubrication performance as function of the lubrication mode of the roller-pin contact is assessed here by assuming a friction coefficient at the roller-pin contact. The coefficient of friction of the roller-pin contact is varied from levels corresponding to full film lubrication to values corresponding to boundary lubrication.

TABLE 3: Reference operating conditions for $\theta = 0°$ and $\theta = 63.5°$.

θ	F **[N]**	R_x **[m]**	u_c **[m/s]**
0°	2250	0.0152	4.62
63.5°	12500	0.0105	3.98

From the results obtained in the previous subsection it is interesting to asses the influence of roller-pin friction coefficient f_{r-p} on the lubrication performance of two specific cam angles, namely 0° and 63.5°. The choice of the aforementioned cam angles leans on the following reasons: At 0° cam angle the highest roller slip occurs (see Figure 12(b)), and at 63.5° cam angle both maximum pressure and minimum film thickness occur (see Figures 12(a) and 12(c)). The operating conditions at these cam angles are kept fixed. Then a parametric sweep is carried out by varying f_{r-p} from 0.0015 to a value which corresponds to a SRR of 2. Note that when the SRR equalizes 2, simple sliding is attained. For the sake of comparison the results are compared with results obtained by assuming a Newtonian behaviour of the lubricant and isothermal conditions. The contact force, reduced radius of curvature and cam surface velocity corresponding to $\theta = 0°$ and $\theta = 63.5°$, are given in Table 3.

4.2.1 Parametric analysis: $\theta = 0°$

The results that will be discussed now correspond to operating conditions at 0° cam angle (see Table 3).

Figure 14(a) shows the variation of the SRR with $f_{\mathrm{r-p}}$. For both non-Newtonian + thermal and Newtonian+isothermal models a substantial increase in SRR is observed for increasing values of $f_{\mathrm{r-p}}$. This can be attributed to the fact that sliding velocity at the cam-roller contact has to increase to compensate for an increase of $f_{\mathrm{r-p}}$. Another remarkable observation is that a dramatic increase in the SRR is observed by taking into account non-Newtonian + thermal effects. Note that both non-Newtonian and thermal effects contribute to viscosity reduction in a non-linear fashion. In fact a deviation between the two models is observed from a $f_{\mathrm{r-p}}$ value of approximately 0.0175. The initiation of this deviation may be attributed to the non-Newtonian effect. In this case related to the characteristic shear stress τ_0 for the Eyring type lubricant. It is worth mentioning that a larger value of τ_0 would shift the starting point of non-Newtonian effect to a higher value of $f_{\mathrm{r-p}}$. Looking at the results for the Newtonian + isothermal model a linear increase in the SRR is observed, whereas for the non-Newtonian + thermal model a strongly non-linear behaviour is noticed.

The results corresponding to the non-Newtonian + thermal model can be explained analogously to a typical traction curve, but then inverted. For low SRRs, the relationship between SRR and shear stress is linear, indicating Newtonian behaviour of the friction response. From some point in the SRR domain (related to the characteristic Eyring shear stress τ_0) and onwards, the friction increases in a non-linear fashion with increasing SRR (indicating non-Newtonian behaviour). Then at considerably large SRRs thermal effects become more pronounced (due to high shear rates) and the friction decreases due to reduction in viscosity (thermal softening).

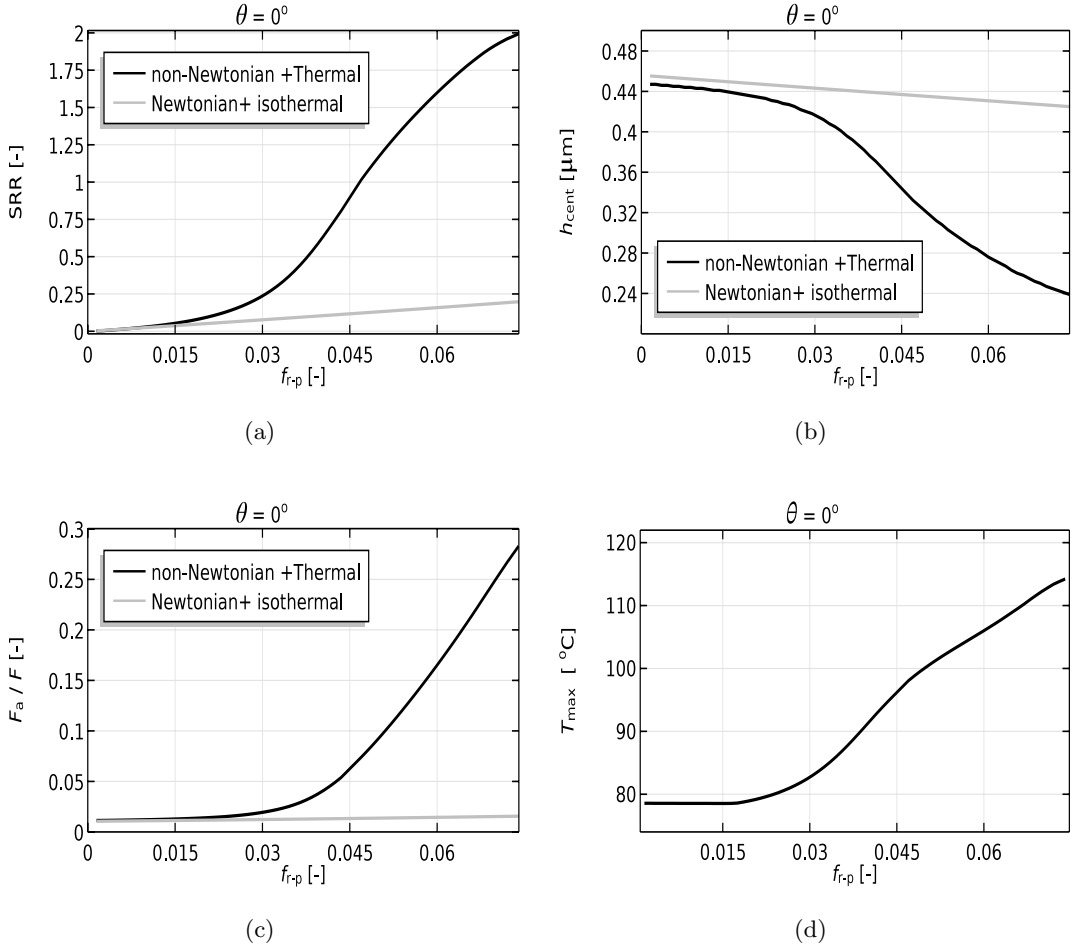

FIGURE 14: Variation of crucial design variables such as a) the SRR, b) central film thickness h_{cent} c) asperity load ratio F_{a}/F and d) maximum contact temperature $T_{\max}$, as a function of the roller-pin friction coefficient $f_{\text{r-p}}$. Results are presented for 0° cam angle.

Now coming back to the non-Newtonian + thermal model results shown in Figure 14(a). After a $f_{\text{r-p}}$ value of approximately 0.0175 the SRR also increases non-linearly to compensate for the increase in $f_{\text{r-p}}$ (indicating non-Newtonian behaviour). Then at considerably large SRRs thermal effects become more pronounced and this non-linear behaviour becomes even more amplified (thermoviscous effects). Note that the calculations were stopped when the SRR reached a value of two, because then it means that u_{r} is zero.

If the behaviour of the SRR versus $f_{\text{r-p}}$ is understood then Figure 14(b), which plots the variation of the central film thickness h_{cent} against $f_{\text{r-p}}$, may be interpreted much easier. It is worth mentioning that for the application studied here an increase in SRR means a decrease in sum velocity. Hence, in both non-Newtonian+ thermal and Newtonian + isothermal models a decrease in film thickness is observed. Note that the Newtonian + isothermal model slightly overestimates the central film thickness even at low values

of f_{r-p}. This discrepancy may be attributed to thermal effects, which cause a larger SRR even at low f_{r-p} values and thus leading to a decrease in sum velocity. As the film thickness in EHL is strongly influenced by the sum velocity the difference between the solutions of two models is much more explainable, i.e. the non-Newtonian + thermal model predicts a dramatic decrease in film thickness after a f_{r-p} value of approximately 0.0175 (which is governed by τ_0 as earlier explained). Note that for the cam-roller contact the film thickness is highly affected by non-Newtonian and thermal effects, due to the coupling between the cam-roller and roller-pin contact, i.e. fluid rheology governs the traction at the cam-roller contact which on its turn governs the relative amount of sliding (and thus the sum velocity).

Figure 14(c) presents the variations of the proportion of load carried by the asperities by means of the ratio F_a/F. A barely noticeable increase in F_a/F is observed for increasing values of f_{r-p} using the Newtonian + isothermal model. This is mainly because the relatively high values of the film thickness which are persistent throughout the whole considered range of f_{r-p}. When considering non-Newtonian + thermal effects the situation is different, because of the dramatic decrease in film thickness. The film thickness and load carried by asperities are directly related to each other by means of the "$h - \bar{p}_a$ curves" (see Figure 11(a)), which is strongly non-linear. Consequently, a sudden increase in F_a/F is observed after a f_{r-p} value of approximately 0.0175.

Finally, in Figure 14(d) the variation of the maximum temperature in the contact T_{max} as function of f_{r-p} is plotted. A clear non-linear increase in T_{max} is observed after a f_{r-p} value of approximately 0.0175. This increase in mainly due to the increase in shear heating of the lubricant, which is proportional to the sliding velocity, but also the asperity frictional heating which increases further in more mixed lubrication conditions together with the increase in sliding velocity.

4.2.2 Parametric analysis: $\theta = 63.5°$

The results that will be discussed now correspond to operating conditions at 63.5° cam angle (see Table 3).

Figure 15(a) depicts the variation of the SRR as a function of f_{r-p} obtained using the non-Newtonian + thermal and Newtonian + isothermal model. Due to the high contact force the SRR remains negligible throughout the full range of chosen f_{r-p} values for the Newtonian + isothermal model. The SRR however, shows a dramatic non-linear increase after a f_{r-p} value of approximately 0.0575 using the non-Newtonian + thermal model.

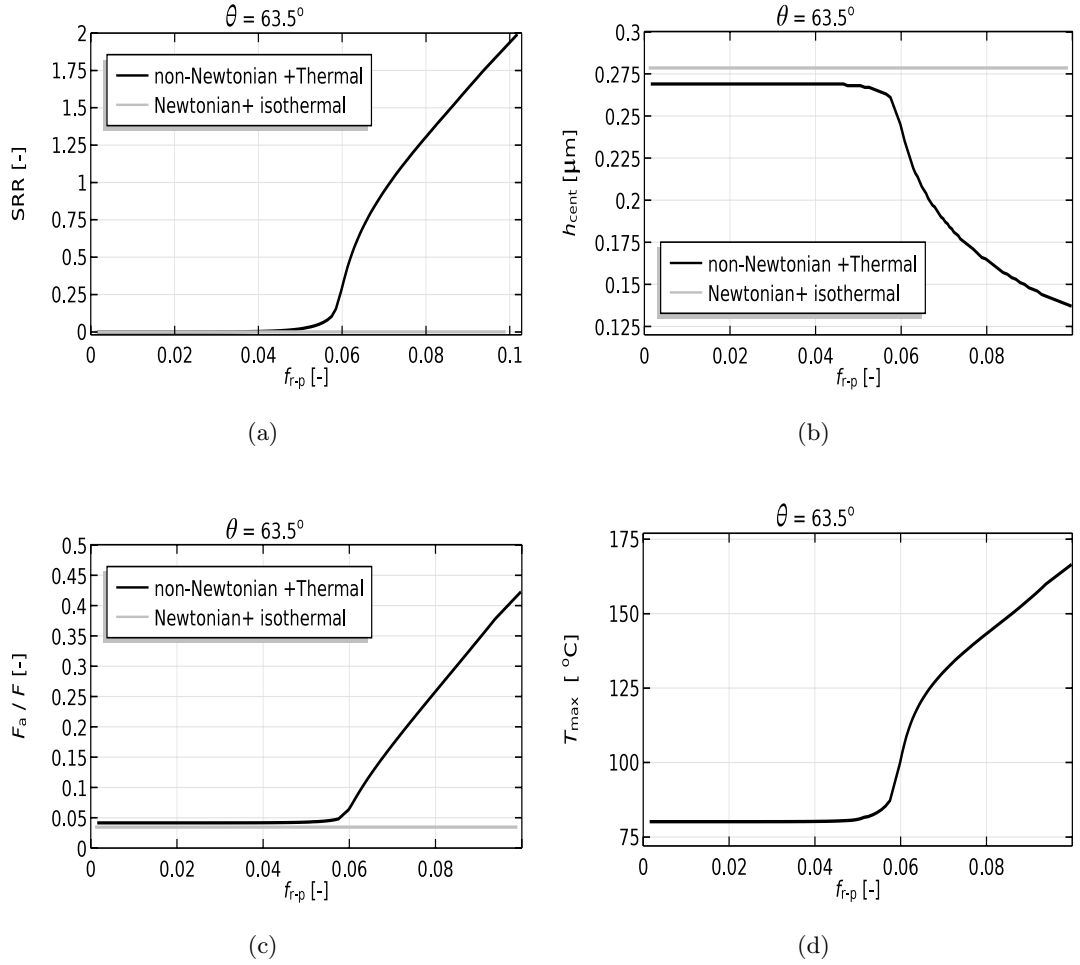

FIGURE 15: Variation of crucial design variables such as a) the SRR, b) central film thickness h_{cent} c) asperity load ratio F_{a}/F and d) maximum contact temperature $T_{\max}$, as a function of the roller-pin friction coefficient $f_{\text{r-p}}$. Results are presented for 63.5° cam angle.

The non-linear increase in SRR can analogously be explained as was done for the $\theta = 0°$ case. Additionally, two other clear features may be distinguished in Figure 15(a). First, the starting point of dramatic increase in the SRR is shifted to a larger value of $f_{\text{r-p}}$ when compared to Figure 14(a). This is mainly due to the fact that due to the significantly higher contact force the Newtonian behaviour of the lubricant persists for higher values of $f_{\text{r-p}}$. This is also evident from the SRR profile obtained using a Newtonian+ isothermal model. In fact, the viscosity increase due to the much higher experienced pressure causes a much less pronounced increase in sliding velocity to compensate for higher values of $f_{\text{r-p}}$. This should highlight the importance of accurately taking into account the viscosity-pressure dependence of the lubricant as it will surely influence the starting point of non-linear behaviour. Also note that due to the shift of the starting point, a larger range of $f_{\text{r-p}}$ is sustained when compared with Figure 14(a). To be more specific,

SRR = 2 at approximately $f_{\mathrm{r-p}} = 0.075$ for $\theta = 0°$, while SRR = 2 at $f_{\mathrm{r-p}} = 0.105$ for $\theta = 63.5°$. The second feature which may be observed from Figure 15(a) are the slopes in the profile for the SRR, obtained using the non-Newtonian + thermal model. A sharp increase in SRR is observed from a $f_{\mathrm{r-p}}$ value of approximately 0.0575 to 0.07. After this the increase in SRR is less steep. This is mainly because of the more pronounced contribution of the asperity component to the friction at the cam-roller contact. It is worth mentioning that if the asperity component would have been left out in the calculation the increase in SRR would be even more dramatic, because of additional reduction of the viscosity due to thermal effects.

Figure 15(b) depicts the variation of the central film thickness h_{cent} as a function of $f_{\mathrm{r-p}}$. It is clear that negligible roller slip, predicted by the Newtonian + isothermal model, the film thickness remains unaffected. However, due to dramatic non-linear increase predicted by the non-Newtonian + thermal model, a significant reduction in film thickness is observed from a $f_{\mathrm{r-p}}$ value of approximately 0.0575. Even at low values of $f_{\mathrm{r-p}}$ there is a small difference between the film thickness profiles obtained using both model. This mainly has to do with thermal effects as a consequence of compressive heating of the lubricant.

Figure 15(c) presents the proportions of the load carried by the interacting asperities as a function of $f_{\mathrm{r-p}}$, obtained using the two different models. As can already be imagined the F_{a}/F almost remains constant (and negligible) for throughout the full range of considered values for $f_{\mathrm{r-p}}$, when non-Newtonian and thermal effects are excluded. The profile for F_{a}/F, obtained using the non-Newtonian + thermal model, shows a rapid increase after a $f_{\mathrm{r-p}}$ value of approximately 0.0575. This can analogously be explained by means of Figure 15(b), as the film thickness and asperity component pressure are directly related.

Finally, Figure 15(d) plots the maximum temperature T_{max} within the contact as a function of $f_{\mathrm{r-p}}$. The trend of the T_{max} profile may analogously be explained using Figure 15(a), as the heat generation within the contact is proportional to the sliding velocity.

5 Conclusions

A load sharing-based mixed-TEHL model, taking into account thermal and non-Newtonian effects, has been developed to study the lubrication performance in a cam-roller follower contact. As such, the model allows roller slippage by means of a roller friction model.

A heavily loaded cam-roller follower unit was analysed by means of a quasi-static analysis. The friction coefficient at the roller-pin contact was assumed to be ideal and constant. The simulation results show that when roller-pin friction levels are low the nearly “pure rolling” condition is maintained and the cam-roller contact will also operate under ideal

circumstance, i.e. negligible slippage occurs, temperatures rise is low and the cam-roller contact almost operates in the full film regime.
Furthermore, the "sensitivity" of the tribological conditions at the cam-roller contact were assessed as a function of lubrication conditions at the roller-pin contact. The friction levels at the roller-pin contact were varied from values corresponding to full film/ ideal lubrication conditions to values corresponding to boundary lubrication conditions. In this study the results were compared with those obtained using a Newtonian + isothermal model. From this assessment the following conclusions may be drawn:

1. Non-Newtonian and thermal effects are very significant when predicting roller surface velocity (and thus the SRR) and can not be neglected.
2. The starting point at which the results between Newtonian + isothermal and non-Newtonian + thermal models deviate, are governed by the contact force, the viscosity-pressure dependency and the rheological parameters describing the non-Newtonian behaviour. In this case the characteristic Eyring shear stress τ_0.
3. Due to the higher contact forces at the nose region the cam-roller contact can sustain a higher level of roller-pin friction as compared to other regions. This mainly due to the fact that the higher contact forces cause a shift to larger friction values in the roller-pin contact (at which rapid increase in the SRR starts).
4. Once the critical value, at which non-Newtonian and thermal effects start to play an important role, the SRR rapidly increases. With this, the lubrication regime rapidly shifts from full film to mixed lubrication.
5. Based on the aforementioned conclusions, the importance of ensuring adequate lubrication in the roller-pin contact is highlighted as this appears to be the critical contact in the cam-roller follower unit.

The developed model in this work certainly contributes towards a better understanding of the coupled tribological behaviour of cam-roller and roller-pin contacts in cam-roller follower units. Therefore the model developed in this work can certainly be used as a design tool for industrial purposes, leading to more robust and efficiently operating cam-follower units.

Acknowledgements

This research was carried out under project number F21.1.13502 in the framework of the Partnership Program of the Materials innovation institute M2i (www.m2i.nl) and the Netherlands Organization for Scientific Research (www.nwo.nl).

References

[1] S. Akbarzadeh and M. Khonsari. Thermoelastohydrodynamic analysis of spur gears with consideration of surface roughness. *Tribology Letters*, 32(2):129–141, 2008.

[2] A. Akchurin, R. Bosman, P. Lugt, and M. van Drogen. On a model for the prediction of the friction coefficient in mixed lubrication based on a load-sharing concept with measured surface roughness. *Tribology Letters*, 59(1):19, 2015.

[3] S. Alakhramsing, M. de Rooij, D. Schipper, and M. van Drogen. Elastohydrodynamic lubrication of coated finite line contacts. *Proceedings of the Institution of Mechanical Engineers, Part J: Journal of Engineering Tribology*, 232(9):1077–1092, 2018.

[4] S. Alakhramsing, M. de Rooij, D. Schipper, and M. van Drogen. A full numerical solution to the coupled cam–roller and roller–pin contact in heavily loaded cam–roller follower mechanisms. *Proceedings of the Institution of Mechanical Engineers, Part J: Journal of Engineering Tribology*, 232(10):1273–1284, 2018.

[5] S. Alakhramsing, M. de Rooij, D. Schipper, and M. van Drogen. Lubrication and frictional analysis of cam–roller follower mechanisms. *Proceedings of the Institution of Mechanical Engineers, Part J: Journal of Engineering Tribology*, 232(3):347–363, 2018.

[6] S. Alakhramsing, M. de Rooij, M. van Drogen, and D. Schipper. On the influence of stick-slip transitions in mixed-friction predictions of heavily loaded cam-roller contacts. *Proceedings of the Institution of Mechanical Engineers, Part J: Journal of Engineering Tribology*, DOI:10.1177/1350650118789515, Epub ahead of print 26 July 2018.

[7] B. Andersson. Paper xviii (iii) company perspectives in vehicle tribology-volvo. *Tribology Series*, 18:503–506, 1991.

[8] S. Bair and W. Winer. A rheological model for elastohydrodynamic contacts based on primary laboratory data. *ASME Journal of Lubrication Technology*, 101:258–264, 1979.

[9] S. Bair and W. Winer. Shear strength measurements of lubricants at high pressure. *Journal of Lubrication Technology*, 101(3):251–257, 1979.

[10] G. Bayada and L. Chupin. Compressible fluid model for hydrodynamic lubrication cavitation. *Journal of Tribology*, 135(4):041702, 2013.

[11] L. Bobach, R. Beilicke, D. Bartel, and L. Deters. Thermal elastohydrodynamic simulation of involute spur gears incorporating mixed friction. *Tribology International*, 48:191–206, 2012.

[12] A. Brandt and A. Lubrecht. Multilevel matrix multiplication and fast solution of integral equations. *Journal of Computational Physics*, 90(2):348–370, 1990.

[13] P. Carreau. Rheological equations from molecular network theories. *Transactions of the Society of Rheology*, 16(1):99–127, 1972.

[14] H. Cheng. A refined solution to the thermal-elastohydrodynamic lubrication of rolling and sliding cylinders. *ASLE Transactions*, 8(4):397–410, 1965.

[15] Y. Chiu. Lubrication and slippage in roller finger follower systems in engine valve trains. *Tribology transactions*, 35(2):261–268, 1992.

[16] L.-M. Chu, H.-C. Hsu, J.-R. Lin, and Y.-P. Chang. Inverse approach for calculating temperature in ehl of line contacts. *Tribology International*, 42(8):1154–1162, 2009.

[17] D. Dowson and G. Higginson. *Elasto-hydrodynamic lubrication: the fundamentals of roller and gear lubrication*, volume 23. Pergamon Press., Oxford, United Kingdom, 1966.

[18] P. Duffy. An experimental investigation of sliding at cam to roller tappet contacts. Technical report, SAE Technical Paper 930691, 1993.

[19] H. Eyring. Viscosity, plasticity, and diffusion as examples of absolute reaction rates. *The Journal of Chemical Physics*, 4(4):283–291, 1936.

[20] E. Gelinck. *Mixed lubrication of line contacts*. PhD Thesis, University of Twente, 1998.

[21] E. Gelinck and D. Schipper. Calculation of stribeck curves for line contacts. *Tribology International*, 33(3):175–181, 2000.

[22] J. Greenwood and J. Williamson. Contact of nominally flat surfaces. *Proc. R. Soc. Lond. A*, 295(1442):300–319, 1966.

[23] C. Gu, X. Meng, Y. Xie, and J. Fan. A thermal mixed lubrication model to study the textured ring/liner conjunction. *Tribology International*, 101:178–193, 2016.

[24] F. Guo, P. Yang, and S. Qu. On the theory of thermal elastohydrodynamic lubrication at high slide-roll ratioscircular glass-steel contact solution at opposite sliding. *Journal of Tribology*, 123(4):816–821, 2001.

[25] W. Habchi. *A Full-system Finite Element Approach to Elastohydrodynamic Lubrication Problems*. PhD thesis, L 'Institut National des Sciences Appliquées de Lyon, France, 2008.

[26] W. Habchi. Coupling strategies for finite element modeling of thermal elastohydrodynamic lubrication problems. *Journal of Tribology*, 139(4):041501–041501–12, 2017.

[27] F. Ji and C. Taylor. A tribological study of roller follower valve trains. part 1: A theoretical study with a numerical lubrication model considering possible sliding. *Tribology Series*, 34:489–499, 1998.

[28] K. Johnson, J. Greenwood, and S. Poon. A simple theory of asperity contact in elastohydrodynamic lubrication. *Wear*, 19(1):91–108, 1972.

[29] K. Johnson and D. Spence. Determination of gear tooth friction by disc machine. *Tribology International*, 24(5):269–275, 1991.

[30] M. Kaneta, T. Shigeta, and P. Yang. Film pressure distributions in point contacts predicted by thermal ehl analyses. *Tribology international*, 39(8):812–819, 2006.

[31] M. Khurram, R. Mufti, R. Zahid, N. Afzal, and U. Bhutta. Experimental measurement of roller slip in end-pivoted roller follower valve train. *Proceedings of the Institution of Mechanical Engineers, Part J: Journal of Engineering Tribology*, 229(9):1047–1055, 2015.

[32] J. Lee and D. Patterson. Analysis of cam/roller follower friction and slippage in valve train systems. Technical report, SAE Technical Paper 951039, 1995.

[33] S. Li, A. Kahraman, N. Anderson, and L. Wedeven. A model to predict scuffing failures of a ball-on-disk contact. *Tribology International*, 60:233–245, 2013.

[34] S. Liu. *Thermomechanical contact analyses of rough bodies*. PhD thesis, Northwestern University, USA, 2001.

[35] T. Lohner, A. Ziegltrum, J.-P. Stemplinger, and K. Stahl. Engineering software solution for thermal elastohydrodynamic lubrication using multiphysics software. *Advances in Tribology*, vol. 2016, Article ID 6507203, 13 pages, DOI:10.1155/2016/6507203., 2016.

[36] M. Masjedi and M. Khonsari. Film thickness and asperity load formulas for line-contact elastohydrodynamic lubrication with provision for surface roughness. *Journal of Tribology*, 134(1):011503, 2012.

[37] M. Masjedi and M. Khonsari. Theoretical and experimental investigation of traction coefficient in line-contact ehl of rough surfaces. *Tribology International*, 70:179–189, 2014.

[38] M. Masjedi and M. Khonsari. An engineering approach for rapid evaluation of traction coefficient and wear in mixed ehl. *Tribology International*, 92:184–190, 2015.

[39] Y. Peiran and W. Shizhu. A generalized reynolds equation for non-newtonian thermal elastohydrodynamic lubrication. *Journal of Tribology*, 112(4):631–636, 1990.

[40] I. Polonsky and L. Keer. A numerical method for solving rough contact problems based on the multi-level multi-summation and conjugate gradient techniques. *Wear*, 231(2):206–219, 1999.

[41] F. Profito, S.-C. Vlădescu, T. Reddyhoff, and D. Dini. Transient experimental and modelling studies of laser-textured micro-grooved surfaces with a focus on piston-ring cylinder liner contacts. *Tribology International*, 113:125–136, 2017.

[42] C. Roelands. *Correlational aspects of the viscosity-temperature-pressure relationship of lubricating oils*. PhD thesis, Delft University of Technology, Delft, The Netherlands, 1966.

[43] L. Rong-Tsong and H. Chao-Ho. A fast method for the analysis of thermal-elastohydrodynamic lubrication of rolling/sliding line contacts. *Wear*, 166(1):107–117, 1993.

[44] F. Sadeghi and T. Dow. Thermal effects in rolling/sliding contacts: Part 2analysis of thermal effects in fluid film. *Journal of Tribology*, 109(3):512–517, 1987.

[45] A. Torabi, S. Akbarzadeh, and M. Salimpour. Comparison of tribological performance of roller follower and flat follower under mixed elastohydrodynamic lubrication regime. *Proceedings of the Institution of Mechanical Engineers, Part J: Journal of Engineering Tribology*, 231(8):986–996, 2017.

[46] A. Turturro, R. Rahmani, H. Rahnejat, C. Delprete, and L. Magro. Assessment of friction for cam-roller follower valve train system subjected to mixed non-newtonian regime of lubrication. In *ASME 2012 Internal Combustion Engine Division Spring Technical Conference*, pages 917–923. American Society of Mechanical Engineers, 2012.

[47] W. Wang, Y. Hu, Y. Liu, and H. Wang. Deterministic solutions and thermal analysis for mixed lubrication in point contacts. *Tribology International*, 40(4):687–693, 2007.

[48] W. Wang, Y. Liu, H. Wang, and Y. Hu. A computer thermal model of mixed lubrication in point contacts. *Transactions-American Society of Mechanical Engineers, Journal of Tribology*, 126(1):162–170, 2004.

[49] X. Wang, Y. Liu, and D. Zhu. Numerical solution of mixed thermal elastohydrodynamic lubrication in point contacts with three-dimensional surface roughness. *Journal of Tribology*, 139(1):011501, 2017.

[50] Y. Wang, H. Li, J. Tong, and P. Yang. Transient thermoelastohydrodynamic lubrication analysis of an involute spur gear. *Tribology International*, 37(10):773–782, 2004.

[51] R. Wolff and A. Kubo. The application of newton-raphson method to thermal elastohydrodynamic lubrication of line contacts. *Journal of Tribology*, 116(4):733–740, 1994.

[52] S. Wu. A penalty formulation and numerical approximation of the reynolds-hertz problem of elastohydrodynamic lubrication. *International Journal of Engineering Science*, 24(6):1001–1013, 1986.

[53] G. Xu and F. Sadeghi. Thermal ehl analysis of circular contacts with measured surface roughness. *Transactions-American Society of Mechanical Engineers, Journal of Tribology*, 118:473–483, 1996.

[54] X. Zhai and L. Chang. A transient thermal model for mixed-film contacts. *Tribology Transactions*, 43(3):427–434, 2000.

[55] D. Zhu and Y.-Z. Hu. A computer program package for the prediction of EHL and mixed lubrication characteristics, friction, subsurface stresses and flash temperatures based on measured 3D surface roughness. *Tribology Transactions*, 44(3):383–390, 2001.

Paper E

The influence of stick-slip transitions in mixed-friction predictions of heavily loaded cam-roller contacts

S.S. Alakhramsing[1], M.B. de Rooij[1], M. van Drogen[2] and D.J. Schipper[1]

Proceedings of the Institution of Mechanical Engineers, Part J: Journal of Engineering Tribology, Epub ahead of print 26 July 2018.
DOI:10.1177/1350650118789515

[1]Faculty of Engineering Technology, University of Twente, P.O. Box 217, 7500 AE Enschede, The Netherlands
[2]Central Laboratory Metals, DAF Trucks N.V., P.O. Box 90065, 5600 PT Eindhoven, The Netherlands

The influence of stick-slip transitions in mixed-friction predictions of heavily loaded cam-roller contacts

Abstract

A load-sharing-based mixed lubrication model, applicable to cam-roller contacts, is developed. Roller slippage is taken into account by means of a roller friction model. Roughness effects in the dry asperity contact component of the mixed lubrication model are taken into account by measuring the real surface topography. The proportion of normal and tangential load due to asperity interaction are obtained from a dry contact stick-slip solver. Lubrication conditions in a cam-roller follower unit, as part of the fuel injection equipment in a heavy duty Diesel engine, are analysed. Main findings are that stick-slip transitions (or variable asperity contact friction coefficient) are of crucial importance in regions of the cam where the acting contact forces are very high. The contact forces are directly related to the sliding velocity/roller slippage at the cam-roller contact and thus also to the static friction mechanism of asperity interactions. Assuming a constant asperity contact friction coefficient (or assuming that gross sliding has already occurred) in highly loaded regions may lead to large overestimation in the minimal required cam-roller contact friction coefficient in order to keep the roller rolling. The importance of including stick-slip transitions into the mixed lubrication model for the cam-roller contact is amplified with decreasing cam rotational velocity.

Keywords: EHL, cam-roller, stick-slip, rolling contact, mixed lubrication, roller slip

1 Introduction

The cam-roller follower unit as part of the fuel injection equipment in heavy duty Diesel engines are subjected to very high loads coming from the fuel injector. The pressures experienced by cam-roller contact range between 0.7GPa - 1.7GPa, corresponding to contact forces in the range of 2.5kN - 17kN.
A schematic of the considered cam-roller follower unit is shown in Figure 1. Taking a look at the cam-roller follower unit then two contacts may be distinguished namely, the cam-roller contact and the roller-pin contact. The former is a non-conformal contact, while the latter is a conformal contact. The roller itself is allowed to freely rotate along its central axis. The roller rotational velocity is a function of the driving torque (acting at the cam-roller contact), the resisting torque (acting at the roller-pin contact) and the torque due to inertial forces, as shown in Figure 1.

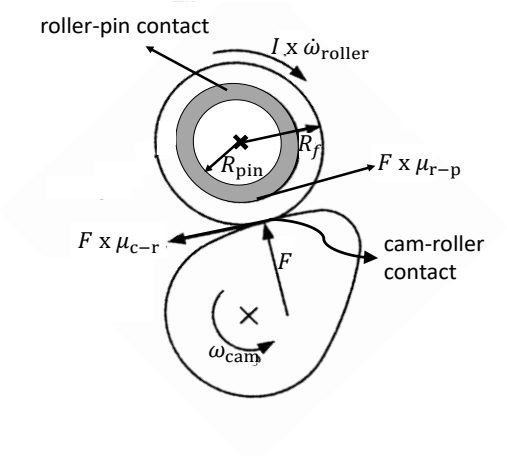

FIGURE 1: Cam-roller follower configuration showing the frictional forces acting at the cam-roller and roller-pin contact.

The preference of roller followers instead of sliding followers is nowadays more often made by manufacturers due to reduced friction losses and wear [28]. In fact, the use of roller followers leads to a very small sliding velocity at the cam-roller contact. The latter is often refereed as roller slip in the literature. Of course, the tribological designers requirement of the cam-roller follower unit is such that the almost "pure rolling" condition at the cam-roller contact should be maintained under all expected operating conditions. Roller slippage has been the subject of a number of theoretical and experimental studies, see for instance references [12, 24, 10, 17, 30]. As explained by Chiu [10] and also demonstrated in the experiments performed by Bair [4], the magnitude of roller slip is strongly governed by the acting contact force, i.e. the higher the contact force the lower the magnitude of experienced roller slippage due to enhanced traction to drive the roller. Chiu [10] and more recently Umar et al. [31] also showed that roughness effects play

an important role in mixed friction calculations of the cam-roller contact. It is worth mentioning that the previously mentioned studies treated the asperity component of the mixed lubrication model using a statistical approach. Also, only lightly loaded cam-roller units (pressures up to 0.7 GPa approximately) were investigated. Tribological behaviour of injection cam-roller follower units have been investigated by Lindholm et al. [25], however their approach relies on semi-analytical formulations for the mixed lubrication model.

Recently Alakhramsing et al. [2] presented a full transient elastohydrodynamic (EHL) model for the coupled cam-roller and roller-pin contact. The aforementioned authors simulated a cam-roller follower unit as part of the fuel injection equipment of heavy duty Diesel engines and showed that a quasi-static analysis is justified for the considered application as transient effects are negligible. Also, the results showed that for low levels of friction in the roller-pin contact the sliding velocity at the cam-roller contact remains very small. Furthermore, the obtained film thickness profiles for the cam-roller contact suggested that the cam-roller contact operates in the mixed lubrication regime.

As mentioned earlier the sliding velocity, and thus also the slide-to-roll ratio (SRR), are strongly governed by the contact force. For the considered application of fuel injection cam-roller follower units the SRR reaches values up to 10^{-6}-10^{-5} in the nose region were the contact forces are the highest [2]), i.e. in the order of 15kN - 17kN. In rolling contact problems the SRR is often referred as the creep ratio, which is a more widely used term in vehicle dynamics [37].

Due to the existence of a finite value of the SRR rather than a zero value, the contact area is divided into micro-stick and slip zones in dry rolling contacts, which are exposed to combined normal and tangential loading. A stick zone can be defined as two contacting elements or group of elements, which have no relative velocity with respect to each other, as they travel through the contact. In slip regions the aforementioned condition does not hold. In fact, when a tangential force is transmitted to the contact the contacting elements deform (elastically). The tangential force, which is related to the SRR, also causes a type of "rigid body displacement/ translation" throughout the contact. A slip element exists when the elastic deformation cannot support the displacement, i.e. the maximum tangential deformation is restricted with an upper limit of shear traction that has been reached. A sticking element is thus defined as to be when the acting shear stress over that element is less than the limiting shear stress. The most convenient way of defining the upper limit of shear traction is according to the Coulomb friction theory, i.e. the maximum (localized) shear traction is the product of normal pressure and a Coulomb friction coefficient. The moment the shear stress of an asperity exceeds this upper limit, the shear stress magnitude over the asperity is set equal to the upper limit. Gross sliding occurs at the moment when a sufficiently large SRR (and thus large tangential force) makes the entire contact area slip, i.e when the stick area disappears.

In literature one may find several (tangential) contact models which are able to compute the shear stress distribution in dry rolling contacts. Carter [7], in 1926, first described the continuum rolling theory. Later on Kalker [21], developed the linear theory. Afterward Johnson [18] and Johnson and Vermeulen [32] generalized Carter's theory to three dimensions. Kalker also developed a "Simplified theory" [22], which is implemented in FASTSIM [23], a program which is widely used in wheel-rail contact problems. Also, Kalker's exact theory CONTACT [33] is widely used as a physical model, especially in wheel-rail contact problems. It is worth mentioning that all aforementioned tractive rolling contact models are based on smooth surfaces. Extension to study the "rough" tangential contact problem, based on real measured surface roughness, were made by Zhu and Olofsson [37] and more recently by Xi et al. [35].

Coming back to cam-roller follower contact modelling, the possibility exists that the stick-slip status of the cam-roller contact under such small SRRs has not yet reached the status of gross sliding, i.e. some contacting asperities may still be in the stick mode. Predicting the mixed frictional force for the cam-roller contact using a dynamic/sliding friction coefficient, also called boundary/asperity friction coefficient in literature, might therefore largely overestimate the friction force.

The problem of large discrepancies in predicted and measured traction coefficients for very low slide-to-roll ratios (SRR) under mixed lubrication conditions, see for instance measurements in the work of Masjedi and Khonsari [27], were recently noticed and investigated by Xi et al. [36]. In reference [36] the authors utilized the concept of a linear complementarity problem (LCP)formulation [35] in order to solve the normal and tangential dry contact problem involving rough surfaces. Their conclusion was that assuming the contribution of the asperity friction contact component as a constant value, i.e. the corresponding sliding friction coefficient, might lead to an overestimation of the overall mixed friction coefficient in the low SRR domain.

From past literature one may notice that mixed-lubrication (using measured surface roughness) in the low SRR domain, where stick-slip transitions are of importance in mixed friction predictions, is not extensively described. Therefore this paper attempts to fill in this gap by presenting an efficient load-sharing-based mixed lubrication model, taking into account the real measured surface roughness and the stick-slip status of contacting asperities. As such, a special emphasize is laid on mixed friction predictions in the low SRR domain.

The model is applied to analyse the tribological behaviour of a heavily loaded cam-roller follower contact. In this study we assume a friction coefficient for the roller-pin contact in order to asses the "sensitivity" of the cam-roller lubrication performance as a function of the lubrication performance of the roller-pin contact. According to the presents author's

knowledge such an analysis, especially applied to the coupled cam-roller and roller-pin contact, has not been carried out earlier. It can be imagined that an overestimation in friction force at the cam-roller contact will automatically lead to an (numerical) increase in the friction force in the roller-pin contact (due to the governing torque balance), leading to a different picture of the overall tribological behaviour of the cam-roller follower unit.

2 Mathematical model: Mixed Lubrication

This section describes the mathematical model including the theory and governing equations. In order to reduce the required computational effort, the exact axial shape of the interacting solids is not taken into account here. Instead, the pressure distribution in the axial direction is assumed to be uniform. This simplifies the problem to that of a classical "infinite" line contact problem, i.e. a 2D problem.

As mentioned earlier, in this paper we study the lubrication conditions of a cam-roller follower unit as part of the fuel injection equipment in heavy duty Diesel engines. In reference [2] the authors motivated that for this application a quasi-static analysis yield sufficiently accurate results. Hence, the model developed in this work also relies on quasi-steady conditions.

Mixed lubrication is treated according to the load-sharing formulation of Johnson et al. [20], i.e. in the mixed lubrication regime the total load is partly carried by the contacting asperities and partly by the fluid film. In equation form this is written is follows:

$$F = \int_{\Omega} (p_{\mathrm{a}} + p_{\mathrm{h}})\, d\Omega \tag{1}$$

where p_{a} and p_{h} denote the asperity and hydrodynamic pressure, respectively. Ω represents the computational domain.

In this work the considered sliding velocities at the cam-roller contact are very small, i.e. SRRs of less than 3% are considered. Hence, the model developed herein is developed assuming isothermal conditions. The complete mixed lubrication model follows a two scale approach consisting of a smooth EHL model (macro-scale) and a dry rough contact model (micro-scale), which are used to evaluate p_{h} and p_{a}, respectively. These two models are interrelated through the separating distance, which in turn depends on the film thickness.

The frictional coefficient acting the contact includes to contribution of lubricant and asperity shear stress:

$$\mu = \frac{\int_{\Omega} (q + \tau)\, d\Omega}{F} \tag{2}$$

where μ is the friction coefficient, q is the asperity contact shear stress and τ is the shear stress of the lubricant. The dry rough contact model solves for the asperity shear traction q, which determines the stick-slip status of the contacting asperities. As explained earlier, the stick-slip status of the contacting asperities ultimately influences the contribution of the asperity frictional force to the total mixed frictional force acting at the cam-roller contact. The mixed frictional force, acting at the cam-roller contact, largely determines the roller surface velocity (and thus the lubricant mean entrainment velocity of the cam-roller contact).

The two aforementioned sub-models are described individually in the subsequent sub-sections.

2.1 Smooth EHL component

The isothermal line contact EHL model presented in this work is based on the finite element method (FEM) and stems from the pioneering work of Habchi et al. [16]. Typical EHL governing equations, applying to the cam-roller contact, are the Reynolds equation, the load balance equation and the classical linear elasticity equations. For details pertaining the numerical procedure and finite element formulations and/or coupling of the governing EHL equations the reader is asked to read reference [16] as only the main features are recalled here.

All EHL equations are presented in non-dimensional form. Hence, the following dimensionless variables are introduced:

$$\begin{aligned} X &= \frac{x}{a} \qquad Z = \frac{z}{a} \qquad P_{\mathrm{h}} = \frac{p_{\mathrm{h}}}{p_{\mathrm{Hertz}}} \quad \tilde{\eta} = \frac{\eta}{\eta_0} \quad \tilde{\rho} = \frac{\rho}{\rho_0} \\ H &= \frac{hR}{a^2} \quad H_0 = \frac{h_0 R}{a^2} \end{aligned} \tag{3}$$

with Hertzian parameters defined as follows:

$$\begin{aligned} p_{\mathrm{Hertz}} &= \frac{2F}{\pi L a} \qquad a = \sqrt{\frac{8FR}{\pi L E'}} \\ E' &= \frac{2}{\frac{1-\nu_{\mathrm{c}}^2}{E_{\mathrm{c}}} + \frac{1-\nu_{\mathrm{r}}^2}{E_{\mathrm{r}}}} \end{aligned} \tag{4}$$

ρ and η denote the density and viscosity of the lubricant respectively. L, E' and F are the axial length, reduced elasticity modulus and contact force, respectively. Subscripts "c" and "r" denote cam and roller, respectively. $R = \frac{1}{\frac{1}{R_{\mathrm{c}}} + \frac{1}{R_{\mathrm{f}}}}$ represents the reduced radius of curvature. R_{f} and R_{c} are the outer radius of the roller follower and the cam radius of curvature and (see Figure 1).

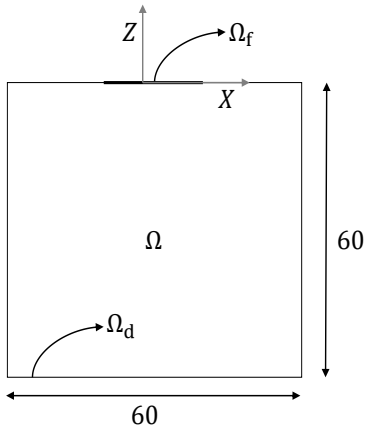

FIGURE 2: Equivalent geometry for EHL analysis of the infinite line contact problem. The dimensions are exaggerated for the sake of clarity.

Figure 2 shows the equivalent EHL computational domain Ω for the cam-roller contact. In order to reduce computational effort an equivalent elastic domain Ω (with equivalent mechanical properties) is chosen in order to accommodate for the total elastic deformation $\tilde{\delta}$. This avoids double calculation of the individual elastic deformations of the interacting solids. The dimensions of Ω, 60×60, are chosen such in order to mimic a half-space [16]. To be more specific, in order to ensure that a zero elastic displacement field is attained in regions far away from the contact region Ω_f. Ω_f denotes the fluid film boundary on which the Reynolds equation is employed, and has the dimensions of $-4.5 \leq X \leq 1.5$. Finally, Ω_d denotes the bottom boundary.

The hydrodynamic pressure distribution P_h in the contact is governed by the Reynolds equation, which is written as follows:

$$\frac{\partial}{\partial X}\left(-\frac{\tilde{\rho}H^3}{\tilde{\eta}\lambda}\frac{\partial P_h}{\partial X} + C_u H\tilde{\rho}\right) = 0 \tag{5}$$

where, $\lambda = \frac{12U_c\eta_0 R_x^2}{a^3 p_{Hertz}}$ is a dimensionless speed parameter and $C_U = \frac{U_c+U_r}{2U_c}$. Eq. 5 includes the following features/assumptions:

- Variation of density and viscosity of lubricant with pressure is simulated using the well-known Dowson-Higginson [11] and Roelands [29] relations respectively.
- The free boundary problem arising at the outlet of the contact is treated according to the penalty formulation of Wu [34].
- Suitable residual-based numerical stabilization techniques, as detailed in [16], are employed in order to stabilize the solution at high loads.
- At the inlet of the contact fully flooded conditions are assumed.

The film thickness in the cam-roller contact is written as follows:

$$H\left(X\right) = H_0 + \frac{X^2}{2} - \tilde{\delta}\left(X\right) \tag{6}$$

where, H_0 is the rigid body displacement and $\tilde{\delta}$ is total elastic deformation of the interacting solids. As mentioned earlier, the calculation of $\tilde{\delta}$ is based on a 2D-elasticity matrix [15].
The rigid body displacement H_0 is obtained by satisfying the load balance, as defined by Johnson et al. [20]:

$$\int_{\Omega_f} P\left(X\right) dX = \int_{\Omega_f} P_{\mathrm{h}}\left(X\right) dX + \int_{\Omega_f} \bar{P}_{\mathrm{a}}\left(X\right) dX = \frac{\pi}{2} \tag{7}$$

where, $\bar{P}_{\mathrm{a}}$ represents the dimensionless dry "auxiliary" mean contact pressure, the calculation of which will be treated in the "Asperity contact component" section. The term "auxiliary" has deliberately been used here as $\bar{P}_{\mathrm{a}}$ does not represent the actual asperity pressure distribution within the contact. Nevertheless, $\bar{P}_{\mathrm{a}}$ links the micro-scale dry contact model to the macroscopic smooth EHL model. As mentioned before, this will be treated in the "Asperity contact component" section. P is the summation of the individual pressure distributions $\bar{P}_{\mathrm{a}}$ and P_{h}, and is called the total pressure distribution for the sake of clarity.
The smooth EHL model for the cam-roller contact is subjected to the following boundary conditions:

- The pressure at the edges of the fluid flow boundary Ω_f equals zero.
- A zero displacement condition is imposed at bottom the boundary Ω_{D}
- For the elastic part a pressure boundary condition, with total pressure P, is imposed on the fluid flow boundary Ω_f.
- On all remaining boundaries zero stress conditions are imposed.

2.2 Asperity contact component

The contact problem between two rough surfaces is translated into that of a rough surface (with equivalent mechanical properties) against a rigid flat. Suppose that the rigid flat surface indents the rough surface by a normal load F_z along the z-axis and tangential loads F_x and F_y are applied parallel to the $x-y$ plane, then the contact interaction results in normal pressure p_a and shear tractions q_x and q_y in the interface. The general

contact model [19], for steady-state rolling contacts, is repeated here for the sake of clarity

$$u_z(x,y) = z(x,y) - h_s(x,y) \tag{8a}$$

$$\frac{\dot{s}_x(x,y)}{0.5(U_c+U_r)} = \xi_x - \frac{\partial u_x(x,y)}{\partial x} \tag{8b}$$

$$\frac{\dot{s}_y(x,y)}{0.5(U_c+U_r)} = \xi_y - \frac{\partial u_y(x,y)}{\partial y} \tag{8c}$$

where, u_x, u_y and u_z are the deformation components along the x, y and z axes, respectively. $z(x,y)$ represents the roughness profile and $h_s(x,y)$ the separating distance. ξ_x and ξ_y are the longitudinal and lateral creepages, respectively, i.e. s_x and s_y are the relative slip distances parallel to the x and y axes, respectively. In this study the tangential load F_y is assumed to be zero at all times. Hence, for the current study only unidirectional creep is considered and thus $\xi_y = 0$. Note that the longitudinal creep ratio ξ_x is nothing else but the SRR, i.e. $\xi_x = \text{SRR} = \frac{U_c - U_r}{0.5(U_c+U_r)}$

In order to solve the rough contact problem subjected to both normal and tangential loads under the stick–slip condition, one should first solve for the distribution of the asperity normal contact pressure p_a. For the current analysis it is assumed that all interacting solids share similar material properties. Hence, we can safely neglect the influence of tangential tractions q_x and q_y on relative normal displacement, and thus normal contact geometry and pressure distribution p_a [8]. With this simplification the normal contact pressure distribution p_a becomes an input for tangential contact problem (also known as the stick-slip problem.)

The complete dry contact model, including both normal contact pressure p_a and shear traction analysis q_x and q_y, is a boundary element method (BEM)-based model. In fact, for the normal contact pressures p_a calculation the elastic - perfectly plastic contact model of Akchurin et al. [1] is employed. For the tangential contact problem, the model of Bazrafshan et al. [5] is employed. Note that the model described in [5] assumes purely elastic contacts. In the current analysis it is assumed that the occurring shear stresses are insignificant to cause yielding. Hence, for the normal contact pressure p_a analysis an elastic-ideal plastic material model is used, while for the shear stress q analysis a purely elastic model is used.

The complete contact model is used to calculate the local dry/solid contact pressures and shear stresses of a representative section of the real measured surface topography. In fact, the contact model is based on the Boussinesq–Cerruti integral equations [19], which relate surface tractions to displacements. For the sake of simplicity the localized hardness and Coulomb friction law are defined as to be the upper limits of contact pressure and shear traction, respectively.

The iterative conjugate gradient method, with the assistance of the discrete convolution and fast Fourier transform (DC-FFT) algorithm, is employed to efficiently determine the unknown contact and stick area. The complete solution of the dry contact model includes the real contact area, pressure p_a, stick areas and tangential tractions q_x and q_y.

Now that the general features of the dry contact model are described, its relation to the macroscopic mixed lubrication model can be treated. Hence, this subsection is divided into two parts. The first part treats the relation of the asperity contact pressure distribution p_a to the macro-setting of the mixed lubrication model. The second part is devoted to the stick-slip problem, i.e. calculation of the local shear tractions q_x, q_y and its relation to the macro-setting of the mixed lubrication model.

2.2.1 Normal contact

The earlier described dry contact model is used to calculate the asperity contact pressures of a representative section of the real measured surface topography. The computational grid size for the contact model contained $N_x \times N_y = 250 \times 250$ data points at intervals of 0.5μm. The dimensions of the dry contact model calculation domain, which is used to solve for p_a, are $L_x \times L_y$ (for x and y-direction respectively). Note that this is the micro-scale dry contact model calculation domain and should not be confused with the macro-scale fluid film domain Ω_f. Periodic boundary conditions are imposed at the edges of the dry contact model calculation domain to calculate the representative section. For both roller and cam a randomly chosen area was used to measure the surface roughness. To give an indication, the R_a-values for the measured surface roughness of cam and roller positions are 0.135μm and 0.095μm, respectively.

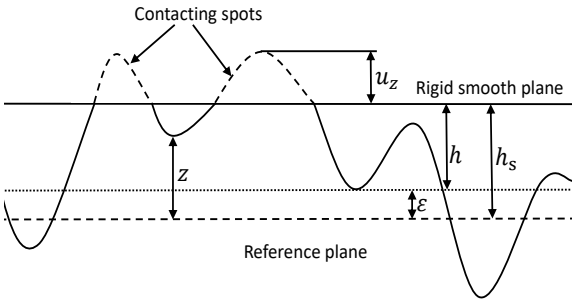

FIGURE 3: Schematic view of the surfaces which are in contact. $z(x, y)$ represents the surface roughness profile, h_s the separating distance and the deflection u_z.

Furthermore, the dry contact model relies on an linear elastic-perfectly plastic material model. Hence, the allowable contact pressures are therefore limited to a pressure $p_{\mathrm{a,lim}}$

at which plastic flow occurs. $p_{\mathrm{a,lim}}$ is therefore an input parameter to the contact model. The methodology used here to obtain the proportion of load carried by the asperities has been introduced by Bobach et al. [6]. This approach will briefly be explained now. In the mixed lubrication model a separation distance h_{s} is required to calculate the asperity contact pressure distribution p_{a} (see Figure 3). The contacting asperities fully penetrate the EHL bulk lubricant film. As defined by Johnson et al. [20], the condition of volume conservation relates the separating distance h_{s} is related to the film thickness h. To be more specific, h_{s} should fulfill the condition that the total lubricant volume between the smooth surfaces should be equal to the volume occupied by the pockets formed by the non-contacting parts between the rough surfaces. In fact, the separation distance h_{s} has the same shape as the film thickness h but with a constant offset ε so that volume conservation is preserved (see reference [1] for more details), as can be inferred from Figure 3. The offset ε is obtained iteratively in the asperity contact model, by satisfying the following equation:

$$\int_{A} h\left(x,y\right) dA = \iint_{\tilde{A}} \left(h_{\mathrm{s}}\left(x,y\right) - z\left(x,y\right) + u_z\left(x,y\right)\right) d\tilde{A} \tag{9}$$

where A is the total area and $\tilde{A}$ is the lubricated area. The set of equations, to be solved for the dry contact model are:

$$\begin{cases} u_z\left(x,y\right) = \dfrac{2}{\pi E'} \iint \dfrac{p_{\mathrm{a}}\left(x',y'\right)}{\sqrt{\left(x'-x\right)^2 + \left(y'-y\right)^2}} dx'\, dy' \\ u_z\left(x,y\right) = z\left(x,y\right) - h_{\mathrm{s}}\left(x,y\right)\ ,\ \forall\, x,y\ \in A_{\mathrm{c}} \\ p_{\mathrm{a}}\left(x,y\right) > 0\ ,\ \forall\, x,y\ \in A_{\mathrm{c}} \\ p_{\mathrm{a}}\left(x,y\right) \leq p_{\mathrm{a,lim}} \end{cases} \tag{10}$$

For the dry contact model the unknowns are $p_{\mathrm{a}}\left(x,y\right)$ and A_{c}, whereas h_{s} is related to the film thickness according to eq. 9. Now, one may define an auxiliary mean asperity contact pressure $\bar{p}_{\mathrm{a}}$ (over calculation domain $L_x L_y$) as follows:

$$\bar{p}_{\mathrm{a}} = \frac{1}{L_x L_y} \int \int p_{\mathrm{a}}\left(x,y\right) dx\, dy = \frac{F_z}{L_x L_y} \tag{11}$$

Now we may establish a functional curve of $\bar{p}_{\mathrm{a}}$ versus h_s (and indirectly h) (see Figure 4). In fact, we basically define a pre-calculated relation between auxiliary mean asperity contact pressure $\bar{p}_{\mathrm{a}}$ and film thickness h, by assuming nominally flat surfaces in contact, so that:

$$\bar{p}_{\mathrm{a}}\left(x\right) = f\left[h\left(x\right)\right] \tag{12}$$

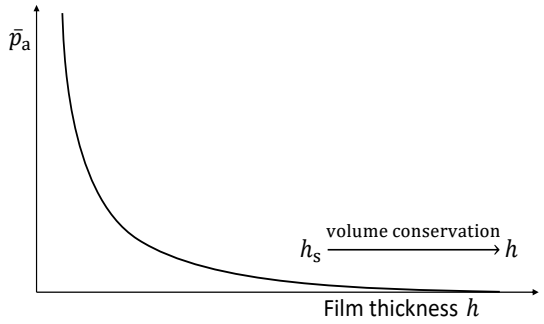

FIGURE 4: Relationship between the auxiliary mean asperity contact pressure $\bar{p}_a$ and film thickness h.

Eq. 12 can interpreted as a relation describing the "stiffness" of the contact, which describes the influence of the measured surface roughness. For the sake of simplicity we the call curve depicted in Figure 4 the "$h - \bar{p}_a$ curve" throughout this paper. It should be noted that eq. 12 can be used to evaluate any dry auxiliary mean contact pressure for any film thickness in the macroscopic setting of the mixed lubrication model.
The pre-calculated relationships eq. 12 always holds for the specific measured contact pair (which is chosen as representative section of the interacting components). The assumption here is that the surface topography does not change in time (which for example is the case in running-in of components). Also note that in study we only deal with highly loaded contacts, meaning an almost uniform film thickness distribution within the contact zone, which also justifies the usage of nominally flat surfaces in contact for the pre-calculation of the relationship given by eq. 12.
So, the developed model in this work basically "lumps/averages" the micro-effects and uses this information in the macroscopic setting of the lubrication model, for mixed friction calculations. The current method offers a more deterministic approach as it uses information from real measured surface roughness.
For usage in the load balance equation Eq. 7 the dimensionless dry auxiliary mean asperity contact pressure $\bar{P}_a$ is computed as follows:

$$\bar{P}_a(x) = \frac{\bar{p}_a(x)}{p_{\text{Hertz}}} \tag{13}$$

2.2.2 Tangential contact

For the cam-roller contact the film thickness/separation may be non-uniform and also varies as a function of the cam angle. Also, the SRR varies as a function of cam angle. In order to solve the tangential contact problem the surface roughness, normal load F_z and SRR are required. However, the way the set of eqns. 8b and 8c are formulated, the complete tangential cam-roller contact problem needs to be solved each time. This

would require huge computational effort, especially when simulating the whole cam's lateral surface. It is therefore wishful to employ a similar strategy as employed for the normal contact problem. Meaning, to establish a pre-calculated relationship between the tangential force F_x, film thickness h and SRR, for nominally flat surfaces in contact. This relationship should always hold for the specific contact pair corresponding to the pre-specified surface roughness profiles. The strategy followed will be explained now.

Tangential contact: Two nominally flat surfaces in contact

As the idea here is to relate the tangential force F_x to the film thickness h in the context of stick-slip transitions we consider, similar as was done for the normal contact problem, two nominally flat surfaces in contact. As the asperity contact pressure distribution p_a is already calculated for the normal contact problem for a given h, transmission of force F_x will induce an additional rigid body translation δ_x in x-direction, which needs to share a similar magnitude as the asperity tangential deformation u_x, for asperities in stick mode. This is evident from the general contact model (for two interacting components at rest, transmitting tangential force F_x) :

$$\begin{aligned} s_x\left(x,y\right) &= u_x\left(x,y\right) - \delta_x \\ s_y\left(x,y\right) &= u_y\left(x,y\right) - \delta_y \end{aligned} \tag{14}$$

The stick-slip code adapted here from Bazrafshan et al. [5] can be employed to solve the set of eqns. 14 for rough surfaces. From the normal asperity contact pressure analysis described earlier, the real contact area A_c is obviously also automatically evaluated. Note that the normal pressure acting on the asperity in this model is solely p_a. One should not confuse $\bar{p}_\mathrm{a}$ with p_a as $\bar{p}_\mathrm{a}$ is an auxiliary pressure and not the actual asperity contact pressure.The aforementioned should be stressed, especially due to its importance when formulating the asperity shear stress q.

The contacting elements are defined to be those where the asperity contact pressure is greater than zero, i.e. $p_{\mathrm{a(x,y)}} > 0, \forall x, y \in A_\mathrm{c}$. The real contact area A_c is composed of stick zones A_st and slip zones A_sl, which are defined as follows:

$$\begin{aligned} &\left\{ |q|_{(x,y)} \leq \mu_\mathrm{a} p_{\mathrm{a}\,(x,y)},\ |s|_{(x,y)} = 0 \right\}, \forall x, y \in A_\mathrm{st} \\ &\left\{ |q|_{(x,y)} = \mu_\mathrm{a} p_{\mathrm{a}\,(x,y)},\ |s|_{(x,y)} \neq 0 \right\}, \forall x, y \in A_\mathrm{sl} \end{aligned} \tag{15}$$

where, $|q|_{(x,y)} = \sqrt{|q_x|^2_{(x,y)} + |q_y|^2_{(x,y)}}$ and $|s|_{(x,y)} = \sqrt{|s_x|^2_{(x,y)} + |s_y|^2_{(x,y)}}$ are the shear stress and relative slip magnitudes, respectively. There is no direct metal-metal contact between contacting asperities due to the presence of boundary layers. μ_a is the Coulomb friction coefficient, which governs the friction a the boundary layers. Basically Eq. 15 states

that in the stick region the shear stress magnitude is less than the static friction and the relative slip distance is zero. The upper limit of shear traction is formulated according to the Coulomb friction theory, i.e. $|q_{\max}|_{(x,y)} = \mu_{\mathrm{a}} p_{\mathrm{a}\,(x,y)}$. The moment the shear stress of an asperity exceeds this upper limit, the shear stress magnitude over the asperity is set equal to the upper limit and micro-slip occurs. This is the most simple way of defining the upper limit for shear traction of the stick-slip problem, for opposing materials with similar mechanical properties. For stick-slip problems involving interacting solids with different hardness values, the upper limit shear stress is often assumed to be governed by hardness of the softer material [9].

The model inputs for the stick-slip model include μ_{a}, material mechanical properties and the normal loads F_z. The tangential load F_x is defined as follows:

$$F_x = \mu_{\mathrm{a}} F_z \tag{16}$$

Note that u_y is zero as F_y is zero.

A suitable initial guess for the rigid tangential translation δ_x is assumed and fed to the model. δ_x is iteratively adjusted so that the numerical integration of $q_x\,(x, y)$ over the calculation domain is equal to the specified tangential force F_x, as given by eq. 16.

If μ_{a} is increased gradually at a constant normal load F_z, then a transition curve from static to sliding friction, as a function of δ_x, can be obtained. The sliding friction coefficient, alternatively known as the asperity friction coefficient $\mu_{\mathrm{a,lim}}$, can be determined experimentally from a pin on disc setup, for example. The asperity friction coefficient $\mu_{\mathrm{a,lim}}$ should serve as an upper limit for the transition curve. Hence, for the present study $\mu_{\mathrm{a,lim}}$ is a model input parameter. In Figure 5 a schematic of such a transition curve is illustrated. Note that when $\mu_{\mathrm{a}} = \mu_{\mathrm{a,lim}}$ gross sliding takes place and $A_{\mathrm{st}} = 0$. It is worth mentioning that in this study quasi-static conditions are assumed, i.e. the loading process is slow and thus inertia effects are neglected here.

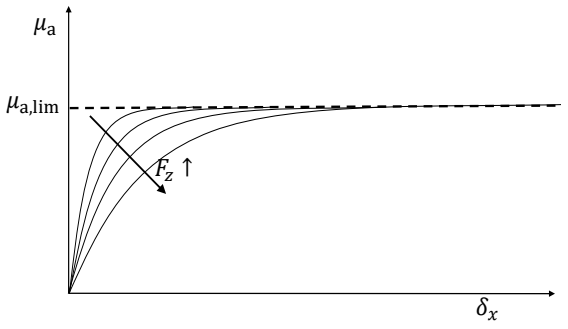

FIGURE 5: Relationship between μ_{a} and δ_x, mapped against normal load F_z. Notice all curves merging at limiting friction coefficient $\mu_{\mathrm{a,lim}}$.

Figure 5 also depicts what happens when the normal load F_z is varied. It is obvious that

when F_z is increased, i.e. the surfaces are pressed harder against each other, the distance before gross sliding takes place increases as more asperities remain in the stick mode. Analogously to eq. 12 it is possible to define a auxiliary asperity shear stress $|\bar{q}|$ as follows:

$$|\bar{q}| = \frac{1}{L_x L_y} \int \int |q|_{(x,y)} \, dx \, dy = \frac{F_x}{L_x L_y} \tag{17}$$

Note that likewise $\bar{p}_\mathrm{a}$, $|\bar{q}|$ does not represent the actual asperity shear traction distribution within the contact. Nevertheless, the purpose of using $|\bar{q}|$ is to link the micro-scale dry contact model to the macroscopic smooth EHL model as will be shown now. Firstly, eq. 16 is rewritten as follows:

$$\mu_\mathrm{a} = \frac{|\bar{q}|}{\bar{p}_\mathrm{a}} \tag{18}$$

Eq. 18 creates the possibility to relate the friction coefficient μ_a to the film thickness h according to eq. 12. Finally, it now becomes possible to establish a pre-calculated relationship between μ_a, the film thickness h and the rigid tangential translation δ_x, from the stick-slip code, as follows:

$$\mu_\mathrm{a} = f\left[h, \delta_x\right] \tag{19}$$

It should be noted that eq. 19 can be used to evaluate any (asperity) friction coefficient for any film thickness (separation) and rigid tangential translation (for the specific contacting surface roughness profiles). In fact, for each film thickness h (corresponding to a normal load F_z) a rigid tangential translation δ_x may be obtained by gradually increasing μ_a. The aforementioned procedure is then repeated for different film thicknesses. Hence, a pre-calculated 3D-map, relating μ_a, h and δ_x can be constructed and be used as an input for mixed friction calculations.

Tangential contact: Relation two nominally flat surfaces tangential contact problem to the macroscopic rolling contact problem

Note that eq. 19 describes the relationship between μ_a, h and δ_x. However, for the macroscopic rolling contact problem the SRR is another variable which needs to be considered. The relationship between SRR and the "rigid tangential displacement" δ_x will be explained now. In order to observe the direct relationship between shear stress and tangential displacements, the rolling contact equations 8b and 8c are integrated with respect to x:

$$\begin{aligned} s_x\left(x,y\right) &= \xi_x x - u_x\left(x,y\right) - C_1\left(y\right) \\ s_y\left(x,y\right) &= \xi_y x - u_y\left(x,y\right) - C_2\left(y\right) \end{aligned} \tag{20}$$

where, again $\xi_x = \mathrm{SRR}$ and C_1 and C_2 are values generated from the integration. Note

that for the current case $\xi_y = 0$ as $F_y = 0$ N. According to Kalker's simplfied theory [22], C_1 and C_2 are zero as the surface tractions q_x and q_y are zero at the leading edge of the contact. If now one compares eqns. 14 and 20 then the macroscopic rigid body displacement for the rolling contact takes the form of $\xi_x x$, i.e. SRR$\cdot x$. To be more specific, the rigid body tangential displacement δ_x as a function of x, in the macroscopic mixed lubrication model, is approximated as follows:

$$\delta_x(x) = \mathrm{SRR} \cdot x \tag{21}$$

So, for each value of x in the contact zone of the macroscopic mixed lubrication model a corresponding value of μ_a can be deduced from the pre-calculated 3D map relating μ_a, h and δ_x (according to eq. 19).
Assuming that the starting point of the $\bar{p}_\mathrm{a}(x)$ curve is $x = x_\mathrm{inlet}$, then $\delta_x(x)$ within the contact zone can be redefined as follows:

$$\delta_x(x) = \mathrm{SRR} \cdot (x - x_\mathrm{inlet}) \tag{22}$$

At this point it is worth noting that the starting point of the $\bar{p}_\mathrm{a}(x)$ curve usually is not $x_\mathrm{inlet} = -a$, i.e. the extend of the effective contact region will usually be larger than $2a$, as still some asperity contact may occur outside the dry Hertzian half-width contact region (in mixed lubrication). Greenwood et al. [14] defined a parameter $\alpha = \frac{\sigma R}{a^2}$, which serves as a measure of the influence of roughness on the Hertzian deformation. σ is the combined roughness of the two surfaces. In fact, for $0 < \alpha < 0.05$, Greenwood et al. [14] claim that the error between the rough and smooth solution is less than 7%. For all calculations in this analysis the aforementioned condition holds. Hence, for the current analysis $x_\mathrm{inlet} = -a$ can safely be used.
Once SRR and $h(x)$ are known in the macroscopic mixed lubrication model, then $\mu_\mathrm{a}(x)$ can be obtained by means of the pre-calculated 3D asperity friction map, relating μ_a, h and δ_x. In fact, for the macroscopic rolling contact problem eq. 19 may be reformulated as follows:

$$\mu_\mathrm{a}(x) = f[h(x), \delta_x(x)] \tag{23}$$

where $\delta_x(x)$ is given by eq. 22.

2.3 Calculation of roller surface velocity

The hydrodynamic shear stress τ is computed as follows:

$$\tau = -\frac{a p_{\text{Hertz}}}{R}\frac{H}{2}\frac{dP_{\text{H}}}{dX} + \frac{\eta_0 R}{a^2}\frac{\tilde{\eta}\,(U_{\text{c}} - U_{\text{r}})}{H} \tag{24}$$

Due to the very high pressures, which the cam-roller contact is subjected to, it is necessary to account for non-linear viscous effects even at low SRRs. For the friction model developed here the Eyring model [13] is adapted. Note that the Reynolds equation eq. 5 does not take into non-Newtonian behaviour as the expected shear rates are such low that its effect on film thickness and pressure distribution are assumed to be negligible. Now that the asperity component friction coefficient (given by eq. 19) is defined, the mixed friction coefficient for the cam-roller contact $\mu_{\text{c-r}}$ can be obtained as follows:

$$\mu_{\text{c-r}} = \frac{aL}{F}\int_{\Omega_{\text{f}}}\left(\tau_0\,\sinh^{-1}\left(\frac{\tau}{\tau_0}\right) + \mu_{\text{a}}\bar{P}_{\text{a}}p_{\text{Hertz}}\right)\,d\Omega \tag{25}$$

where subscript "c-r" corresponds to the cam-roller contact and L is axial length of the contact. Note that the Erying friction law is directly incorporated in eq. 25, i.e. τ_0 is the characteristic Eyring shear stress. It is also important to stress here that the asperity component friction coefficient μ_{a} is also a function of X, as defined by eq. 19. At this point it is again worth stressing that $\mu_{\text{a}}\bar{P}_{\text{a}}p_{\text{Hertz}}$ represents an up-scaling of actual shear contribution of asperities q (as defined by eq. 15) to the macro-scale.

The torque balance, which governs the roller surface velocity U_{r} is written as follows (see Figure 1):

$$\underbrace{\mu_{\text{c-r}}R_f F}_{\text{tractive torque}} = \underbrace{\mu_{\text{r-p}}R_{\text{pin}}F}_{\text{resisting torque}} + \underbrace{I\,\dot{\omega}_{\text{r}}}_{\text{inertia torque}} \tag{26}$$

where subscript "r-p" corresponds to the roller-pin contact, R_{pin} is the pin radius and ω_{r} is roller rotational velocity. In this study we consider only conditions where SRR $< 3\%$. Hence, ω_{r} can be estimated assuming pure rolling conditions and $\dot{\omega}_{\text{r}}$ can directly be obtained from graphical differentiation of ω_{r} (with respect to time).

In this study the influence of the lubrication conditions at the roller-pin contact is studied, in terms of its friction coefficient $\mu_{\text{r-p}}$, on the lubrication performance at the cam-roller contact. Hence, $\mu_{\text{r-p}}$ is an input parameter.

2.4 Numerical procedure

Figure 6 depicts the solution flow chart for the mixed lubrication model which has been developed for the cam-roller contact. In the simplified asperity contact modelling approach adapted here (subsection "Asperity contact component"), the asperity contact pressure $\bar{P}_{\mathrm{a}}$ is a direct function of the film thickness H. Furthermore, the asperity component friction coefficient μ_{a} is also a direct function of film thickness H and rigid tangential body translation δ_x (see eq. 21). The pre-calculated $h - \bar{p}_{\mathrm{a}}$ curve ($\bar{p}_{\mathrm{a}}(x) = f[h(x)]$) and asperity contact friction transition map ($\mu_{\mathrm{a}}(x) = f[h(x), \delta_x(x)]$) are valid at all times for the specific contacting surface roughness profiles studied.

Therefore the unknowns of the FEM-based mixed lubrication model are: $\left(P_{\mathrm{h}}, \tilde{\delta}, H_0, U_{\mathrm{r}}\right)$. Note that $\tilde{\delta} = \{U, W\}$ is elastic displacement vector, where U and W are deformation components in X and Z -direction, respectively.

The problem is formulated as a set of strongly coupled non-linear partial differential equations. The resulting systems of non-linear equations is then solved using a monolithic approach where all the dependent variables $(P_{\mathrm{h}}, U, W, H_0, U_{\mathrm{r}})$ are collected in one vector of unknowns and simultaneously solved using a Newton-Raphson iterative scheme. Convergence is achieved according to user specified tolerances. For specific numerical details pertaining the weak finite element formulation of the governing equations and mesh element size distribution, see references [3, 16]as only the main features are recalled here.

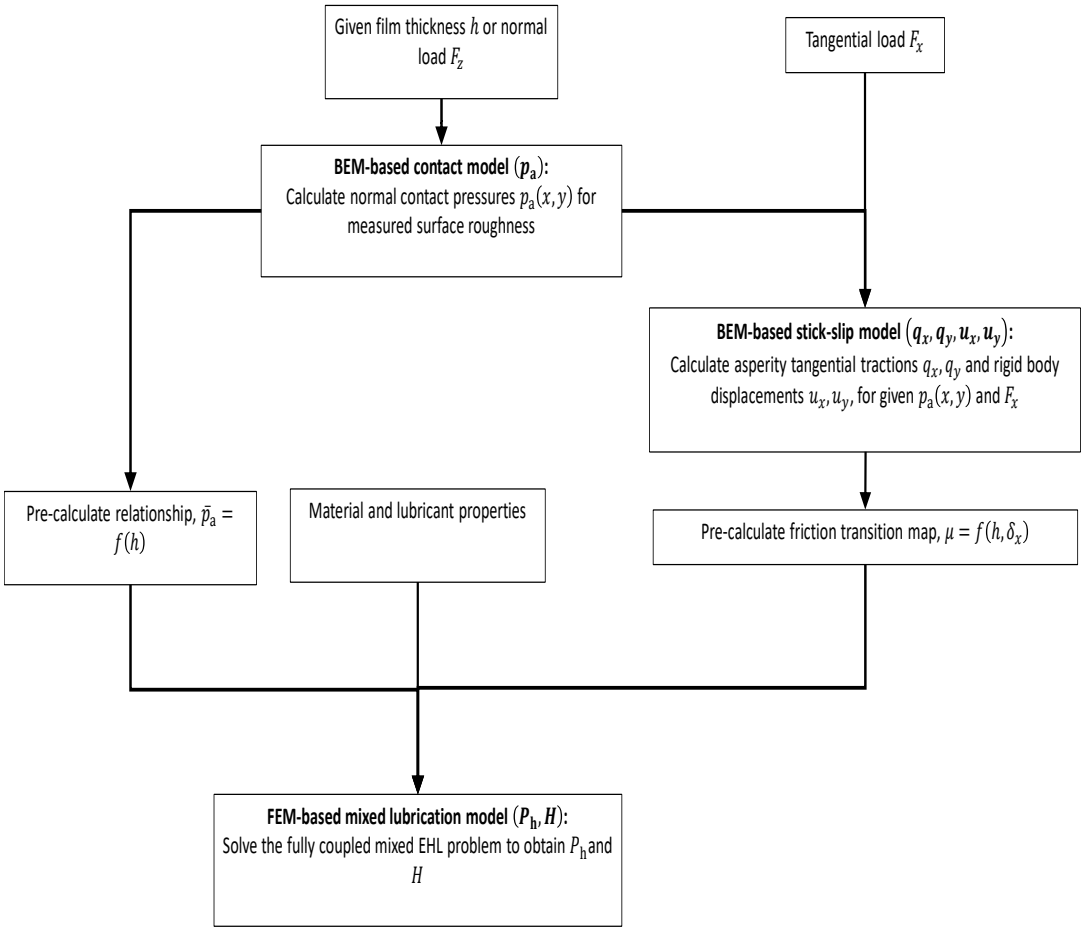

FIGURE 6: Numerical solution scheme for the cam-roller lubrication model.

3 Results

The lubricant, material, and geometrical properties of the heavily loaded cam-roller follower unit, analysed in this study, are listed in Table 1. The analysed cam-roller follower unit is part of the fuel injection system in heavy duty Diesel engines. The listed material and geometrical properties are similar to those presented in reference [2].

TABLE 1: Reference operating conditions and geometrical parameters for cam-roller follower lubrication analysis.

Parameter	Value	Unit
E_c	200	GPa
E_r	200	GPa
ν_c	0.3	-
ν_r	0.3	-
ρ_0	870	kg/m^3
α	1.84E-8	Pa^{-1}
η_0	0.013	Pa·s
τ_0	5	MPa·s
R_f	0.018	m
R_{pin}	0.0091	m
L	0.021	m
$\mu_{a,lim}$	0.12	-
$p_{a,lim}$	6	GPa

Figure 7(a) shows the calculated $h - \bar{p}_a$ curve which has been deduced by means of the mathematical model described in the "Asperity contact component" section. Again, the $h - \bar{p}_a$ curve provides the relationship between the film thickness h and auxiliary mean asperity contact pressure $\bar{p}_a$, which always holds for measured surface roughness which were used as input for the dry contact model.

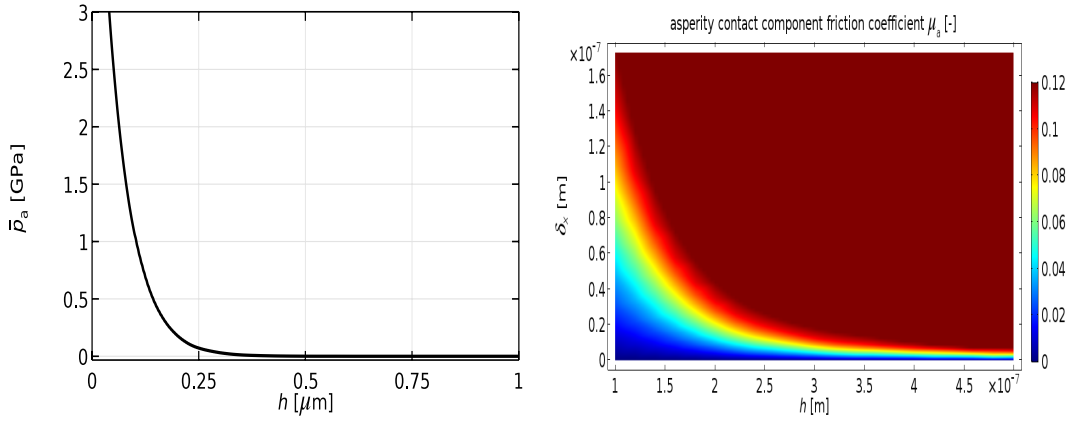

(a) (b)

FIGURE 7: a) Calculated "$h - \bar{p}_a$ curve" and b) 3D-map for the asperity contact friction coefficient μ_a as a function of the the film thickness h and rigid tangential displacement δ_x.

Similarly, Figure 7(b) presents the calculated map for the asperity contact friction coefficient μ_a as a function of the the film thickness h and rigid body tangential translation

δ_x, which has been obtained from the stick-slip model. One can directly observe the major characteristics of this asperity friction transition map. To elaborate somewhat, for a decreasing film thickness (thus for increasing normal contact loads) the distance δ_x before gross sliding takes place increases. This is expected since with increasing normal loads the asperity contact area increases, so that a larger pre-(gross) sliding distance δ_x is required.

The pre-calculated Figures 7(a) and 7(b) serve as input to the (macroscopic) mixed lubrication model (as discussed earlier by means of Figure 6). In fact, the asperity friction map is specified in n data points for different combinations of h and δ_x. The n data points are spline-interpolated with respect to h and δ_x, i.e. the discrete relation according to eq. 19 is interpolated to obtain a third-order piecewise continuous polynomial fit for μ_a versus h and δ_x. A similar procedure was utilized, but then in 2D, in order to obtain the $h - \bar{p}_\mathrm{a}$ curve.

3.1 Parametric sweep: the influence of roller-pin friction

In this section a parametric sweep is carried out in order to asses lubrication conditions at the cam-roller contact as a function of lubrication conditions in the roller-pin contact. This exercise is carried out here by means of a specified friction coefficient at the roller-pin contact. In the ideal situation the friction coefficient at the roller-pin contact, which could be classified as a lubricated journal bearing, would be dependent on the applied load. The roller-pin contact has been modelled in reference [2] in which extremely low levels of friction in the order of 0.003 were calculated. In unideal situations the frictional behaviour at the roller-pin contact may increase due external factors such as insufficient oil supply (starvation), manufacturing errors (deviation in tolerances), misalignment, particle entrapment etc. Detailed investigation into the external factors is beyond the scope of the present study. From a designers perspective it is interesting to assess the "sensitivity" of cam-roller lubrication performance as a function of the lubrication performance in the roller-pin contact. This is done here by assuming a friction coefficient at the roller-pin contact. This assessment might provide useful insight into the coupled tribological behaviour of the two contacts. Note that the friction coefficient at the roller-pin contact is independent of the applied load in this study, i.e. the resisting torque at roller-pin contact is independent from the load.

As this paper deals with the relation between roller slippage and the variable asperity coefficient μ_a (see eq. 21), it is interesting to asses two positions on the cam namely: i) the base circle, where the contact forces are the lowest and ii) the nose where the contact forces are the highest. As explained earlier in the "Introduction" section. The contact force directly influences the sliding velocity via the torque balance eq. 26. As discussed

in earlier works [2, 3], a higher contact force induces a larger tractive torque and thus less roller slippage.

Hence, for the current analysis we consider lubrication conditions at the base circle and nose position. The operating conditions are listed in Table 2 and correspond to a cam rotational velocity ω_c of 950 rpm.

TABLE 2: Reference operating conditions for base circle and nose position.

Position	F **[N]**	R **[m]**	u_c **[m/s]**
Base circle	2250	0.0152	4.62
Nose	12500	0.0105	3.98

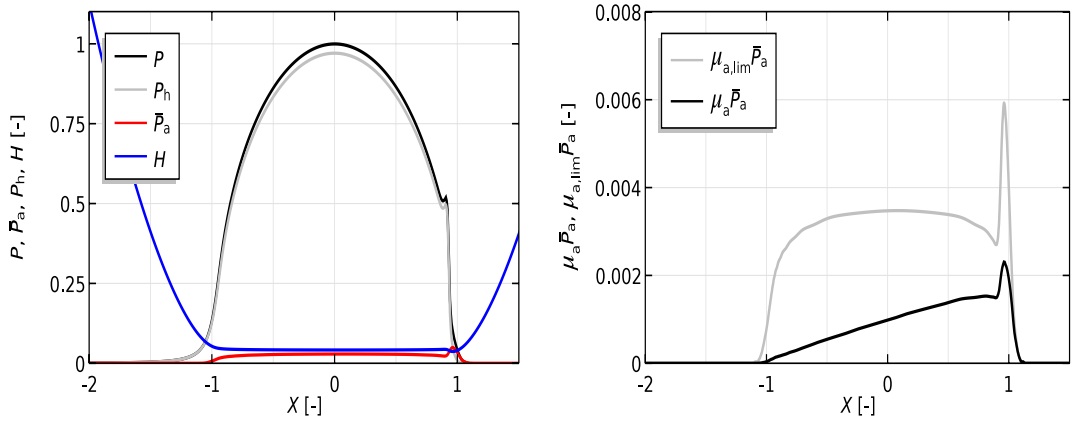

(a) (b)

FIGURE 8: a) Pressure, film thickness, and b) shear traction distributions for nose position, with $\mu_{r-p} = 0.013$.

Figure 8(a) presents the hydrodynamic, asperity and total pressure distributions, together with the dimensionless film thickness distribution for the nose position, with $\mu_{r-p} = 0.013$. Note that these profiles do not capture the actual distribution of the asperity and lubricant pressure. However, they do provide important information regarding the fraction of load carried by asperities/lubricant, and also regarding the film thickness/separation. The film thickness distribution provides information at which locations there may be potential asperity contact. From Figure 8(a) it is evident that for the considered operating conditions the asperity component pressure distribution is a small fraction of the total pressure distribution. Furthermore, when carefully looked, one may observe that still some asperity interaction occurs near the outlet of the contact as the asperity contact pressure distribution spans out further than the hydrodynamic pressure distribution. This effect is amplified in more mixed lubrication conditions (see for instance reference [26]).

As can be seen from Figure 8(b) gross-sliding has not yet been attained, for $\mu_{\mathrm{r-p}} = 0.013$, as the current asperity traction distribution $\mu_{\mathrm{a}}\bar{P}_{\mathrm{a}}$ has not fully filled up the traction bound $\mu_{\mathrm{a,lim}}\bar{P}_{\mathrm{a}}$ yet. Furthermore, from Figure 8(b) classical features of smooth rolling contacts may be observed, i.e. in the static friction regime, the traction distribution starts from a zero value at the leading edge of the contact and increases throughout the contact until the gross-sliding condition ($\mu_{\mathrm{a}}(x) = \mu_{\mathrm{a,lim}}$) has been met. It is worth mentioning that the traction does not increase linearly, which for instance is the case for Kalker's simplified theory [22]. The shear traction displacement relationship is a non-linear one which is reflected in the 3D-map relating μ_{a}, h and δ_x (see Figure 7(b)).

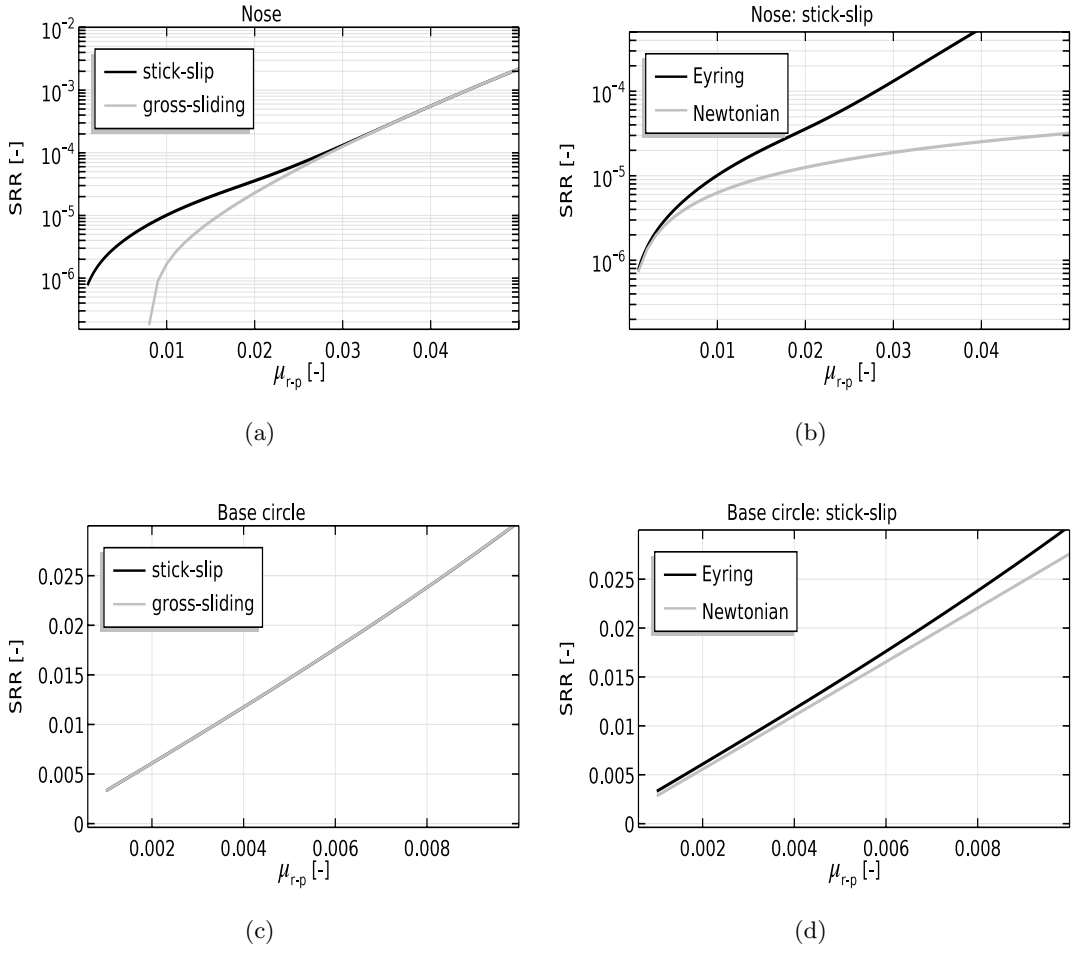

FIGURE 9: Influence of $\mu_{\mathrm{r-p}}$ on lubrication conditions at a-b) nose position and c-d) base-circle position.

Simulations are carried out in which the roller-pin friction coefficient $\mu_{\mathrm{r-p}}$ is increased from 0.001 with increments of 0.001. The simulations are stopped whenever a SRR of 3% is reached.

Figure 9(a) provides the relation between increasing values of $\mu_{\mathrm{r-p}}$ and SRR, for the

nose position. In this Figure the stick-slip results (meaning a variable asperity friction coefficient according to Figure 7(b)) are compared with those obtained by assuming the asperity friction coefficient as to be a constant and equal to $\mu_{\mathrm{a,lim}}$, i.e. assuming gross sliding. Note that SRR and $\delta_x\,(x)$ are mutually dependent through eq. 22 altogether with Figure 7(b). It is also worth explaining that an increase in $\mu_{\mathrm{r-p}}$ means that $\mu_{\mathrm{c-r}}$ automatically needs to increase proportionally. To do so, the sliding velocity needs to increase. Note that for the current application an increase in sliding velocity means a decrease in sum velocity. With this it is obvious that an increase in $\mu_{\mathrm{r-p}}$ leads to an increase in $\delta_x\,(x)$ and thus also $\mu_{\mathrm{a}}\,(x)$. Understanding this makes the interpretation of Figure 9(a) a lot easier.

Initially for low values of $\mu_{\mathrm{r-p}}$, due to the extremely high contact force the sliding velocity is naturally very small, leading to a small rigid tangential displacements $\delta_x\,(x)$. Note that during the full parametric sweep the central film thickness, which is largely dependent on the sum velocity, remains constant as SRR $< 3\%$. For the nose position the central film thickness is approximately 0.27μm. So for the initial values of $\mu_{\mathrm{r-p}}$, the combination of h and $\delta_x\,(x)$ (see Figure 9(a)) reveals that the gross sliding inception has not occurred yet, i.e. some asperities are still in the stick mode. Hence, the $\mu_{\mathrm{a}}\,(x)$ is still lower than $\mu_{\mathrm{a,lim}}$. As $\mu_{\mathrm{r-p}}$ is increased further SRR increases, and so does $\delta_x\,(x)$, up to the inception of gross sliding, which automatically explains the unification of the curves depicted in Figure 9(a). Nevertheless, the difference between the obtained results, especially for low values of $\mu_{\mathrm{r-p}}$, is large. Assuming a constant asperity friction coefficient would lead to large overestimation in the friction coefficient for both cam-roller and roller-pin contact. At this point is worth to remember that simulations were carried out with a starting value of $\mu_{\mathrm{r-p}} = 0.001$, and gradually increased. However, if one takes the look at Figure 9(a), then it is clear that under the assumption of gross sliding the value of $\mu_{\mathrm{r-p}} = 0.001$ is never attained for the gross sliding case. This can be explained as follows; the analysis here is carried out such that the shape of the film thickness/separating distance is hardly affected, i.e. the considered sliding velocities are very small. This implies that the load carried by the asperities is also hardly affected (see eq. 12). Now as earlier explained, for a given $\mu_{\mathrm{r-p}}$, the only thing which may be affected is the sliding velocity. If one assumes gross sliding, i.e. $\mu_{\mathrm{a}}\,(x) = \mu_{\mathrm{a,lim}}$, then the asperity contact contribution to the torque balance remains unchanged. Furthermore, if the specified $\mu_{\mathrm{r-p}}$ is so small such that the tractive torque due to asperity interaction on its own is already greater than the resisting torques $\left(R_{\mathrm{f}} a p_{\mathrm{Hertz}} L \int\limits_{\Omega_{\mathrm{f}}} \mu_{\mathrm{a,lim}} \bar{P}_{\mathrm{a}}\; d\Omega > (\mu_{\mathrm{r-p}} R_{\mathrm{pin}} F + I\dot{\omega}_{\mathrm{r}}) \right)$, then from a numerical perspective it means that the sliding velocity has to increase in a negative way to balance out eq. 26 by means of the hydrodynamic shear stress. To be more specific, $U_{\mathrm{r}} > U_{\mathrm{c}}$, meaning that the roller is driving the cam which of course is unrealistic. Hence, in the simulations we consider $\mu_{\mathrm{r-p}}$ from the point when SRR > 0. This explain the

discrepancy between the starting points of the curves depicted in Figure 9(a). This simply means that, under the assumption of a constant asperity contact friction coefficient, for the current operating conditions a minimum/starting value of $\mu_{\mathrm{r-p}} \approx 0.008$ for roller-pin traction would be required in order to let the cam drive the roller anyway.

Another feature of Figure 9(a) is that when a constant asperity friction coefficient is assumed the overall cam-roller contact friction coefficient is also overestimated, which logically comes along with an overestimation in tractive torque. An increase in tractive torque means a decrease in sliding velocity. This is also the reason why the minimum value of $\mu_{\mathrm{r-p}} \approx 0.008$ is coupled with a smaller value of SRR when compared to the curve obtained considering stick-slip transitions.

In the developed model in this work the Erying friction model is adapted. Even though there are much more advanced non-linear viscous models, Figure 9(b) highlights the importance of incorporating non-linear viscous effects. Figure 9(b) is obtained by accounting for stick-slip transitions. Note that the considered sliding velocities may be small but the viscosity within the lubricant film increases drastically under the high experienced pressures. It is apparent form Figure 9(b) that discrepancy between the Newtonian and Eyring friction model increases for increasing values of $\mu_{\mathrm{r-p}}$. In fact for larger values of $\mu_{\mathrm{r-p}}$ the Eyring model predicts larger SRRs. This seems to be obvious because with the Eyring model the "effective lubricant viscosity" is basically suppressed, meaning that the sliding speed needs to increase in order to compensate for this "loss" in traction.

For the base circle position no difference can be observed between the results corresponding to the stick-slip and gross sliding case (see Figure 9(c)). This is mainly due to the fact that a low contact force naturally comes with a higher SRR. Hence, $\delta_x(x)$ also is much higher for the considered range of $\mu_{\mathrm{r-p}}$. For the base circle position the inception of gross sliding has already occurred for the full range of $\mu_{\mathrm{r-p}}$ which is why nothing spectacular happens.

A similar statement can be made about the difference between results corresponding to an Eyring and Newtonian type friction model (see Figure 9(d)). In fact, due to "suppression" of the hydrodynamic shear stress in the Eyring model, the SRR is always somewhat smaller for a given $\mu_{\mathrm{r-p}}$ (when compared to the Newtonian model). As can observed from Figure 9(d), this difference increases as $\mu_{\mathrm{r-p}}$ increases. As explained earlier, this mainly due to the fact that the sliding velocity needs to increase, in the sense to increase the asperity friction (as the sum velocity decreases) and hydrodynamic friction (as the sliding velocity increases), in order to equalize the specified $\mu_{\mathrm{r-p}}$. Nevertheless, for the considered range of $\mu_{\mathrm{r-p}}$ (with SRR $< 3\%$) the non-linear viscous behaviour of lubricant is negligible as the viscosity increase is much less pronounced when compared to the nose position.

3.2 Parametric sweep: variation of cam rotational speed

From the results obtained in the previous section it can be extracted that, considering the acting contact forces at the cam-roller and roller-pin contact, including stick-slip transitions in the mixed lubrication model is important for the nose position whereas for the base-circle position these are negligible. In fact, the results showed that when a constant asperity friction coefficient is assumed for the nose position, i.e. gross sliding, the cam-roller contact friction coefficient μ_{c-r} (and thus also μ_{r-p}) are greatly overestimated. This leads to a false picture of the tribological behaviour of the contact.
Knowing this, it is also interesting to investigate what happens when for the nose position the cam rotational velocity is varied. This analysis is also carried out by means of a parametric sweep. The variation of reduced radius of curvature R, contact force F and cam surface velocity U_c as a function of the cam rotational velocity is depicted in Figure 10(a). The trend of F as a function of cam rotational velocity is extracted from a worse case scenario mapping of cam rotational speed versus the pumping load on the valve train mechanism (see reference [3] for more details on this).

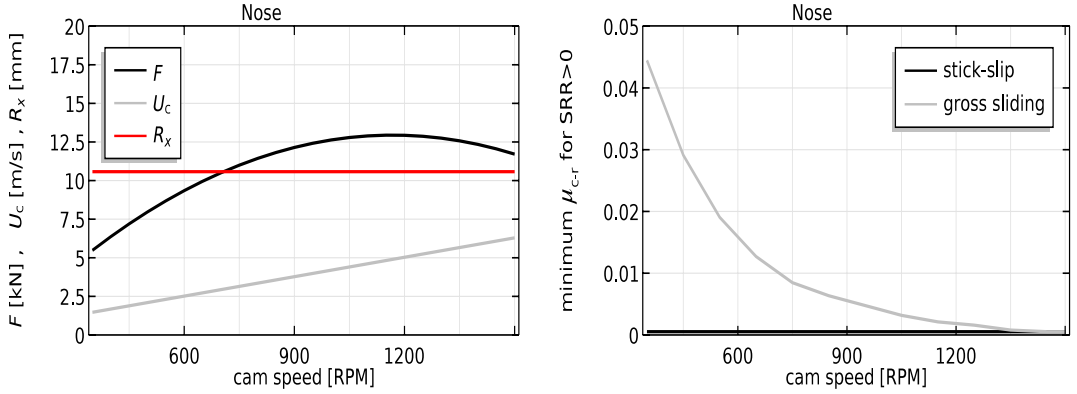

(a) (b)

FIGURE 10: a) Variation of R, F and U_c as a function of cam rotational velocity and b) minimum value of μ_{c-r} required to drive roller, as a function of cam rotational velocity.

As explained earlier the minimum value of μ_{r-p} or μ_{c-r} at which the curve SRR versus μ_{c-r} starts is defined as to be when SRR > 0. This value of μ_{c-r} represents the minimum friction coefficient which is required in order to let the cam drive the roller anyway. For a cam rotational velocity of 950RPM, this was $\mu_{c\text{ - }r} = \frac{R_{pin}\mu_{r\text{ - }p}}{R_f} + \frac{I\dot{\omega}_r}{R_f F} \approx 0.005$ (see Figure 9(a)). In Figure 10(b) the minimum required friction coefficient μ_{c-r}, in order to drive the roller, is depicted as a function of the cam rotational velocity. Results obtained by assuming a constant asperity friction coefficient (gross sliding) are compared with those considering stick-slip transitions. It is clear from this Figure that with decreasing

cam rotational speed the discrepancy between the results increases. A decrease in cam rotational velocity comes along with a direct decrease in sum velocity, meaning that the film thickness decreases. This also implies that asperity interaction increases (moving more in to the mixed lubrication regime), so that the contribution of asperity contact friction to the torque balance increases. Assuming a constant asperity friction coefficient thus automatically implies that the overall friction coefficient $\mu_{\mathrm{c-r}}$ will increase naturally. Note that the same story, explained earlier, applies here. To be more specific, given a roller-pin friction coefficient $\mu_{\mathrm{r-p}}$ and an increase in asperity friction at the cam-roller contact will directly mean a decrease in sliding velocity. Meaning that the minimum required value of $\mu_{\mathrm{c-r}}$ so that SRR > 0 will increase, i.e. the minimum required value of $\mu_{\mathrm{c-r}}$ so that the cam can actually drive the roller will increase. The aforementioned explains the trend in Figure 10(b) for the gross sliding case.

Note that the procedure for obtaining the minimum value of $\mu_{\mathrm{c-r}}$ is similar as was done in the "Parametric sweep: the influence of roller-pin friction" subsection. In fact from a starting value of $\mu_{\mathrm{r-p}} = 0.001$, $\mu_{\mathrm{r-p}}$ is gradually increased with increments of 0.001. The moment a value of $\mu_{\mathrm{r-p}}$ is archived when the condition SRR > 0 holds, the corresponding value of $\mu_{\mathrm{c\,-\,r}} = \frac{R_{\mathrm{pin}}\mu_{\mathrm{r\,-\,p}}}{R_{\mathrm{f}}} + \frac{I\dot{\omega}_{\mathrm{r}}}{R_{\mathrm{f}}F}$ is approximated as to be the minimum required friction cam-roller contact friction coefficient in order to let the cam drive the roller.

Taking a look at the curve in Figure 10(b), which accounts for stick-slip transitions than a huge difference is observed. In fact, the minimum value for $\mu_{\mathrm{c-r}} \approx 0.0005$ remains constant for the full range of cam rotational velocities considered here. This may be attributed to the fact that for the stick-slip case the asperity friction coefficient has the "ability" to adapt itself, meaning that μ_{a} basically decreases as the film thickness decreases with decreasing cam rotational velocity. This is in line with the asperity contact friction map (see Figure 7(b)). Note that the contact force also decreases with decreasing cam rotational velocity (see Figure 10(a)), however the predicted SRRs corresponding to the minimal required $\mu_{\mathrm{c-r}}$ (which are not presented here) were still small enough to keep the asperity contact component still in the static friction regime.

4 Conclusions

In this paper a FEM-based mixed lubrication model, applicable to cam-roller contacts, is developed. Surface roughness effects are efficiently taken into account by making use of the real measured surface topography. In order to calculate the proportion of normal and tangential load carried by the asperities an uncoupled approach was utilized in which pre-calculated values for the asperity friction coefficient and normal contact pressure, obtained from a BEM-based dry contact stick-slip solver, were used in the macroscopic setting of the mixed lubrication model.

The lubrication performance in a cam-roller follower unit, as part of the fuel injection equipment in heavy duty Diesel engines, was analysed. The lubrication conditions in two regions of the cam were analysed, namely specific positions on the base circle and nose region. Results show that stick-slip effects on asperity scale are of crucial importance in regions of the cam where high contact forces occur such as the nose region. Assuming a constant asperity contact friction coefficient (or gross sliding) in these regions may lead to large overestimation in required friction coefficient in order to let the cam actually drive the roller. For the constant asperity friction coefficient case (in the nose region) the overestimation in required cam-roller friction coefficient increases with decreasing cam rotational velocity as the film thickness decreases (and thus the asperity frictional force increases). The importance of including stick-slip transitions into the mixed lubrication model for the cam-roller contact is thus amplified with decreasing cam rotational velocity. In order to simulate non-linear viscous behaviour of the lubricant in the frictional model, the Eyring friction model was adapted for the sake of simplicity. It was highlighted that for the heavily loaded regions, such as the nose, non-linear viscous behaviour influences the SRR and thus also the stick-slip transitions.
For the base-circle regions the acting contact forces are much less when compared to the nose regions. Consequently, the roller slippage is much larger on base circle positions and thus has the inception of gross sliding already occurred. Hence, for base-circle regions inclusion of stick-slip effects are negligible. Also, for the considered range of SRRs in this study, non-linear viscous effects of lubricant in base-circle positions are negligible due to the lower pressures which the lubricant experiences.
The focus of this work was on the low SRR domain. At higher levels of friction at the roller-pin contact the SRR will increase indicating that non-Newtonian and thermal effects will become highly important. As such, highly non-linear effects may occur. Thus, for a more "unified" model (i.e. also valid for the high SRR domain, i.e. high shear rates) more up to date rheological formulations (see for instance [16]) should be used, and also inclusion of non-Newtonian and thermal effects become inevitable.

Acknowledgements

This research was carried out under project number F21.1.13502 in the framework of the Partnership Program of the Materials innovation institute M2i (www.m2i.nl) and the Netherlands Organization for Scientific Research (www.nwo.nl).

References

[1] A. Akchurin, R. Bosman, P. Lugt, and M. van Drogen. On a model for the prediction of the friction coefficient in mixed lubrication based on a load-sharing concept with measured surface roughness. *Tribology Letters*, 59(1):19, 2015.

[2] S. Alakhramsing, M. de Rooij, D. Schipper, and M. van Drogen. A full numerical solution to the coupled cam–roller and roller–pin contact in heavily loaded cam–roller follower mechanisms. *Proceedings of the Institution of Mechanical Engineers, Part J: Journal of Engineering Tribology*, 232(10):1273–1284, 2018.

[3] S. Alakhramsing, M. de Rooij, D. Schipper, and M. van Drogen. Lubrication and frictional analysis of cam–roller follower mechanisms. *Proceedings of the Institution of Mechanical Engineers, Part J: Journal of Engineering Tribology*, 232(3):347–363, 2018.

[4] S. Bair and W. Winer. Paper vi (v) A technique for measuring roller follower skidding on automotive camshafts. *Tribology Series*, 18:157–162, 1991.

[5] M. Bazrafshan, M. de Rooij, and D. Schipper. On the role of adhesion and roughness in stick-slip transition at the contact of two bodies: A numerical study. *Tribology International*, 121:381–388, 2018.

[6] L. Bobach, R. Beilicke, D. Bartel, and L. Deters. Thermal elastohydrodynamic simulation of involute spur gears incorporating mixed friction. *Tribology International*, 48:191–206, 2012.

[7] F. Carter et al. On the action of a locomotive driving wheel. In *Proc. R. Soc. Lond. A*, volume 112, pages 151–157. The Royal Society, 1926.

[8] W. Chen and Q. Wang. A numerical model for the point contact of dissimilar materials considering tangential tractions. *Mechanics of Materials*, 40(11):936–948, 2008.

[9] W. Chen and Q. Wang. A numerical static friction model for spherical contacts of rough surfaces, influence of load, material, and roughness. *Journal of Tribology*, 131(2):021402–021402–8, 2009.

[10] Y. Chiu. Lubrication and slippage in roller finger follower systems in engine valve trains. *Tribology Transactions*, 35(2):261–268, 1992.

[11] D. Dowson and G. Higginson. *Elasto-hydrodynamic lubrication: the fundamentals of roller and gear lubrication*, volume 23. Pergamon Press., Oxford, United Kingdom, 1966.

[12] P. Duffy. An experimental investigation of sliding at cam to roller tappet contacts. Technical report, SAE Technical Paper 930691, 1993.

[13] H. Eyring. Viscosity, plasticity, and diffusion as examples of absolute reaction rates. *The Journal of Chemical Physics*, 4(4):283–291, 1936.

[14] J. Greenwood, K. Johnson, and E. Matsubara. A surface roughness parameter in Hertz contact. *Wear*, 100(1-3):47–57, 1984.

[15] W. Habchi. Coupling strategies for finite element modeling of thermal elastohydrodynamic lubrication problems. *Journal of Tribology*, 139(4):041501–041501–12, 2017.

[16] W. Habchi, D. Eyheramendy, P. Vergne, and G. Morales-Espejel. Stabilized fully-coupled finite elements for elastohydrodynamic lubrication problems. *Advances in Engineering Software*, 46(1):4–18, 2012.

[17] F. Ji and C. Taylor. A tribological study of roller follower valve trains. part 1: A theoretical study with a numerical lubrication model considering possible sliding. *Tribology Series*, 34:489–499, 1998.

[18] K. Johnson. The effect of a tangential contact force upon the rolling motion of an elastic sphere on a plane. *Journal of Applied Mechanics*, 25(3):339–346, 1958.

[19] K. Johnson. *Contact Mechanics.* Cambridge University Press, London, 1985.

[20] K. Johnson, J. Greenwood, and S. Poon. A simple theory of asperity contact in elastohydro-dynamic lubrication. *Wear*, 19(1):91–108, 1972.

[21] J. Kalker. *On the rolling contact of two elastic bodies in the presence of dry friction.* PhD thesis, Delft University of Technology, Delft, The Netherlands, 1967.

[22] J. Kalker. Simplified theory of rolling contact. *Delft Progress Rep.*, 1(1):1–10, 1973.

[23] J. Kalker. A fast algorithm for the simplified theory of rolling contact. *Vehicle System Dynamics*, 11(1):1–13, 1982.

[24] M. Khurram, R. Mufti, R. Zahid, N. Afzal, and U. Bhutta. Experimental measurement of roller slip in end-pivoted roller follower valve train. *Proceedings of the Institution of Mechanical Engineers, Part J: Journal of Engineering Tribology*, 229(9):1047–1055, 2015.

[25] P. Lindholm, C. Spiegelberg, S. Andersson, and S. Björklund. Contact conditions in a cam and roller contact. In *World Tribology Congress WTC 2001*, page 4, 2001.

[26] M. Masjedi and M. Khonsari. Film thickness and asperity load formulas for line-contact elastohydrodynamic lubrication with provision for surface roughness. *Journal of Tribology*, 134(1):011503, 2012.

[27] M. Masjedi and M. Khonsari. An engineering approach for rapid evaluation of traction coefficient and wear in mixed ehl. *Tribology International*, 92:184–190, 2015.

[28] N. Miyamura. Fuel saving in internal-combustion engines. *Journal of Japanese Society of Tribologists*, 36(11):855–859, 1991.

[29] C. Roelands. *Correlational aspects of the viscosity-temperature-pressure relationship of lubricating oils*. PhD thesis, Delft University of Technology, Delft, The Netherlands, 1966.

[30] A. Turturro, R. Rahmani, H. Rahnejat, C. Delprete, and L. Magro. Assessment of friction for cam-roller follower valve train system subjected to mixed non-newtonian regime of lubrication. In *ASME 2012 Internal Combustion Engine Division Spring Technical Conference*, pages 917–923. American Society of Mechanical Engineers, 2012.

[31] M. Umar, R. Mufti, and M. Khurram. Effect of flash temperature on engine valve train friction. *Tribology International*, 118:170–179, 2017.

[32] P. Vermeulen and K. Johnson. Contact of nonspherical elastic bodies transmitting tangential forces. *Journal of Applied Mechanics*, 31:338, 1964.

[33] E. Vollebregt. User guide for contact, Vollebregt & Kalkers rolling and sliding contact model. *Techical report TR09-03, version*, 13, 2013.

[34] S. Wu. A penalty formulation and numerical approximation of the reynolds-hertz problem of elastohydrodynamic lubrication. *International Journal of Engineering Science*, 24(6):1001–1013, 1986.

[35] Y. Xi, A. Almqvist, Y. Shi, J. Mao, and R. Larsson. Linear complementarity framework for 3d steady-state rolling contact problems including creepages with isotropic and anisotropic friction for circular hertzian contact. *Tribology Transactions*, 60(5):832–844, 2017.

[36] Y. Xi, M. Björling, Y. Shi, J. Mao, and R. Larsson. Traction formula for rolling-sliding contacts in consideration of roughness under low slide to roll ratios. *Tribology International*, 104:263–271, 2016.

[37] Y. Zhu and U. Olofsson. An adhesion model for wheel–rail contact at the micro level using measured 3D surfaces. *Wear*, 314(1-2):162–170, 2014.